Nano-Enabled Electronic Devices for Sensing and Energy Harvesting

A thesis submitted

in partial fulfillment of the requirements

for the degree of

Doctor of Philosophy

by

Mitradip Bhattacharjee

Centre for Nanotechnology

Indian Institute of Technology Guwahati

November 2018

C E R T I F I C A T E

It is certified that the works contained in this thesis entitled **"Nano-Enabled Electronic Devices for Sensing and Energy Harvesting"**, by Mr. Mitradip Bhattacharjee, have been carried out under our supervision and have not been submitted as a thesis elsewhere for a Ph.D degree.

Thesis supervisors

Dr. Dipankar Bandyopadhyay
Associate Professor
Department of Chemical Engineering
Indian Institute of Technology Guwahati

Dr. Harshal B. Nemade
Professor
Department of Electronics and Electrical Engineering
Indian Institute of Technology Guwahati

November 2018

Declaration

I hereby declare that the thesis entitled "Nano-enabled electronic devices for sensing and energy harvesting" contains original research work. Any content of the thesis has not been taken from anywhere else. This thesis has not been submitted elsewhere for obtaining the degree of Doctor of Philosophy.

Mitradip Bhattacharjee
Research Scholar
Centre for Nanotechnology
Indian Institute of Technology Guwahati, India.

ACKNOWLEDGEMENT

Working for the accomplishment of this thesis has been the most incredible journey of my life, which would not have been possible without these people.

First and foremost, I would like to thank my thesis supervisors **Prof. Dipankar Bandyopadhyay** and **Prof. Harshal B. Nemade** for giving me an opportunity to work in a very interesting area of research. I am very grateful to them for their continuous guidance, important advices and stimulating discussions. In spite of their busy schedule, they always happily spent time to analyze the problems and gave needed suggestions for the betterment of my work. Some of their remarkable qualities such as, patience and devotion towards their work, their continuous zeal to achieve perfection, and a very attractive communication skill, will always inspire me. The experience of working with them will definitely have far-reaching influence in my life. I consider it an honor to work under them.

I wish to thank my doctoral committee members, **Prof. Animes Kr. Golder**, and **Prof. Partho Sarathi Gooh Pattader**, Department of Chemical Engineering, **Prof. B. Anand**, Department of Biosciences and Bioengineering, for their valuable suggestions and efforts during my thesis work.

My sincere thanks to **Dr. A. Ananth Praveen Kumar** and **Dr. Kartick Mondal,** alumni from our research group, and **Dr. Nayanmani Das,** Institute Post-Doctoral Fellow, for their co-operative assistance in learning the basic concepts and providing me with continuous encouragement throughout my PhD tenure. I wish to express my deepest gratitude to **Prof. Sarmishtha Banerjee, Mr. Ankit Chowdhury, and Mr. Poorvish Shah** Department of Design for her insightful comments and suggestions regarding the design and aesthetics of the prototypes developed. I also wish to extend my gratitude to **Mr. Sahil Jagnani** from Forus Electric Pvt. Ltd. New Delhi for his support, suggestion and help to develop commercial prototypes. Also, I am particularly grateful to **Mr. Amit Kumar Singh, Mr. Viswanath Pasumarthi, Mr. Joydip Chaudhuri, Dr. Seim Timung, Mr. Sagnik Middya, Ms. Prasfutita Paul, Dr. Madhumita Das** and **Mr. Nilanjan Mandal,** for their supports in experiments and computations.

I am also thankful to all of our research group members **Ms. Abhijna Das, Mr. Abhinav Sharma, Mr. Abir Ghosh, Mr. Amit Kumar Singh, Dr. Seim Timung, Mr. Ankur Pandey, Ms. Anuja Tripathi, Mr. Bhaskarjyoti Sharma, Mrs. Binita Nath, Mr. Bolleddu Ravi, Mr. Debdatta Ghosh, Mr. Debendra Nath Sarkar, Mr. Divesh Ranjan, Mr. Jayant Borana, Mr. Joydip Chaudhuri, Mr. Manash Pratim Borthakur, Mr. Nilanjan Mandal, Mr. Pritam Roy, Md. Rashid Ali Faridi, Dr. Saptak Rarotra, Ms. Satarupa Dutta, Mr. Shaik Shahid, Ms. Snigdha Chakraborty, Ms. Shreya Mukherjee, Mr. Shirsendu Mitra, Mr. Siddharth Thakur, Dr. Sunny Kumar, Mr. Surjendu Maity, Mr. Anvesh Dixit, Mr. Ankit Chowdhury, Mr. Poorvish Shah, Mrs. Tamanna Bhuyan, Ms. Tanusree Ghosal, Mr. Subhradip Ghosh, Mr. Prathu Parmar, Ms. Mitali Basak** and last but not the least **Mr. Viswanath Pasumarthi.** I cannot forget to thank my friends and seniors **Mr. Abhik Bhattacharjee, Mr. Ashim Malakar**, **Mr. Biki Teron, Mr. Jitendra Kumar, Mr. Shyam Trivedi, Mr. Ujjowl Barman, Dr. Ravi Biroju, Mr. Rajan Singh, Ms. Paromita Bhattacharjee, Mr. Siddhanta Roy, Ms. Upashi Goswami, Dr. Madhumita Das, Mr. Somorjit Singh, Ms. Deepanjali Dutta, Ms. Larionette Mawlong, Ms. Anamika Dey, Ms. Anamika Kalita, Mr. Ashish Singh, Mr. Dipjyoti Das** and **Mrs. Namami Goswami,** for the lovely support in making my stay at IIT Guwahati memorable.

My special thanks goes to all the faculty and staff members of **Centre for Nanotechnology**, and **Central Instruments Facility**, **IIT Guwahati,** for their supports and co-operations during all this time.

I also wish to convey my sincere gratitude to obtain financial support through the **MeitY grant no. 5(9)/2012-NANO** and facilities through the **DST-SERB, grant no. SR/S3/CE/0079/2010**.

Above all, I wish to thank my **parents, friends,** and **family members** for their love and support throughout everything, as always.

I dedicate this thesis to my *Family.*

MITRADIP BHATTACHARJEE

SYNOPSIS

Nano-Enabled Electronic Devices for Sensing and Energy Harvesting

The present thesis explores a host of pathways to develop proof-of-concept prototypes targeting biomedical applications, environmental monitoring, and renewable energy harvesting. The technical chapters in the thesis are preceded by an introductory chapter in the CHAPTER 1 while at the end of the thesis the CHAPTER 10 containing the summary and future scopes. The technical chapters of the thesis have been divided into three primary sub-sections which include, (I) Microfluidic Sensors, (II) Paper Sensors, and (III) Electronic Sensors. The Microfluidic Sensor part contains two different technical chapters, (i) CHAPTER 2 – Self-spinning nanoparticle laden microdroplets for sensing and energy harvesting and (ii) CHAPTER 3 – Droplet based detection of blood α-amylase employing thermal Marangoni effect. The Paper Sensor part contains three different technical chapters, (i) CHAPTER 4 – Paper based flexible touchpad and hand tremor detection device; (ii) CHAPTER 5 – Nano-enabled paper humidity sensor for mobile based point-of-care lung function monitoring; and (iii) CHAPTER 6 – Paper Based GMR Nanobiosensor for α-Amylase Estimation under Impulse Magnetic Field. Finally, the Electronic Sensors part contain three more chapters, (i) CHAPTER 7 – A nano-BG-FET for point-of-care estimation of ammonia and urea in human urine, (ii) CHAPTER 8 – A body-potential detection system employing micro/nano patterned electrode, and (iii) CHAPTER 9 – Conversion of Observed Speed of a Moving Object to Diagnose Tunnel Vision. A brief detail of outcomes of this thesis in terms of publications, patents, conferences, and awards has been provided as an APPENDIX.

Objective – 1: Self-Spinning Nanoparticle Laden Microdroplets for Sensing and Energy Harvesting

In this chapter, a droplet based organic vapor sensor and energy harvester have been demonstrated. Exposure of a volatile organic vapor could set in powerful rotational motion in a microdroplet composed of an aqueous salt solution loaded with metal nanoparticles. The solutal Marangoni motion on the surface originating from the sharp difference in the surface tension of water and organic vapor stimulated the strong vortices inside the droplet.

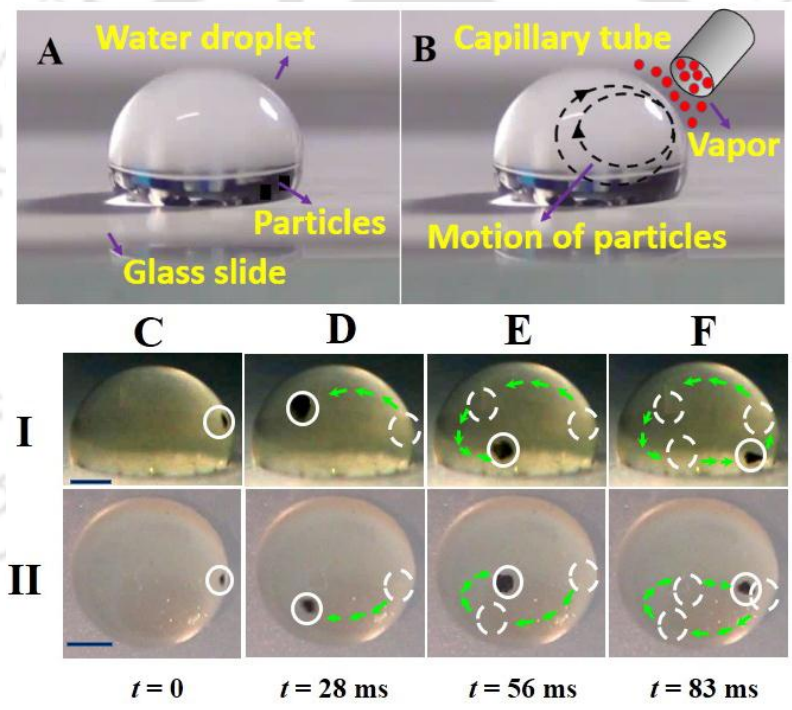

Figure 1: Experimental demonstration of the phenomenon. (A) A water droplet loaded with some microparticles was placed on a glass slide. The microparticles helped in quantification of the rotational motion inside the droplet. (B) A rotational current was observed on the droplet when a vapor source of diethyl ether was brought into the immediate vicinity of the droplet surface. (C – F) Experimental images of particle motion. Rows I and II show the side and the top views of the motion under the exposure of the organic vapor when loaded with a single microparticle. The length of the scale bars on the images is 0.5 mm.

The vapor sources of methanol, ethanol, diethyl ether, toluene, and chloroform stimulated motions of different magnitudes, which could easily be correlated to the surface tension gradient on the drop-surface. Interestingly, when the nanoparticle laden droplet of aqueous

salt solution was connected to an external electric circuit through a pair of electrodes, ~85 – 95% reduction in the electrical resistance was observed across the spinning droplet. The extent of reduction in the resistance was found to have correlation with the difference in the surface tension of the vapor source and the water droplet, which could be employed to distinguish the vapor sources. Remarkably, the power density of the same prototype was estimated to be around 7 $\mu W/cm^2$, which indicated the potential of the phenomenon in converting surface energy into the electrical one in a non-destructive manner and under ambient condition. Theoretical analysis uncovered that the difference in the ζ-potential near the electrodes was the major reason for the voltage generation. The prototype could also detect the repeated exposure and withdrawal of vapor sources, which helped in the development of a proof-of-concept detector to sense alcohol issuing out of the human breathing system.

Objective – 2: Droplet Based Detection of Blood α-Amylase Employing Marangoni Flow

In this chapter, a droplet based α-amylase sensor has been demonstrated. A droplet based microfluidic amylase detection technique was developed employing the thermal Marangoni effect. A rotational motion was observed inside a water droplet when it was placed on a hot surface. The motion was quantified with a ~120 μm particle and it was found that the motion was ~12 rpm when the hot surface temperature was maintained at 60^0C. A finite element computational study shows that the variation in surface tension near the plate and away from the plate due to the temperature variation gives rise to the rotational motion of the fluid inside the droplet. The temperature distribution inside the droplet was studied to understand the physics.

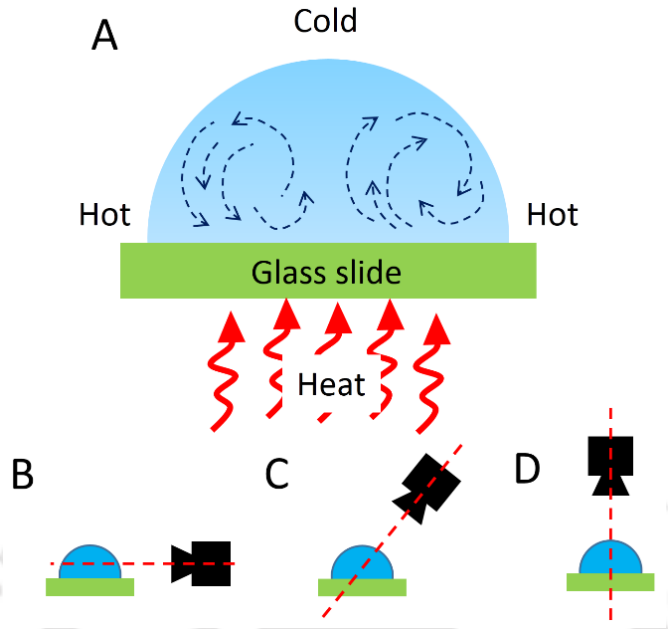

Figure 2: Image (A) shows the schematic diagram of the experimental set-up for characterizing the microfluidic phenomenon. Images (B – D) shows the placement of digital or thermal camera for imaging.

It was observed that the temperature near the plate was higher compared to away from the surface as shown by the computational study. Starch was dissolved in the conductive droplet and the droplet system was further employed for detecting amylase concentration in blood serum. A concentration of 20-90 U/L could be detected faithfully. Experimental study suggested that the detection was most efficient at 40^0C substrate temperature. This system can be employed as point-of-care testing device to detect amylase in blood serum.

Objective – 3: Paper based flexible touchpad and hand tremor detection device

In this chapter, development of a paper based economic resistive touchpad and the application in hand tremor detection has been discussed. An economic and eco-friendly resistive touchpad was designed, fabricated, and tested from commonly available materials such as paper, poly-dimethylsiloxane (PDMS), and graphite coating issuing out of the pencil tips. While the graphite coating on one side of a paper surface transformed the

dielectric paper surface into an electrically conducting one, the dielectric PDMS thin film on the other side of the paper acted as a protective coating.

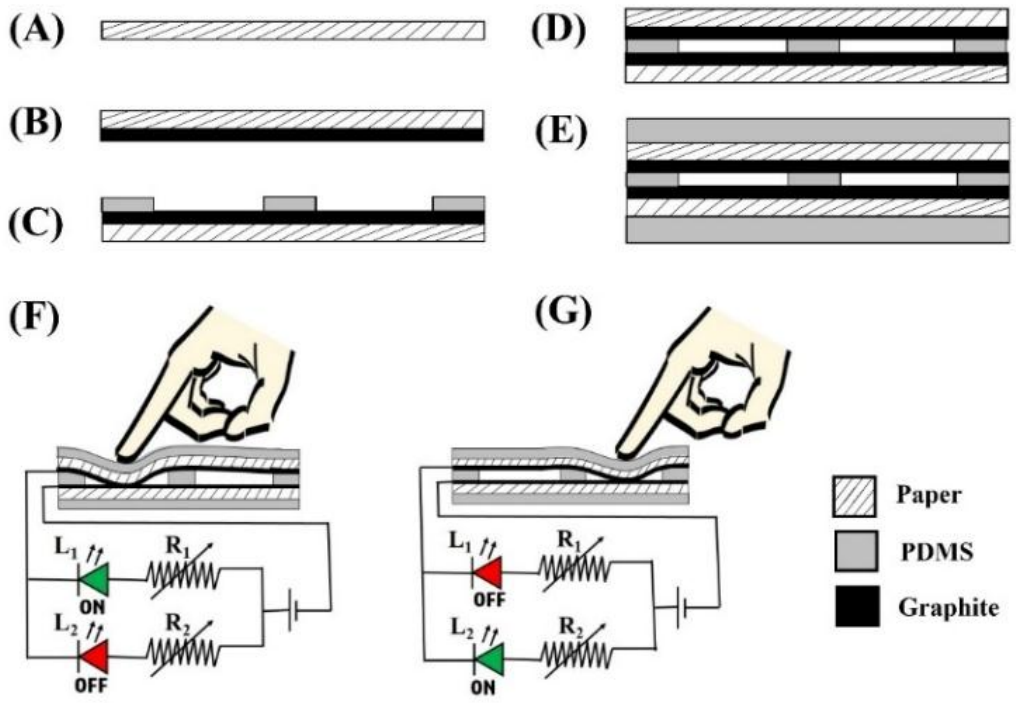

Figure 3: This figure shows the fabrication process and illustration of working. Image (A) - (F) show the different steps of fabricating the touchpad device. Image (F) and (G) illustrates the working of the touchpad.

A pair of such graphite and PDMS coated paper surfaces was integrated together in such a manner that there was an air gap maintained in between them with the help of a dielectric PDMS spacer. The PDMS thin films coated on the outer surface of the paper were aimed to host the touch locations, the graphitic coating on the inner side of the paper provided the required electrical conductance to develop the 'resistive' pad, and the PDMS spacer in the middle of two such papers surfaces created the necessary air gap between the pair of confining paper surfaces. The work was further extended into development of a biomedical device to detect hand tremor in order to diagnose different neurological disorders such as Parkinson's disease. In this case, a single location of touchpad was fabricated as discussed earlier and employed vertically to develop the hand tremor detection system.

Objective – 4: Nano-Enabled Paper Humidity Sensor for Mobile Based Point-of-Care Lung Function Monitoring

In this chapter, the research is about a nano-enebled paper humidity sensor for monitoring lung health. The frequency of breathing and peak flow rate of exhaled air are necessary parameters to detect chronic obstructive pulmonary diseases (COPDs) such as asthma, bronchitis, or pneumonia. We developed a lung function monitoring point-of-care-testing device (LFM-POCT) consisting of mouthpiece, paper-based humidity sensor, micro-heater, and real-time monitoring unit. The mouthpiece of optimal length was ensured that the exhaled air was focused on the humidity-sensor. The resistive relative humidity sensor was developed using a filter paper coated with nanoparticles, which could easily follow the frequency and peak flow rate of the human breathing. Adsorption followed by condensation of the water molecules of the humid air on the paper-sensor during the forced exhalation reduced the electrical resistance of the sensor, which was converted to an electrical signal for sensing. A micro-heater composed of a copper-coil embedded in a polymer matrix helped in maintaining an optimal temperature of the sensor, which ensured that water condensed only during forcible breathing and the sensor recovered rapidly after the exhalation was complete by desorption of water molecules.

Two types of real-time monitoring units were integrated into the device based on light emitting diodes (LEDs) and smart phones. The LED based unit displayed the diseased, critical, and fit conditions of the lungs by flashing LEDs of different colors. In comparison, for the mobile based monitoring unit, an application was developed employing an open source software, which established a wireless connectivity with the LFM-POCT device to perform the tests.

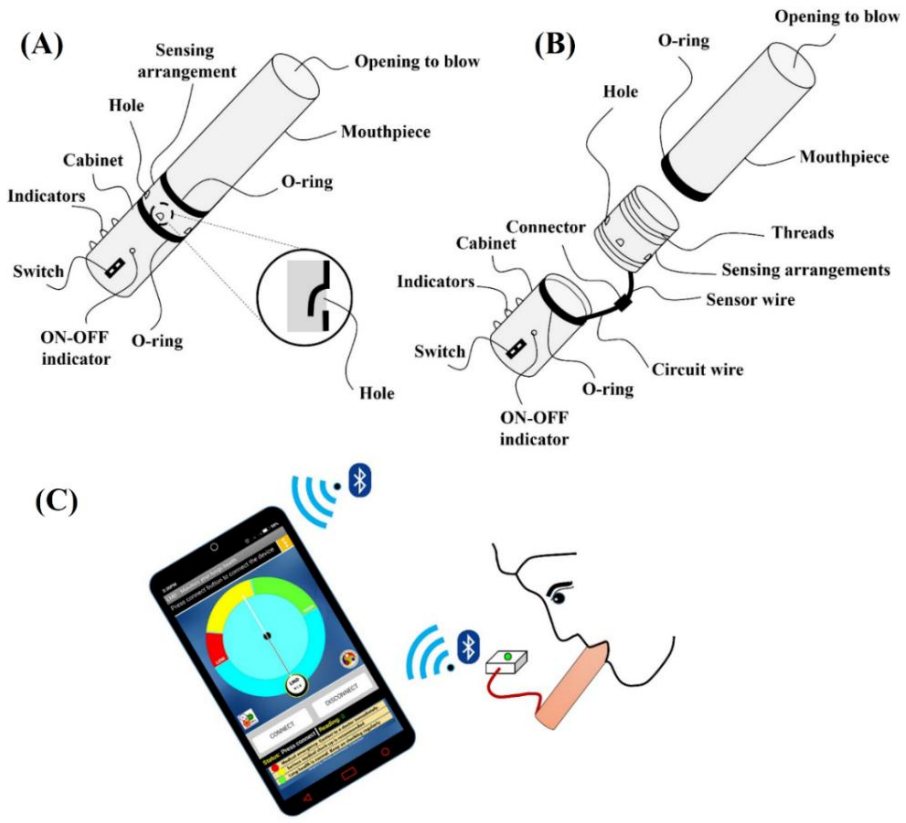

Figure 4: Image (A) and (B) schematically shows the components of the mobile based LFM-POCT device. Image (C) illustrates the device connected with a smart phone through Bluetooth and perform a wireless lung function test through the open standard software.

Objective – 5: A Multipurpose and Reusable Nano-BG-FET for Point-of-Care Estimation of Ammonia in Air and Urea in Human Urine

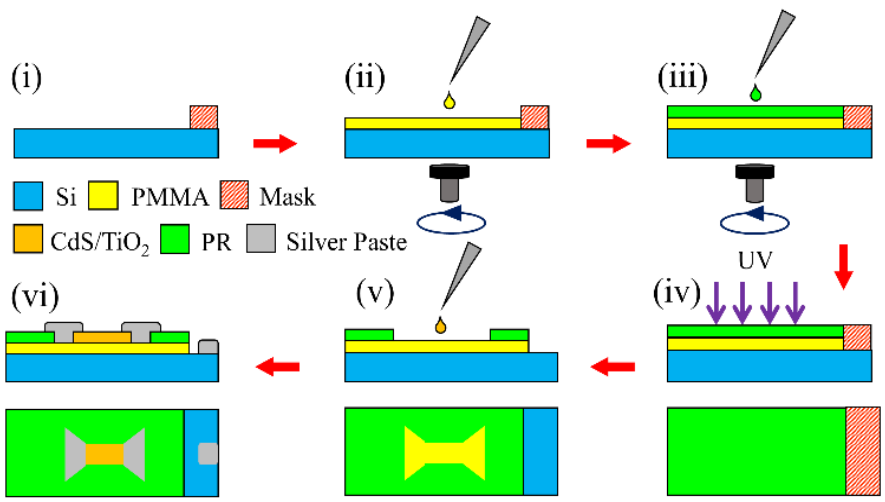

Figure 5: Schematic steps to fabricate the BG-FET device. Side views - (i) masking of the Si wafer; (ii) coating of PMMA on the Si Wafer; (iii) Coating of the photoresist (PR) on the PMMA layer; (iv)

UV exposure through photo lithography and development of the patters; (v) CdS-TiO_2 deposition through drop casting; and (vi) electrode deposition through silver paste. The bottom row in the images (iv) - (vi) show the top schematic view.

In this chapter, we discuss about a nanoparticle based back-gated (BG) FET for detection of ammonia. The cleaners, farmers, or industrial workers everyday come under the exposure of hazardous and pyrophoric ammonia gas or vapour, which cause severe health disorders in them. However, there is hardly any point-of-care-testing (POCT) device, which can detect the level of ammonia in real-time. Further, activity of ammonia and urea the body fluids such as breath, urine, and blood are the biomarkers for kidney or liver functions. Herein a highly sensitive and reusable back-gate-field-effect-transistor (BG-FET) has been developed to selectively detect ammonia in air together with ammonia and urea in a human urine. The BG-FET was prepared on a p-type Si substrate with a n-type channel material of CdS-TiO_2 nanocomposite and a poly-methyl methacrylate (PMMA) film as the dielectric layer. In order to make the sensor reusable, it was employed as a cover to a chamber where the ammonia gas or the urine sample was placed. The response of the BG-FET was analyzed by measuring the I-V characteristics, which showed increase in the drain current with ammonia release from the chamber. The underlying principle of the BG-FET enabled the creation of more (fewer) charge carriers for the reducing (oxidizing) gases such as ammonia upon adsorption on the nanostructures of the CdS-TiO_2 as the channel material. Control experiments with different gases/vapors suggested that the change in the current-to-voltage response of the BG- FET could be calibrated to selectively measure the activity of diverse hazardous gases. The lowest concentration of ammonia which could be detected was ~0.85 ppm at a response time of 30 s with an operating gate voltage of less than 0.5 V, which were significantly superior than the previously reported any ammonia sensor. Urease enzyme was added to the urine sample to liberate ammonia proportionately, which could also be detected employing the same

sensor. The urea-urease lock-and-key enzyme catalysis reaction made the sensor specific in detecting the biomarker. The performance of the calibrated BG-FET was also compared and contrasted with the standard clinical urea detection methodologies. The reliability, accuracy, reusability, and fast response time of the device could be employed to develop a point-of-care biomedical-device for ammonia and urea detection.

Objective – 6: Paper Based Magnetoresistance with Core-Shell Nanoparticles in Impulse Magnetic Field

Pancreatitis, a condition in which the pancreas becomes inflated calls for utmost attention in order to be diagnosed aptly at an early stage to avoid critical condition. Symptoms like abdominal pain, food malabsorption often indicate pancreatitis, acute or chronic. Human pancreas secretes two enzymes, lipase and amylase- elevated levels of which can be used as basis for the diagnosis of pancreatitis. Biosensors are widely exploited today in healthcare sector because of their rapid, accurate and reliable response. Giant Magneto resistance (GMR) is a phenomenon where resistance of alternate ferromagnetic and non-magnetic materials changes with a change in external magnetic field. In the last decade, GMR based biosensors have shown immense potential in clinical diagnosis for their high sensitivity, output and cost-effectiveness. We have developed a GMR based biosensor using paper as a substrate to detect levels of α-amylase in human blood serum. Nickel-Silver nanoparticles capped with starch was synthesized and deposited on filter papers, which were then placed one at a time between electromagnets.

Ag/Ni Core- shell nanoparticles showed a change in resistance under impulse magnetic field. This paper and nanoparticles based magnetoresistance was studied at room temperature. The maximum magnetoresistance achieved was more than 50% at room temperature. A computational analysis of change in magnetization in ferromagnetic

material was also performed as a proof of concept. It was observed that an applied magnetic field creates a disturbance in magnetization direction for few nanoseconds and the magnetization switching time depends on the size of particle. Moreover an atomistic model was also computed to study the magnetoresistance in a similar atomistic device.

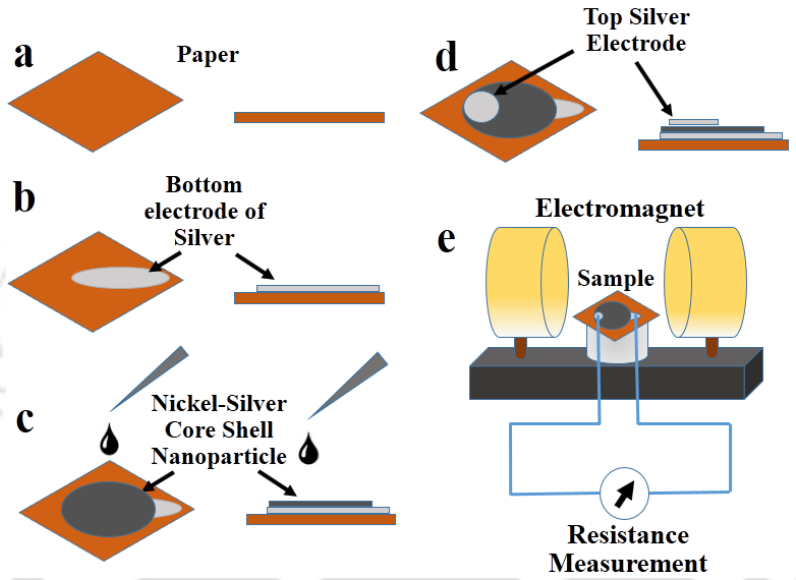

Figure 6: The steps of fabrication are shown in the images (a) to (d) and the schematic diagram (e) shows the experimental set-up for the magnetoresistance experiment where the sensor was kept in between two electromagnets, which produces pulsed magnetic field.

Objective – 7: A Point-of-Care-Testing device for Tunnel Vision Harnessing the Distance and Angle of View an Observer during motion

In this chapter, the proposed invention discusses about a method of measuring distance of an object and angle of view of eyes employing concept of observed speed or velocity. It is found that the measurement of distance of celestial objects, measurement of distance of a moving car, height of airplanes, distance of moving ships on ocean etc. are very important in different fields like astronomy, defence, security and surveillance. Moreover, the angle of view of eyes is also a potential parameter to detect many diseases like retinitis pigmentosa, hypovolemia etc. Thus, herein a simple concept is proposed to detect and

measure the distance and angle of view employing a simple theory. This concept also gives us an explanation of the fact that the speed of the object far from us seems less than that of the nearer one even though they are moving at same speed or velocity. The observed speed of the object becomes slower with increase in distance because of the fact that the visual length increases with the increase in distance.

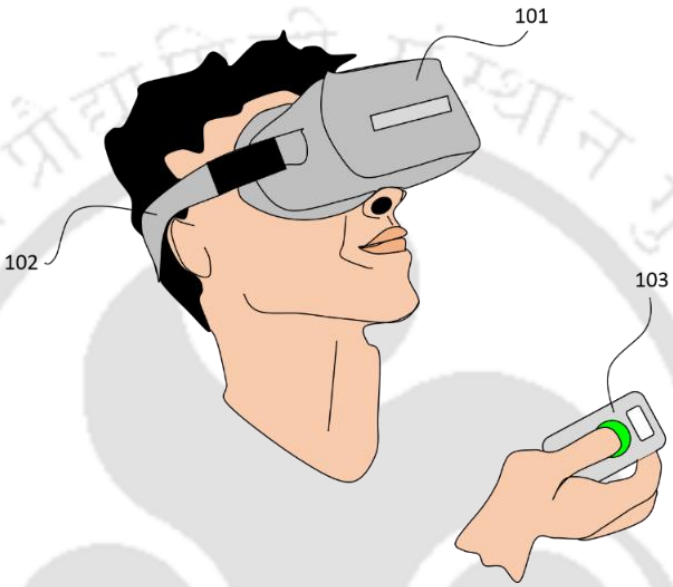

Figure 7: This figure shows the method of detecting angle of view of a person. The number 101 refers to a headset which contains a display and 102 is the belt to adjust the headset. The number 103 refers to an instrument similar to stopwatch which measures the time.

This concept of observed speed or velocity can be employed to measure the distance of an object by analyzing a motion picture. Moreover, angle of view can also be measured if one optimizes the distance from observer to display of motion picture and the speed of moving object in the motion picture. The concept is capable of measuring the distance of different objects and can also give us an idea about angle of view of a person. Measurement of angle of view is very important in eye disease diagnosis and hence the concept can be applied to detect diseases associated with tunnel vision. Thus, this proposed method and theory is capable of being used as a POCT device to diagnose diseases and disorders associated with tunnel vision.

Objective – 8: A Body-Potential Detection System Employing Micro/Nano Patterned Electrode

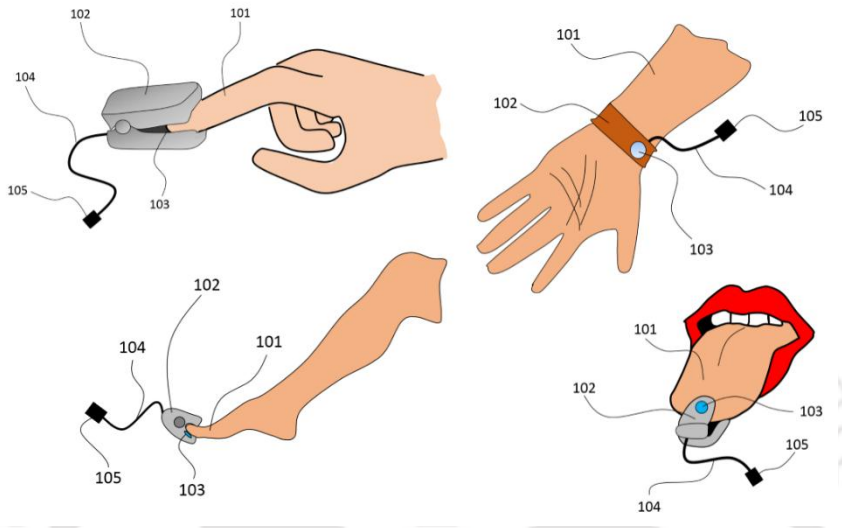

Figure 8: This figure shows body potential detecting device. The number 101 refers to human organ preferably index finger 102 and 103 refers to the outer cabinet and the sensor with the connecting wire 104 and the plug 105.

In this chapter, design and development of an affordable, user-friendly, and portable body-potential detection device has been reported. The device is composed of three major parts, namely, a sensor arrangement, a processing unit, and a power supply. The sensor arrangement consists of a flexible and soft sensor and associated connector components. The substrate of the sensor was made of flexible and soft material preferably PDMS. The flexible or soft material can also be put on a rigid support like glass depending upon handling issues. A deposited conductive layer preferably of aluminum and RGO on the substrate helps in detecting the body potential once it comes in contact with an organ of human body preferably index finger or wrist. The electrical signal generated by the sensor is sent to the processing unit which further transmitted the signal to a mobile android application for displaying the result. The device is useful for detecting many diseases or disorders related to heart, nerves and muscles.

In summary, in the present thesis, we describe different sensing platforms with variety of applications such as sensing, diagnostics, energy harvesting, and therapeutics. The sensors have been developed employing different principles such as microfluidics, spintronics, MEMS, and FET. Different nanomaterials have been employed to develop the sensors. Apart from fabrications and experimentation, multiple computational and theoretical studies also have been performed to understand the under lying physics and working principles of the proof-of-concept prototypes developed.

List of Figures

Figure 1.1: This image shows the different body parts that need a monitoring device to detect the early stage of diseases associated with the organ. 11

Figure 2.1: Figures (A) and (C) are the TEM images of Ag and Au nanoparticles. Respective SAED patterns are shown in images (B) and (D). The EDX images (E) and (F) confirmed the presence of Ag and Au. The numbers 1 – 9 on the image (E) and (F) represent the peaks of Cl, Ca, C, O, Cu, Si, Ag, and Au, respectively. 28

Figure 2.2: Experimental demonstration of the phenomenon. (A) A water droplet loaded with some microparticles was placed on a glass slide. (B) A rotational current was observed on the droplet when a vapour source of diethyl ether was brought into the immediate vicinity of the droplet surface. (C – F) Experimental images of particle motion. Rows I and II show the side and the top views of the motion under the exposure of the organic vapour when loaded with a single microparticle. The length of the scale bars on the images is 0.5 mm. 31

Figure 2.3: Image (A) shows the streamlines (continuous lines) and velocity vectors (arrowheads) of Marangoni flow inside a droplet of diameter 1.5 mm. Image (B) shows the change in average angular velocity (ω) with surface tension gradient ($\Delta\gamma$). 33

Figure 2.4: Characterization of electrolytes employed in the experiments. The plots show the variations in (A) viscosity, η, (B) density, ρ, and (C) electrical conductance G, of aqueous salt solutions of concentration (C_S) composed of four different salts $FeSO_4.7H_2O$, $NaHSO_4$, Na_2CO_3, and NaCl. 37

Figure 2.5: The plots show the variations in the, (A) electrical conductance (G_{max}) when the droplet was rotating at its maximum speed under organic vapour excitation and (B) percentage change in resistance in such a situation, $\Delta R = 100 \times \left[(R_0 - R_{\min}) / R_0 \right]$, with the concentration of salt (C_S). Plots (C) and (D) show the variations in ΔR and maximum power density ($P_D^{\max}$)

across the droplet of aqueous 0.85M $Fe_2SO_4.7H_2O$ suspended with different types of nanoparticles. In all the experiments, the nanoparticles and the aqueous salt solution were mixed in 1:1 (v/v) ratio. 40

Figure 2.6: Image (A) shows the experimental setup to measure the change in the electrical resistance (*R*) across the droplet. The inset in the bottom-right corner shows the magnified side view of the droplet resting on a pair of Cu electrodes. Plot (B) shows the variation in normalized resistance ($R_N = R/R_0$) with time (*t*) across a microdroplet composed of 0.2M, 0.45M, 0.85M, 1.3M, and saturated solutions of $FeSO_4.7H_2O$. The plot (C) shows the percentage change in resistance (ΔR) with C_S inside the droplet. Plot (D) shows the variation of R_N with time (*t*) across a microdroplet having suspensions of 1:1 and 3:1 (v/v) of Ag or Au nanoparticles in 0.85M aqueous $FeSO_4.7H_2O$ solution. 42

Figure 2.7: Energy harvesting from the microdroplet rotation. Schematic diagrams in the row (A) illustrate different ways (i – iii) of introducing the vapour and row (B) shows the corresponding output of potential difference (ΔV_D) with time (*t*). 45

Figure 2.8: The variations in the maximum potential difference (V_D^{max}) across the electrodes for the droplets composed of, plot (A) DI water at different pH and plot (B) salt-water (1.7M aqueous NaCl soln.) at different pH. The rotational motion was triggered with the help of diethyl ether vapour. 47

Figure 2.9: The variation of potential difference ($\Delta\psi$) with the difference in the concentration of the counter ions near the electrode (ΔC_{EDL}). 50

Figure 2.10: Image (A) shows the initial configuration of the computational domain at 0 s, with 100 nm thick $FeSO_4$ deposited at the electrodes. Image (B) shows the streamlines (continuous lines), velocity vectors (orange arrows), and the magnitude of the convective flux (colour map contours, $\mathbf{N}_{i,conv} = C_s\mathbf{u}_2$) inside a droplet of diameter 1.5 mm after 0.01 s. The surface tension of the droplet, γ_1 = 72.7 mN/m and diethyl ether, γ_2 = 17.0 mN/m at the arc of length 0.05

mm created a surface tension gradient of $\Delta\gamma$ = 55.7 mN/m across the interface. 53

Figure 2.11: Power generation from the microdroplet rotation. Plot (A) shows the variation in ΔV_D with t across the electrodes for the droplets having a 0.85M $FeSO_4.7H_2O$ solution and DI water. Images (B) and (C) show the variation in the maximum potential difference (ΔV_D^{max}) and maximum power density (P_D^{max}) with Cs. Image (D) shows the variation of P_D^{max} in μW cm-2 with and without the Ag or Au nanoparticle loading inside the droplets of 0.85M aqueous salt solution. Here 1:1 and 1:3 salt solution stands for the (v/v) proportion of 0.85M aqueous salt solution and prepared Ag or Au nanoparticle solution. 55

Figure 2.12: Experimental results of voltage generation in multiple droplets. Image (A) shows the schematic diagram of the experimental setup where three droplets were connected in series and diethyl ether vapour was introduced from one side. Image (B) and (C) show the variation of maximum voltage generation (ΔV_D^{max}) and power (P) for multiple numbers (N_D) of droplets, respectively. 57

Figure 2.13: Experimental results of the alcohol vapour sensor. Images (A) and (B) show the schematic diagram of the experimental setup where the LED was turned off (on) in the absence (presence) of the vapour excitation. Image (C) shows the change R_N with different concentrations (v/v) of diethyl ether in water (C_D) and image (D) shows variation ΔR with C_D. Image (E) shows the variation in R_N with t when the stimulus was different vapour sources such as diethyl ether (DEE), toluene, chloroform, ethanol, and methanol. Image (F) shows the variation in R_N with t when three cycles of the exposure of diethyl ether and alcohol were repeated on a microdroplet of 0.85M aqueous salt solution mixed with Ag nanoparticles in 1:1 proportion (v/v). 59

Figure 3.1: Image (A) shows the schematic diagram of the experimental set-up for characterizing the microfluidic phenomenon. Images (B – D) shows the placement of digital or thermal camera for imaging. 75

Figure 3.2: Images (A – D) shows the snapshot images of side-view of the droplet at different time intervals to illustrate the motion of a ~120 um particle inside the droplet. The scale bar is of 2 mm. 76

Figure 3.3: Images (A) and (B) shows the thermal image of the droplet when the substrate temperature was ~55^{0}C. The bottom right corner inset schematic of both the images shows the placement of the thermal imager. Images (C) and (D) shows the corresponding temperature distribution plot with respect to distance x and y along X and Y axis, respectively. The scale bars are of 2 mm. 78

Figure 3.4: (A) shows the schematics of the computational domain employed in this study. All the necessary dimensions of the domain are shown in the schematic. Images (B) shows the rotational effect inside the droplet due to the thermal Marangoni, natural convection, and combined effect. The colored contour, white continuous lines, and orange arrows show the temperature distribution, streamlines and velocity vectors of water inside the droplet, respectively. Images (i) – (iii), (iv) – (vi), and (vii) – (ix) show the temperature gradient created inside the droplet after t = 1 s of simulation for ΔT = 10°C, 30^{0}C, and 50^{0}C respectively. Plot (C) shows the variation of rotational speed (ω) with the change in the thermal conductivity (k) of the hot substrate. The dotted lines shows the slope of the curve. The dominance $D = (NC/TM) \times 100\%$ of thermal marangoni (TM) over natural convection (NC) is also illustrated with the green line. Plot (D) shows the variation of rotational speed (ω) with the temperature difference (ΔT) between the hot substrate and room temperature. The red line plot shows the corresponding experimental values of rotational motion (ω) with temperature difference (ΔT). The green line shows the dominance of NC over TM. The average value (Avg) shows the rotation due to combined effect. 83

Figure 3.5: Image (A) shows the experimental set-up for sensing and measuring the concentration of α-amylase in a sample. Image (B) shows the temporal response of the sensor for C_A = 20 U/L of amylase at a substrate temperature of 26^{0}C. Image (C) shows the response of the system for different concentration of α-amylase at 3 different temperatures. The scattered red

points are the response of the system due to introduction of blood serum sample. 87

Figure 3.6: This image shows the base resistance of three different droplets for three different days. 90

Figure 4.1: This shows the fabrication process and illustration of working. Images (A) – (D) show the different steps of assembling the touchpad device, (A) PDMS coating on paper, (B) paper substrate with inner-graphite and outer-PDMS coating, (C) placement of the PDMS spacer, and (D) the entire assemblage of resistive pad. Images (E) and (F) illustrates the working principle of the touchpad in which different locations of finger-press turned on different light emitting diodes (LEDs, L_1 and L_2) while the current passed through different resistors (R_1, and R_2). Images (G) – (J) show the schematic illustration of the working for a single touch location. Images (G) and (I) show the side view of the pressed touch location along with a simplified circuit model, whereas images (H) and (J) show the corresponding top views. Image (K) shows the change in the resistance (R) with applied weight (W) on the touch location. The solid lines show the theoretical calculations for different values of $\boldsymbol{\alpha}$ and the scattered points represent the experimental data for different thickness of touch layer. 104

Figure 4.2: Details of the electrical parts with dimensions. Image (A) shows the outer surface view with PDMS coating and Cu connect of the top surface, image (B) shows the configuration of the PDMS spacer with four holes, and image (C) shows the inner surface of the paper substrate with the Cu connect. Image (D) shows the assembly of the parts to form the touchpad and image (E) illustrates the circuit associated with the device having four locations. Images (F) and (G) show simplified circuit models for understanding purpose when switch S_1 is pressed and switch S_2 is pressed, respectively. All dimensions are in cm. 106

Figure 4.3: Characterizations of the touchpad prototype. Image (A) shows the microscope image of the cross-section of the graphite coated paper. Image (B) shows the FESEM image of the graphite coating on top of the paper.

Image (D) shows the optical microscopic image of the cross-section of the touchpad with three different layers. Image (D) shows the Raman spectroscopy analysis of the deposited graphite layer. Image (E) shows the current (*I*) versus voltage (*V*) characteristics of the graphite coatings provided in the different locations 1 to 4 on the pad. Image (F) shows the variations in the electrical response of different locations with time highlighting the stability of the sensors. 108

Figure 4.4: Experimental demonstration of the prototype. Images (A) – (C) show that the glowing of four, three and one LED(s) depending upon the touch location. Image (D) shows the output resistances of the different touch locations 1 to 4, as shown in the image (E). Image (F) shows the repetition of the output current for multiple touches made at location A. 111

Figure 4.5: Electrical response of the different locations of the resistive touchpad. Image (A) shows the variation in the output current (*I*) of the touchpad with time (*t*) during a touch incident in the locations 1 to 4. The image (B) shows the variation in the peak output resistance (RP) after 600 trials in the locations 1 to 4. 113

Figure 4.6: Detection of hand-tremor using the resistive pad. Image (A) shows the sensor that detects the hand tremor. Image (B) shows the mechanism of the sensor. Image (C) shows the fluctuation of the current due to hand tremors which can be used for quantification of tremors. Images (D) and (E) show the circuit model and front view of the sensor in a bent condition. Image (F) illustrates the quantification of bending schematically. The images (G) and (H) shows the real images of sensors in related and bent condition, respectively. Image (I) shows the theoretical (solid line) and experimental (scattered points) response of the sensor with the bending. The theoretical data in the image (I) are plotted for different values of β . 114

Figure 4.7: The device plan of the prototype. Image (A) shows the outside getup of the proposed device. The images (B) and (C) show the cross-sectional image of the prototype under relaxed and pressed conditions. The mechanical ‘bias’ in the embodiment ensures that the sensor bend towards left when the ‘knob’ at

the top is pressed. Image (D) shows an image of the prototype. The electrical connect at the bottom connects the sensor to the controller unit, as shown in the image (E). Image (F) shows the fluctuation of the current due to hand tremors are transferred to the mobile interface with the help of the Bluetooth module integrated to the controller unit. 117

Figure 4.8: The images show the variations in the normalized resistance [$\Delta R/R_0 = (R - R_0)/R_0$] with time ($t$) for (A) mild, (B) moderate, and (C) high hand tremors. Here R_0 refers to the base resistance of the sensor and ΔR is the variation in the resistance. Image (D) shows the response of the sensor for mild, moderate and high tremor. Images (E) and (F) shows the sensor stability analysis. Image (E) shows the stability of the sensor with time and image (F) shows the merit of the four different sensors. 119

Figure 4.9: This images (A – D) show the variation in $\Delta R/R_0$ with time t for four different patients (A – D) having a hand tremor. Plot (E) shows the calculated response of the sensor for patients (A – D). Table (F) shows the descriptions of response and corresponding implications. 121

Figure 5.1: Schematic diagram showing the components of the paper-based humidity sensor. The image shows the coating of the CdSNPs and Ag electrodes, which was integrated with the micro-heating arrangement. The micro-heater composed of a Cu coil embedded inside a PDMS matrix is shown in the side. 135

Figure 5.2: The images (A) – (C) show the TEM snapshot, SAED patterns, and EDS of the CdSNPs. The images (D) – (F) show the TEM snapshot, SAED patterns, and EDS of the synthesized AuNPs. Images (G) and (H) show the FESEM snapshot of the paper surface and AuNPs embedded on the paper surface, respectively and image (I) shows the FESEM image of the CdSNPs deposited on the AuNP treated paper surface. 136

Figure 5.3: Images (A) and (B) show the XRD analysis and Raman spectroscopy of CdSNPs with the characteristics peaks of CdS and image (C) shows the typical UV-Vis spectroscopy data of CdSNPs. 137

Figure 5.4: This figure shows the fabrication steps (i-iii) of the sensor along with the FESEM image of the paper surface, TEM image of the CdSNPs, a photographic image of the fabricated sensor, and a FESEM image of the paper embedded with CdSNPs. The scale bar in the sensor image is of 1.5 mm. 138

Figure 5.5: The image shows the circuit employed to ensure continuous supply of heat to the paper-sensor while experiments are performed. 141

Figure 5.6: The image shows the circuit arrangement for the LED-based real-time monitoring unit. 142

Figure 5.7: Images (A) and (B) show description and illustration of the detection circuit of the control assembly for two different situations of the illumination of the red and green LEDs. In case of the image (A), the F_R is below the desired level (S) as shown in the imaginary scale peak expiratory flow (PEF) meter. In contrast, image (B) shows the situation where F_R is above the safety level (S). It may be noted here that the ΔR is more in case of the image (B) than that of the image (A). 143

Figure 5.8: Image (A) shows the variation in temperature (T) with time (t) for different current (I) inputs to the micro-heater. The current source was turned on for first 60 s before turned off. Image (B) shows the temperature ($T_{t=60s}$) generated on the micro-heater surface after 60 s at different current flow (I). Image (C) shows the current input (I) and temperature output (T) employed for the micro-heater. 144

Figure 5.9: Image (A) schematically illustrates the step by step adsorption and desorption processes of the sensing mechanism. Image (B) shows the current-voltage (I-V) characteristics of the sensor for different relative humidity conditions. Image (C) shows the change in resistance (ΔR) of the sensor at different RH. Image (D) shows the change in ΔR of the sensor due to the pulsed exposure of ~97 % humid air at different Q. Image (E) shows the time taken by a paper substrate to reach 50ºC when the paper was, (i) devoid of Au NPs and (ii) embedded with Au NPs while the paper substrate was kept on a heated surface at 65°C. Image (F) shows the change in ΔR and recovery time (t_{rec}) at different temperatures of the paper-sensor. Image (G) shows the response of the sensor

with time for different magnitudes of current (I) flown through the micro-heater when air flow rate was ~450 L/min. 147

Figure 5.10: Image (A) schematically shows the experimental set up composed mouthpiece, paper-sensor, micro-heater, and multimeter to measure the various parameters during exhalation. The insets show the real images of paper-sensor and micro-heater where the scale bars are of 5 mm. Image (B) shows the variation in the normalized resistance ($R_N = R/R_i$) with time (t) for six cycles of breathing alongside a control experiment with dry N_2 gas. Image (C) shows the variation in the ΔR for different length of the mouthpiece (L_{MP}). 148

Figure 5.11: Images (A) and (B) show the photographs of the device. Image (C) shows the variation in ΔR because of different peak flow rate (F_R) of the exhaled air. Image (D) shows the comparison of results between a commercial device, JSB N02 peak flow meter and the proposed device along with a schematic illustration of the corresponding LED and mobile response. 150

Figure 5.12: Image (A) and (B) schematically shows the components of the mobile-based LFM-POCT device. Image (C) illustrates the device connected to a smartphone through Bluetooth and perform a wireless lung function test through the open standard software (*Patent filed*). [63] 151

Figure 5.13: Image (A) shows the experimental set-up for measuring the response of the sensor. The experimental section, which is considered as the computational domain is marked with a red dotted line and magnified above. The inlet, flow of humid gas, and position of CdSNP adsorption surface are indicated in the magnified figure. The equivalent 2D computational geometry is illustrated in the image (B). 152

Figure 5.14: Image (A) shows the contour plot of the concentration of adsorbate molecule (C) in the pipe for 300 L/min in linear approximation. The white curve shows the concentration of molecules measured along the cut-line (broken line) with distance (L_d). Image (B) shows the variation of adsorbed molecule concentration (C_a) under linear and logarithmic approximation with different flowrates (F_R). 156

Figure 5.15: The plot (A) schematically shows the band energy E vs. z-coordinate normal to sensor-surface to illustrate band bending of the n-type CdSNPs near the surface of the sensor (left-side) due to the space charge layer. The notations N_{ss}, E_V, E_D, E_F and E_C show the surface charge density and the energies corresponding to valance band, donor level, Fermi level and conduction band of the sensor. Plots (B) to (D) show the volume charge density (ρ), electric field (ε) in the space charge layer and the electric potential (Φ) characteristics with z-coordinate, respectively. The surface and bulk electric field potentials are denoted by Φ_s and Φ_b and the thickness of space charge layer is denoted by d. The notations Q_{SS}, Q_{SC}, N_{SS}, and eV_S denotes surface state charge, space charge, surface state charge density, and band bending at the surface. 157

Figure 5.16: The variation in the electrical conductivity ($\Delta\sigma$) with the flowrate of humid gas (F_R) due to the variation in the adsorption of water molecules on the sensor. The solid lines show the simulated values for the linear (black) and logarithmic (red) variations in F_R of the humid gas with the concentration of the adsorbed molecules. The scattered circular symbols show the experimental results. 160

Figure 6.1: Image (A) shows the TEM image of Ni-Ag core shell nanoparticles. Image (B) shows the FESEM image of Ni-Ag core shell nanoparticles deposited on a paper substrate. Image (C) shows the XRD of Ni-Ag core shell nanoparticle. Image (D) shows the SAED pattern of Ni-Ag nanoparticles. 176

Figure 6.2: Images (A) to (D) show the steps of fabrication of the magnetoresistive sensor on a paper substrate. Image (E) schematically shows the experimental set-up employed for the magnetoresistance experiment where the sensor was kept in between two electromagnets, which produces pulsed magnetic field. 177

Figure 6.3: Image (A) shows the change in normalized resistance with time due to applied impulse magnetic field. Image (B) shows the magnetoresistance percentage (MR%) due to applied magnetic impulse. The applied magnetic impulse is shown in plot (C). Image (D) shows the computational result of the change in magnetization in X, Y, and Z direction after applying an external magnetic field in X-direction in a Ni nanoparticle. 180

Figure 6.4: Image (A) shows the computational result of the switching of X-directional magnetization for different sized Ni nanoparticles. Image (B) shows the experimental magnetoresistance (MR%) values of fabricated magnetoresistive sensor for different sized Ni-Ag nanoparticle. 181

Figure 6.5: Image (A) shows the computational geometry of the atomistic system under consideration. The left electrode (LE), central scattering region and right electrode (RE) of the system are demarcated using vertical dotted lines. In this image, the green spheres represent Ni atoms and orange spheres represent Ag atoms. Images (B) and (C) show the transmission spectrum of up and down spin electrons for parallel (P) and anti-parallel (AP) configuration respectively. The Fermi energy E_F of the system is denoted by the broken lines in images (B) and (C). 183

Figure 6.6: Image (A) shows the spin polarized current for spin up and spin down electrons in parallel (P) configuration, whereas image (B) shows the spin polarized current for spin up and spin down electrons for anti-parallel (AP) configuration. Images (C) and (D) show the density of states (DOS) of electron for parallel and anti-parallel configuration, respectively. Dotted lines in images (C) and (D) represents the Fermi energy E_F of the system. 184

Figure 6.7: This figure shows the UV-Vis spectra of the synthesized Ni-Ag nanoparticles, Ag-starch and Ni-Ag starch nanoparticles. 186

Figure 6.8: This figure shows the FTIR spectra for the starch and Ag-starch composite to confirm the attachment of starch to the Ag surface. 187

Figure 6.9: This figure shows the EDS spectra for (A) Ni-Ag and (B) Ni-Ag-starch composite to confirm the presence of elements in the prepared samples. 187

Figure 6.10: This figure shows the calibration plot for the detection of α-amylase. The red scattered points are indicating the bio-sample values. 188

Figure 7.1: Schematic steps to fabricate the BG-FET device. Side views - (i) masking of the Si wafer; (ii) coating of PMMA on the Si Wafer; (iii) Coating of the photoresist (PR) on the PMMA layer; (iv) UV exposure through photo lithography and development of the patters; (v) CdS-TiO_2 deposition through

drop casting; and (vi) electrode deposition through silver paste. The bottom row in the images (iv) - (vi) show the top schematic views. 205

Figure 7.2: Material characterisation of CdS-TiO_2. (A) Raman spectra of the CdS-TiO_2 nanocomposite in which the inset shows the magnified view of the same. (B) X-Ray diffraction analysis of the composite nanoparticles. 207

Figure 7.3: Image (A) shows the schematic diagram of the BG-FET device and the electrical connections. The magnified inset shows the effect of applying a negative bias at the gate electrode (V_G < 0 V). Image (B) shows FESEM image of the 100 µm x 20 µm channel region on the photoresist after photolithography. Image (C) is the FESEM image of the active region and drain-source electrodes. Image (D) shows a magnified view of the active region depicting the surface morphology of the CdS-TiO_2 nanostructures. Scale bar for (B) and (C) is 100 µm and 1 µm for (D). 209

Figure 7.4: Electrical characterization of the FET in absence of ammonia. (A) I_D vs V_G characteristics of the FET at a constant drain bias, V_D = 1 V. (B) I_D vs V_D response of the FET at different gate biases, V_G = 0 V, –0.2 V, and –0.5 V. 210

Figure 7.5: (A, B) Schematic diagram of the closed setup for ammonia sensing. (C) Comparison between current responses in the open and the closed system for 3 different concentrations, 50µM, 100µM, and 200µM. (D) I_D vs V_D characteristics of the FET at a fixed gate voltage, V_G = -0.2 V, for different concentrations of aqueous ammonia solution in the closed system. 211

Figure 7.6: Schematic representation of ammonia sensing: (A) Small current flowing through CdS-TiO_2 active surface in absence of ammonia. (B) Adsorption of ammonia molecules on the surface and resultant enhancement of current. (C) Electron transfer process between the ammonia molecules and CdS-TiO_2 nanoparticles (NPs) leading to the formation of weak coordinate-covalent bonds. 214

Figure 7.7: Comparison of the normalised change in I_D for different volatile samples, 500 µM NH_3, 500 µM HCl, toluene and ethanol. 216

Figure 7.8: Sensor response for human urine samples. (A) Normalised device responses for urine samples before the introduction of urease (represented by filled

triangles W, X, Y and Z) along with the linear fitted responses for known calibration samples. (B) Normalised device responses before (filled triangles) and after (unfilled triangles) the introduction of urease, superposed with liner fitted responses for known calibration samples. W', X', Y' and Z' are the modified responses after urease was introduced. (C) Comparison between the actual and calibrated responses for 4 different urine samples W, X, Y and Z. 218

Figure 8.1: The figure shows mechanism of resting and action potential formation on cell membrane. Images (A) and (B) show the formation of resting and action potential on the cell membrane, respectively. Image (C) shows the concentration of three majorly contributing ions Na^+, K^+, and Cl^- in during resting potential condition, inside and outside the cell. The concentrations are in mmol/l. Images (D) and (E) show the recorded low and high frequency voltage signals, respectively from the surface of index finger. 233

Figure 8.2: The figure shows fabrication steps and the schematic diagram of the patterned electrode. Images (i) to (ix) are the different steps of fabrications. Image (A) shows the schematic isometric view of the pattern on PDMS. Image (B) shows the final electrode schematically after Al deposition. 237

Figure 8.3: This figure shows the sensor optimization, characterization, and experimental set-up. Images (A) – (C) show the fabricated patterns for the sensor electrode along with the FESEM images. Image (D) shows the Raman spectroscopy of the fabricated metal electrode of Al coated glass substrate (blue) and patterned electrode based on RGO, Al, and PDMS. Image (E) shows the experimental set-up to record the surface electrical potential of a body part. Image (F) shows the associated amplifier circuit employed to detect the surface potential. Images (G) and (H) shows the real experimental image with an indicator LED to demonstrate the generation of surface electric potential. 239

Figure 8.4: This figure shows sensor results. Image (A) shows the power spectrum of the RSEMG signal received from the index finger. Image (B) shows the smoothed signal received by patterned electrode (PE) and metal electrode (ME) whereas image (C) shows the signal as received by the electrode. Images (D) and (E) show the schematic representation of the patterned

electrode and the arrangement of placing the electrode on index finger. Image (F) shows the real image of the fabricated sensor. 241

Figure 8.5: The figure shows the response of the PE sensor at rest for index finger (A), wrist (B), big toe (C), and tongue (D). Here, V_N refers to the normalized voltage signal from the respective organs in arbitrary units (a.u.) and t is the time. 242

Figure 8.6: The figure shows the response of the PE sensor attached to the wrist at rest condition (A) and while working (B – D) for different time. Plot (E) and (F) show the change in normalized voltage (V_N) and frequency (f_N) of the body potential signal, respectively, for the cases described in images (A – D). Here, V_N refers to the normalized voltage and f_N stands for normalized frequency of the signal from the respective organs in arbitrary units (a.u.) and t is the time. 243

Figure 8.7: The figure shows the response of the PE sensor attached to index finger (A) at rest condition and after working out for (B) 5 min and (C) 10 min. Plot (D) and (E) show the change in normalized voltage (V_N) and frequency (f_N) of the body potential signal, respectively for the cases described in images (A-C). Here, V_N refers to the normalized voltage and f_N stands for normalized frequency of the signal from the respective organs in arbitrary units (a.u.) and t is the time. 245

Figure 8.8: The figure shows the change in normalized voltage (V_N) and frequency (f_N) of the body potential signal detected by a PE sensor attached to index finger for relaxed and stressed body condition due to work out of 10 min. 246

Figure 8.9: This figure shows the stability analysis of the sensor electrode. Image (A) shows the stability of the sensor with time. Image (B) shows the comparison between different sensors. 247

Figure 8.10: This figure shows the sensor arrangement and processing unit. The sensor is fabricated on a flexible or soft substrate of say PDMS. The processing unit contains a socket for connecting the connector of the sensor. The processing unit also contains an indicator LED and an ON-OFF switch. 248

Figure 9.1: This figure shows the concept of visual planes. Images (a) shows the imaginary visual planes in between the object and observer. Image (b) shows how an object enters in a narrower visual plane with respect to the observer, when it comes closer to the observer. Image (C) shows the concept of visual lengths. Image (d – e) shows the different experimental set-up employed in the experiments. 261

Figure 9.2: This figure shows the effect of angle between the camera-axis with the object. Image (a) shows the schematic illustration of the situation where the angle between the camera-axis with the object is denoted by α_C. The distance between the object and camera is denoted by $\boldsymbol{d}$ while $\boldsymbol{a}$ is the length of the object. The visual planes corresponds to two edges of the object, which is denoted by l_1 and l_2. The distance between the visual planes is denoted by Δd and $2\theta_a$ denotes the angle of view of the camera. Images (b) – (d) show the experimental observation with different values of $\boldsymbol{\alpha c}$ such as, 90^0, 80^0, and 70^0 and the corresponding ratio (l_r) of the upper side of the quadrilateral to the lower side as indicated in the top right corner. 262

Figure 9.3: This figure shows the study of different parameters. Row I schematically shows the different parameters under considerations. Image (a) shows the change in the distance between two objects (x) and the normalized value (x_N) in a motion picture for three different set of objects having actual distances of 1 cm, 2 cm, and 3 cm between them with the distance between the object and the camera (d). Images (b) and (c) show the same study for different motion picture width and angle of view, respectively for a set of objects having 1 cm distance between them. Image (d) shows the change in x_N with time (t) for two different average velocity of the camera. 265

Figure 9.4: This figure shows the associated concept schematically. The two images are showing a photograph taken from the side window of a moving car in a certain time interval. Two of the objects are marked as A and B. The object A which is a tree is nearer to the observer compared to object B which is a tower

situated at a larger distance. The displacement of object A and B in the photos are also marked as X_A and X_B, respectively. 267

Figure 9.5: This figure shows the schematic illustration of the associated theory. Image (a) shows the displacement of moving objects A and B, situated at a distance d_A and d_B in our different vision length l_A and l_B. 269

Figure 9.6: The figure shows the experimental images (a and b) for measuring the distance of three objects A, B, and C. The images were taken by a moving (at ~7.5 cm/s) digital camera at t = 0 s and t = 1 s, respectively. Image (c) shows the calculated distances of objects A, B, and C. Image (d) shows the associated error (*Er*) in measurement. 270

Figure 9.7: The figure shows the images (a) and (b) of moon at t = 0 s and t = 180 s, respectively. Image (c) shows the calculated distance of moon at diffent time intervals. The dotted red line shows the reported distance of moon from earth. Image (d) shows the associated deviation in terms of percentage error (*Er*) while measuring the distance between moon and earth for different time intervals using the proposed theory of observation. 271

Figure 9.8: The figure shows the measurement of angle of view using the proposed methodology. Image (a) shows the concept of angle of view and image (b) shows the measured angle of view of a person with and without specs. Images (c) and (d) illustrate normal vision and tunnel vision effects, respectively in order to explain the biomedical importance of measuring angle of view. Thus, the proposed method can be useful in detection diseases associated with tunnel vision. 273

Figure 9.9: Image (a) shows the interior of the headset. The head-set consists of two eye-pieces that allow to watch a video in the display. Image (b) shows the method of detecting angle of view of a person. The system consists of a headset which contains a display and a belt to adjust the headset. There is an instrument similar to stopwatch which measures the time. 275

Nomenclature

TEM	Transmission Electron Microscopy
EDX	Energy Dispersive X-ray Spectroscopy
EDS	Energy Dispersive X-ray Spectroscopy
DEE	Di-ethyl Ether
DI	Deionized
LED	Light Emitting Diode
EDL	Electrical Double Layer
NC	Natural Convection
TM	Thermal Marangoni
PDMS	Polydimethylsiloxane
FESEM	Field Emission Scanning Electron Microscope
SAED	Selected Area Electron Diffraction
CdSNP	Cadmium Sulphide Nanoparticle
UV-Vis	Ultraviolet–visible
RH	Relative Humidity
PEF	Peak Expiratory Flow
XRD	X-ray Diffraction
MR	Magnetoresistance
GMR	Giant Magnetoresistance

FTIR	Fourier-Transform Infrared Spectroscopy
FET	Field Effect Transistor
BG-FET	Back Gated Field Effect Transistor
PMMA	Poly(methyl methacrylate)
PR	Photoresist
DOS	Density of States
NP	Nanoparticle
RGO	Reduced Graphene Oxide
EMG	Electromyography
RSEMG	Raw Surface Electromyography
PE	Patterned Electrode
ME	Metal Electrode
CFD	Computational Fluid Dynamics

Contents

Topic **Page No.**

CHAPTER 1: Introduction

1.1. Overview 3
1.2. Classification of Sensors 5
1.2.1 Microfluidic Sensors 6
1.2.2 Paper-based Sensors 7
1.2.3 Spintronic Sensors 8
1.2.4 Electronic Sensors 9
1.3 Objective of the Thesis 12
References 13

Section I: Microfluidic Sensors

CHAPTER 2: Self-spinning Nanoparticle Laden Microdroplets for Sensing and Energy Harvesting

ABSTRACT 23
2.1. Introduction 24
2.2. Experimental Section 26
2.2.1. Materials 26
2.2.2. Synthesis 27
2.2.3. Methods 29
2.3. Results and Discussion 32
2.3.1 Experimental Results on the Phenomenon 32
2.3.2 Theoretical Explanation of the Phenomenon 33
2.3.3 Experimental Optimization of Salt and Nanoparticle Loading in the Droplet 38
2.3.4 Electrical Response of the Phenomenon 41
2.3.5 Experimental Results on Energy Harvesting 44
2.3.6 Theoretical Basis of Voltage Generation 49
2.3.7 Computational Simulations to Estimate Potential Drop on the Electrodes 51
2.3.8 Power Density and Conversion Efficiency 55
2.3.9. Sensor Application 59
2.4. Conclusions 61
References 62

CHAPTER 3: Droplet Based Detection of Blood α-Amylase Employing Thermal Marangoni Effect

ABSTRACT 71
3.1. Introduction 72
3.2. Experimental Section 75
3.2.1 Materials 75
3.2.2 Sensor Fabrication and Set-up 75
3.2.3 Experimental Method for Microfluidics 76
3.2.4 Experimental Method for Electrical Characterization 76
3.2.5 Experimental Procedure of α-amylase Sensing 77
3.3. Results and Discussion 78
3.3.1 Experimental Study on Effect of Temperature 78
3.3.2 Computational Analysis 79
3.3.3 Experimental Analysis 88
3.4. Conclusions 90
References 91

Section II: Paper Based Electronic Sensors

CHAPTER 4: Paper Based Flexible Touchpad and Hand Tremor Detection Device

ABSTRACT 99
4.1. Introduction 100
4.2. Materials and Methods 103
4.2.1 Materials 103
4.2.2 Methods 105
4.2.3 Characterizations 109
4.3. Results and Discussion 110
4.3.1 Resistive Touchpad 110
4.3.2 Hand Tremor Detector 115
4.4. Conclusions 123
References 124

CHAPTER 5: Nano-Enabled Paper Humidity Sensor for Mobile Based Point-of-Care Lung Function Monitoring

ABSTRACT 131
5.1. Introduction 132
5.2. Experimental Section 136
5.2.1 Materials 136

5.2.2 Synthesis and Characterizations of Nanoparticles 136
5.2.3 Fabrication of the Sensor, Micro-heater and their Integration 139
5.2.4 Experiments to Create Environment with different relative humidity 140
5.2.5 Description of Circuits for Heating and LEDs 141
5.2.6 Methods 144
5.3. Results and Discussion 145
5.3.1 Response of Paper Humidity Sensor 145
5.3.2 Response of LFM-POCT Device 149
5.3.3 LFM-POCT Device Architecture 152
5.3.4 Experimental and Simulation to Study the Dependence of Flowrate 153
5.3.5 Computational Analysis of Adsorption 154
5.3.6 Effect of Adsorption on CdS 157
5.4. Conclusions 161
References 162

CHAPTER 6: Paper Based GMR Nanobiosensor for *α*-Amylase Estimation under Impulse Magnetic Field

ABSTRACT 171
6.1. Introduction 172
6.2. Materials and Methods 175
6.2.1 Materials 175
6.2.2 Ni-Ag Core Shell Nanoparticle Synthesis 176
6.2.3 Sensor Fabrication and Experimental method 178
6.2.4 Computational Details 179
6.3. Results and Discussion 181
6.3.1 Magnetoresistance in Impulse Magnetic Field 181
6.3.2 *α*-Amylase Detection 186
6.4. Conclusions 189
References 190

Section III: Other Electronic Sensors and POC Devices

CHAPTER 7: A Nano-BG-FET for Point-of-Care Estimation of Ammonia and Urea in Human Urine

ABSTRACT 199
7.1. Introduction 200
7.2. Materials and Methods 205
7.2.1 Materials 205
7.2.2 Fabrication of BG-FET 206
7.2.3 Synthesis and Characterization of Nanocomposite 207

7.2.4 Material Characterization of the CdS-TiO_2 Composite Nanoparticles 207
7.2.5 Calibration 208
7.3. Results and Discussion 208
7.3.1 Electrical Characterization 208
7.3.2 Ammonia Sensing 212
7.3.3 Mechanism for Ammonia Detection 214
7.3.4 Selectivity of BG-FET 215
7.3.5 Sensing of Human Urine Samples 217
7.3.6 Calculation of Ammonia and Urea in Human Urine Samples 219
7.4. Conclusions 221
References 222

CHAPTER 8: A Prototype for Point-of-Care Stress Detection at Different Body Parts

ABSTRACT 231
8.1. Introduction 232
8.2. Experimental Section 238
8.2.1 Materials 238
8.2.2 Fabrication 238
8.2.3 Optimization and Characterization of Patterned Electrode 240
8.2.4 Experimental Method 241
8.3. Results and Discussion 243
8.4. Conclusions 249
References 250

CHAPTER 9: Conversion of Observed Speed of a Moving Object to Diagnose Tunnel Vision

ABSTRACT 257
9.1. Introduction 259
9.2. Experimental Section 263
9.2.1 Materials 263
9.2.2 Characterization Techniques 263
9.2.3 Methods 263
9.3. Results and Discussion 264
9.3.1 Visual Plane 264
9.3.2 Effect of Recording Angle 266
9.3.3 Effect of Other Parameters 267
9.3.4 Concept of Observed Speed 268
9.3.5 Detection of Tunnel Vision 273
9.4. Conclusions 276
References 277

CHAPTER 10: Summary and Future Scope

10.1. Summary 283
10.2. Future Scope 287

Appendix-I: Comparison and Limitations 289

Appendix-II: Publications, Patents, and Conferences 299

CHAPTER 1

Introduction

Contents

1.1. Overview 3
1.2. Classification of Sensors 5
1.2.1 Microfluidic Sensors 6
1.2.2 Paper-based Sensors 7
1.2.3 Spintronic Sensors 8
1.2.4 Electronic Sensors 9
1.3 Objective of the Thesis 12
References 13

भारतीय प्रौद्योगिकी संस्थान गुवाहाटी
Indian Institute of Technology Guwahati

1.1. Overview

The recent upsurge in the inventions and innovations associated with the micro- and nano-electronics has shown all signs towards a world where most of the activities of a human life are closely guided by an electronic gadget. Right from communication, data transfer, or social networking to the healthcare and diagnostics, technological interference to human life has perhaps expanded its base exponentially in the past few decades.[1-4] Presently, although the technological invasion to the human life has already been very fast, the researchers around the globe have been trying to make progress even at a faster rate. In this regard, since the challenges are rather diversified in nature, the technological developments are no longer confined solely to the electronic gadgets and their miniaturization.[5, 6]

For example, use of the chemical and physical aspects of materials science, nanoscience, bioscience, biotechnology, and nanotechnology have opened up a larger scope of development especially in the field of micro or nanoscale sensors and electronic devices.[7-10] In recent research activities, nanomaterials have got a large focus in the fields of electronics, microfluidics, biology, medicine, optoelectronics, and drug delivery, because of the enhancement of their efficiency with the use of the special properties emerging at the nanoscale.[11-16] Availability of higher surface to volume ratio, use of a smaller amount of materials, cost-effectiveness, and emergence of various distinct optical, electromagnetic, mechanical and thermophysical properties of the nanomaterials have attracted the attention of researchers in a diverse set of applications. In particular, the use of the nanoelectronic gadgets integrated with the specialties from the smart materials and nanoscale science have opened up the avenues in the development of sensors for the healthcare, environmental monitoring, and energy harvesting application, to alleviate the

current issues prevalent in our society associated with the energy, environment, and healthcare.[17-23] The present thesis aims at the design and development of a host of nano-enabled sensors targeting a set of biomedical applications, energy harvesting, and environmental monitoring.

The background of the choice of the aforementioned topics is associated with the ever-increasing health hazards associated with the urbanization and industrialization in the modern world. The world citizens have been suffering from various kinds of health issues, which are directly related to the pollutions in the ambient air, water, and soil.[24-26] Importantly, many of these diseases cannot even be diagnosed at the early stages due to the lack of awareness or due to the absence of facilities at the patients' site. Thus, most of the patients visit a doctor once the disease reaches an advanced state. In view of this situation, presently, people are looking for devices that may detect diseases at the early stage to increase the awareness about them as well as monitor their status on a daily basis. World Health Organization (WHO) also have declared the need of affordable, reliable, rapid, and portable point-of-care-testing (POCT) devices to diagnose the common and fatal diseases on-site to prevent them at their early stages.[27-29]

In current scientific and technological organizations, many of the recent research works are directed towards this end. Presently, researchers, as well as the commercial giants such as Samsung, Apple, or Google, have initiated the process to integrate the electronic devices, which can be operated with mobile phone or wristwatch, or an eyeglass to obtain the diverse health-related parameters, such as blood pressure and temperature, body-mass-index, heartbeat, or pulse, which heuristically help in deciding the quality of health of a human being. Integration of sensors with clothes, spectacles, and directly to different body

parts have also been demonstrated.[30, 31] Further, flexible and wearable electronics-based sensors are also found extensively in the prior arts.[32]

Apart from the biomedical devices, environmental monitoring with the help of the POCT devices have become another front where a rapid progress has been made. Development of sensors to detect diverse hazardous vapors or gases, pH, particles, pollens, or allergens, in the atmosphere have also gained a lot of interest due to their importance in environmental monitoring.[33, 34] In this regard, another important aspect is to power these sensors or the POCT devices in an efficient manner. The POCT devices with a significantly low power rate can lead to an economic device, which can be made popular immediately due to their effectiveness at a lower cost. Thus, the integration of the renewable energy resources with the POCT devices have become almost synonymous wherein novel pathways of energy harvesters with high power density have been explore.[35-38] In particular, the use of the specialties of the smart nanomaterials like nanoparticles, nanosheets, nanotubes, nanofibers, or nanowire of metal, metal oxides, semiconductors, carbon allotropes such as fullerene or graphene, liquid crystals, or biomaterials have been extensively employed in various electronic prototypes such as micro-electro-mechanical-systems (MEMS),[39, 40] field effect transistors (FET),[41] or surface acoustic wave (SAW)[42, 43] devices. Further, the use of various micro or nanofluidic, magnetoresistive, and photovoltaic phenomena have been employed to develop proof-of-concept prototypes targeting biomedical applications, environmental monitoring, and renewable energy harvesting.

1.2. Classification of Sensors

Recently, an extensive research and development have taken place in the field of sensing. Variety of applications has been demonstrated harnessing the attributes of variety of

scientific domain such as microfluidics, electronics, or spintronics, among others. In this section, a glimpse of the sensors from different kinds has been described.

1.2.1 Microfluidic Sensors

Integration of special features of nanotechnology in the microfluidic applications is supporting the dream of fabricating simple, economic, portable, and multitasking devices in near future.[44, 45] In this direction, few recent works have demonstrated the proficiency of the miniaturized self-motile objects[1, 46, 47] to serve as sensors as well as delivery vehicles by harnessing chemical energy,[48] surface tension force,[46, 49] photonic or acoustic[50, 51] and external electric or magnetic field.[52] Microfluidics has become one of the major research area in the field of sensing due to the attributes of fluid flow in a micro and nanometer domain.[53, 54] Many recently reported sensors are based on microfluidic phenomenon.[55-57] The controlled fabrication of microchannel, and involvement of fluid flow make the platform suitable platform for most of the bio-sensing applications. Modification of the surfaces of the microchannel has opened up a new era in the field of sensing. Moreover, the integration of electrodes in the microchannels have given an option to apply external energy like electric potential which in turn has been utilized to generate turbulence or small fluid features in many microfluidic applications. Droplet-based sensors are also reported widely in the literature,[58, 59] however, the droplet sensors has been employed as a medium of bio-analytes. Thus, an electronic component is attached with the droplet sensor to decode the electrical response after the desired sensing mechanism. Apart from the sensing there are also different droplet and microchannel based energy harvester reported in the literature.[45] The surface charges of the nano/microfluidic channels has been utilized to produce energy from the microfluidic system.

1.2.2 Paper-based Sensors

Paper is a widely used material for different applications for example, printing, writing, packaging etc. However, the application of paper in the field of engineering, electronic or electromechanical fabrication has been stated recently.[60, 61] The thickness of the paper can easily be varied during the preparation. The main component of a paper is cellulose fibers and this fiber networks allows fluid to flow through them without any external pumping. This feature of the paper makes it very popular in the field of fluid mechanic and bio-sensing applications. Moreover, the flexible nature of paper substrate helps researchers to develop wearable sensors.[62] The recent trend of sensor development is director towards the flexible devices, thus a major sensor development is based on the flexible substrates of polymers such as PDMS or paper.[63, 64] Of late, a large number of paper-based sensors has been reported for detecting a wide range of materials such as, gas, vapor, bio-analyte etc.[65, 66] Paper-based sensors are not only popular for electronic sensing applications but also extensively employed in other sensing methodologies such as microfluidics,[67, 68] colorimetric applications etc. The cellulose fibers of a paper substrate can be functionalized with biomolecules which in turn helps in developing bio-sensors based on a paper substrate. Leading research groups across the world have started developing paper-based electronic devices and sensors as the use of paper makes the sensors and devices flexible, replaceable, and wearable. Paper-based micro-channel fabrication for developing electronic sensors for the detection of multiple analytes has already been demonstrated. However, there is a need to develop more paper-based electronic devices and sensors so that a large section of sensing applications can be performed in the paper-based platform.

1.2.3 Spintronic Sensors

The advancement of nanotechnology has opened up a new avenue of research by introducing nanomagnetism. The application of nanomagnetism have enriched and empowered the field of mico-nanoelectronics significantly.[69, 70] One of the major developments in the field of mico-nanoelectronics is the discovery of different spintronic phenomenon. Spintronics is a field of study, which deals with the spin of electrons. Most of the spintronic applications include magnetoresistance where the electrical conductance of a single or composite material can be varied by applying external magnetic field. The magnetoresistance can be achieved in different way such as by controlling the spin-dependent tunneling and scattering of electrons using external magnetic field. In this direction, many magnetoresistance-based devices and nanosensors have been developed employing Giant magnetoresistance (GMR), Anisotropic magnetoresistance (AMR) and Tunneling magnetoresistance (TMR) using metals, semiconductors and oxides nanoparticles.[71] The AMR effect can be realized by measuring the change in resistance in ferromagnetic materials with change in the direction of current and magnetization. However, GMR effect takes place in multilayers and granular structures of ferromagnetic and non-magnetic materials. The antiferromagnetic exchange coupling between ferromagnetic and non-magnetic materials cause the change in resistance in presence of external magnetic field.[72] However, the TMR effect depends on the spin-dependent tunneling effect in presence of external magnetic field in a multilayer structure or magneto tunneling junction having an dielectric thin layer in between two magnetic material.[71, 73] Prior-art suggests that spintronic sensors have high sensitivities due to the involvement of electron spins. The sensors are generally rapid in detection, portable, and comparatively economical. Thus, spintronic sensors are extensively used in chemical and bio-sensing

applications.[74, 75] One of the major contribution of spintronics has been observed in development of memory devices. In recent studies, people have shown the recent advancements of spintronic and magnetoresistance based bio-sensing.[76, 77] Magnetic nanoparticles labeled with specific molecules on spintronic platform are employed to detect the target bio-molecules, which upon attachment with magnetic nanoparticle functionalized biomolecules shows a deflection in spin-polarized currents through the spintronic sensor.[78] The deflection in the current is then calibrated with the concentration of the analyte in order to perform quantitative measurement. The current through a spintronic sensor changes in presence of external magnetic field only if the specific bio-attachment takes place.[78, 79]

1.2.4 Electronic Sensors

Similar to other types of sensors, different electronic sensors have also been developed to monitor the environment and health parameters.[80, 81] There are different kinds of electronic sensors evolved over the past few decades. Broadly, they can be categorized as resistive,[82-84] capacitive,[85] FET based,[86-88] MEMS,[89] and electrochemical[14, 90] systems. Prior reports have demonstrated many of the resistive and capacitive gas and vapor sensors. Resistive biosensors are also illustrated extensively in recent past.[80, 82] On the other hand, field effect transistors (FET) are one of the extensively used electronic device in almost every field of electronic gadgets. Since the advent of sensors, FET has been employed for a variety of sensing applications such as gas sensing, chemical sensing, bio-sensing etc.[91, 92] The FET devices provide an extra control terminal called gate, which offers higher sensitivity and an extra possibility in detection technique. The gate electrode can be modified in order to fabricate a sensor. Multiple parameters like current, threshold voltage etc. can be utilized in order to increase the sensitivity of a sensor.[93] In this direction, new nanomaterials and

their attributes at nanoscale has created a new avenue in fabricating electronic sensors.[94] The presence of nanomaterials at the active surface of a sensor provides salient advantages such as desirable electrical, mechanical and chemical properties. Thus, helps in improving the sensitivity of the device.[95] The high surface to volume ratio of nanomaterials facilitates immobilizing the relevant sensing elements. Presence of nanomaterial in an electrical sensor also creates higher number of active sites for any biological or chemical reaction, which plays the sensing role in the device. However, many of the developed electronic sensors do not follow a conventional pathway in comparison with existing technology,[95, 96] though the devices are well capable of sensing the target molecules. An advancement in developing even higher sensitive and selective sensors for environmental and healthcare application is still required.

Among different other types of electronic sensors, FET sensors are widely used and thus are discussed in this thesis. The electronic sensing can be broadly divided in three different parts such as (i) sensing mechanisms, (ii) transducing, and (iii) electronic signal acquisition or measurement. The sensing mechanism can be reversible or irreversible. The reversible processes generally involve adsorption, thermal excitation such as heating-cooling, or a reversible chemical reaction. In this kind of situation, a sensor becomes reusable and the active site undergoes non-destructive process while sensing. However, an irreversible mechanism destroys the active site of the sensor after a single sensing process. In such a case, the sensor is fabricated for one-time use. Most of the bio-sensing platforms undergoes irreversible mechanism and thus needs economic materials for fabricating such sensor. Moreover, the biosensors sometimes are intentionally made for one-time use, to avoid the risk of contaminations in the consecutive tests. There are four major types of

sensing interactions such as DNA-DNA interaction, antigen-antibody interaction, interaction of different ions, and enzymatic reactions.

The above mentioned interactions are generally irreversible and are extensively used in bio and chemical sensing. The sensing mechanism correlates the extent of reaction with the electrical signal such as a change in current, voltage, resistance etc. based on the kind of the electrical transducer or device, which can be resistive, capacitive or FET based. The output from the electronic device is then measured, recorded or analyzed to quantify the concentration of target molecule which is to be detected and is involved in the sensing mechanism.

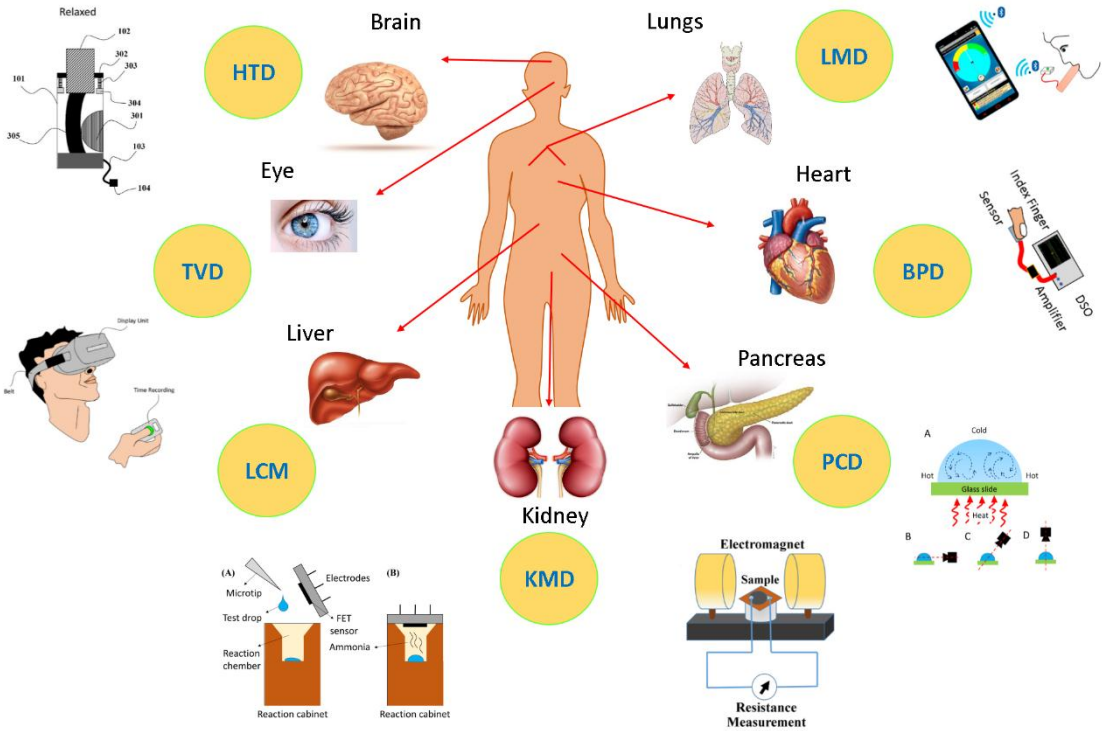

Figure 1.1: This image shows the different body parts that need a monitoring device to detect the early stage of diseases associated with different organs. In image multiple devices are highlighted such as, Hand Tremor Detection (HTD) device, Lung Monitoring Device (LMD), Tunnel Vision Detection (TVD) device, Body Potential Detection (BPD) device, Liver Condition Monitoring (LCM) device, Pancreas Condition Detection (PCD) device, and Kidney Monitoring Device (KMD) to monitor kidney health.

1.3 Objective of the Thesis

The thesis targets the development of different bio-medical devices for point-of-care testing applications. In order to develop such sensors, different pathways have been explored such as microfluidics, spintronic, and electronic. The idea is to develop the effective point-of-care testing device, which can be utilized to monitor the health parameters. Figure 1.1 shows a schematic of the proposed objectives which is necessary to develop in order to increase the awareness about the diseases. At the same time, as discussed earlier, it is also necessary to decentralize the pathological activity, so that people can have easy access to the diagnosis facilities.

With this background, the present thesis explores a host of pathways to develop proof-of-concept prototypes targeting biomedical applications, environmental monitoring, and renewable energy harvesting. The thesis is divided into three different sections, namely, (I) Microfluidic Sensors, (II) Paper-Based Electronic Sensors, and (III) Other Electronic Sensors and POC Devices. Each section contains two or more technical chapters. In total, the thesis contains eight different technical chapters such as, (i) self-spinning nanoparticle laden microdroplets for sensing and energy harvesting, (ii) droplet based detection of blood α-amylase employing thermal Marangoni effect, (iii) paper based flexible touchpad and hand tremor detection device, (iv) nano-enabled paper humidity sensor for mobile based point-of-care lung function monitoring, (v) paper based GMR nanobiosensor for α-amylase estimation under impulse magnetic field, (vi) a nano-BG-FET for point-of-care estimation of ammonia and urea in human urine, (vii) a prototype for point-of-care stress detection at different body parts, and (viii) conversion of observed speed of a moving object to diagnose tunnel vision. The technical chapters in the thesis are preceded by an introductory chapter while at the end of the thesis a chapter containing the summary and

future scopes are included. A brief detail of outcomes of this thesis in terms of patents, publications, conferences, and awards has also been provided at the end of the thesis.

References

1. G. Brettlecker, C. Cáceres, A. Fernández, N. Fröhlich, A. Kinnunen, S. Ossowski, H. Schuldt and M. Vasirani, Basel, 2008.
2. P. Sungmee and S. Jayaraman, *IEEE Engineering in Medicine and Biology Magazine*, 2003, **22**, 41-48.
3. J. Øvretveit, T. Scott, T. G. Rundall, S. M. Shortell and M. Brommels, *International Journal for Quality in Health Care*, 2007, **19**, 259-266.
4. J. M. Goh, G. Gao and R. Agarwal, *Information Systems Research*, 2011, **22**, 565-585.
5. R. W. Keyes, *IBM Journal of Research and Development*, 1988, **32**, 84-88.
6. M. J. Madou, *Fundamentals of Microfabrication: The Science of Miniaturization, Second Edition*, Taylor & Francis, 2002.
7. Y. Cui and C. M. Lieber, *Science*, 2001, **291**, 851.
8. G. Eda, G. Fanchini and M. Chhowalla, *Nature Nanotechnology*, 2008, **3**, 270.
9. P. L. McEuen, *Nature*, 1998, **393**, 15.
10. J. Taylor, H. Guo and J. Wang, *Physical Review B*, 2001, **63**, 245407.
11. S. Park, M. Vosguerichian and Z. Bao, *Nanoscale*, 2013, **5**, 1727-1752.
12. R. Jayakumar, D. Menon, K. Manzoor, S. V. Nair and H. Tamura, *Carbohydrate Polymers*, 2010, **82**, 227-232.
13. G. Aragay, J. Pons and A. Merkoçi, *Chemical Reviews*, 2011, **111**, 3433-3458.

14. J. Wang, *Electroanalysis*, 2005, **17**, 7-14.

15. E. Duguet, S. Vasseur, S. Mornet and J.-M. Devoisselle, *Nanomedicine*, 2006, **1**, 157-168.

16. Y. Song, J. Hormes and C. S. S. R. Kumar, *Small*, 2008, **4**, 698-711.

17. K. K. Jain, *Technology in Cancer Research & Treatment*, 2005, **4**, 407-416.

18. S. K. Vashist, A. G. Venkatesh, K. Mitsakakis, G. Czilwik, G. Roth, F. von Stetten and R. Zengerle, *BioNanoScience*, 2012, **2**, 115-126.

19. Z. L. Wang and W. Wu, *Angewandte Chemie International Edition*, 2012, **51**, 11700-11721.

20. O. Pummakarnchana, N. Tripathi and J. Dutta, *Science and Technology of Advanced Materials*, 2005, **6**, 251-255.

21. V. Raffa, O. Vittorio, C. Riggio and A. Cuschieri, *Minimally Invasive Therapy & Allied Technologies*, 2010, **19**, 127-135.

22. A. Amine, H. Mohammadi, I. Bourais and G. Palleschi, *Biosensors and Bioelectronics*, 2006, **21**, 1405-1423.

23. Y. Qi and M. C. McAlpine, *Energy & Environmental Science*, 2010, **3**, 1275-1285.

24. C. C. Conrad and K. G. Hilchey, *Environmental Monitoring and Assessment*, 2011, **176**, 273-291.

25. J. D. Spengler and K. Sexton, *Science*, 1983, **221**, 9.

26. M. H. Yu, H. Tsunoda and M. Tsunoda, *Environmental Toxicology: Biological and Health Effects of Pollutants, Third Edition*, Taylor & Francis, 2011.

27. P. B. Luppa, A. Bietenbeck, C. Beaudoin and A. Giannetti, *Biotechnology Advances*, 2016, **34**, 139-160.

28. A. J. Jenkins and B. A. Goldberger, *On-Site Drug Testing*, Humana Press, 2002.

29. R. W. Peeling and D. Mabey, *Clinical Microbiology and Infection*, 2010, **16**, 1062-1069.

30. S. Schneegass and O. Amft, *Smart Textiles: Fundamentals, Design, and Interaction*, Springer International Publishing, 2017.

31. M. J. McGrath, C. N. Scanaill and D. Nafus, *Sensor Technologies: Healthcare, Wellness and Environmental Applications*, Apress, 2014.

32. G. Appelboom, E. Camacho, M. E. Abraham, S. S. Bruce, E. L. P. Dumont, B. E. Zacharia, R. D'Amico, J. Slomian, J. Y. Reginster, O. Bruyère and E. S. Connolly, *Archives of Public Health*, 2014, **72**, 28.

33. A. O. Fung and N. Mykhaylova, *Journal of Laboratory Automation*, 2014, **19**, 225-247.

34. R. E. Clement, P. W. Yang and C. J. Koester, *Analytical Chemistry*, 1999, **71**, 257-292.

35. F. Sharifi, S. Ghobadian, F. R. Cavalcanti and N. Hashemi, *Renewable and Sustainable Energy Reviews*, 2015, **52**, 1453-1472.

36. S. Choi, *Biotechnology Advances*, 2016, **34**, 321-330.

37. G. O. F. Parikesit, F. Prasetia, G. A. Pribadi, D. C. Simbolon, G. Y. Pradhana, A. R. Prastowo, A. Gunawan, K. Suryopratomo and I. Kusumaningtyas, *The Journal of The Textile Institute*, 2012, **103**, 1077-1087.

38. X. Wei, T. Tian, S. Jia, Z. Zhu, Y. Ma, J. Sun, Z. Lin and C. J. Yang, *Analytical Chemistry*, 2016, **88**, 2345-2352.

39. S. Saadon and O. Sidek, *Energy Conversion and Management*, 2011, **52**, 500-504.

40. A. R. Jha, *MEMS and Nanotechnology-Based Sensors and Devices for Communications, Medical and Aerospace Applications*, CRC Press, 2008.

41. M. Curreli, R. Zhang, F. N. Ishikawa, H. K. Chang, R. J. Cote, C. Zhou and M. E. Thompson, *IEEE Transactions on Nanotechnology*, 2008, **7**, 651-667.

42. W. Tsung-Tsong, C. Yung-Yu and C. Tai-Hsu, *Journal of Physics D: Applied Physics*, 2008, **41**, 085101.

43. W. Wei-Shan, W. Tsung-Tsong, C. Tai-Hsu and C. Yung-Yu, *Nanotechnology*, 2009, **20**, 135503.

44. J. K. Moon, J. Jeong, D. Lee and H. K. Pak, *Nature Communications*, 2013, **4**, 1487.

45. T. Krupenkin and J. A. Taylor, *Nature Communications*, 2011, **2**, 448.

46. M. Bhattacharjee, V. Pasumarthi, J. Chaudhuri, A. K. Singh, H. Nemade and D. Bandyopadhyay, *Nanoscale*, 2016, **8**, 6118-6128.

47. A. Nourhani, V. H. Crespi and P. E. Lammert, *Physical Review Letters*, 2015, **115**, 118101.

48. Z. Wu, Y. Wu, W. He, X. Lin, J. Sun and Q. He, *Angewandte Chemie International Edition*, 2013, **52**, 7000-7003.

49. Y. S. Song and M. Sitti, *IEEE Transactions on Robotics*, 2007, **23**, 578-589.

50. A. A. Solovev, E. J. Smith, C. C. Bof' Bufon, S. Sanchez and O. G. Schmidt, *Angewandte Chemie International Edition*, 2011, **50**, 10875-10878.

51. W. Wang, L. A. Castro, M. Hoyos and T. E. Mallouk, *ACS Nano*, 2012, **6**, 6122-6132.

52. W. F. Paxton, S. Sundararajan, T. E. Mallouk and A. Sen, *Angewandte Chemie International Edition*, 2006, **45**, 5420-5429.

53. S. Cheng and Z. Wu, *Lab on a Chip*, 2012, **12**, 2782-2791.

54. C. Rivet, H. Lee, A. Hirsch, S. Hamilton and H. Lu, *Chemical Engineering Science*, 2011, **66**, 1490-1507.

55. M. B. Fox, D. C. Esveld, A. Valero, R. Luttge, H. C. Mastwijk, P. V. Bartels, A. van den Berg and R. M. Boom, *Analytical and Bioanalytical Chemistry*, 2006, **385**, 474.

56. B. Kuswandi, Nuriman, J. Huskens and W. Verboom, *Analytica Chimica Acta*, 2007, **601**, 141-155.

57. H. Andersson and A. van den Berg, *Sensors and Actuators B: Chemical*, 2003, **92**, 315-325.

58. S. Ralf, B. Martin, P. Thomas and H. Stephan, *Reports on Progress in Physics*, 2012, **75**, 016601.

59. V. Srinivasan, V. K. Pamula and R. B. Fair, *Analytica Chimica Acta*, 2004, **507**, 145-150.

60. J. Lessing, A. C. Glavan, S. B. Walker, C. Keplinger, J. A. Lewis and G. M. Whitesides, *Advanced Materials*, 2014, **26**, 4677-4682.

61. A. Russo, B. Y. Ahn, J. J. Adams, E. B. Duoss, J. T. Bernhard and J. A. Lewis, *Advanced Materials*, 2011, **23**, 3426-3430.

62. C.-C. Yang and Y.-L. Hsu, *Sensors*, 2010, **10**, 7772.

63. J. R. Windmiller and J. Wang, *Electroanalysis*, 2013, **25**, 29-46.

64. M. Segev-Bar and H. Haick, *ACS Nano*, 2013, **7**, 8366-8378.

65. C. Li, E. T. Thostenson and T.-W. Chou, *Composites Science and Technology*, 2008, **68**, 1227-1249.

66. A. W. Martinez, S. T. Phillips, G. M. Whitesides and E. Carrilho, *Analytical Chemistry*, 2010, **82**, 3-10.

67. R. Fobel, A. E. Kirby, A. H. C. Ng, R. R. Farnood and A. R. Wheeler, *Advanced Materials*, 2014, **26**, 2838-2843.

68. T. S. Park, W. Li, K. E. McCracken and J.-Y. Yoon, *Lab on a Chip*, 2013, **13**, 4832-4840.

69. A. P. Guimarães, *Principles of Nanomagnetism*, Springer Berlin Heidelberg, 2009.

70. S. D. Bader, *Reviews of Modern Physics*, 2006, **78**, 1-15.

71. T. Shinjo, *Nanomagnetism and Spintronics*, Elsevier Science, 2013.

72. I. Ennen, D. Kappe, T. Rempel, C. Glenske and A. Hütten, *Sensors (Basel, Switzerland)*, 2016, **16**, 904.

73. S. A. Wolf, D. D. Awschalom, R. A. Buhrman, J. M. Daughton, S. von Molnár, M. L. Roukes, A. Y. Chtchelkanova and D. M. Treger, *Science*, 2001, **294**, 1488.

74. P. P. Freitas, R. Ferreira, S. Cardoso and F. Cardoso, *Journal of Physics: Condensed Matter*, 2007, **19**, 165221.

75. S. Parkin, J. Xin, C. Kaiser, A. Panchula, K. Roche and M. Samant, *Proceedings of the IEEE*, 2003, **91**, 661-680.

76. D. R. Baselt, G. U. Lee, M. Natesan, S. W. Metzger, P. E. Sheehan and R. J. Colton, *Biosensors and Bioelectronics*, 1998, **13**, 731-739.

77. J. Llandro, J. J. Palfreyman, A. Ionescu and C. H. W. Barnes, *Medical & Biological Engineering & Computing*, 2010, **48**, 977-998.

78. D. A. Hall, R. S. Gaster, T. Lin, S. J. Osterfeld, S. Han, B. Murmann and S. X. Wang, *Biosensors and Bioelectronics*, 2010, **25**, 2051-2057.

79. D. L. Graham, H. A. Ferreira and P. P. Freitas, *Trends in Biotechnology*, 2004, **22**, 455-462.

80. W. P. Eaton and J. H. Smith, *Smart Materials and Structures*, 1997, **6**, 530.

81. Q. He, S. Wu, Z. Yin and H. Zhang, *Chemical Science*, 2012, **3**, 1764-1772.

82. C. C. Wang, S. A. Akbar and M. J. Madou, *Journal of Electroceramics*, 1998, **2**, 273-282.

83. K. M. Tripathi, A. Sachan, M. Castro, V. Choudhary, S. K. Sonkar and J. F. Feller, *Sustainable Materials and Technologies*, 2018, **16**, 1-11.

84. C. Gonçalves, A. Ferreira da Silva, J. Gomes and R. Simoes, *Inventions*, 2018, **3**, 14.

85. A. Salim and S. Lim, *Sensors*, 2017, **17**, 2593.

86. L. Torsi, M. Magliulo, K. Manoli and G. Palazzo, *Chemical Society Reviews*, 2013, **42**, 8612-8628.

87. A. Dodabalapur, *Materials Today*, 2006, **9**, 24-30.

88. C. M. Hangarter, M. Bangar, A. Mulchandani and N. V. Myung, *Journal of Materials Chemistry*, 2010, **20**, 3131-3140.

89. N.-C. Tsai and C.-Y. Sue, *Sensors and Actuators A: Physical*, 2007, **134**, 555-564.

90. Y. Shao, J. Wang, H. Wu, J. Liu, I. A. Aksay and Y. Lin, *Electroanalysis*, 2010, **22**, 1027-1036.

91. B. L. Allen, P. D. Kichambare and A. Star, *Advanced Materials*, 2007, **19**, 1439-1451.

92. G. Eranna, B. C. Joshi, D. P. Runthala and R. P. Gupta, *Critical Reviews in Solid State and Materials Sciences*, 2004, **29**, 111-188.

93. J.-O. Lee, H.-M. So, E.-K. Jeon, H. Chang, K. Won and Y. H. Kim, *Analytical and Bioanalytical Chemistry*, 2008, **390**, 1023-1032.

94. X. Huang, Z. Zeng and H. Zhang, *Chemical Society Reviews*, 2013, **42**, 1934-1946.

95. F. Patolsky and C. M. Lieber, *Materials Today*, 2005, **8**, 20-28.

96. E. Bekyarova, M. Davis, T. Burch, M. E. Itkis, B. Zhao, S. Sunshine and R. C. Haddon, *The Journal of Physical Chemistry B*, 2004, **108**, 19717-19720.

I. Microfluidic Sensors

CHAPTER 2

Self-spinning Nanoparticle Laden Microdroplets for Sensing and Energy Harvesting

Contents

ABSTRACT 23
2.1. Introduction 24
2.2. Experimental Section 26
2.2.1. Materials 26
2.2.2. Synthesis 27
2.2.3. Methods 29
2.3. Results and Discussion 32
2.3.1 Experimental Results on the Phenomenon 32
2.3.2 Theoretical Explanation of the Phenomenon 33
2.3.3 Experimental Optimization of Salt and Nanoparticle Loading in the Droplet 38
2.3.4 Electrical Response of the Phenomenon 41
2.3.5 Experimental Results on Energy Harvesting 44
2.3.6 Theoretical Basis of Voltage Generation 49
2.3.7 Computational Simulations to Estimate Potential Drop on the Electrodes 51
2.3.8 Power Density and Conversion Efficiency 55
2.3.9. Sensor Application 59
2.4. Conclusions 61
References 62

भारतीय प्रौद्योगिकी संस्थान गुवाहाटी
Indian Institute of Technology Guwahati

ABSTRACT

Exposure of a volatile organic vapor could set in powerful rotational motion in a microdroplet composed of an aqueous salt solution loaded with metal nanoparticles. The solutal Marangoni motion on the surface originating from the sharp difference in the surface tension of water and organic vapor stimulated the strong vortices inside the droplet. The vapor sources of methanol, ethanol, diethyl ether, toluene, and chloroform stimulated motions of different magnitudes, which could easily be correlated to the surface tension gradient on the drop-surface. Interestingly, when the nanoparticle-laden droplet of the aqueous salt solution was connected to an external electric circuit through a pair of electrodes, ~85 – 95% reduction in the electrical resistance was observed across the spinning droplet. The extent of reduction in the resistance was found to have a correlation with the difference in the surface tension of the vapor source and the water droplet, which could be employed to distinguish the vapor sources. Remarkably, the power density of the same prototype was estimated to be around 7 $\mu W/cm^2$, which indicated the potential of the phenomenon in converting surface energy into the electrical one in a non-destructive manner and under ambient condition. Theoretical analysis uncovered that the difference in the ζ-potential near the electrodes was the major reason for the voltage generation. The prototype could also detect the repeated exposure and withdrawal of vapor sources, which helped in the development of a proof-of-concept detector to sense alcohol issuing out of the human breathing system.

This chapter is published in *Nanoscale*. **11**, 6118-6128 (2016).

2.1. Introduction

Integrating the special features of nanotechnology in the microfluidic applications is expected to realize the dream of fabricating simple, economical, portable, and multitasking devices in near future.[1-3] In this direction, a number of recent works have shown the capability of the minuscule self-motile objects[4-7] to serve as sensors as well as delivery vehicles by harnessing chemical energy,[8] surface tension force,[9] photonic[10] or acoustic[11] or thermal excitations,[12] and external electric[13] or magnetic field.[14] The modern sensors composed of field effect transistors,[15] electrochemical detectors,[16] photo-detectors,[17] piezo-materials,[18] nano-cantilevers,[19] plasmonic[20] or microfluidic devices[21] have also been benefiting significantly from the specialties of nanowires, nanoparticles, or nanotubes of functional materials.[22-25] Importantly, these micro or nanoscale objects are also found to be equally efficient in converting the different other forms of energies into electrical energy while accomplishing their stipulated tasks.[25-28] The power density of many of the conventional macroscopic processes[3, 29] such as radio frequency (~ 1 $\mu W/cm^2$), solar irradiation (~100 mW/cm^2), ambient illumination (~100 $\mu W/cm^2$), thermoelectric (~60 $\mu W/cm^2$) or vibration generators (~ 10 – 800 $\mu W/cm^3$), or ambient airflow (~1 mW/cm^2) are found to be comparable with some of the newly developed micro or nanoscale energy harvesters.[1-3] The vision here is to develop applications involving miniaturized self-motile systems, which can harvest high-density power in addition to performing tasks simultaneously as sensor, mixer, separator, or transporter. Herein, we show that a simple nanoparticle-laden water microdroplet could simultaneously sense and distinguish different types of organic vapors alongside harvesting high-density power.

The previous studies indicate that so far the most popular and robust method to detect vapors or gases has been to employ the electrochemical sensors composed of semiconductor metal oxides.[30, 31] The modern sensors based on conducting[32, 33] and doped polymers[34] or carbon black[35] have also been prepared for this purpose and faced the limitation with their lower percentage of response. Even the high-precision sensors composed of nanotubes[36] or nanotube-polymer composites[37, 38] have been facing difficulties on their larger recovery time. Importantly, all these sensors perform detection by estimating the variance in either of the electrical or electronic properties, or mass, or the color of the transmitted or reflected rays.[39, 40] In this situation, we aim to employ the specialties of nanotechnology into the microfluidic systems to design and develop state-of-art sensors, which are easy to fabricate, reliable, economic, highly sensitive, and robust.

A number of recent studies indicated that the self-motile microdroplets can simultaneously be employed for high-precision sensing[41, 42] and energy harvesting.[2] The droplet motions under diverse excitations was also found to be an exciting scientific phenomenon over the years.[43-46] In particular, the surface tension gradient stimulated Marangoni rotation, translation, and actuation of liquid droplets attracted attention not only because of the interesting physics associated with them but also for their appearance in a wide range of applications.[47-56] For example, a very recent study had shown that a water microdroplet could easily propel under the exposure of ethanol vapor.[56] However, there is hardly any study, which exploits the knowledge associated with the Marangoni motions inside miniscule systems for sensing and energy harvesting.

In the present work, we uncovered that a simple nanoparticle-laden water microdroplet could simultaneously sense the volatile organic vapors and harvest energy. The solutal Marangoni motion on the surface of the droplet stimulated by an external vapor source generated strong vortices inside the droplet. The strength of the rotational currents was found to be as high as 720 rpm. Different sources such as methanol, ethanol, diethyl ether, toluene, and chloroform engendered similar rotational currents of different magnitudes because of the variation in the surface tension gradient on the surface of the water droplet. Interestingly, when the nanoparticle-laden microdroplet was dispensed at the junction of a pair of electrodes, which were connected to an external power source, we noticed ~85 – 95% reduction in the electrical resistance across the rotating droplet under vapor stimulation. The reduction in the resistance was found to have a correlation with the difference in the surface tension of the vapor source and the water droplet, which in turn could be employed to distinguish the vapor sources. Further, repeated exposure and withdrawal of the vapor sources could also be traced with the help of this prototype. Remarkably enough, the power density of the rotational currents was ~7 $\mu W/cm^2$, which indicated the potential of the system for energy harvesting.

2.2. Experimental Section

2.2.1. Materials

Iron (II) sulfate heptahydrate ($FeSO_4.7H_2O$), hydrochloric acid (HCl), sodium hydroxide (NaOH) pellets, sodium chloride (NaCl), 99.8% methanol, 99.5% ethanol, 99% diethyl ether, poly-vinylpyrrolidone (PVP) were procured from Merck, India. Gold (III) chloride ($HAuCl_4.3H_2O$), silver nitrate ($AgNO_3$), sodium borohydride ($NaBH_4$), 98% hydrazine monohydrate ($N_2H_4.H_2O$), 99.8% toluene, 99.5% chloroform were obtained from Sigma-

Aldrich, India. The chemicals were of analytical grade and employed in the experiments without further purification. The Milli-Q grade water was used for cleaning and to prepare the solutions.

2.2.2. Synthesis

Silver (Ag) nanoparticles were synthesized by reducing the $AgNO_3$ salt with $NaBH_4$.[57] In this process, 30 ml of 2mM $NaBH_4$ solution was poured into a beaker, which was kept in an ice bath to maintain an isothermal condition at 4ºC. Thereafter, 2 ml of 1mM $AgNO_3$ solution was added slowly to the $NaBH_4$ solution. The Ag nanoparticles were formed as the $AgNO_3$ solution mixed with the $NaBH_4$ solution and reduced over a period of time. In order to prevent agglomeration of the nanoparticles, the solution in the beaker was gently stirred for ~20 minutes while the entire $AgNO_3$ solution was added to the $NaBH_4$ solution. The suspension of the Ag nanoparticles was stabilized by adding a few drops of 1.5M NaCl solution, which led to a yellow colored suspension. Finally, 0.3% PVP solution was added to obtain a stable suspension of Ag nanoparticles. The suspended Ag nanoparticles were preserved and later employed in the experiments on the nanoparticle-laden droplets. Transmission Electron Microscope (TEM – JEOL, JEM 2100) was employed to examine the size and shape of the Ag nanoparticles and Energy Dispersive X-Ray Analysis (EDX) was performed to confirm the presence of Ag.

Gold (Au) nanoparticles were synthesized by the $NaBH_4$ reduction of $HAuCl_4.3H_2O$ salt.[58] We prepared a 50mM aqueous solution of $AuCl_4^-$ (solution I) by mixing $HAuCl_4.3H_2O$ with HCl in the equal molar ratio which stabilized the nanoparticles. Following this, a 50mM of BH_4^- solution (solution II) was prepared by dissolving $NaBH_4$ in aqueous 1mM NaOH in equal molar ratio. Thereafter, 100 µl of solution I was mixed with water in such

a manner that the concentration of gold ions in the resultant solution was 0.5mM. Then, 300 µl of solution II was added to the aqueous solution I while the solution was stirred continuously. The formation of the Au nanoparticles was indicated by the change in color of the solution from light yellow to orange in the beginning and then to red after ~1 minute of stirring. The Au nanoparticle suspensions were preserved and later employed in the experiments. TEM was employed to examine the size and shape of the Au nanoparticles while EDX was performed to confirm the presence of Au. The details of the TEM images are discussed in Figure 2.1.

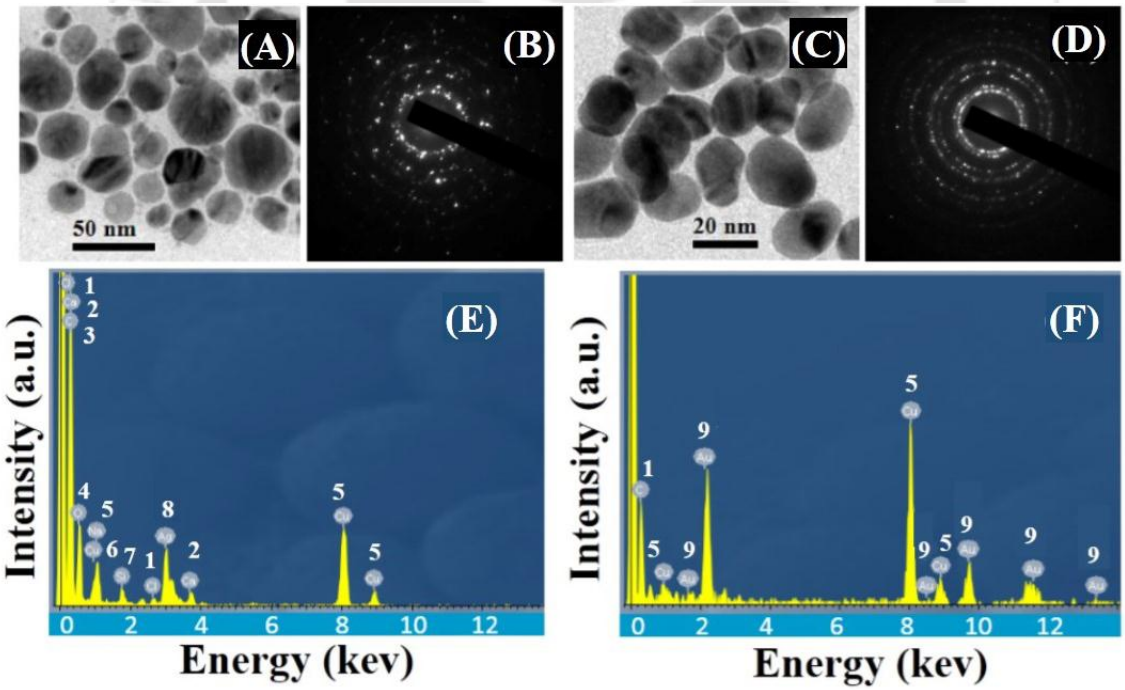

Figure 2.1: Figures (A) and (C) are the TEM images of Ag and Au nanoparticles. Respective SAED patterns are shown in images (B) and (D). The EDX images (E) and (F) confirmed the presence of Ag and Au. The numbers 1 – 9 on the image (E) and (F) represent the peaks of Cl, Ca, C, O, Cu, Si, Ag, and Au, respectively.

Characterizations of Ag and Au nanoparticles have been shown in Figure 2.1. Figure 2.1A and 2.1C show the TEM images of Ag and Au nanoparticles with their respective SAED

patterns in the images 2.1B and 2.1D. EDX analyses in the Figure 2.1E and 2.1F confirmed the presence of Ag and Au in the sample. The images (A) and (E) show that the diameters of the Ag nanoparticles were about 10 nm to 50 nm whereas the Au nanoparticles were about 10 nm to 20 nm. The numbers 1 – 9 on the image (E) and (F) represent the peaks of Cl, Ca, C, O, Cu, Si, Ag, and Au, respectively.

2.2.3. Methods

A water microdroplet was initially mixed with a collection of iron/iron oxide microparticles and then dispensed on a glass slide. Following this, a capillary tube filled with a volatile organic liquid such as diethyl ether was brought near the surface of the microdroplet. The organic vapors issued out of the capillary tube from a distance of ~1 cm came in contact with the microdroplet and stimulated a strong rotational motion inside the droplet. The rotational motion inside the droplet instigated motion to the microparticles inside the microdroplet. The experiments were repeated with droplets having single microparticles, which helped us in analyzing the strength of the rotational currents. The experiments were recorded as images and movies with the help of a digital camera. The reported rotational speed of the droplet was obtained by evaluating the number of revolutions of the microparticle per unit time from the recorded movies.

The aforementioned volatile organic vapor induced motion of a microdroplet was converted into an energy harvester and vapor sensor with the help of following experimental arrangements. In the beginning, a saturated aqueous salt solution of $FeSO_4.7H_2O$ was prepared at room temperature and stabilized for 15 minutes. Following this, a pair of Cu (copper) electrodes separated by a distance of ~1 mm was placed on a glass slide. Thereafter, a 7 µl droplet of the saturated salt solution was dispensed at the junction of the electrodes. The electrodes were then connected to a direct current (DC)

power source (DC power supply unit, Aplab India) and a yellow light emitting diode (LED). A preset of 10 kΩ was connected in series with a power source of 6 V and the microdroplet was also connected in series with the DC power source and preset. Subsequently, a vapor source was introduced from the top of the droplet surface through a capillary tube to stimulate rotational motion inside the droplet. Consequently, decrease in resistance across the droplet due to the motion turned on the LED. The Cu electrodes were also connected separately to a digital multimeter (Mastech, India, range: 0 – 2 MΩ ± 1.0%), which helped in measuring the variation in resistance across the stationary or rotating microdroplets. For the energy harvesting experiments, instead of connecting a digital multimeter, the Cu electrodes were connected to a nanovoltmeter to measure the potential difference.

In order to obtain the sensitivity of the droplet rotation on the various process parameters, the experiments were repeated for different concentrations of $FeSO_4.7H_2O$ solution. Influences of the different types of volatile organic vapors such as diethyl ether, methanol, ethanol, toluene, and chloroform were analyzed. Further, diethyl ether was mixed with water at different proportions (v/v) to prepare solutions of concentration 15%, 25%, 50%, and 75% which were employed later to uncover the effect of the vapor concentrations on the change in resistance across the droplet.

The aforementioned experiments were also repeated with the nanoparticle-laden microdroplets. For this purpose, initially, the suspension of Ag or Au nanoparticles were mixed with the 0.85M aqueous solution of $FeSO_4.7H_2O$. The nanoparticle suspensions were mixed in 1:1 and 1:3 (v/v) ratios with the 0.85M aqueous solution of $FeSO_4.7H_2O$ in order to analyze the influence of the nanoparticles on the phenomenon. The experiments

were repeated by dispensing a 7 µl nanoparticle-laden microdroplet on the junction of the Cu electrodes. The motions of the droplets composed of 1:1 and 1:3 (v/v) ratios of Ag and Au nanoparticle suspensions with 0.85M $FeSO_4.7H_2O$ solution were reported. Influence of the different types of the volatile organic vapors such as diethyl ether and ethanol on the motion of the nanoparticle-laden microdroplet was also analyzed.

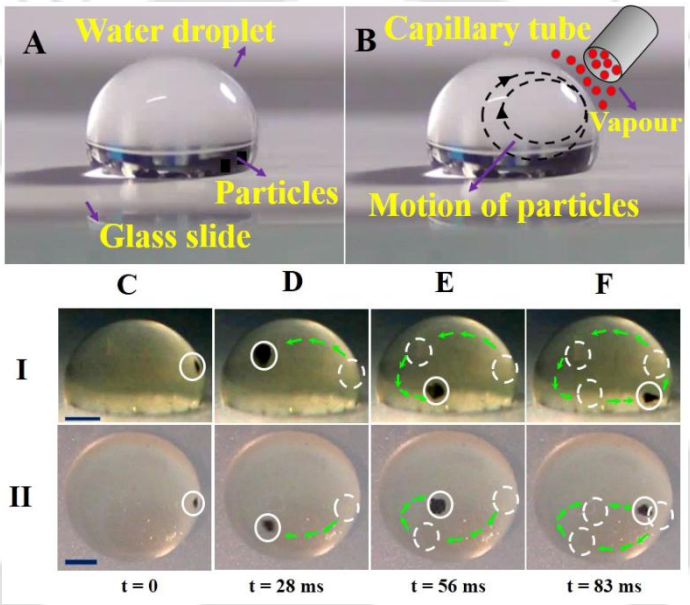

Figure 2.2: Experimental demonstration of the phenomenon. (A) A water droplet loaded with some microparticles was placed on a glass slide. (B) A rotational current was observed on the droplet when a vapor source of diethyl ether was brought into the immediate vicinity of the droplet surface. (C-F) Experimental images of particle motion. Rows I and II show the side and the top views of the motion under the exposure of the organic vapor when loaded with a single microparticle. The length of the scale bars on the images is 0.5 mm.

The motions of the moving particles in microdroplet due to different vapor introduction were recorded with a Sony Cybershot DSC-HX100V digital camera (Sony Corp., Japan) and high speed camera (Basler, piA640-210gc). DC power supply for the experiment was given by the DC power source (Aplab India). The resistance across the droplets in different experiments was measured with a digital multimeter (Mastech, India, range: 0 – 2 MΩ ± 1.0%). The potential difference across the droplet was measured using a

nanovoltmeter (Keithley 2182A). Electron microscopy and Selected Area Electron Diffraction (SAED) images were taken using a TEM (JEOL – JEM 2100). Energy-dispersive X-ray spectroscopy (EDX) analysis was performed using INCA EDX spectroscopy detector (Oxford Instruments, Buckinghamshire, UK) integrated with TEM.

2.3. Results and Discussion

2.3.1 Experimental Results on the Phenomenon

Figure 2.2 shows the rotational motion of a droplet when brought under the exposure of a vapor source of diethyl ether. Figures 2.2(A) and 2.2(B) show the initial configuration of the droplet and its motion when exposed to the vapor. A few iron/iron oxide microparticles were deliberately added inside the droplet for easy visualization of trajectories of the motion. It was found that when a water droplet loaded with a collection of iron microparticles was exposed to the diethyl ether, the rotational currents could cause rapid mixing of the particles. Figure 2.2(C) – 2.2(F) in the rows (I) – (III) show the trajectories of a single microparticle inside the droplet during rotation. When the microdroplet was exposed to the volatile organic vapor, initially, the vapor molecules adsorbed on the drop-surface to locally reduce the surface tension. Consequently, the gradient of surface tension between the zone of exposure and the other part of the droplet triggered a Marangoni motion at the air-water interface. The Marangoni flow at the interface induced the strong vortices inside the droplet. The magnitude of the rotational motion was found to be as high as ~720 RPM for a microparticle of diameter ~300 μm. The motion could easily be initiated and terminated with the exposure and removal of the vapor source. These motions could also be generated with the help of a wide range of common volatile organic materials which include chloroform, toluene, ethanol, and methanol, other than diethyl ether.

2.3.2 Theoretical Explanation of the Phenomenon

Mimicking the experiments in the Figure 2.2, we simulated the rotational motions of a two-dimensional (2-D) water droplet resting on a flat surface and surrounded by air, as shown in the Figure 2.3. We solved Navier-Strokes equations for a two-phase system with appropriate boundary conditions to analyze the phenomenon. A two-dimensional (2-D) semi-circular water droplet of diameter 1.5 mm, resting on a flat surface and surrounded by air was chosen to be the computational domain, as shown in the image (A) of Figure 2.3. The rectangular domain was of length 3 mm and width 1 mm.

The droplet was placed at 0.75 mm downstream from the air inlet. The surface tension gradient ($\Delta\gamma = \gamma_1 - \gamma_2$) at the interface was induced by changing the magnitude of surface tension at the arc length of 0.05 mm of the deformable air-water interface, as shown in the image (A) of Figure 2.3. The streamlines shown on Figure 2.3(A) represent the rotational currents originating from the surface tension gradient at the air-water deformable interface. The arrows represent the local velocity vectors.

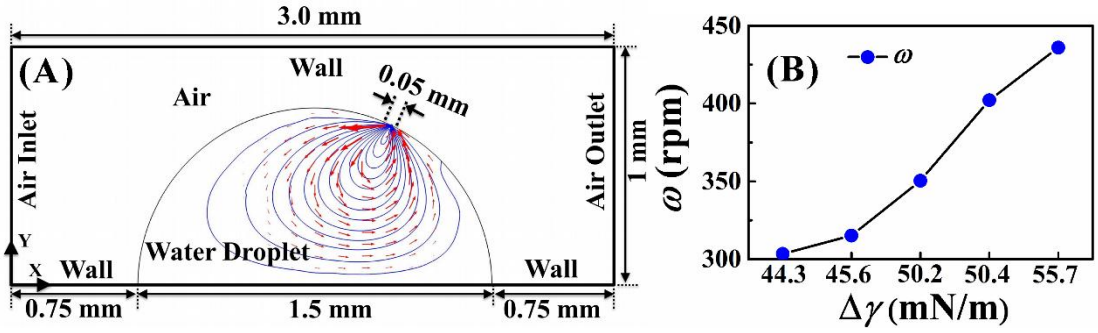

Figure 2.3: Image (A) shows the streamlines (continuous lines) and velocity vectors (arrowheads) of Marangoni flow inside a droplet of diameter 1.5 mm. Image (B) shows the change in average angular velocity (ω) with surface tension gradient ($\Delta\gamma$).

In the computations, the air (gas) and water (liquid) phases were assumed to be immiscible, Newtonian, and incompressible. The following continuity and equations of motion were employed to describe the motion of the i^{th} phase,

$$\nabla \cdot \mathbf{u}_i = 0 \,, \tag{2.1}$$

$$\rho \left(\dot{\mathbf{u}}_i + \mathbf{u}_i \cdot \nabla \mathbf{u}_i \right) = \nabla \cdot \left[-p_i \mathbf{I} + \eta_i \left(\nabla \mathbf{u}_i + \nabla \mathbf{u}_i^{\,T} \right) \right] + \mathbf{f}_{st} + \rho \mathbf{g} \,. \tag{2.2}$$

Here, the subscript i corresponds to air (i = 1) and water (i = 2) phases. The over-dot symbol denotes the time derivative. The velocity vector, density, viscosity, and pressure of the i^{th} phase were denoted by notations, u_i, ρ_i, η_i, and p_i respectively. The notation g was the acceleration due to gravity vector which was acting in the negative y-direction. The surface tension force was defined as, $\mathbf{f}_{st} = G \nabla \phi$, a product of the chemical potential (G) and the gradient of the phase field parameter (ϕ). The surface tension force was determined by minimizing the total free energy inside fluid domain as a function of the phase field variable (ϕ),

$$F(\phi) = \int_{\Omega} \left(f(\phi) + \frac{1}{2} \lambda \left| \nabla^2 \phi \right| \right) d\Omega \,. \tag{2.3}$$

where, Ω was computational volume and the total free energy, $F(\phi)$ was a combination of double well potential, $f(\phi) = \lambda / 4N^2 \left(\phi^2 - 1 \right)^2$, and surface energy. The parameter N was calculated by the following equation, $N = 0.5 h_m$ where h_m is the maximum element size in the computational domain. To evaluate surface energy, mixing energy density (λ) was estimated as, $\lambda = (3\gamma N) / \left(2\sqrt{2} \right)$ in which γ was surface tension and N was the thickness of the diffused interface. In order to track the rotational Marangoni motion of the droplet at the air-water interface and in the bulk, the phase-field method was employed.[59-61] In this method, the transport equation was written in terms of the phase field parameter (ϕ) as,

$$\dot{\phi} + \mathbf{u}_i \cdot \nabla \phi = \nabla \cdot \chi (\nabla G) \,. \tag{2.4}$$

Where the chemical potential (G) was defined as a derivative of the free energy functional, $G = F'(\phi) = \lambda\left[-\nabla^2\phi + \phi\left(\phi^2 - 1\right)/N^2\right]$. The interfacial density (ρ), and viscosity (μ) were evaluated in terms of f as, $a = 0.5\left[a_1(1+\phi) + a_2(1-\phi)\right]$, where a can be any of ρ and μ. The symbol χ represents the mobility tuning parameter, which was chosen to be 10 m s/kg to avoid mass loss in the conventional phase field model. The lower flat surface of the droplet was assumed to be non-slipping and impermeable while the curved air-water interface was considered to be the deformable one. The velocity of air at the inlet and outlet were set to zero. The upper wall of the computational domain was assumed to be non-slipping and impermeable. The contact angle of water droplet on the substrate was considered to be 90°. The surface tension at the air-water interface was assumed to be constant at 72.7 mN/m (γ_1) and changed locally in the domain of 0.05 mm arc length to a smaller value (γ_2) to create the surface tension gradient ($\Delta\gamma = \gamma_1 - \gamma_2$), as shown in the image (A) of Figure 2.3.

The 2-D geometry was divided into 7642 triangular elements to obtain the grid independent solutions. The unsteady governing equations (2.1) – (2.4) together with the boundary conditions were solved using the commercially available COMSOL™ Multiphysics software based on the finite element method.[5] In this method, the spatial terms of the governing equations were initially discretized to obtain an ordinary differential equation (ODE) in time, which was time-marched to obtain the evolution of the streamline flow patterns inside the droplet. We employed the built-in Galerkin least-square (GLS) method to discretize nonlinear convective diffusion equations, which was stabilized through streamlining and crosswind diffusions. The segregated predictor-

corrector method had been used to obtain the velocity and pressure profiles by incremental pressure correction.

Image (B) in Figure 2.3 shows the variation in the average angular velocity (ω) with a change in surface tension gradient ($\Delta\gamma$) for different vapors sources. The typical values of $\Delta\gamma$ were obtained for the computations from Ref. 71 as, toluene-water (44.3 mN/m), chloroform-water (45.6 mN/m), methanol-water (50.2 mN/m), ethanol-water (50.4 mN/m), and diethyl ether-water (55.7 mN/m). The plot clearly suggests that ω increased monotonically with $\Delta\gamma$. The simulations confirmed that indeed the magnitude of droplet rotations was a function of the $\Delta\gamma$ at the air-water interface. Average angular velocity (ω) describes the local spinning of the velocity vector field near the reference point at which the angular velocity is to be calculated. The velocity vector field ($\mathbf{u}$) components (u, v) in a 2-D computational domain are obtained by solving the coupled Navier-Stokes equation and continuity equation. Therefore, the vorticity (ω_v) of the system can be calculated as, $\boldsymbol{\omega}_v = \nabla \times \mathbf{u}$, where, ∇ represents the del operator, whereas $\mathbf{u}$ represents the velocity vector. According to the definition of vorticity ($\boldsymbol{\omega}_v$), it is equal to twice of the mean angular velocity ($\boldsymbol{\omega}_{mean}$) of the velocity field, which means, $\boldsymbol{\omega}_{mean} = \boldsymbol{\omega}_v / 2 = (\nabla \times \mathbf{u}) / 2$. This expression provides the mean angular velocity ($\boldsymbol{\omega}_{mean}$) at each and every grid points in the computational domain, which was then averaged over the whole 2-D computational domain in order to obtain the average angular velocity (ω).

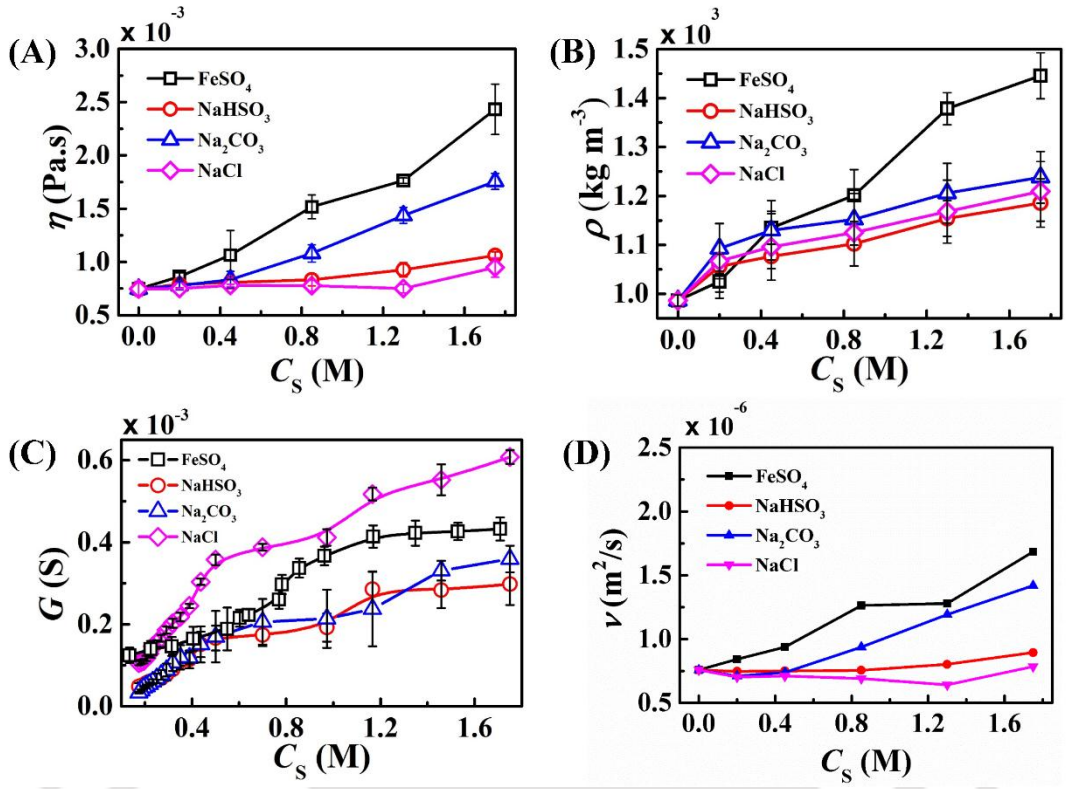

Figure 2.4: Characterization of electrolytes employed in the experiments. The plots show the variations in (A) dynamic viscosity, η, (B) density, ρ, (C) electrical conductance G, and (D) the kinematic viscosity, ν of aqueous salt solutions of concentration (C_S) composed of four different salts $FeSO_4.7H_2O$, $NaHSO_4$, Na_2CO_3, and NaCl.

The line-contours (arrows) depict the steady state streamlines (velocity vectors) obtained from the simulations, which indicate the formation of a strong rotational motion inside the droplet due to the surface tension gradient at the air-water interface. Image (B) shows that average angular velocity (ω) for such rotational motions inside the droplet monotonically increased from 300 to 450 rpm as $\Delta\gamma$ was increased. It may be noted here that the γ_1 values employed to calculate $\Delta\gamma$ in the simulations correspond to toluene, chloroform, methanol, ethanol and diethyl ether. Figure 2.3 confirmed that indeed the rotational motions observed in the experiments had their origin to the surface tension gradient induced Marangoni motion.

2.3.3 Experimental Optimization of Salt and Nanoparticle Loading in the Droplet

It is well known that deionized water is electrically non-conducting and the addition of salt improves its electrical conductance significantly. Importantly, an increase in the salt-loading also increases the viscosity and density of a liquid. We employed four different types of salts, $FeSO_4.7H_2O$, $NaHSO_4$, Na_2CO_3, and NaCl, to identify the type of salt to be employed in the experiments.

The plots (A) – (D) in Figure 2.4 show the variations in viscosity (η), density (ρ), electrical conductance (G) and kinematic viscosity (ν) with the concentration of different salts (C_s) in water. The dynamic viscosities of the salt-water electrolyte were measured employing the interfacial rheometer (Anton Paar, Physica MCR301) following the ASTM Standard procedure D1331-11 (2001). The kinematic viscosity was calculated using the standard formula, $\nu = \eta/\rho$. The densities of the electrolytes were obtained by measuring the mass of 10 ml salt-water solutions in a high precision weighing machine with digital output (Metlar Toledo, ME204). The electrical resistance of the salt-water solutions was measured with the help of a digital multimeter (Mastech, India, range: 0 – 2 MΩ ± 1.0%) by placing a pair of cylindrical electrodes (diameter ~ 2 mm) into a solution of 20 ml electrolyte. The inverse of this resistance is reported as the electrical conductance (G) in the plot (C). The plots suggest that apart from the increase in the electrical conductance (G), the dynamic viscosity (η), kinematic viscosity (ν), and density (ρ) of the electrolytes increased with C_s. The plots also suggest that G values were significantly higher for the salts $FeSO_4.7H_2O$ and NaCl, which prompted us to choose the salt in between these two materials.

We also carried out a series of experiments with rotating droplets to optimize the salt concentration and the nanoparticle loading inside the droplet. Images (A) and (B) in Figure 2.5 show that the variations in the electrical conductance (G_{max}) when the droplets were rotating at the maximum speed under the organic vapor excitation and the corresponding percentage variation in resistance ($\Delta R = 100 \times (R_0 - R_{min})/R_0$) with the change in C_s. In this study, R_0 is the experimentally measured electrical resistance of the stationary droplet, R_{min} is the minimum resistance measured for a rotating droplet when its speed is at maximum, and R_N^{min} ($= R_{min}/R_0$) is the ratio of the previous two parameters.

In these experiments, the electrical resistance was measured with the help of a digital multimeter (Mastech, India, range: 0 – 2 MΩ ± 1.0%) by placing a pair of cylindrical electrodes (diameter ~170 µm) into a microdroplet of diameter ~2 mm. Plot (B) suggests that the electrical resistance of the stationary droplet (R_0) had been always higher than the rotating one, and it reached a minimum value (R_{min}) when the droplet reached the maximum rotational speed under the organic vapor excitation. The plots (A) and (B) suggest that the variations in G_{max} and ΔR were rather non-monotonic with an increase in the C_s when the salts were NaCl and $FeSO_4.7H_2O$. We observed that with an increase in C_s, ΔR and G_{max} for the rotating droplets increased to a maximum value before reducing sharply at very high salt-loading. The sharp reduction at higher C_s could be attributed to the weakening of the rotational motion beyond a threshold salt-loading due to the increase in viscosity and density of the droplet. The experiments suggested that among all the salts tested at various concentrations, a water droplet loaded with 0.85M $FeSO_4.7H_2O$ showed maximum variation in ΔR when the microdroplet rotated at a maximum speed under the

organic vapor stimulation. Thus, the aqueous solution of 0.85M $FeSO_4.7H_2O$ was chosen to be the system for study.

In order to understand the impact of suspended nanoparticles on the droplet motion and their influence on the electrical properties of the droplet, we tested with different types of nanoparticles, for example, Ag, Au, Ni, Si, and Ni-Ag core shell. The nanoparticles were introduced because of three reasons, (i) they were insoluble and non-reactive to water, (ii) presence of nanoparticles helped in retaining the point of minimum resistance (R_{min}) for a longer duration, and (iii) the energy and power generation was higher in presence of the suspended nanoparticles because of the increase in the electrical conductance of the droplet.

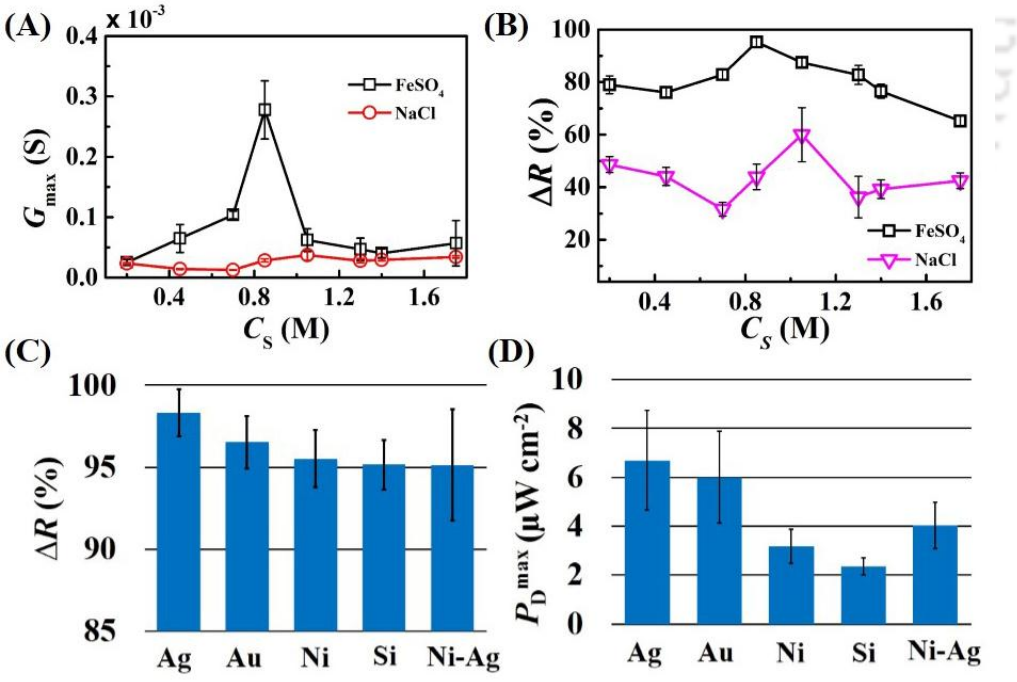

Figure 2.5: The plots show the variations in the, (A) electrical conductance (G_{max}) when the droplet was rotating at its maximum speed under organic vapor excitation and (B) percentage change in resistance in such a situation, $\Delta R = 100 \times (R_0 - R_{min}) / R_0$, with the concentration of salt (Cs). Plots (C) and (D) show the variations in ΔR and maximum power density (P_D^{max}) across the

droplet of aqueous 0.85M $Fe_2SO_4.7H_2O$ suspended with different types of nanoparticles. In all the experiments, the nanoparticles and the aqueous salt solution were mixed in 1:1 (v/v) ratio.

Plots (C) and (D) in Figure 2.5 show the variation in ΔR and maximum power density (P_D^{max}) for different nanoparticles when suspended in the salt-water droplet in a 1:1 (v/v) ratio. The plots clearly suggest that the power density obtained was higher for the Ag and Au nanoparticles than the other nanoparticles and this was the basis to employ the Ag and Au nanoparticles in the experiments reported in the main manuscript. The suspended Ag and Au inside the droplet enhanced the electrical conductance of the salt-water droplet, which eventually helped in lowering the resistance while it rotated under the organic vapor excitation.

2.3.4 Electrical Response of the Phenomenon

The image (A) in Figure 2.6 shows the experimental setup, which was employed to measure the change in resistance across the water droplet undergoing the rotational motion. For these experiments, initially, a pair of Cu electrodes was placed on a glass slide with a separation distance of ~1 mm and a water droplet (~7 µl) composed of an aqueous solution of $FeSO_4.7H_2O$ was dispensed at the junction of the electrodes. The presence of the salt ions ensured that the droplet was electrically conducting. It is well known that a droplet of DI water is electrically non-conducting and the addition of an inorganic salt increases the electrical conductance of the water droplet. It is also well known that suspending metal nanoparticles can also significantly change the electrical conductance of the electrolytes. Thus, we performed a series of experiments to finalize the concentration and the types of salt and/or nanoparticles to be used for the experiments as discussed in the section 2.3.3.

The inset in Figure 2.6(A) shows the side view of the experimental setup where the salt-water droplet was resting on a pair of Cu electrodes. Initially, with the help of a digital multimeter, we measured the electrical resistance (R_0) across the stationary microdroplet. Subsequently, a capillary tube filled with diethyl ether was brought near the surface of the droplet to create the difference in surface tension across the air-water interface. The stimulation from organic vapor initiated the rotational motion inside the droplet, which progressively reduced the electrical resistance (R) across the droplet with time (t).

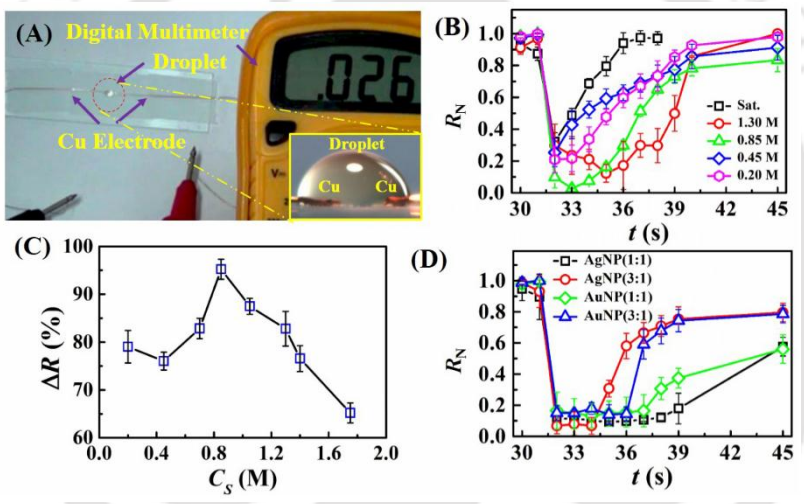

Figure 2.6: Image (A) shows the experimental setup to measure the change in the electrical resistance (R) across the droplet. The inset in the bottom-right corner shows the magnified side view of the droplet resting on a pair of Cu electrodes. Plot (B) shows the variation in normalized resistance ($R_N = R/R_0$) with time (t) across a microdroplet composed of 0.2M, 0.45M, 0.85M, 1.3M, and saturated solutions of $FeSO_4.7H_2O$. The plot (C) shows the percentage change in resistance (ΔR) with C_S inside the droplet. Plot (D) shows the variation of R_N with time (t) across a microdroplet having suspensions of 1:1 and 3:1 (v/v) of Ag or Au nanoparticles in 0.85M aqueous $FeSO_4.7H_2O$ solution.

It may be noted here that in the experiments the vapor source was introduced in a 'pulse mode', which meant the vapor exposure was given for a very short time. The entire event had three stages: (i) initially, the resistance of the stationary droplet was measured to be R_0 ; (ii) following this, the introduction of the vapor source in a 'pulse' mode triggered the

rotational motion and with time the electrical resistance across the droplet (R) reduced to a minimum value of R_{min}; (iii) finally, after the droplet became stationary, R increased near to the base value R_0.

Image (B) in Figure 2.6 shows the variation in the normalized resistance ($R_N = R/R_0$) across the droplet with time (t) at different salt concentrations inside the droplet. It may be noted here that the R_N value was nearly constant when the droplet was stationary from t = 0 to t = 30 s until the diethyl ether vapor was introduced. With the introduction of the vapor source at t = 31 s in a 'pulse' mode, the rotational motion was triggered, which persisted until 45 s. The plot indicates that the magnitude of R_N reduced to a minimum value ($R_N^{min} = R_{min}/R_0$) as the motion inside the droplet was triggered. We observed that a smaller value of R_N^{min} was an indicator of a stronger rotational current inside the droplet. Image (C) in Figure 2.6 shows that the percentage variation in resistance, $\Delta R = 100\left[1 - R_N^{min}\right]$, with salt concentration inside the microdroplet. The experiments suggested that the variation in Δ_R was maximum at $C_s \sim 0.85$M because of the increase in the electrical conductance of the droplet with salt-loading. The maximum value of ΔR indicated that the rotational motion was fastest when, $C_s \sim 0.85$M. The salt loading beyond 0.85M led the reduction in the rotational speed because of the increase in the viscosity and density of the droplet with salt-loading. Thus, despite there was an increase in the electrical conductance when the salt loading was greater than 0.85M, reduction in the strength of the vortices at a higher viscosity and density led to the decline in ΔR.

Image (B) in Figure 2.6 shows that for the pulse mode of vapor stimulation, although the resistance across the droplet reduced to R_N^{min}, the duration was rather momentary. In

comparison, the image (D) in Figure 2.6 shows that, even in the pulse mode of excitation, R_N^{min} could be retained for a longer duration when Ag or Au nanoparticles were suspended inside the microdroplet. Again, in these experiments, the salt loading was kept at 0.85M. The details of the experimental optimization of nanoparticles are provided in the Section 2.3.3. The nanoparticles laden salt-water droplet showed typical retention times for R_N^{min} to be ~3 – 6 s. The longer retention of R_N^{min} could be attributed to the additional inertia from the moving Ag or Au nanoparticles inside the droplet. Further, the drop in resistance during the rotation of a nanoparticle laden droplet was found to be higher than the simple salt-water droplet. In the Section 2.3.7, it is shown that this additional drop in resistance helped in increasing the power density renewed from this phenomenon. The experiments also showed that these added attributes specific to nanoparticles took place only beyond a critical loading of the nanoparticles in the droplet matrix.

2.3.5 Experimental Results on Energy Harvesting

Recent studies indicated that reverse electrowetting[2, 62] or modulations in the electrical double layer[1] of microdroplets could be converted into high-density electrical energy. Further, studies showed that motion of fluids under confinement could easily be associated with the electron transfer and transport.[63-66] In similar lines, we explored the potential of the present system for energy harvesting. We employed the same experimental setup as described in Figure 2.6 to evaluate the power density of the rotating droplets. However, instead of connecting a digital multimeter, the Cu electrodes were connected to a nanovoltmeter to measure the potential difference (ΔV_D) across the droplet. Surprisingly, the rotational motion inside the droplet due to exposure of vapor was found to generate a significant amount of voltage across the electrodes.

Figure 2.7 shows the variations in ΔV_D employing the proposed system in different situations. While row (A) schematically illustrates the different ways of introducing the vapor, the row (B) shows the nature of ΔV_D vs. time (t) plots observed. The arrowheads show the tentative location of the vapor source stimulation. The positive and negative symbols indicate the way the nanovoltmeter was integrated with the droplet to measure ΔV_D.

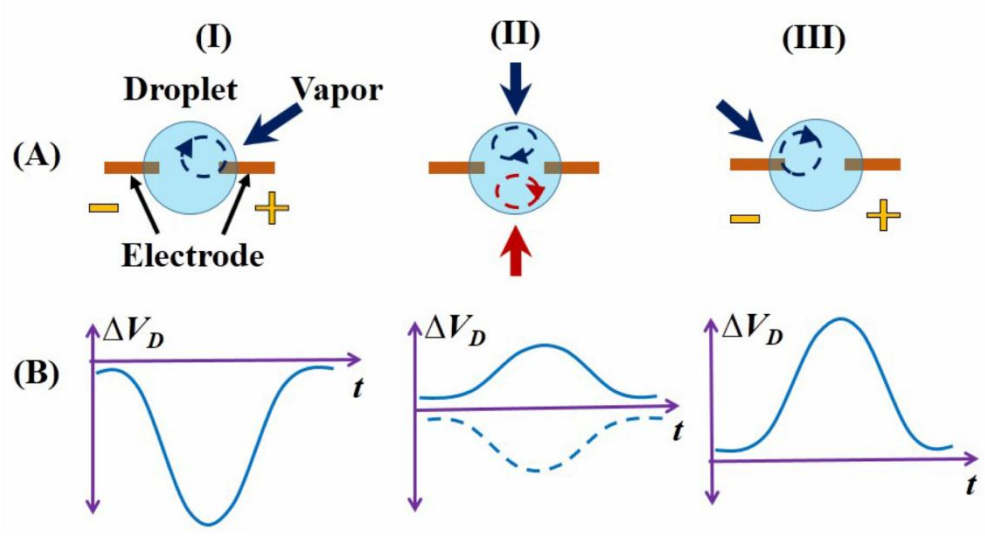

Figure 2.7: Energy harvesting from the microdroplet rotation. Schematic diagrams in the row (A) illustrate different ways (i – iii) of introducing the vapor and row (B) shows the corresponding output of potential difference (ΔV_D) with time (t).

The images suggest that the magnitude of ΔV_D was larger when the vapor was introduced near the electrodes (columns I and III) as compared to the situation when the vapor was introduced in between the electrodes (column II). For example, image (I) of row B in Figure 2.7 shows that when the vapor was introduced near the electrode connected to the positive side of the nanovoltmeter, the ΔV_D readily reduced to a minimum negative voltage with time before recovering back to the zero potential after the vapor source was removed.

It is well known that the Cu electrodes in water possess a negative ζ-potential (– 29 mV) due to the formation of an electrical double layer (EDL).[67, 68] It is also well known that when an EDL collapses due to the salt loading in an electrolyte, the effective ζ-potential around a surface becomes negligible. Thus, in the present scenario, it could easily be envisaged that the surface of the Cu electrodes on which the salt-water droplet was resting would possess negligible ζ-potentials. This was reflected in the experiments and we observed ΔV_D to be negligible across the electrodes when the salt-water droplet was stationary. However, when the organic vapor source was introduced near one of the electrodes, the strong rotational motion disturbed the EDL near the very electrode to partially restore its ζ-potential. Importantly, since the disturbance due to the rotational motion was rather weak near the other electrode, the restoration of the ζ-potential was relatively small. Consequently, for a rotating droplet, we observed a finite drop in potential ΔV_D across the Cu electrodes.

In order to corroborate the aforementioned hypothesis, we performed the following control experiments. For example, image (I) of row B in Figure 2.7 shows the appearance of a negative ΔV_D, which could be attributed to the fact that the positive and negative sides of the nanovoltmeter were connected to the opposite negative and positive sides of the system. Very often, this phenomenon could be observed when the positive (negative) side of a battery have been connected to the negative (positive) side of a voltmeter. Thus, when the organic vapor was introduced near the electrode connected to the negative side of the voltmeter, we observed a positive potential difference, as shown in the image (III) of the rows (A) and (B). In this situation, again the EDL could partially be restored around the very Cu electrode near which the vapor source was introduced. More precisely, the strong

vortices near one of the electrodes could dislodge enough counter ions from the dormant EDL to restore a part of the ζ-potential of Cu in water. Moreover, when the vapor source was introduced almost equidistant away from the electrodes, the formation of nearly symmetric vortices across the droplet led to a much smaller potential difference across the electrodes. In such situation, although the vortices led to the recovery of a part the negative ζ-potential near the surface of both the electrodes, a near similar reduction led to a lower difference in potential, as schematically shown in column (ii) of the rows (A) and (B).

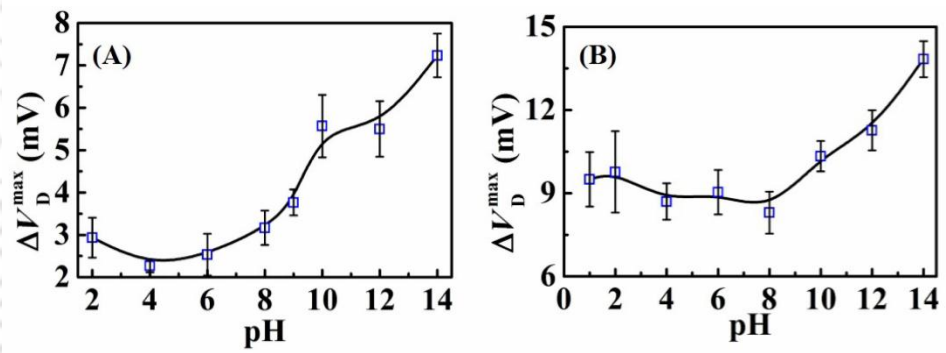

Figure 2.8: The variations in the maximum potential difference (V_D^{max}) across the electrodes for the droplets composed of, plot (A) DI water at different pH and plot (B) salt-water (1.7M aqueous NaCl soln.) at different pH. The rotational motion was triggered with the help of diethyl ether vapor.

We performed further experiments where the pH of the water droplet was varied. The pH of the droplet was adjusted by adding HCl and NaOH solutions in water. In these experiments, we placed the DI water droplets between the Cu electrodes and instigated the rotational motions inside them with the help of diethyl ether vapor. The maximum of the potential difference (ΔV_D^{max}) was measured with the help of a nanovoltmeter when the droplet was rotating at a maximum speed.

Plot (A) in Figure 2.8 suggests that with the increase in alkalinity of a DI water droplet, the ΔV_D^{max} between the Cu electrodes increased. Previous studies indicate the negative ζ-potential Cu increases from -29 mV to -50 mV with an increase in the alkalinity of the solution.[69] Thus, it was expected that both the electrodes would possess similar values of ζ-potential with nearly zero potential difference when the droplet was stationary. However, when the organic vapor stimulus prompted the rotational motion on one side of the droplet, we observed some potential difference across the electrodes. Interestingly, ΔV_D^{max} values were rather was low at lower pH region and found to be significantly higher in the region of high pH, as shown in the image (A) of Figure 2.8. This happened because, at lower values of pH, the excess H^+ ions present in the droplet bonded strongly with the surface of the Cu electrodes having negative ζ-potential. These bondages were strong enough to be disturbed by the rotational motion inside the droplet, which led to a smaller ΔV_D^{max}. In contrast, at higher values of pH, firstly, the excess OH^- ions present in the droplet increase ζ-potential from –29 mV to –50 mV. However, the OH^- ions bond rather weakly with the surface of the Cu electrodes because they already had a negative ζ-potential. In such a situation, the onset of the rotational motion near one of the electrodes of the droplet dislodged some of the loosely bonded OH^- ions to engender the potential difference. Therefore, higher values ΔV_D^{max} were observed at higher values of pH.

The magnitude of ΔV_D^{max} could further be increased if the experiments were initiated with 1.7M aqueous NaCl solution and then the pH of the solution was adjusted by addition of HCl and NaOH. It is important to note here that we added NaCl as salt instead of $FeSO_4.7H_2O$ in these experiments because the latter reacts with NaOH. We have already discussed in the Section 2.3.3 that NaCl was the second best choice for these experiments.

Plot (B) in Figure 2.8 shows that the presence of the salt inside the droplet enhances the ΔV_D^{max} by almost two-fold across the droplet at the higher pH region. In this case, the addition of salt destroyed the EDL across the Cu electrodes to ensure that the potential difference was zero across the stationary droplet. However, the introduction of the organic vapor in one side of the droplet prompted the rotational motion which in turn dislodged some of the Na^+ ions from the very Cu electrode to create potential difference. Concisely, experiments shown in Figure 2.8 indicated that indeed the potential difference across the droplet was generated because of the difference in the ζ-potential of the Cu electrodes.

2.3.6 Theoretical Basis of Voltage Generation

In order to corroborate the aforementioned hypothesis for energy harvesting, we performed following theoretical calculations and CFD simulations. The electrokinetic potential of the EDL near the electrodes was theoretically analysed with the help of the Poisson's equation for electrostatic field, $\nabla^2\psi = \rho_e / \varepsilon\varepsilon_0$, in which ρ_e is the charge density, ε is the dielectric constant, and ε_0 is the permittivity of free space.[70] Assuming a Boltzmann's distribution for counter ion concentration near the electrodes and enforcing Debye-Hückel's approximation, the Poisson's equation was transformed into the simpler form, $\nabla^2\psi = \psi / \lambda_D^2$. Where, $\lambda_D = \left[N_A e^2 / \varepsilon\varepsilon_0 kT \sum_i z_i^2 C_i \right]^{-0.5}$, is the Debye length and N_A, e, k, T, z_i, and C_i denote Avogadro's number, electronic charge, Boltzmann constant, temperature, valency, and concentration of the ions of type i. The one-dimensional Poisson-Boltzmann's equation under the Debye-Hückel approximation, $d^2\psi / dx^2 = \psi / \lambda_D^2$, has the simple analytical solution, $\psi = C_1 e^{-x/\lambda_D} + C_2 e^{x/\lambda_D}$, in which x is the independent variable signifying the distance away from the electrodes, and the notations C_1 and C_2

were the integration constants. The constants could be evaluated from the boundary conditions, $\psi = \psi_0$, at $x = 0$, and $\psi = 0$, at $x = \infty$, which led to the final solution as, $\psi = \psi_0 e^{-x/\lambda_D}$. The experimentally obtained ζ-potential of Cu in water, –29 mV at a distance λ_D helped in obtaining ψ_0 to be –78.8 mV.[68]

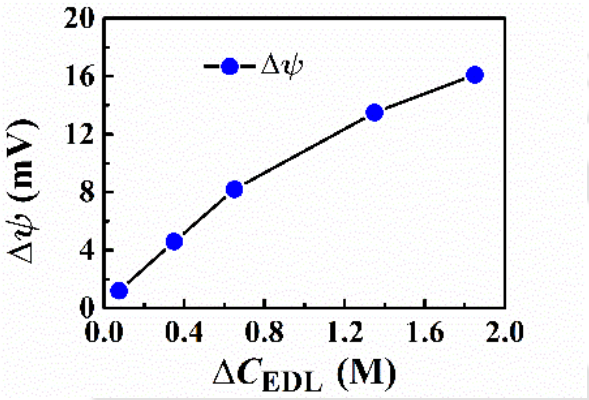

Figure 2.9: The variation of potential difference ($\Delta\psi$) with the difference in the concentration of the counter ions near the electrode (ΔC_{EDL}).

As anticipated previously, for a 0.85M aqueous $FeSO_4$ solution we obtained λ_D~ 0.16 nm at 298 K, which indicated that the thickness of EDL near the Cu surface was rather negligible. Also, the expression for potential, $\psi = \psi_0 e^{-x/\lambda_D}$, near the electrodes clearly indicated that the difference in the concentration of the counter ions near the Cu electrodes, $\Delta C_{EDL} = f(\lambda_D)$, which could be the main reason for the potential difference as observed in the experiments. Figure 2.9 shows the variation of potential difference ($\Delta\psi$) with the difference in the concentration of the counter ions near the electrodes (ΔC_{EDL}). Strikingly, the Figure 2.9 suggests that a marginal variation in ΔC_{EDL} could indeed generate a few millivolts of energy.

Previously, the origin of the difference in counter ion concentration near the electrodes and the subsequent difference in the electric field potentials was attributed to the stronger vortices near one of the electrodes. We performed CFD simulations in support of this argument. In Figure 2.10, we show a simple qualitative CFD analysis where we employed the same 2-D geometry as shown in Figure 2.10, with a simple modification near the base of the droplet where electrodes of length 0.45 mm were introduced, mimicking the experimental setup for energy harvesting. Herein, we solved Navier-Strokes equations for a two-phase system coupled with the species balance equation for the salt with appropriate boundary conditions to identify the convective flux of the salt near the electrodes.

2.3.7 Computational Simulations to Estimate Potential Drop on the Electrodes

The same experimental set-up as shown in Figure 2.6 in the manuscript was employed for energy harvesting. In the beginning of the experiment, a salt-water droplet was placed on a pair of Cu electrodes and the vapor source was introduced near the air-water interface to induce the rotational motion inside the droplet. The entire event could be divided into three stages: (i) initially, the resistance of the stationary droplet was measured to be R_0; (ii) following this, the introduction of the vapor source triggered the rotational motion and with time R progressively reduced to a minimum value of R_{min}; (iii) finally, after the withdrawal of the vapor excitation when the droplet became stationary, R increased near to the base value R_0. In this situation, the change in the electrical resistance was measured with a multimeter. Importantly, with the same system, we obtained a potential difference across the electrodes while the droplet was undergoing the rotational motion and a nanovoltmeter was connected to the electrical circuit replacing the multimeter. As described in the previous section 2.3.5 that it is well known that when a Cu electrode is

immersed in water, a negative ζ-potential (– 29 mV) is generated due to the formation of an electrical double layer (EDL).[68] Further, in such a situation, it is also well known that the thickness of the EDL can shrink and become non-existent upon salt loading in the water. Thus, a stationary salt-water droplet is expected to show zero potential difference across the Cu electrodes, which we observed in the experiments. However, when the vapor source was introduced near one of the electrodes, the rotational motion inside the droplet could dislodge a part of the salt ions from the EDL to partially restore the negative ζ-potential. Importantly, since the vapor source stimulation was towards one of the sides of the droplet, a stronger rotational motion near one of the electrodes ensured that the salt particles dislodged asymmetrically from the EDLs near the Cu electrodes to create the potential difference between them.

In Figure 2.10, we show a simple qualitative computational analysis, which justifies the onset of the potential difference across the electrodes during the droplet rotation. It may be noted here that we employed the same 2-D geometry as shown in Figure 2.10, with a simple modification near the base of the droplet where electrodes of length 0.45 mm were introduced, mimicking the experimental setup. Further, in addition to the governing equations (2.1) – (2.4) shown in section II, we solved the following convection-diffusion equation for the salt-water droplet,

$$\frac{\partial C_s}{\partial t} + \nabla \cdot \left(-D \nabla C_s \right) + \mathbf{u}_2 \cdot \nabla C_s = \mathbf{0} . \qquad (2.5)$$

Here the concentration and diffusivity of salt in water are denoted by C_s and D whose values were taken to be, 0.85 M and 10^{-12} m^2/s, respectively, inside the droplet. It may be noted here that the diffusion coefficient was chosen to be very small in order to restrict

any diffusion of salt from the electrodes. The conditions set in the simulations ensured that the salt molecules stayed near the electrodes until or unless a very strong convective current dislodged them from the electrode premises.

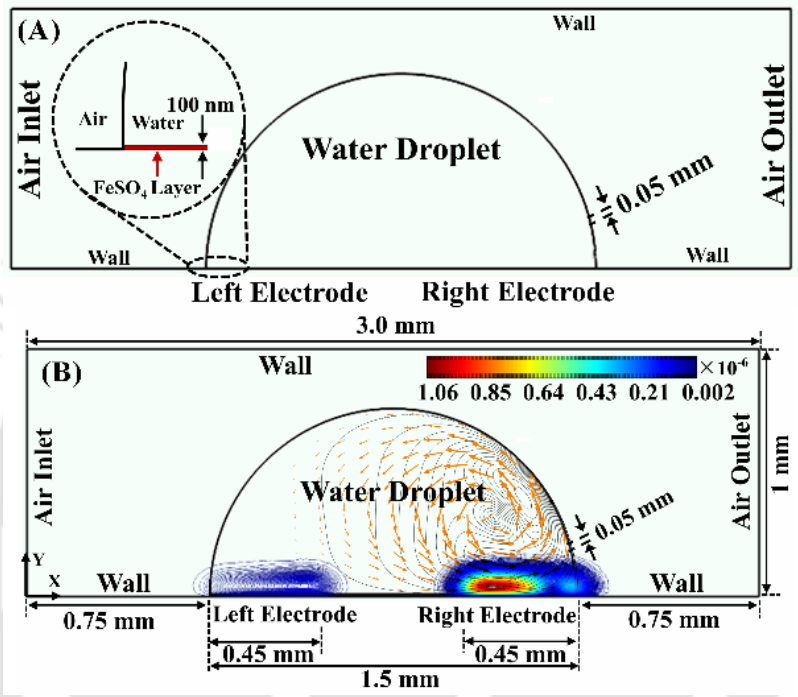

Figure 2.10: Image (A) shows the initial configuration of the computational domain at 0 s, with 100 nm thick $FeSO_4$ deposited at the electrodes. Image (B) shows the streamlines (continuous lines), velocity vectors (orange arrows), and the magnitude of the convective flux (colour map contours, $\mathbf{N}_{i,conv} = C_s \mathbf{u}_2$) inside a droplet of diameter 1.5 mm after 0.01 s. The surface tension of the droplet, γ_1 = 72.7 mN/m and diethyl ether, γ_2 = 17.0 mN/m at the arc of length 0.05 mm created a surface tension gradient of $\Delta\gamma$ = 55.7 mN/m across the interface.

The 2-D geometry was divided into 127653 triangular elements not only to obtain the grid independent solutions but also to resolve the EDL near the electrode for an aqueous salt solution of 0.85 M. The refined grid placing ensured that the first layer of the cells was of the thickness similar to the EDL for a salt-water droplet. The boundary conditions and the computational methodology employed for this analysis remained similar to the one

discussed previously in section II. It may be noted here that the lower wall was assumed to be impermeable for any salt diffusion to take place.

Image (A) in the Figure 2.10 shows the initial configuration of the computational domain where the rectangular areas of height 100 nm above the electrode regions were assumed to have higher concentration of the salt while in the other parts of the droplet the salt concentration was 0.85M. Image (B) in the Figure 2.10 shows the streamlines and velocity vectors after 0.01 s, once the rotational motion was set inside the droplet. Image (B) in the Figure 2.10 also shows the magnitude of the convective flux ($\mathbf{N}_{i,conv} = C_s \mathbf{u}_2$) near the electrodes inside the droplet after 0.01 s of diethyl ether vapor exposure. Clearly, the image (B) suggests that the rotational motion inside the droplet created an asymmetric convective flux near the electrodes, which in turn led to the difference in the concentration of salt near the Cu electrodes. The convective flux on the right side of the droplet was found to be ~10^3 times stronger than the same on the left side of the droplet. The simulations suggested that the right-heavy rotational motion was capable of dislodging significant amount of counter ions from the EDLs to the bulk of water droplet.

Image (A) in the Figure 2.10 shows the initial configuration of the computational study where the rectangular areas of height 100 nm above the electrode regions were assumed to have a higher concentration (e.g. 1M) of the salt while in the other parts of the droplet the salt concentration was 0.85 M. Image (B) in the Figure 2.10 shows the streamlines and velocity vectors of the vortices after 0.01 s. The image also shows the magnitude of the convective flux ($\mathbf{N}_{i,conv} = C_s \mathbf{u}_2$) near the electrodes after 0.01 s. Clearly, the image suggests that the onset of Marangoni rotation on the right-hand side of the droplet could create a convective flux of magnitude ~10^3 times larger than the same near the left

electrode. The results shown in the Figures 2.9 and 2.10 qualitatively confirmed that the strong vortices coupled with a differential counter ion concentration of the EDLs near the electrodes were the reason for the voltage generation.

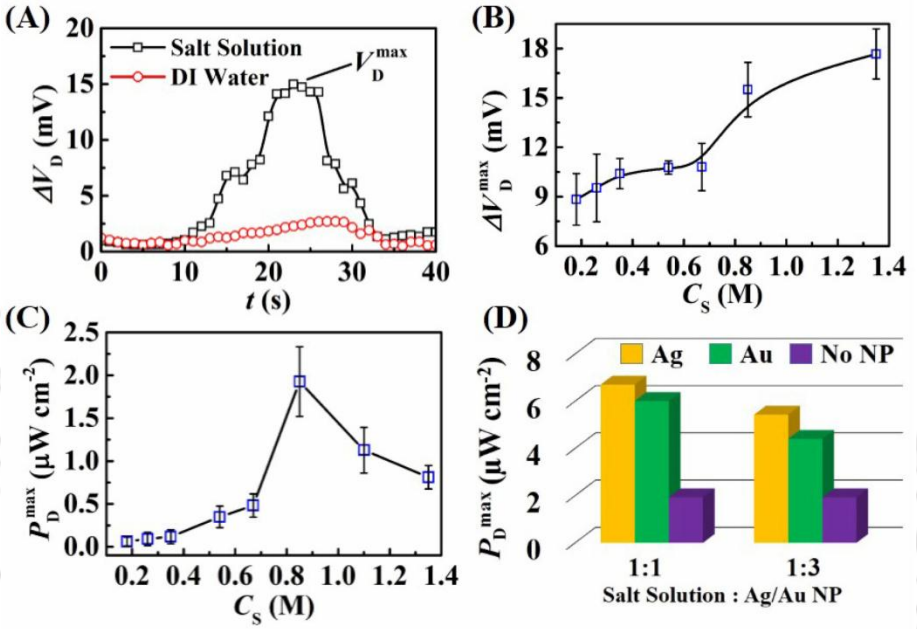

Figure 2.11: Power generation from the microdroplet rotation. Plot (A) shows the variation in ΔV_D with t across the electrodes for the droplets having a 0.85M $FeSO_4.7H_2O$ solution and DI water. Images (B) and (C) show the variation in the maximum potential difference (ΔV_D^{max}) and maximum power density (P_D^{max}) with Cs. Image (D) shows the variation of P_D^{max} in μW cm-2 with and without the Ag or Au nanoparticle loading inside the droplets of 0.85M aqueous salt solution. Here 1:1 and 1:3 salt solution stands for the (v/v) proportion of 0.85M aqueous salt solution and prepared Ag or Au nanoparticle solution.

2.3.8 Power Density and Conversion Efficiency

Plot (A) in the Figure 2.11 shows the typical ΔV_D vs. t obtained in the experiments for the salt-water and DI water droplets. The control experiment with DI water showed the voltage generation was minimal (circular symbols) whereas the salt-laden droplet showed a maximum potential difference, ΔV_D^{max} ~ 15 mV (square symbols).

Plot (B) shows that ΔV_D^{max} monotonically increased with C_S. Importantly, ΔV_D^{max} could also be converted to power using the simple relation, $P = (\Delta V_D^{max})^2 / R_{min}$ where R_{min} was the

minimum resistance across the droplet while in motion. The power density (P_D^{max}) was obtained by dividing *P* by the area occupied by the droplet. Remarkably, the plots (C) and (D) in the Figure 2.11 indicate that the motion could lead to P_D^{max} as high as ~2 μW/cm^2 when the salt loading inside the droplet was 0.85M. However, nearly a fourfold jump in P_D^{max} ~7 μWcm^{-2} was observed when the Ag or Au nanoparticles were loaded inside the droplet of 0.85M aqueous salt solution. The presence of the nanoparticles enhanced (reduced) the electrical conductance (resistance) across the droplet to improve the power density. The power density plots show the potential of the proposed methodology for energy harvesting.

Remarkably enough the maximum generated voltage (ΔV_D^{max}) and total power (*P*) of the system kept increasing with increase in the number of droplets (N_D), as illustrated in the Figure 2.12. This experiment highlighted the potential of the system for a very large scale integration (VLSI). Image (A) shows the typical setup for this experiment when there were three droplets. The circuit at the bottom of image (A) shows the Thevenin equivalent circuit for the single droplet generator employed during efficiency calculation. Images (B) and (C) together shows that when multiple droplets connected in series ΔV_D^{max} and *P* monotonically increase with N_D. Importantly, we also observed similar behavior when the droplet diameter was 500 μm or less. Thus, a VLSI of ten thousand (million) microdroplets can lead to a power in the range of mW (W). The proposed methodology showed a simple and non-destructive way to convert the surface energy into the electrical one under ambient conditions.

We also evaluated the power conversion efficiency of the process, which can be estimated as, $\eta_P = (P_{out} / P_{in}) \times 100\%$, where P_{in} is the power originating from the surface energy gradient and P_{out} is the electrical power measured experimentally. In order to evaluate P_{in}, we initially calculated the difference in Helmholtz free energy ($\Delta F = F_f - F_i$) due to the change in the surface energy, which was the measure of maximum work that an isothermal system could perform.

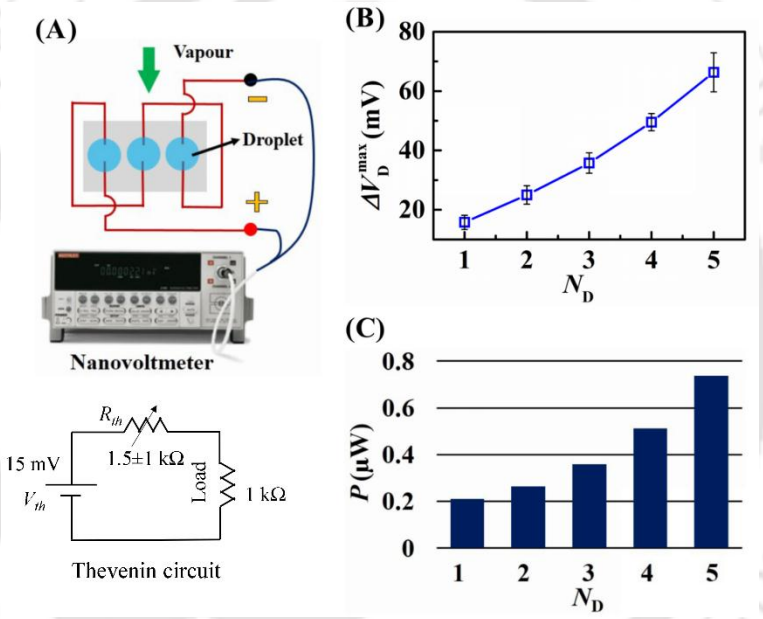

Figure 2.12: Experimental results of voltage generation in multiple droplets. Image (A) shows the schematic diagram of the experimental setup where three droplets were connected in series and diethyl ether vapor was introduced from one side. The circuit at the bottom of image (A) shows the Thevenin equivalent circuit for the generator employed during efficiency calculation. Image (B) and (C) show the variation of maximum voltage generation (ΔV_D^{max}) and power (P) for multiple numbers (N_D) of droplets, respectively.

Here the subscripts f and i denote the free energies of the final and initial states, respectively. We assumed that the initial configuration was the stationary hemispherical water droplet of area, $2\pi R^2$, radius, R = 1 mm, surface energy γ_w = 0.072 J/m^2,[71] and $F_i = 2\pi R^2 \gamma_w$. It was also assumed that the organic vapor stimulation was provided only

to the area, which was equivalent to the cross-sectional area of the capillary tube of radius, r = 0.5 mm. In such a scenario, the final Helmholtz free energy was evaluated as, $F_f = \left[2\pi R^2 \gamma_w - \pi r^2 \gamma_w + \pi r^2 \gamma_{wd} \right]$, where γ_{wd} = 0.017 J/m^2 is the interfacial tension water-diethyl ether interface.[71]

The variation in the Helmholtz free energy for a droplet rotating under vapor stimulation was computed to be, $\Delta F = -\pi r^2 \gamma_w + \pi r^2 \gamma_{wd}$. The time scale ($\tau = L^2 / D_{DA}$) for the diffusion of the diethyl ether vapor on the droplet surface could be obtained from the diffusion coefficient of diethyl ether in air,[72] D_{DA} = 0.918 × 10^{-5} m^2/s and the average distance, L ~ 1 mm, at which the capillary was placed to instigate the motion. The aforementioned values provided the magnitude of the input power (P_{in}) as, $P_{in} = \Delta F / \tau = \left(-\pi r^2 \gamma_w + r^2 \pi \gamma_{wd} \right) / \tau$. Substituting in the numerical values to this expression we obtained P_{in} ~ 0.432 µW for a water droplet rotating with diethyl ether excitation. Since the P_{out} ~ 0.21 µW in the experiments, the power conversion efficiency was, η_P ~ 48.61%. Following the aforementioned methodology, we also compared and contrasted the power conversion efficiency of a 35 µl droplet with five 7 µl droplets to uncover the effect of miniaturization. The calculations suggested that the latter system could show η_P ~ 34.26% as compared to η_P ~ 6.8% for the 35 µl droplet. The experiments confirmed that the power conversion efficiency increased with miniaturization of the droplets.

Apart from energy harvesting, the phenomenon could also be employed to detect the different kinds of volatile organic vapors. Experimental setup shown in the images (A) and

(B) of the Figure 2.13 demonstrate a simple way to sense the organic vapors where a 7 µl droplet loaded with salt and nanoparticle (1:1) was dispensed at the junction of a pair of Cu electrodes and the vapor source was brought near the surface to trigger the droplet motion.

2.3.9. Sensor Application

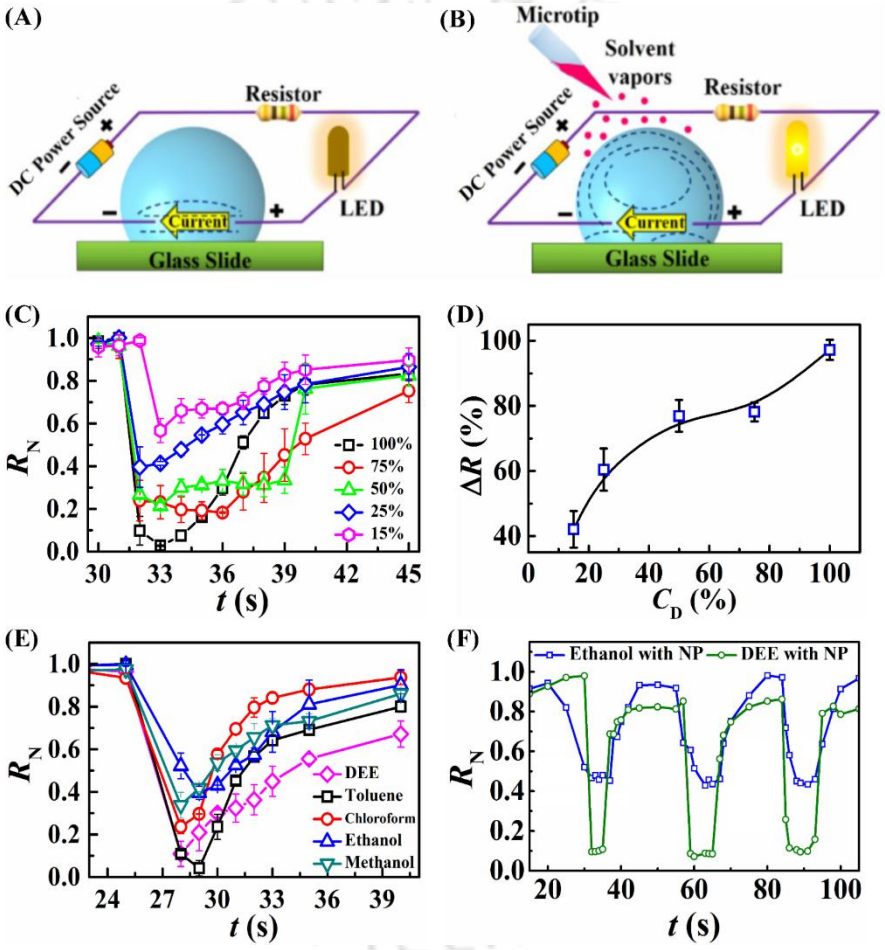

Figure 2.13: Experimental results of the alcohol vapor sensor. Images (A) and (B) show the schematic diagram of the experimental setup where the LED was turned off (on) in the absence (presence) of the vapor excitation. Image (C) shows the change R_N with different concentrations (v/v) of diethyl ether in water (C_D) and image (D) shows variation ΔR with C_D. Image (E) shows the variation in R_N with t when the stimulus was different vapor sources such as diethyl ether (DEE), toluene, chloroform, ethanol, and methanol. Image (F) shows the variation in R_N with *t* when three cycles of the exposure of diethyl ether and alcohol were repeated on a microdroplet of 0.85M aqueous salt solution mixed with Ag nanoparticles in 1:1 proportion (v/v).

The electrical circuit was also integrated with an LED, which was turned off when the drop was stationary, in the absence of the vapor excitation. Following this, under the organic vapor exposure, the reduction of the resistance due to vortices inside the droplet illuminated the LED. The response time of the device was of the order of seconds, which could also resolve the periodic exposure and withdrawal of the vapor indicated by the turning on and off of the LED.

Image (C) of the Figure 2.13 shows the variation in R_N with *t* when the vapor source was composed of aqueous solutions (v/v) of diethyl ether. The change in the concentration of diethyl ether from 15% to 100% was faithfully detected by the variation in the ΔR with the concentration of diethyl ether (C_D) in the solution, as shown in the plots of the image (C). Image (D) shows the percentage change in resistance (ΔR) reduced significantly as the proportion of the C_D reduced in the vapor. Remarkably, different types of vapor sources such as diethyl ether, toluene, chloroform, ethanol, and methanol showed different values ΔR, as shown in the plot (E). The variation in ΔR with the change in the vapor source could be correlated to the gradient of surface tension on the drop-surface, which was discussed previously with Figure 2.13.

Image (F) shows that the repeated introduction and removal of an alcohol vapor source could also be detected through this prototype. For example, when the alcohol vapor source was introduced and withdrawn for three times in a 'pulse mode' near the surface of the droplet, we could record three cycles of variation R_N with *t* in which each minima signified the introduction of the vapor source while the maxima indicated the withdrawal of the same. Interestingly, the addition of Ag or Au nanoparticles in the droplets helped in retaining the signal for the 'pulse mode' for a longer duration. The experiment

demonstrated the proof-of-concept of a minuscule, simple, economic, and portable prototype, which holds the potential to detect alcohol in the human breathing cycles.

2.4. Conclusions

Water microdroplets showed the powerful rotational motion of magnitude as high as ~720 rpm when exposed to an external source of volatile organic vapor. The adsorption of the organic vapor on the surface of the water droplet reduced the surface tension locally near the point of exposure, which triggered a Marangoni motion on the droplet surface. The strong vortices on the drop-surface induced the explosive rotational motion inside the droplet. The phenomenon led to the development of a proof-of-concept prototype for sensing cum energy-harvesting.

The microdroplet composed of aqueous salt solution and loaded with Ag or Au nanoparticles showed the potential to produce power density as high as ~7 $\mu W/cm^2$. A VLSI of thousands (millions) of such rotating microdroplets can lead to a non-destructive and pseudo-perpetual system generating power in the range of mW (W) under ambient condition. Theoretical and experimental analyses uncovered that the difference in the ζ-potential near the electrodes was the major reason for the voltage generation.

Further, when the nanoparticle-laden droplet was dispensed at the junction of a pair of electrodes connected to an external power source, we observed ~85 – 95% reduction (increase) in the electrical resistance (conductance) once the vapor source stimulated the rotational currents in the droplet. The extent of reduction (increase) of the electrical resistance (conductance) could easily be employed to differentiate the sources of organic vapors such as diethyl ether, chloroform, methanol, ethanol, and toluene. Mimicking the

human breathing system, the repeated exposure and withdrawal of the vapor sources could also be traced with the help of the prototype.

Concisely, the study showcases a simple, reliable, and economic prototype capable of multitasking such as harvesting energy, sensing organic vapors and detecting alcohol issuing out of human breathing.[73] The proposed methodology can also be employed for mixing or emulsification of multiple phases. Further, the devices made of water droplets also face limitations with temperature and humidity fluctuations as well as evaporation. We keep these aspects as future scopes of research work.

References

1. J. K. Moon, J. Jeong, D. Lee and H. K. Pak, *Nature Communications*, 2013, **4**, 1487.
2. T. Krupenkin and J. A. Taylor, *Nature Communications*, 2011, **2**, 448.
3. J. A. Paradiso and T. Starner, *IEEE Pervasive Computing*, 2005, **4**, 18-27.
4. A. A. García, A. Egatz-Gómez, S. A. Lindsay, P. Domínguez-García, S. Melle, M. Marquez, M. A. Rubio, S. T. Picraux, D. Yang, P. Aella, M. A. Hayes, D. Gust, S. Loyprasert, T. Vazquez-Alvarez and J. Wang, *Journal of Magnetism and Magnetic Materials*, 2007, **311**, 238-243.
5. N. Chaturvedi, Y. Hong, A. Sen and D. Velegol, *Langmuir*, 2010, **26**, 6308-6313.
6. A. K. Singh, K. K. Dey, A. Chattopadhyay, T. K. Mandal and D. Bandyopadhyay, *Nanoscale*, 2014, **6**, 1398-1405.

7. S. Kumar, A. K. Singh, A. K. Dasmahapatra, T. K. Mandal and D. Bandyopadhyay, *Carbon*, 2015, **89**, 31-40.

8. R. F. Ismagilov, A. Schwartz, N. Bowden and G. M. Whitesides, *Angewandte Chemie International Edition*, 2002, **41**, 652-654.

9. S. Yun Seong and M. Sitti, *Robotics, IEEE Transactions on*, 2007, **23**, 578-589.

10. A. A. Solovev, E. J. Smith, C. C. Bof' Bufon, S. Sanchez and O. G. Schmidt, *Angewandte Chemie International Edition*, 2011, **50**, 10875-10878.

11. W. Wang, L. A. Castro, M. Hoyos and T. E. Mallouk, *ACS Nano*, 2012, **6**, 6122-6132.

12. H.-R. Jiang, N. Yoshinaga and M. Sano, *Physical Review Letters*, 2010, **105**, 268302.

13. G. Loget and A. Kuhn, *Nat Commun*, 2011, **2**, 535.

14. T. R. Kline, W. F. Paxton, T. E. Mallouk and A. Sen, *Angewandte Chemie*, 2005, **117**, 754-756.

15. B. Cai, S. Wang, L. Huang, Y. Ning, Z. Zhang and G.-J. Zhang, *ACS Nano*, 2014, **8**, 2632-2638.

16. D. Grieshaber, R. MacKenzie, J. Vörös and E. Reimhult, *Sensors*, 2008, **8**, 1400-1458.

17. J. R. Wojciechowski, L. C. Shriver-Lake, M. Y. Yamaguchi, E. Füreder, R. Pieler, M. Schamesberger, C. Winder, H. J. Prall, M. Sonnleitner and F. S. Ligler, *Analytical Chemistry*, 2009, **81**, 3455-3461.

18. K. Länge, B. Rapp and M. Rapp, *Analytical and Bioanalytical Chemistry*, 2008, **391**, 1509-1519.

19. C. Steffens, F. L. Leite, C. C. Bueno, A. Manzoli and P. S. D. P. Herrmann, *Sensors*, 2012, **12**, 8278-8300.

20. X. Guo, *Journal of Biophotonics*, 2012, **5**, 483-501.

21. P. M. Valencia, O. C. Farokhzad, R. Karnik and R. Langer, *Nat Nano*, 2012, **7**, 623-629.

22. N. S. Ramgir, Y. Yang and M. Zacharias, *Small*, 2010, **6**, 1705-1722.

23. S. Kruss, A. J. Hilmer, J. Zhang, N. F. Reuel, B. Mu and M. S. Strano, *Advanced Drug Delivery Reviews*, 2013, **65**, 1933-1950.

24. C. Li and G. Shi, *Journal of Photochemistry and Photobiology C: Photochemistry Reviews*, 2014, **19**, 20-34.

25. S. K. Sailapu and A. Chattopadhyay, *Angewandte Chemie International Edition*, 2014, **53**, 1521-1524.

26. A. Khaligh, Z. Peng and Z. Cong, *Industrial Electronics, IEEE Transactions on*, 2010, **57**, 850-860.

27. T. N. Krupenkin, *Journal*, 2011.

28. F. H. J. van der Heyden, D. J. Bonthuis, D. Stein, C. Meyer and C. Dekker, *Nano Letters*, 2007, **7**, 1022-1025.

29. S. Meninger, J. O. Mur-Miranda, R. Amirtharajah, A. P. Chandrakasan and J. H. Lang, *Very Large Scale Integration (VLSI) Systems, IEEE Transactions on*, 2001, **9**, 64-76.

30. J. Huang and Q. Wan, *Sensors*, 2009, **9**, 9903.

31. S. Kanan, O. El-Kadri, I. Abu-Yousef and M. Kanan, *Sensors*, 2009, **9**, 8158.

32. H. R. Hwang, J. G. Roh, D. D. Lee, J. O. Lim and J. S. Huh, *Met. Mater. Int.*, 2003, **9**, 287-291.

33. S. V. Patel, M. W. Jenkins, R. C. Hughes, W. G. Yelton and A. J. Ricco, *Analytical Chemistry*, 2000, **72**, 1532-1542.

34. G. Xie, P. Sun, X. Yan, X. Du and Y. Jiang, *Sensors and Actuators B: Chemical*, 2010, **145**, 373-377.

35. M. C. Lonergan, E. J. Severin, B. J. Doleman, S. A. Beaber, R. H. Grubbs and N. S. Lewis, *Chemistry of Materials*, 1996, **8**, 2298-2312.

36. Y. Wang and J. T. W. Yeow, *Journal of Sensors*, 2009, **2009**, 24.

37. Y. Zhou, Y. Jiang, G. Xie, X. Du and H. Tai, *Sensors and Actuators B: Chemical*, 2014, **191**, 24-30.

38. T. Someya, J. Small, P. Kim, C. Nuckolls and J. T. Yardley, *Nano Letters*, 2003, **3**, 877-881.

39. N. A. Rakow and K. S. Suslick, *Nature*, 2000, **406**, 710-713.

40. G. S. Kulkarni, K. Reddy, Z. Zhong and X. Fan, *Nat Commun*, 2014, **5**.

41. T. Ban, K. Tani, H. Nakata and Y. Okano, *Soft Matter*, 2014, **10**, 6316-6320.

42. Y. Zhu and Q. Fang, *Analytica Chimica Acta*, 2013, **787**, 24-35.

43. S. Chandrasekhar, *The Stability of a Rotating Liquid Drop*, 1965.

44. N. Bohr and J. A. Wheeler, *Physical Review*, 1939, **56**, 426-450.

45. R. J. A. Hill and L. Eaves, *Physical Review Letters*, 2008, **101**, 234501.

46. K. Ohsaka and E. H. Trinh, *Physical Review Letters*, 2000, **84**, 1700-1703.

47. L. E. Scriven and C. V. Sternling, *Nature*, 1960, **187**, 186-188.

48. S. Nakata, M. Nagayama, H. Kitahata, N. J. Suematsu and T. Hasegawa, *Physical Chemistry Chemical Physics*, 2015, **17**, 10326-10338.

49. A. A. Darhuber and S. M. Troian, *Annual Review of Fluid Mechanics*, 2005, **37**, 425-455.

50. M. Su, *Applied Physics Letters*, 2007, **90**, 144102.

51. C. Luo, H. Li and X. Liu, *Journal of Micromechanics and Microengineering*, 2008, **18**, 067002.

52. A. Diguet, R.-M. Guillermic, N. Magome, A. Saint-Jalmes, Y. Chen, K. Yoshikawa and D. Baigl, *Angewandte Chemie International Edition*, 2009, **48**, 9281-9284.

53. D. Okawa, S. J. Pastine, A. Zettl and J. M. J. Fréchet, *Journal of the American Chemical Society*, 2009, **131**, 5396-5398.

54. J. M. Gomba and G. M. Homsy, *Journal of Fluid Mechanics*, 2010, **647**, 125-142.

55. H. Jin, A. Marmur, O. Ikkala and R. H. A. Ras, *Chemical Science*, 2012, **3**, 2526-2529.

56. M. Sellier, V. Nock, C. Gaubert and C. Verdier, *Eur. Phys. J. Spec. Top.*, 2013, **219**, 131-141.

57. M. S. Kandarp Mavani, *International Journal of Engineering Research & Technology (IJERT)*, 2013, **2**, 5.

58. M. N. Martin, J. I. Basham, P. Chando and S.-K. Eah, *Langmuir*, 2010, **26**, 7410-7417.

59. M. Plapp, *Philosophical Magazine*, 2011, **91**, 25-44.

60. I. Steinbach, L. Zhang and M. Plapp, *Acta Materialia*, 2012, **60**, 2689-2701.

61. P. Yue, C. Zhou, J. J. Feng, C. F. Ollivier-Gooch and H. H. Hu, *Journal of Computational Physics*, 2006, **219**, 47-67.

62. M. Frieder and B. Jean-Christophe, *Journal of Physics: Condensed Matter*, 2005, **17**, R705.

63. S. Ghosh, A. K. Sood and N. Kumar, *Science*, 2003, **299**, 1042-1044.

64. B. Bourlon, J. Wong, C. Miko, L. Forro and M. Bockrath, *Nat Nano*, 2007, **2**, 104-107.

65. P. Král and M. Shapiro, *Physical Review Letters*, 2001, **86**, 131-134.

66. X. Gong, J. Li, H. Lu, R. Wan, J. Li, J. Hu and H. Fang, *Nat Nano*, 2007, **2**, 709-712.

67. X. Li, D. Zhu and X. Wang, *Journal of Colloid and Interface Science*, 2007, **310**, 456-463.

68. A. Manikandan and M. Sathiyabama, *Journal of Nanomedicine and Nanotechnology*, 2015, **6**, 1000251-1000255.

69. P. Zhu, Y. Masuda and K. Koumoto, *Journal of Materials Chemistry*, 2004, **14**, 976-981.

70. A. V. Delgado, F. González-Caballero, R. J. Hunter, L. K. Koopal and J. Lyklema, *Journal of Colloid and Interface Science*, 2007, **309**, 194-224.

71. J. A. Dean and N. A. Lange, *Lange's handbook of chemistry*, McGraw-Hill, 1992.

72. G. A. Lugg, *Analytical Chemistry*, 1968, **40**, 1072-1077.

73. M. Heilig, D. Goldman, W. Berrettini and C. P. O'Brien, *Nature reviews. Neuroscience*, 2011, **12**, 670-684.

भारतीय प्रौद्योगिकी संस्थान गुवाहाटी
Indian Institute of Technology Guwahati

I. Microfluidic Sensors

CHAPTER 3

Droplet Based Detection of Blood *α*-Amylase Employing Thermal Marangoni Effect

Contents

ABSTRACT 71
3.1. Introduction 72
3.2. Experimental Section 75
3.2.1 Materials 75
3.2.2 Sensor Fabrication and Set-up 75
3.2.3 Experimental Method for Microfluidics 76
3.2.4 Experimental Method for Electrical Characterization 76
3.2.5 Experimental Procedure of α-amylase Sensing 77
3.3. Results and Discussion 78
3.3.1 Experimental Study on Effect of Temperature 78
3.3.2 Computational Analysis 79
3.3.3 Experimental Analysis 88
3.4. Conclusions 90
References 91

भारतीय प्रौद्योगिकी संस्थान गुवाहाटी
Indian Institute of Technology Guwahati

ABSTRACT

We report the development of a droplet-based microfluidic sensor for the detection of α-amylase in human blood serum. The principle of detection was based on a rotational motion inside a droplet, which manifested when the droplet was placed on a hot glass surface. The rotational motions originated because of the temperature difference between the base and top parts of the droplet leading to, (i) a Marangoni motion due to the difference in the surface tension across the liquid-air interface and (ii) a recirculating motion due to the Rayleigh-Benard convection. The rotational motion was found to be ~12 rpm for a 10 μL droplet when the glass surface temperature at the base was maintained at 40°C while the top surface of the droplet was exposed to the ambient condition. A series of computational fluid dynamic simulations uncovered the salient features of the recirculating motions obtained due to the Marangoni and natural conventions. In order to develop the sensing arrangements, initially, the droplet was made conducting by dissolving salt before starch was loaded in an excess amount. The starch and salt loaded droplet showed a variation in the electrical resistance when placed on the hot glass surface owing to the enhancement in the electrical conductance due to the generation of the Marangoni and natural convention vortices. Interestingly, the variation in the resistance was found to enhance when α-amylase was added at different proportions into the droplet before the system was heated from the bottom. Amylase broke down specifically the starch molecules to develop lower molecular weight carbohydrates which in turn increased the electrical conductance of the droplet due to the combined influence of the Marangoni and natural convention vortices. The variation in the electrical resistance was found to be as high as ~80% across the droplet at 40°C glass surface temperature. We could detect a concentration range of 20-110 U/L aqueous solution of amylase to generate the calibration, which was later employed to detect the unknown amylase level of the real-life human blood serum samples. The proposed proof-of-concept prototype showed significant potential to develop into a low-cost and portable point-of-care-testing (POCT) microfluidic device for the real-time detection of α-amylase in human serum for easy prognosis of pancreatic disorders.

Manuscript under preparation.

3.1. Introduction

Design and developments of the point-of-care-testing (POCT) devices for the primary health care of various ailments have become one of the major focus of research in the recent years.[1, 2] The POCT detection of health parameters enable a prognosis of various ailments at the patient's site. This enables intervention of the medical experts at the early stages of the disease to prevent or delay the chronic ailments. The upcoming generation of the POCT devices is expected to make an early diagnosis of various life-threatening diseases in an easier, user-friendly, and cost-effective manner at the user's site.[3] In general, POCT devices are composed of an input segment, sensing arrangement, signal processing unit, and output segment with an analyzer. Among all these components, the most important one is the sensor arrangement, which enables the detection of pulmonary, thyroid, liver, pancreatic, or cardiac health.[4] In order to aid this initiative, in past few decades, a large array of sensors have been developed to detect various biomarkers specific for the different illnesses.

Among the other existing biomarkers for disease detection, the amount of α-amylase (endo-1,4-α-d-glucan glucanohydrolase, EC 3.2.1.1) in saliva, urine, sebum or blood serum helps the physicians to decide the diseased or healthy state of a human.[5] Amylase is synthesized in the pancreas and salivary glands to hydrolyze starch into glucose, maltose, and dextrin.[6] A healthy human serum contains about 25 – 85 U/L (units/liter) amylase in serum.[7] An enhanced amylase is serum indicates the potential onset of various dreaded diseases which include acute pancreatitis, pancreatic cancer, salivary gland infection, bile duct blockage, or gastroenteritis, among many others. In contrast, a reduced level of this enzyme indicates pancreatic or kidney malfunctioning, and toxemia in pregnancy,[7] among others. The amylase activity in human serum is in general detected by various methods

which include spectroscopy,[8-10] colorimetry,[11] fluorometry,[12] chromatography,[13] weight based detections,[14] electrochemical methods,[15] electromagnetic sensing,[16] and immunological methods.[17] Presently, the most dependable method of estimation is spectrophotometry.[18] However, this method is expensive, non-portable, and requires skills for operation and analysis. Unfortunately, until now, there are very few available methods suitable for the POCT detection of α-amylase in the various types of human body fluids.[19]

In this regard, of late, the advent of the smart materials in conjunction with specialties of the micro or nanoscale technologies have enriched the research associated with sensor fabrication.[20] The principles associated with the microfluidics,[21] MEMS,[22] NEMS,[23] nanophotonics,[24] micro or nanoelectronics,[25] amperometry,[26] or FET [27] have been now routinely employed to develop high-performance sensors to detect important biomarkers, environmentally hazardous vapors or gases,[21] and pathogens[28], among others. However, most of the sensors developed so far have many of the following limitations if not all: (i) costly and complex protocols for fabrication, (ii) require engineering and medical experts to analyze the results, (iii) available through some centralized agencies, (iv) larger time for detection and analysis, and (v) requirement of controlled environment for real-life operations, among many others. Thus, a large part of research efforts have been directed towards developing the sensors, which are devoid of these limitations to perform a real-time monitoring of biomarkers at a lower cost at the user's site.[29-31]

For example, the readily available but costly solid-state sensors [32, 33] have now been replaced by the sensors based on microfluidics.[34, 35] The microfluidic sensors have some advantages in, they are easy to prepare, economic, can be made reusable, can lead to the flexible device, and easy to store and use under ambient conditions.[36, 37] Thus, extensive efforts have been invested over the past few decades to develop future technologies for

sensing, energy harvesting, and biomedical applications exploiting the specialties of the fluid mechanical principles inside the microfluidic devices. In this regard, one of the major challenges the generation and sustenance of the electrical responses alongside the other desired attributes of sensing mechanism inside the fluidic environment during their operation.[38] For example, flow-based dynamic microfluidic systems have been found to be useful for cell sorting, heat, mass, momentum transport, and bio-molecule detections. [34, 39, 40] On the other hand, a number of previous works show the use of microdroplets to develop microbots, sensors, and energy harvesters.[41-43] However, the previous works suggest that the droplets are generally formed in the two-phase microfluidic flows inside a micro-channel[44] while there are a very few attempts have been made to convert a single droplet into a sensor.[21]

In view of the above, herein we discuss a single microdroplet based sensor to detect alpha-α-amylase in blood serum. The droplet underwent a rotational motion when heated from the bottom owing to the combined influence of natural convection in the bulk and thermal Marangoni flows at the liquid-air interface. The motion was found to have a magnitude of ~12 rpm for an applied temperature of ~55°C. Finite element based computational fluid dynamic (CFD) simulations uncovered the various attributed of the natural and Marangoni convections to unveil the physics behind the rotational motion. A salt-laden microdroplet could show a variation in the electrical resistance under mild heating when placed on an electrical circuit, which has been exploited to detect α-amylase in blood serum. The droplet was initially mixed with starch, which broke into lower molecular weight carbohydrates upon addition of amylase. Subsequently, the rotational speed of the droplet and the electrical conductivity across the same varied with the variation in the amylase

loading. The results reported ensured the capability of the prototype to be used as a biomedical device for the POCT detection of pancreatitis at the user's site.

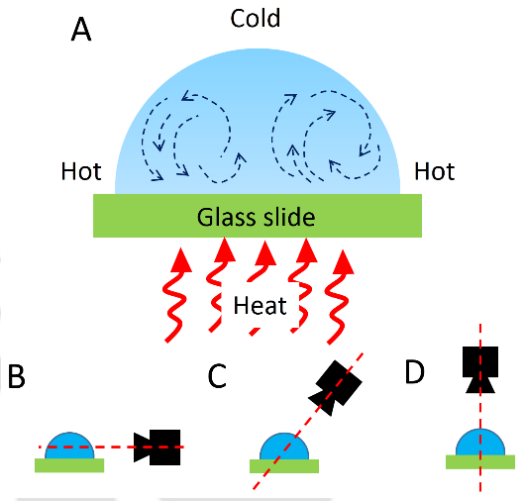

Figure 3.1: Image (A) shows the schematic diagram of the experimental set-up for characterizing the microfluidic phenomenon. Images (B – D) show the placement of digital or thermal camera for imaging.

3.2. Experimental Section

3.2.1 Materials

Iron (II) sulfate heptahydrate ($FeSO_4.7H_2O$), Starch were procured from Merck, India. Amylase was obtained from Sigma-Aldrich, India. The chemicals were of analytical grade and employed in the experiments without further purification. The Milli-Q grade water was used for cleaning and to prepare the solutions.

3.2.2 Sensor Fabrication and Set-up

The droplet-based sensor was developed on a glass substrate. Initially, a water droplet was placed on a glass slide which was kept on a hot plate. Thereafter, the temperature of the hot plate was varied to quantify the dependency of the rotational motion with temperature. A temperature sensor was placed on the glass substrate to monitor the temperature of the substrate. A digital camera (Sony Handycam) was employed to record the rotational

motion inside the droplet and a thermal imager (Testo 865) was used to characterize the temperature distribution.

3.2.3 Experimental Method for Microfluidics

The experiments were performed in ambient condition. A droplet was placed on the glass substrate using a micropipette as shown in Figure 3.1A. The diameter of the droplet was ~8 mm. A digital and thermal camera was placed just in front of the system to take the side view and on top to capture the top view of the system. The arrangement of camera is illustrated in images (C – D) of Figure 3.1A particle of ~200 um was placed inside then droplet to quantify the motion of the fluid.

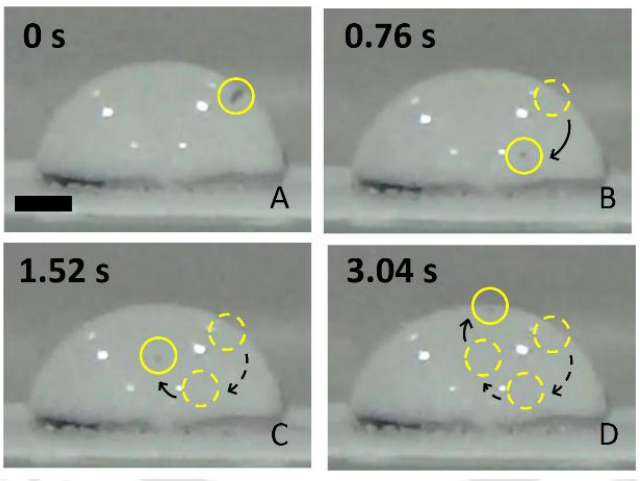

Figure 3.2: Images (A – D) show the snapshot images of side-view of the droplet at different time intervals to illustrate the motion of a ~120 um particle inside the droplet. The scale bar is of 2 mm.

3.2.4 Experimental Method for Electrical Characterization

The droplet system was further employed for electrical characterization. In this situation, the droplet was made conductive by adding 0.85M $FeSO_4$ salt. The conductive droplet was then placed in between two cylindrical copper wires of ~180 μm diameter separated by ~ 1 mm. The wires were connected to a digital multimeter (MASTECH M92A(H)) which was kept beside the system to measure the electrical response of the sensor arrangement.

3.2.5 Experimental Procedure of α-amylase Sensing

Initially, 10% (w/v) starch solution and 1M $FeSO_4$ was prepared by dissolving appropriate amounts of the solvents in DI water. The solutions were mixed in equal volumes to form the reaction mixture. The $FeSO_4$ solution was freshly prepared each time before performing the experiments. Starch is a specific substrate for α-amylase enzyme while the presence of electrolyte $FeSO_4$ helps to achieve the optimum conductivity. Porcine pancreatic amylase, obtained from Sigma Aldrich was dissolved in 1x Phosphate buffer. A 10 μL drop of the well-shaken reaction mixture of DI water, salt, starch, and solution of amylase was dispensed symmetrically between the electrodes. The amylase was introduced at the later stage as a ~2 μl droplet.

The electrical resistance measurement setup was prepared by fixing two electrodes of thin copper wires on a scotch tape covered glass substrate at 1 mm separation and connecting the electrodes to a multimeter. The glass substrate was placed on a temperature controllable hot plate. The scotch tape was used to make the surface hydrophobic and prevent spreading out of the droplet. The 10 μL droplet of the reaction mixture was introduced into the drop after ~30 s for the resistance reading in the multimeter to stabilize. The subsequent resistance values were recorded at regular intervals for the next 1 min. The same procedure repeated for 3 different temperatures, 26^{o}C (room temperature), 40 ± 1^{o}C, and 50 ± 2^{o}C. The individual experiments were completed within 60 - 90 s to avoid resistance fluctuations owing to evaporation. In every case, a decreasing trend in the resistance value was observed post α-amylase introduction. Percentage change in resistance of the drop within a time interval of ~50 - 60 s was adopted as a quantitative measure for sensing the α-amylase concentration.

3.3. Results and Discussion

3.3.1 Experimental Study on Effect of Temperature

The effect of temperature on the droplet was studied using digital camera and thermal imager. The temperature of thermal imager was calibrated with the known temperature of the hotplate. Image (A) of Figure 3.1 illustrates the set-up of the experiment schematically where a droplet was dispensed on a glass surface and the system was exposed to heat from the bottom of the substrate. Images (B) to (C) shows how the digital and thermal imagers was placed to characterize the motion of droplet and temperature distribution as discussed in the earlier section.

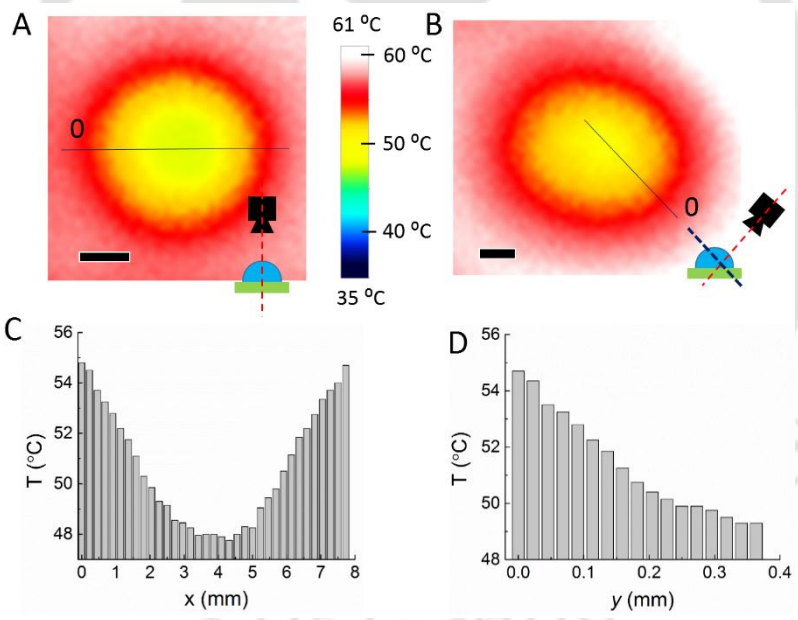

Figure 3.3: Images (A) and (B) shows the thermal image of the droplet when the substrate temperature was ~55^{0}C. The bottom right corner inset schematic of both the images shows the placement of the thermal imager. Images (C) and (D) show the corresponding temperature distribution plot with respect to distance x and y along X and Y axis, respectively. The scale bars are of 2 mm.

In order to track the motion of the droplet a particle of ~120 um was suspended in the droplet. It was observed that due to heat exposure, the particle inside the droplet performed a rotational motion as shown in images (A - D) of Figure 3.2. The rotation was

due to the temperature difference across the vertical direction of the droplet. The droplet experienced a difference of surface tension due to the temperature gradient that leads to thermal Marangoni effect. The phenomenon was investigated computationally in the later section of this paper. However, the temperature characterizations were performed experimentally with a thermal imager.

Thermal images (A) and (B) of Figure 3.3 show the distribution of temperature across the droplet horizontally and vertically, respectively. The inset of the images shows the position of the camera while taking the thermal images. In case of vertical set-up, it was difficult for the imager to take an exact side view of the droplet due to the droplet size and hot surface beneath, hence the image was taken in a tilted position which can be assumed to be the side view of the droplet as the difference of temperature at any horizontal plane is negligible.

Images (C) and (D) show a variation of temperature in x and y-direction along the cut-plane shown the thermal image. The "0" in the images (A) and (B) of Figure 3.3 at one side of the cut-plane indicates the $x = 0$ (in case of image (A)) and $y = 0$ (in case of image (B)) from which the distance was measured. The temperature distributions in images (A) and (B) clearly show that the temperature of the droplet was high near the substrate compared to the top surface of the droplet. This difference of the temperature created a thermal Marangoni flow inside the droplet. A finite element computational study was performed to understand the physics behind the motion.

3.3.2 Computational Analysis

Problem Formulation: In this computational study, we show a simple qualitative computational analysis along with experimental evidence, which justifies the onset of the rotational motion due to the combined effect of thermal Marangoni and natural convection

inside a water droplet. A two-dimensional (2-D) semi-circular water droplet of diameter 8 mm, resting on a flat hot solid substrate of thickness 100 μm and surrounded by air was chosen to be the computational domain, as shown in Figure 4(A). The rectangular domain was of length 2 mm and width 1 mm as shown in Figure 4(A). The droplet was placed at 0.5 mm downstream from the air inlet.

In the computational fluid dynamic (CFD) model, air (gas, i = 1) and water (liquid, i = 2) phases were assumed to be immiscible, and Newtonian. The surface tension of water is modelled as a linear function of the temperature gradient between the hot solid substrate and the fluid domain (water droplet and surrounding air) as, $\gamma = \gamma_0 + \alpha(\Delta T)$, where, γ_0 (= 72.8 mN/m) is the surface tension of water at 20°C, α is the slope (= – 0.2063 mN/m°C)[45], and ΔT (~5–30°C) is the temperature gradient between the hot solid surface and the fluid domain. The density of water is varied with temperature gradient as approximated by Boussinesq[46]. According to the approximation, the density of water can be modelled as a linear function of the temperature gradient between the hot solid substrate and the fluid domain (water droplet and surrounding air), $\rho_2 = \rho_0(1 - \beta \Delta T)$, where, ρ_0 (= 1000 kg/m^3) is the density of water at 4^{0}C, β is the thermal expansion coefficient (= 69×10^{-6} K^{-1} at 20^{0}C)[47], and ΔT (~5–30^{0}C) is the temperature gradient between the hot solid surface and the fluid domain. The following continuity and equations of motion were employed to describe the motion of the i^{th} phase,

$$\nabla \cdot \mathbf{u}_i = 0 , \tag{3.1}$$

$$\rho\left(\dot{\mathbf{u}}_i + \mathbf{u}_i \cdot \nabla \mathbf{u}_i\right) = \nabla \cdot \left[-p_i \mathbf{I} + \eta_i\left(\nabla \mathbf{u}_i + \nabla \mathbf{u}_i^{\,T}\right)\right] + \mathbf{f}_{st} + \rho \mathbf{g} . \tag{3.2}$$

The velocity vector, density, viscosity, and pressure of the i^{th} phase were denoted by notations u_i, ρ_i, η_i, and p_i respectively. The over-dot symbol denotes the time derivative and g signifies the acceleration due to gravity vector which was acting in the negative *y*-direction. The surface tension force was defined as, $\mathbf{f}_{st} = G\nabla\phi$, a product of the chemical potential (*G*) and the gradient of the phase field parameter (ϕ). The surface tension force was determined by minimizing the total free energy inside fluid domain as a function of the phase field variable (ϕ),

$$F(\phi) = \int_{\Omega}\left(f(\phi) + \frac{1}{2}\lambda\left|\nabla^2\phi\right|\right) d\Omega \,. \tag{3.3}$$

where, Ω was computational volume and the total free energy, $F(\phi)$ was a combination of double well potential, $f(\phi) = \lambda/4N^2\left(\phi^2-1\right)^2$, and surface energy. The parameter *N* was calculated by the following equation, $N = 0.5h_m$ where h_m is the maximum element size in the computational domain. To evaluate surface energy, mixing energy density (λ) was estimated as, $\lambda = (3\gamma N)/\left(2\sqrt{2}\right)$ in which γ was surface tension and *N* was the thickness of the diffused interface. In order to track the rotational Marangoni motion of the droplet at the air-water interface and in the bulk, the phase-field method was employed[44, 48-51]. In this method, the transport equation was written in terms of the phase field parameter (ϕ) as,

$$\dot{\phi} + \mathbf{u}_i\cdot\nabla\phi = \nabla\cdot\chi(\nabla G)\,. \tag{3.4}$$

Where, the chemical potential (*G*) was defined as a derivative of the free energy functional, $G = F'(\phi) = \lambda\left[-\nabla^2\phi + \phi\left(\phi^2-1\right)/N^2\right]$. The interfacial density (ρ), and viscosity (μ) were evaluated in terms of f as, $a = 0.5\left[a_1(1+\phi) + a_2(1-\phi)\right]$, where a can be

any of ρ and μ. The symbol χ represents the mobility tuning parameter, which was chosen to be 10 m s/kg to avoid mass loss in the conventional phase field model.

To identify the temperature distribution across the droplet, and subsequently calculate the temperature dependent surface tension, the generalized heat diffusion equation is employed,

$$\rho C_p \frac{\partial \mathrm{T}}{\partial t} + \rho C_p \mathbf{u}_i \cdot \nabla \mathrm{T} - k \nabla^2 \mathrm{T} = 0 . \tag{3.5}$$

For the flat hot solid substrate, or generally, to compute heat transfer in solids, the generalized heat diffusion equation becomes,

$$\rho C_p \frac{\partial \mathrm{T}}{\partial t} - k \nabla^2 \mathrm{T} = 0 . \tag{3.6}$$

In the Eqs. (3.5) and (3.6), C_p is the heat capacity of the material, k is the thermal conductivity of the material, and T is the temperature.

Boundary Conditions: The lower flat surface of the droplet was assumed to be non-slipping and impermeable while the curved air-water interface was considered to be the deformable one. The velocity of air at the inlet and outlet were set to zero. The upper wall of the computational domain was assumed to be non-slipping and impermeable. The contact angle of water droplet on the substrate was considered to be 90° unless mentioned otherwise[21]. We assumed that the lower surface of the hot plate was at constant temperature T_0 and was varied in the simulations in order to get different thermal gradient across the computational domain. At the upper surface and the side surfaces of the hot plate, the heat flux due to conduction from the solid plate was assumed to be same as that

of the heat flux due to convection in the fluid domain. The upper wall of the computational domain was assumed to be thermally insulated.

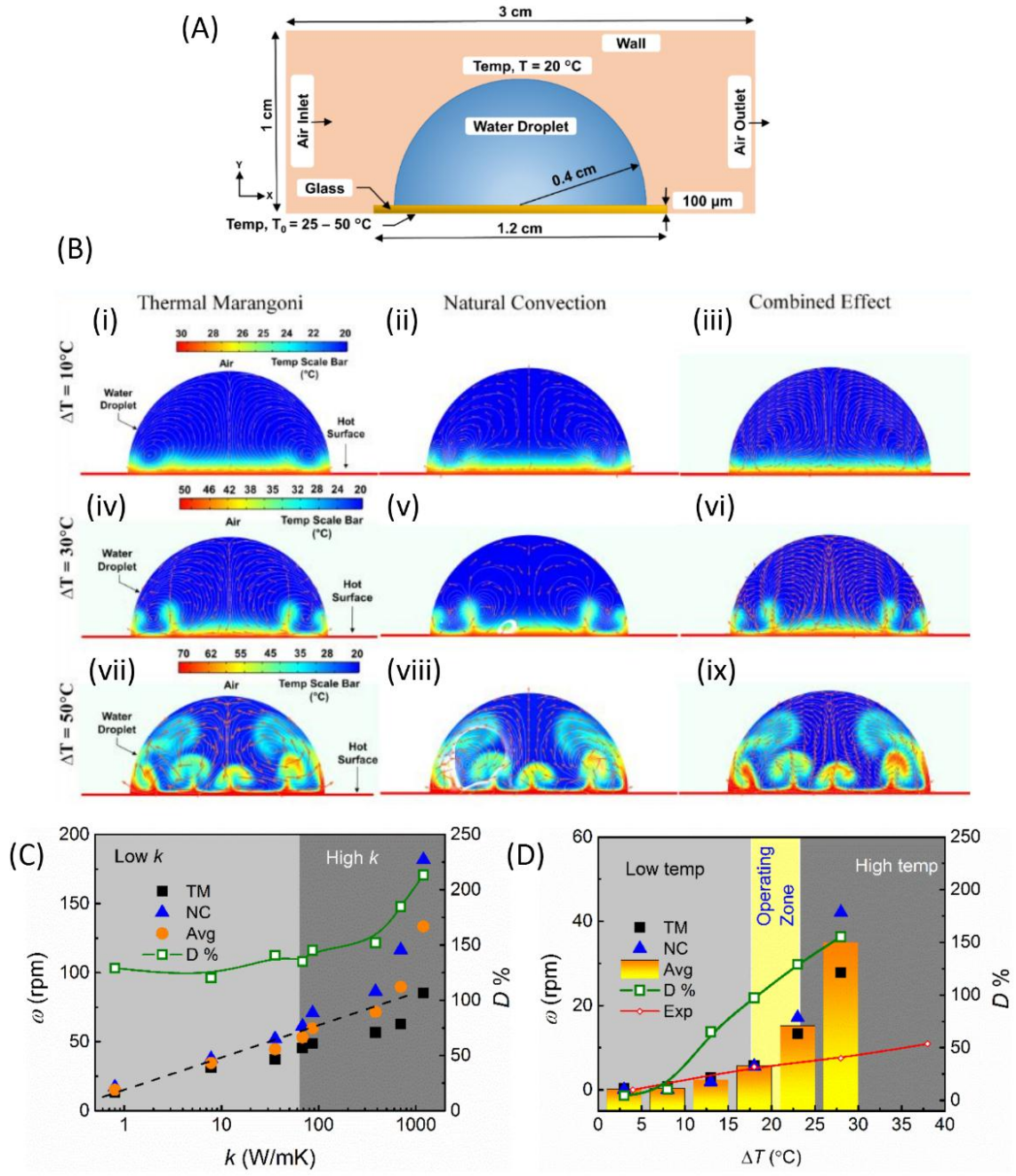

Figure 3.4: (A) shows the schematics of the computational domain employed in this study. All the necessary dimensions of the domain are shown in the schematic. Images (B) shows the rotational effect inside the droplet due to the thermal Marangoni, natural convection, and combined effect. The colored contour, white continuous lines, and orange arrows show the temperature distribution,

streamlines and velocity vectors of water inside the droplet, respectively. Images (i)-(iii), (iv)-(vi), and (vii)-(ix) show the temperature gradient created inside the droplet after t = 1 s of simulation for ΔT = 10^0C, 30^0C, and 50^0C respectively. Plot (C) shows the variation of rotational speed (ω) with the change in the thermal conductivity (k) of the hot substrate. The dotted lines show the slope of the curve. The dominance ($D = (NC/TM) \times 100\%$) of thermal Marangoni (TM) over natural convection (NC) is also illustrated with the green line. Plot (D) shows the variation of rotational speed (ω) with the temperature difference (ΔT) between the hot substrate and room temperature. The red line plot shows the corresponding experimental values of rotational motion (ω) with temperature difference (ΔT). The green line shows the dominance of NC over TM. The average value (Avg) shows the rotation due to combined effect.

Solution Methodology: The unsteady governing equations (1) – (6), and the boundary conditions were solved using the commercially available COMSOL^{TM} Multiphysics software based on the finite element method. In this method, the spatial terms of the governing equations were initially discretized to obtain an ordinary differential equation (ODE) in time, which was time-marched to obtain the evolution of the streamline flow patterns inside the droplet. The 2-D geometry was divided into ~87653 triangular elements to obtain the grid independent solutions. We employed the built-in Galerkin least-square (GLS) method to discretize nonlinear convective diffusion equations, which was stabilized through streamlining and crosswind diffusions. The segregated predictor-corrector method had been used to obtain the velocity and pressure profiles by incremental pressure correction.

To computationally study the effect of thermal gradient inside a water droplet, we have modelled the system using the computational domain as shown in Figure 3.4(A). In the schematics, all the dimensions and some boundary conditions of the domain is shown. Figure 3.4(B) (i) – (iii), (iv) – (vi), and (vii) – (ix) show the temperature gradient created inside the droplet after t = 1 s of simulation for ΔT = 10^0C, 30^0C, and 50^0C, respectively. The color bar above shows the respective temperatures at different locations. It is quite evident from the contour plot that, there is a sharp thermal gradient (for example, 3×10^6

^{0}C/m for ΔT = 30°C case) created near the contact line of the water droplet, due to which the surface tension and density of water changes significantly near the contact line as we have modelled both the parameters as a linear function of temperature gradient. Whereas, near the top of the droplet the temperature remains to be almost equal to the ambient temperature (20^{0}C), which ensures that there is a surface tension gradient and natural convection created inside the water droplet due to the hot substrate (50^{0}C) placed below the droplet. This spatial variation of surface tension and density creates a rotational motion inside the droplet which is shown by the streamlines and the velocity vectors. The first, second and third column of the figure shows the rotational motions inside the droplet due to the thermal Marangoni, natural convection and the combined effect of thermal Marangoni and natural convection, respectively. It can be visualized from the images that, for a particular temperature gradient, the rotational flow due to surface tension gradient occurs throughout the droplet whereas, the rotational flow due to natural convection occurs in the vicinity of the local hot spots inside the droplet-like near the contact line of the droplet. For lower temperature gradients like, ΔT = 10^{0}C, the thermal Marangoni flow is comparatively higher than the rotations due to natural convection as illustrated in images (i – iii), whereas, for higher temperature gradients like, ΔT = 50^{0}C, flow due to natural convection overpowers the effect of thermal Marangoni flow as shown in images (vii – ix). In the moderate temperature gradients like, ΔT = 30°C, both the effects of natural convection and thermal Marangoni is present inside the water droplet as illustrated in images (iv – vi). In summary, both the thermal Marangoni flow and natural convection creates the rotational motion inside the droplet for all the temperature gradients, however the dominance of thermal Marangoni (natural convective) flow is higher in the lower (higher) temperature gradients. Figure 3.4(C) shows the effect of thermal conductivity (*k*)

on the rotational speed (ω). An increase in *k* causes an increase in the rate of heat transfer from the hot substrate to the droplet. Subsequently, the temperature gradient between the hot substrate and the droplet increases which induces a higher rotational motion owing to the accompanying increase in surface tension gradient and natural convective (NC) flow. The values of *k* in the simulation has been selected based on the practical values of different materials such as glass (0.8 W/mK), mercury (7.82 W/mK), lead (35.6 W/mK), tin (68.2 W/mK), iron (86.5 W/mK), and copper (385 W/mK)[45]. Beyond a critical value of k (~100 W/mK), the rotational flow due to the natural convection is significantly higher than the rotation due to the thermal Marangoni (TM) flow. A dominance factor ($D = (NC/TM) \times 100\%$) of natural convection over thermal Marangoni is calculated to understand the contribution at different temperature difference and thermal conductivity values. The plot follows a linear trend in the range of 0.8 to 700 W/mK of *k* values as indicated by dotted lines in the logarithmic plot (C), which indicates that for high *k* region the dependence of ω over *k* saturates because the distribution of temperature across the droplet spreads faster towards the top surface due to high *k* value that lead to gradual change in the surface tension compared to a drastic change in the low *k* region. Although, the ω value increases at 1200 W/mK, the increase in the slope is not drastic. Thus, a low *k* material is well suitable for the bio-sensing application as the rotation of the droplet in that domain is considerably sufficient and tunable, in addition, the system gets more time to perform complete reaction with faster gain of electrical stability. This is why, glass (*k* = 0.8 W/mK) as a substrate material is suitable for this bio sensing platform. Moreover, all metallic substrates are not feasible as they short the device electrically. Figure 3.4(D) shows the effect of temperature difference ($\Delta T = T - T_0$, where T_0 is room temperature ~

22^0C) of the hot substrate on the effect of rotation (ω). As ΔT increases, the temperature gradient across the hot substrate and the water droplet increases (from 0.5×10^6 ^{0}C/m to 3×10^6 ^{0}C/m) which induces a higher surface tension gradient along with higher natural convection and consequently the higher rotational motion inside the droplet is observed.

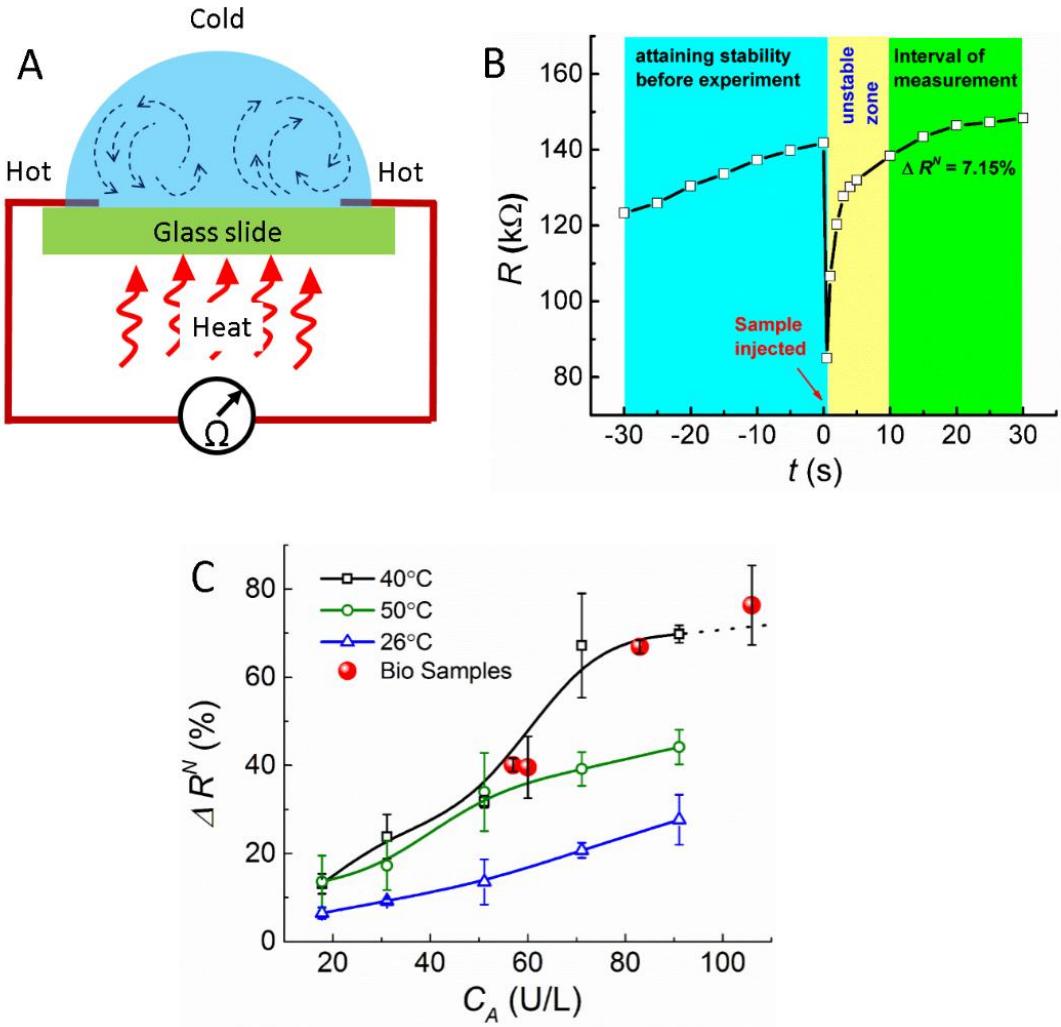

Figure 3.5: Image (A) shows the experimental set-up for sensing and measuring the concentration of *α*-amylase in a sample. Image (B) shows the temporal response of the sensor for C_A = 20 U/L of amylase at a substrate temperature of 26ºC. Image (C) shows the response of the system for different concentration of *α*-amylase at 3 different temperatures. The scattered red points are the response of the system due to introduction of blood serum sample.

However, the experimental blue line-plot in Figure 4(D) shows a close match with the simulated result up to ~ ΔT = 24^{0}C. However, for a high temperature condition, similar to a high thermal conductivity, the temperature distributes across the droplet very fast from bottom to top and the radiated heat from the hot surface increases the air temperature in the near vicinity in practical situation and thus, a low rotational speed (ω) was observed compared to the computational value. The low temperature suffers from a low rotational motion and the high-temperature zone is not suitable for electrical instability due to evaporation and bio-sample degradation issues. Moreover, in the proposed system the high temperature was also not providing a significant improvement in rotational speed (ω) beyond ~40°C. Hence, a temperature ~40 – 45°C was selected to be the operational temperature in an experimental situation.

3.3.3 Experimental Analysis

The set-up of the sensing application is illustrated in image (A) of Figure 3.5. In this case, the salt water droplet having starch was placed in between two cylindrical copper electrodes. A test sample having α-amylase of 5 µl was added to the base drop in order to detect the α-amylase concentration. The test was performed for three different substrate temperature of 26, 40 and 50°C as discussed earlier. It was observed that the change in normalized resistance (ΔR_N) was higher in case of higher concentration of amylase. In this situation, the big molecules of starch create a barrier in the ion transport inside the droplet.

However, in presence of α-amylase, the starch breaks down to smaller molecules glucose and maltose, which reduces the hindrance in the passage of ions which lead to a higher change in resistance in presence higher concentration of amylase. Moreover, the

intermediate oxocarbenium ion formation due to the reaction or due to nucleophilic displacement reduces the resistance across the droplet. Besides that, the catalytic ionizable groups of amylase often create protonated carboxyl ions. These ions play the role to reduce the resistance across the reaction.[52-54] Image (B) of Figure 3.5 shows the temporal response of the sensor for amylase concentration, C_A = 20 U/L at a substrate temperature of 26°C. The whole experimental situation was divided in three zones, such as (i) the sensor is attaining stability before the reaction starts, (ii) the mechanical unstable zone due to the injection of sample, and (iii) the interval of measurement as illustrated in image (B) of Figure 3.5. The response of the droplet was obtained in the third zone as described here. The best response was found to be at the temperature of ~40°C, which can be explained by the fact that the free α-amylase shows highest activity at the temperature range of 37–42°C. Moreover, higher temperature leads to evaporation of the droplet which is not feasible for the stabilized electrical response and high temperature also shows a saturated rotational motion beyond 40^0C as shown and discussed in Figure 3.4 (D).

Experiments with biological samples were also performed and it was observed that the responses were close to the calibration curve. The bio-samples were tested in 40°C. The results are shown in Figure 3.5(B) with scattered points. The stability of the sensor was also checked by measuring the base resistance of droplets from 3 different freshly prepared solutions for 3 different days as illustrated in Figure 3.6. The plot suggests that the droplet solution is stable and reusable for the experiments.

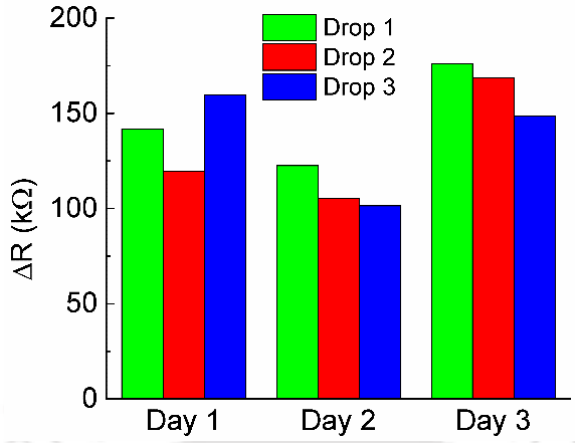

Figure 3.6: This image shows the base resistance of three different droplets for three different days.

3.4. Conclusions

In summary, this study reveals the effect of heat on a water droplet. The rotational motion was observed inside a water droplet when it was placed on a hot substrate. The rotational motion increased with the increase in the temperature of the substrate temperature. A motion of magnitude ~12 rpm was recorded for a substrate temperature of 60°C when a particle of diameter ~200 μm placed inside the droplet. A finite element computational study was performed to understand the phenomenon and it was found that the change in interfacial tension across the droplet due to variation of temperature was the reason behind the rotational motion. A study was performed to understand the contribution of thermal Marangoni and natural convection. The computational studies suggested that, for a particular temperature gradient, the rotational flow due to surface tension gradient occurs throughout the droplet whereas, the rotational flow due to natural convection occurs in the vicinity of the local hot spots inside the droplet-like near the contact line of the droplet. The thermal Marangoni flow is comparatively higher for a lower temperature gradients ($\Delta T = 10^{o}$C) whereas, for higher temperature gradients ($\Delta T = 50^{o}$C), flow due to natural

convection overpowers the effect of thermal Marangoni flow. The droplet system was further extended in biomedical application to detect α-amylase in blood serum. Experimental studies showed the capability of detecting blood serum in the range of 20 – 110 U/L, which is suitable to diagnose the pancreatitis at early stage. The computational study suggested the operation in substrates having low thermal conductivity would provide better practical feasibility in case of sensing. It was also found that the temperature ranges between 40 – 45°C was best for the sensing operation. Tests with human blood serum was also carried out and the results were in the range of pathological data. Hence, the proposed system can be used for biomedical application to diagnose pancreatitis at its early stages.

References

1. J. Wang, *Biosensors and Bioelectronics*, 2006, **21**, 1887-1892.
2. A. Niemz, T. M. Ferguson and D. S. Boyle, *Trends in Biotechnology*, 2011, **29**, 240-250.
3. Y. Fan, J. Liu, Y. Wang, J. Luo, H. Xu, S. Xu and X. Cai, *Biosensors and Bioelectronics*, 2017, **95**, 60-66.
4. H.-Y. Lin, C.-H. Huang, J. Park, D. Pathania, C. M. Castro, A. Fasano, R. Weissleder and H. Lee, *ACS Nano*, 2017, **11**, 10062-10069.
5. S. Dutta, N. Mandal and D. Bandyopadhyay, *Biosensors and Bioelectronics*, 2016, **78**, 447-453.
6. D. Metzler, *Biochemistry: The Chemical Reactions Of Living Cells*, Elsevier Science, 2012.

7. L. W. Wilkins, *Diagnostic Tests Made Incredibly Easy!*, Lippincott Williams & Wilkins, 2009.

8. F. J. Gella, G. Gubern, R. Vidal and F. Canalias, *Clinica Chimica Acta*, 1997, **259**, 147-160.

9. J. F. van Staden and L. V. Mulaudzi, *Analytica Chimica Acta*, 2000, **421**, 19-25.

10. M. S. Attia, H. Zoulghena and M. S. A. Abdel-Mottaleb, *Analyst*, 2014, **139**, 793-800.

11. A. Y. Foo and R. Bais, *Clinica Chimica Acta*, 1998, **272**, 137-147.

12. Z. Zhang, W. R. Seitz and K. O'Connell, *Analytica Chimica Acta*, 1990, **236**, 251-256.

13. V. G. Battershell and R. J. Henry, *Journal of Cereal Science*, 1990, **12**, 73-81.

14. T. Sasaki, T. R. Noel and S. G. Ring, *Journal of Agricultural and Food Chemistry*, 2008, **56**, 1091-1096.

15. L. Zajoncová, M. Jílek, V. Beranová and P. Peč, *Biosensors and Bioelectronics*, 2004, **20**, 240-245.

16. S. Wu, Y. Zhu, Q. Cai, K. Zeng and C. A. Grimes, *Sensors and Actuators B: Chemical*, 2007, **121**, 476-481.

17. E. Svens, K. Kapyaho, P. Tanner and T. H. Weber, *Clinical Chemistry*, 1989, **35**, 662-664.

18. *United States Pat.*, US4963479, 1990.

19. P. B. Luppa, A. Bietenbeck, C. Beaudoin and A. Giannetti, *Biotechnology Advances*, 2016, **34**, 139-160.

20. B. Robert, *Sensor Review*, 2008, **28**, 12-17.

21. M. Bhattacharjee, V. Pasumarthi, J. Chaudhuri, A. K. Singh, H. Nemade and D. Bandyopadhyay, *Nanoscale*, 2016, **8**, 6118-6128.

22. Y. Lim, D. Sharma and H. Shin, 2017.

23. J. L. Arlett, E. B. Myers and M. L. Roukes, *Nature Nanotechnology*, 2011, **6**, 203.

24. E. Morales-Narváez, L. Baptista-Pires, A. Zamora-Gálvez and A. Merkoçi, *Advanced Materials*, 2017, **29**, 1604905-n/a.

25. M. Bhattacharjee, H. B. Nemade and D. Bandyopadhyay, *Biosensors and Bioelectronics*, 2017, **94**, 544-551.

26. P. Bollella, L. Medici, M. Tessema, A. A. Poloznikov, D. M. Hushpulian, V. I. Tishkov, R. Andreu, D. Leech, N. Megersa, M. Marcaccio, L. Gorton and R. Antiochia, *Solid State Ionics*, 2018, **314**, 178-186.

27. C. M. Hangarter, M. Bangar, A. Mulchandani and N. V. Myung, *Journal of Materials Chemistry*, 2010, **20**, 3131-3140.

28. B. H. Park, S. J. Oh, J. H. Jung, G. Choi, J. H. Seo, D. H. Kim, E. Y. Lee and T. S. Seo, *Biosensors and Bioelectronics*, 2017, **91**, 334-340.

29. S. Niu, Y. Hu, X. Wen, Y. Zhou, F. Zhang, L. Lin, S. Wang and Z. L. Wang, *Advanced Materials*, 2013, **25**, 3701-3706.

30. S. Choi, H. Lee, R. Ghaffari, T. Hyeon and D.-H. Kim, *Advanced Materials*, 2016, **28**, 4203-4218.

31. H. H. Asada, J. Hong-Hui and P. Gibbs, 2004.

32. D. B. Papkovsky, *Sensors and Actuators B: Chemical*, 1993, **11**, 293-300.

33. L. De Vico, L. Iversen, M. H. Sorensen, M. Brandbyge, J. Nygard, K. L. Martinez and J. H. Jensen, *Nanoscale*, 2011, **3**, 3635-3640.

34. V. Srinivasan, V. Pamula, M. Pollack and R. Fair, 2003.

35. V. Srinivasan, V. K. Pamula and R. B. Fair, *Analytica Chimica Acta*, 2004, **507**, 145-150.

36. H. Andersson and A. van den Berg, *Sensors and Actuators B: Chemical*, 2003, **92**, 315-325.

37. B. Kuswandi, Nuriman, J. Huskens and W. Verboom, *Analytica Chimica Acta*, 2007, **601**, 141-155.

38. M. W. Royal, N. M. Jokerst and R. B. Fair, *IEEE Sensors Journal*, 2013, **13**, 4733-4742.

39. D. A. Boehm, P. A. Gottlieb and S. Z. Hua, *Sensors and Actuators B: Chemical*, 2007, **126**, 508-514.

40. K. Jan, S. Kirat, O. N. Alan, J. Carl, M. Alan and O. B. Peter, *Journal of Micromechanics and Microengineering*, 2002, **12**, 486.

41. M. Bhattacharjee, V. Pasumarthi, J. Chaudhuri, A. K. Singh, H. Nemade and D. Bandyopadhyay, 3rd International Conference on Emerging Electronics (ICEE), 2016.

42. B. Ravi, S. Chakraborty, M. Bhattacharjee, S. Mitra, A. Ghosh, P. S. Gooh Pattader and D. Bandyopadhyay, *ACS Applied Materials & Interfaces*, 2017, **9**, 1066-1076.

43. A. K. Singh, K. K. Dey, A. Chattopadhyay, T. K. Mandal and D. Bandyopadhyay, *Nanoscale*, 2014, **6**, 1398-1405.

44. A. Sharma, J. Chaudhuri, V. Kumar, S. Timung, T. K. Mandal and D. Bandyopadhyay, *RSC Advances*, 2015, **5**, 29545-29551.

45. N. B. Vargaftik, B. N. Volkov and L. D. Voljak, *Journal of Physical and Chemical Reference Data*, 1983, **12**, 817-820.

46. A. Demuren and H. Grotjans, *Numerical Heat Transfer, Part B: Fundamentals*, 2009, **56**, 1-22.

47. N. M. Putintsev and D. N. Putintsev, *Journal of Thermal Science*, 2017, **26**, 125-131.

48. A. Sharma, V. Tiwari, V. Kumar, T. K. Mandal and D. Bandyopadhyay, *ELECTROPHORESIS*, 2014, **35**, 2930-2937. LOWER CASE

49. S. Timung, J. Chaudhuri, M. P. Borthakur, T. K. Mandal, G. Biswas and D. Bandyopadhyay, *ELECTROPHORESIS*, 2017, **38**, 1450-1457.

50. D. Jacqmin, *Journal of Computational Physics*, 1999, **155**, 96-127.

51. Y. Lin, P. Skjetne and A. Carlson, *International Journal of Multiphase Flow*, 2012, **45**, 1-11.

52. H. Kaneko, T. Kuriki and S. Okada, *Journal of Applied Glycoscience*, 1999, **46**, 187-197.

53. S. Chiba, *Bioscience, Biotechnology, and Biochemistry*, 1997, **61**, 1233-1239.

54. J. B. Kempton and S. G. Withers, *Biochemistry*, 1992, **31**, 9961-9969.

भारतीय प्रौद्योगिकी संस्थान गुवाहाटी
Indian Institute of Technology Guwahati

II. Paper Based Electronic Sensors

CHAPTER 4

Paper Based Flexible Touchpad and Hand Tremor Detection Device

Contents

ABSTRACT 99
4.1. Introduction 100
4.2. Materials and Methods 103
4.2.1 Materials 103
4.2.2 Methods 105
4.2.3 Characterizations 109
4.3. Results and Discussion 110
4.3.1 Resistive Touchpad 110
4.3.2 Hand Tremor Detector 115
4.4. Conclusions 123
References 124

भारतीय प्रौद्योगिकी संस्थान गुवाहाटी
Indian Institute of Technology Guwahati

ABSTRACT

A resistive touchpad was developed employing paper, pencil graphite, and polydimethylsiloxane (PDMS). One side of a piece of paper was coated with pencil graphite to make it electrically conducting while the other side was coated with the polymer to make the same an insulating one. A pair of such flexible substrates were assembled with the help of an intercalated polymer spacer in such a manner that the holes present in the spacer allowed the inner graphitic layers of the paper surfaces to come in contact with each other when these locations were touched or pressed. An external electrical circuit was designed to detect the variations in the output electrical resistances. The resistive pad was further modified to develop a point-of-care-testing (POCT) device to detect the hand tremors associated with the neurological disorders such as Parkinson's disease. The proof-of-concept POCT pad showed variations in the electrical resistance when pressed with a pair of human fingers, which were under tremor, due to the variation in the area of graphitic contact at the inner layers of the paper surface. Simplified circuit-models have been discussed to explain the operating principles of the resistive pad and the POCT device for hand tremor detection. The response from the detection unit helped in evaluating the different types of real-time hand tremor levels of patients. The POCT prototype was able to detect the early to chronic stages of tremor and then differentiate the severity of the same, which showed usefulness in the prototype for the POCT of diverse neurological disorders.

Manuscript under preparation.

4.1. Introduction

The design and development of the modern electronic touch sensors have significant analogy to the 'touch' sensations generated at the epidermal layer of a human skin by the hypodermal nerves[1]. The artificial electronic gadgets employ tactile sensors to detect the location and motion of a touch on the surface by measuring the variations in electrical resistance,[2] capacitance,[3] impedance,[4] or inductance.[5] Apart from sensing the human interferences, the touch-sensors can also detect force or pressure applied[6] or the movements before triggering various actions based on the magnitude and direction of the finger impress.

Of late, the integration of the specialties of micro or nanoscale science[7] and bio- and smart-materials[8] into the touchscreen devices and other sensors[9] have played a pivotal role in improving their affordability, efficiency, and biocompatibility.[10-15] Particularly, extensive research efforts have been directed towards developing radically economic touchpads.[3, 16] This is because, apart from the tele-interfaces, the wearable touch sensors are also in extensive use for the affordable primary health care devices.[17] Thus, the development of a low-cost, portable, flexible, sensitive, reliable, and robust touchpad is one of the major focus of contemporary research.

However, most of the commercially available touchscreen devices are of relatively higher cost because they employ, (i) silicon or liquid crystal or ITO coated glass/acrylic substrates for fabrication,[18-20] and (ii) high-end instruments physical or chemical vapor deposition and lithography techniques for fabrication.[21] In view of the above, we report the development of an affordable, eco-friendly, and biodegradable touchpad employing filter paper, polydimethylsiloxane (PDMS), and pencil-graphite as the building blocks. The

concept is further extended to develop a primary health care prototype, which can detect the hand tremors of a Parkinson's patient.

The touchpads can broadly be classified into capacitive and resistive types.[2, 6] Resistive panels are affordable with a relatively lower clarity while the costly capacitive ones are more suitable for the high-end applications.[22-25] A resistive pad consists of two conducting sheets sandwiching a dielectric material.[26] The outer sheet is in general made flexible for the touch sensation while the rigid inner layer provides mechanical stability to the device. The flexible resistive sheet makes contact with the rigid one to generate signal due to touch sensation.[2, 27] On the other hand, the capacitive touch-panels are composed of an insulator coated with a transparent conductor[3, 6] on which the variation of the electrostatic field with the touch is correlated with the change in capacitance.

A touch-screen is in general operated by an analogue to digital controller (ADC) unit, which is programmed to differentiate action-reaction cycles for the necessary triggers.[25, 28] The popular touch pads employ n-wire configurations for the detection of the output. For example, to identify the coordinates (X, Y) of a 'touch' position on a 4-wire screen, initially, a voltage is applied in the Y-direction at the receipt of the touch sensation. The 'touch' location splits the Y-axis into two parts by acting as a voltage divider having two different resistances on the sides. This scheme helps in the identification of Y-location of the touch sensation. Following this, the voltage in the Y-direction is turned off and an X-directional voltage is applied to obtain the X-location to finally obtain the coordinate (X, Y) of the touch.[18]

A few of the seminal contributions have shown the use of paper as one of the building blocks to develop the capacitive touchpads and sensors.[20, 29] Further, the touchpads composed of diverse nanomaterials and nanostructures have also been reported in the

recent past.[3, 30-32] Interestingly, a large number of studies have shown the potential of carbonaceous materials for electronics as a replacement of silicon-based technologies.[33-36] In view of this, we employ coating of pencil graphite on a piece of paper as the base material[6, 37-40] to develop a resistive touchpad. The prototype emulates the principles employed by a number of recent works for the development of carbon-based electrodes, circuits, and devices.[10-12, 41-47] In a way, we replace all the costly materials and fabrication methodologies by simple methods and economic resources to fabricate the resistive-pad. The concept is then extended further to develop a hand-tremor monitoring device for the detection of the neurological disorders at the early stages.

It is now well known that neurological disorders represent 7.1% of the global burden of diseases, cutting across the cause and age.[48] Importantly, symptoms of these disorders are nearly imperceptible at the early stages and the patients approach medical professionals only when the disorder becomes chronic. Most of the neurological disorders are associated with abnormal or involuntary tremors in the different parts of human body.[49, 50] For example, a 'rest' tremor in a freely hanging limb is a common symptom of the extrapyramidal disorder, e.g., Parkinson's disease.[51, 52] On the other hand, the 'intention' tremor during the deliberate movement of a limb increases due to degeneration of the cerebellum and basal ganglia, which magnifies during the multiple sclerosis, Parkinson's or Wilson's disease.[53] Measurement and differentiation of such tremors at the early stages of disorders at the patient's site can be of immense significance in reducing the adversities of various types of neurological diseases.

Among other neurological disorders, presently, the Parkinson's disease is perhaps the most dreaded one, which starts with marginal hand tremors. Over the years, a few detection techniques for these tremors have been developed, which involves accelerometers,[54]

motion sensors, or optical and mechanical arrangements.[55, 56] However, all these devices are not easily available to the patients for their regular use because, (i) they are available mostly at the centralized agencies, (ii) they use of multi-step complex and sophisticated methods for detection, (iii) they require medical and/or engineering expertise for initial analysis, (iv) they are non-portable, (v) of their higher cost of production and maintenance, and (vi) of their time requirement for analysis.

In this direction, we extend the principle of the resistive pad to develop a proof-of-concept prototype, which can be employed at the user's site for the regular monitoring of the hand tremor. The prototype is capable of differentiating the normal and abnormal tremors. Further, the prototype has been tested with the real-life Parkinson's patients to detect the kind and extent of the abnormal tremors. The affordable, portable, flexible, sensitive, and robust point-of-care testing (POCT) prototype may help in the early stage non-invasive detection of various neurological disorders at the user's site.

4.2. Materials and Methods

4.2.1 Materials

Glass slides were procured from AB Chemicals, India. The HB pencils, A4 size papers, and adhesive were procured from local vendor. The Milli-Q grade de-ionized (DI) water was used for cleaning and preparation of solutions. The polydimethylsiloxane (PDMS - Sylgard184 kit) was procured from Dow Corning Corporation. The Cu wire was procured from Surgeon Sons, India. The other chemicals acetone (C_2H_6O), and ethanol (C_2H_5OH) were procured from Merck, India, which were of analytical grade and used without further purification. LEDs, resistances, and other electrical components were obtained from local vendor.

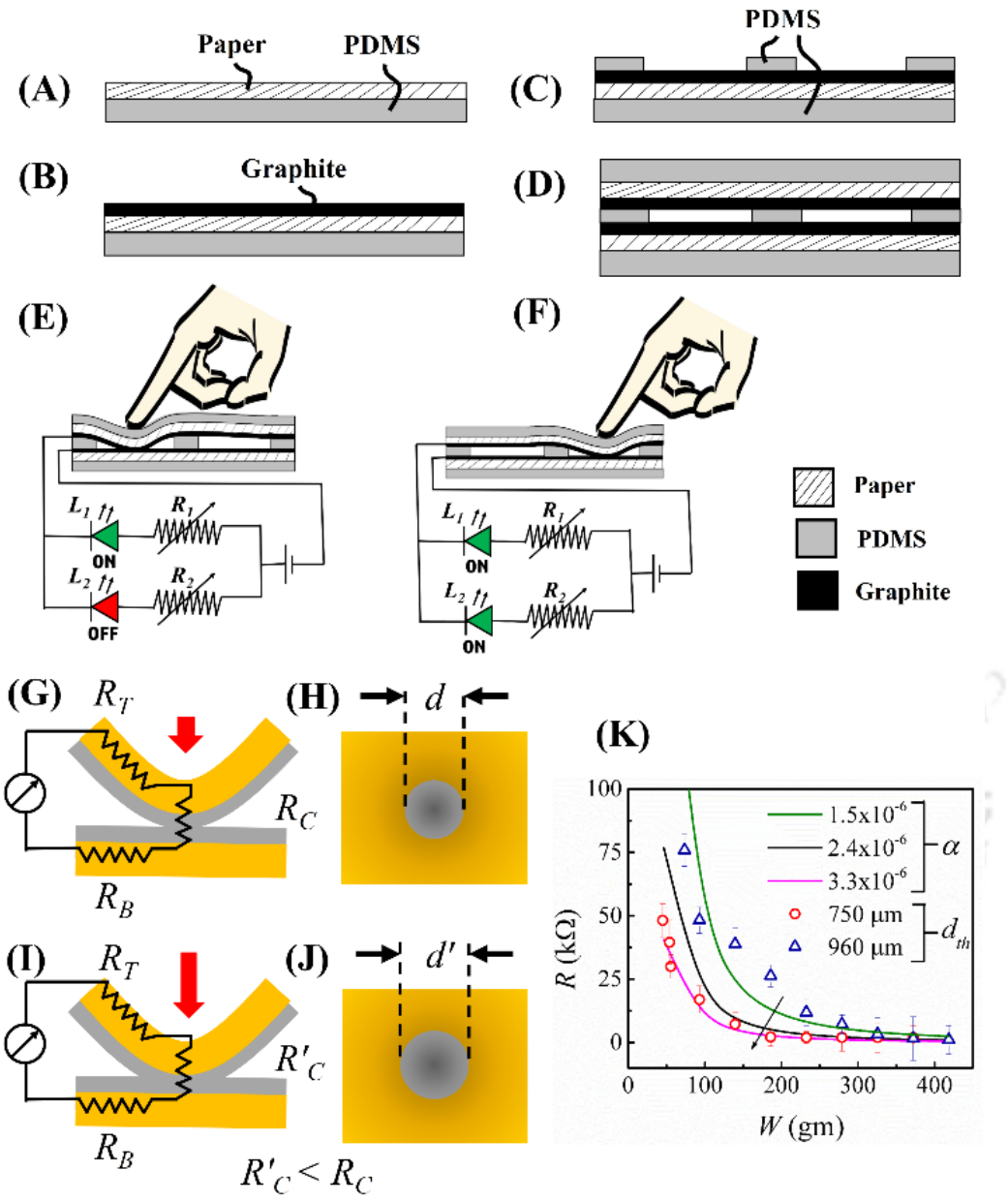

Figure 4.1: This figure shows the fabrication process and illustration of working. Images (A) – (D) show the different steps of assembling the touchpad device, (A) PDMS coating on paper, (B) paper substrate with inner-graphite and outer-PDMS coating, (C) placement of the PDMS spacer, and (D) the entire assemblage of resistive pad. Images (E) and (F) illustrates the working principle of the touchpad in which different locations of finger-press turned on different light emitting diodes (LEDs, L_1 and L_2) while the current passed through different resistors (R_1, and R_2). Images (G) – (J) show the schematic illustration of the working for a single touch location. Images (G) and (I) show the side view of the pressed touch location along with a simplified circuit model, whereas images (H) and (J) show the corresponding top views. Image (K) shows the change in the resistance (R) with applied weight (W) on the touch location. The solid lines show the theoretical calculations for different values of α and the scattered points represent the experimental data for different thickness of touch layer.

4.2.2 Methods

The fabrication steps and different layers of the touchpad is described in the Figures 4.1 and 4.2, respectively. The touchpad was made of commercial A4 paper with graphite coating on the inner surface using HB pencil, as shown in the images (A) and (B) of the Figure 4.1. The PDMS film was also applied as the protective coatings at the outer surfaces of the paper substrates, as shown in the image (B). Two such graphite coated papers were then separated from each other using a PDMS spacer, as shown in the images (C) and (D) in the Figure 4.1. The touchpad paper substrates disposed one above the other in such a manner that the graphite coated conductive layer of one substrate faces towards graphite coated conductive layer of the other substrate. Further, the graphite coated inner surfaces of the paper substrates maintained a contactless disposition with an air gap in between for touch and press. The spacer PDMS film had multiple holes, which allowed the inner graphite layers of the paper substrates to come in contact when force was applied on the top surface, as shown in the images (E) and (F) of Figure 4.1. In this process, approximately 7 – 9 gm of PDMS, 0.5 x 2 cm Cu strip, and 100 – 120 graphite strokes per cm^2 were employed.

The contact between the conducting coating of the paper substrates during press motion triggered the 'switching on' while the loss of contact during the removal of the press action led to the 'switching off'. The images (E) and (F) show that the press at different locations of the pad turned on both the LEDs (L_1 and L_2) or one LED while the current passed through resistors (R_1 and R_2). Images (G) – (J) show the schematic illustration of the working for a single touch location. Images (G) and

(I) show the side view along with a simplified circuit model of the pressed touch location, whereas images (H) and (J) show the corresponding top views.

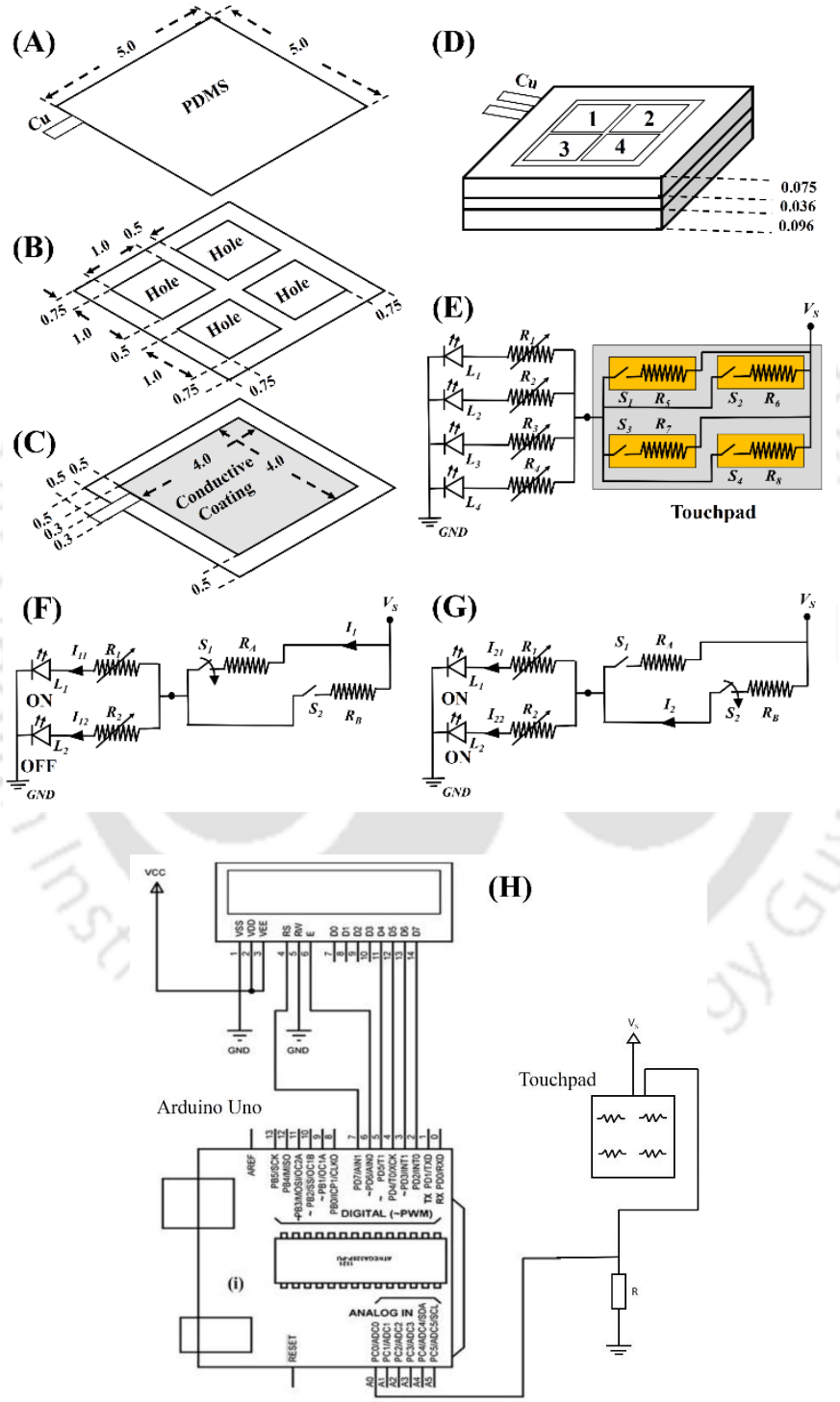

Figure 4.2: Details of the electrical parts with dimensions. Image (A) shows the outer surface view with PDMS coating and Cu connect of the top surface, image (B) shows the configuration of the

PDMS spacer with four holes, and image (C) shows the inner surface of the paper substrate with the Cu connect. Image (D) shows the assembly of the parts to form the touchpad and image (E) illustrates the circuit associated with the device having four locations. Images (F) and (G) show simplified circuit models for understanding purpose when switch S_1 is pressed and switch S_2 is pressed, respectively. Image (H) shows a prospective interfacing of the touchpad with ATmega328 microcontroller using Arduino Uno. All dimensions are in cm.

The touch area between the two conductive surfaces increased with the increase in the pressure as shown in the schematic top views (H and J). This increase in the touch area primarily contributed to the decrease in the resistance. The circuit model in the images (G) and (I) are described in details in the later section of this paper.

The dimensions and the different layers of the touchpad are described in Figure 4.2. Image (A) shows the outer PDMS coating of the top paper substrate with a Cu connect at the inner surface; image (B) shows the configuration of the PDMS spacer with four holes; image (C) shows the inner surface of the bottom paper substrate with Cu connect; and Image (D) shows the assembly with four distinct locations of touch indicated by the numerals 1, 2, 3, and 4. The image (E) illustrates the controlling circuit associated with the device. The controlling module was enabled to receive current flow from the supply voltage specific to the touch location. This happened when one of the touch locations in the top surface was pressed to bend and touch bottom one. The graphite coatings on the inner side of the top and bottom substrates came in contact, which enabled a flow of current through the controlling module.

The controlling module included resistive circuits having four variable resistances, each corresponding to one touch location. They were connected to an operational input by means of the cooperative electronic applications. The associated circuit diagram for the touchpad is shown in the image (E) of Figure 4.2 where R_1 to R_4 are the variable resistances connected to the LEDs L_1 to L_4, respectively.

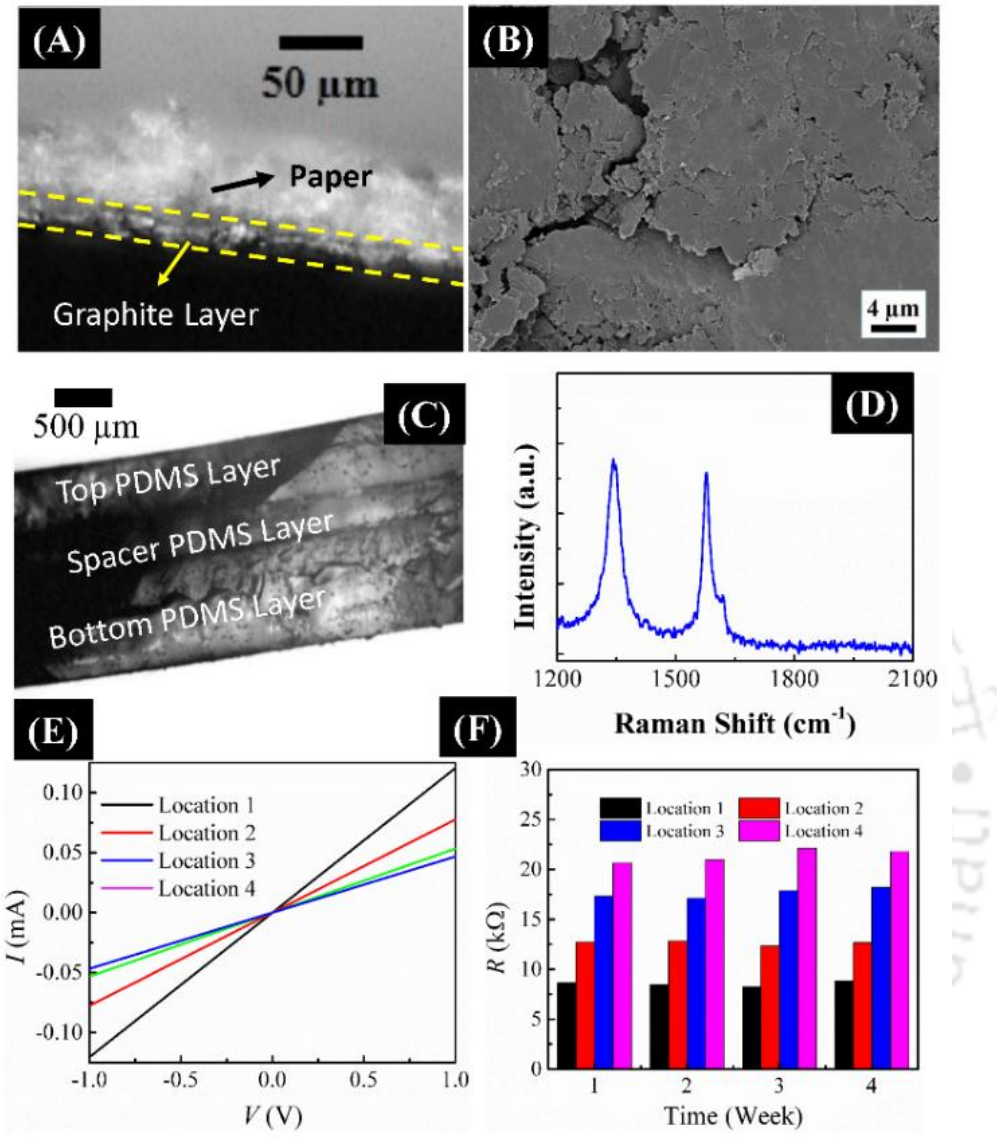

Figure 4.3: Characterizations of the touchpad prototype. Image (A) shows the microscope image of the cross-section of the graphite coated paper. Image (B) shows the FESEM image of the graphite coating on top of the paper. Image (D) shows the optical microscopic image of the cross-section of the touchpad with three different layers. Image (D) shows the Raman spectroscopy analysis of the deposited graphite layer. Image (E) shows the current (I) versus voltage (V) characteristics of the graphite coatings provided in the different locations 1 to 4 on the pad. Image (F) shows the variations in the electrical response of different locations with time highlighting the stability of the sensors.

The resistors were tuned according to the touch area resistances R_5 to R_8, respectively. The switches S_1 to S_4 represent each touch area in the touchpad. The

supply voltage V_S was connected to the touchpad and LED, as shown in circuit. The variable resistances were tuned according to the touch location resistances of the touchpad. This enabled combined resistance of the touch location and the corresponding variable resistance high enough to flow of a minimum required current to the operational input in order to generate a specific output signal at the LEDs. For the sake of understanding, the circuit for two touch locations are illustrated in images (F) and (G), which are elaborated later to understand the working of the concept. Image (H) shows a prospective interfacing of the touchpad with ATmega328 microcontroller using Arduino Uno. The touchpad in this case has been connected to the Analog pin A0 which receives the voltage signal from the voltage divider configuration as illustrated in the circuit.

4.2.3 Characterizations

The optical microscopic (Make-Leica, Model-DM500) and FESEM (Make- JEOL, Model- 7610F) images of different parts of touchpad are shown in the Figure 4.3. The thickness of the conductive graphite layer was found to be ~15 µm after 20 repetitive strokes of the HB pencil, as shown in optical micrograph image (A). Image (B) shows the FESEM image of the graphite coating on paper surface. Image (C) shows a cross-sectional image of the fabricated touchpad where three layers of PDMS are shown. Image (D) shows the Raman (Make- Horiba, Model- LabRam HR800) spectra having two characteristics peaks, which confirms the presence of graphite on the paper substrate. Image (E) shows the electrical characterization of the fabricated touchpad. The I-V characteristics of four different touch locations are shown in this plot. The stability of the touchpad was verified using time-dependent analysis of different touch locations, as shown in image (F).

4.3. Results and Discussion

4.3.1 Resistive Touchpad

The resistive touchpad was designed and operated based on the output electrical resistance of different touch location. A simplified circuit model has been introduced in the images (G) and (I) of Figure 4.1 to understand the resistive response of a touch location upon touching. The output electrical resistance (R) of a touch location had three major components, (i) top electrode resistance (R_T), (ii) contact resistance (R_C), and (iii) bottom electrode resistance (R_B). The resistances were connected in series to give the output resistance as,

$$R = R_T + R_C + R_B . \tag{4.1}$$

As the top and bottom electrode materials and positions were fixed throughout the pressed condition, the R_T and R_B were assumed to be constant. The variation in the resistance upon pressing was assumed due to the contact resistance (R_C). Thus, the resistance can be rewritten in terms of physical properties such as, resistivity (ρ), contact area (A_C), and length (l) associated with R_C as,

$$R = R_T + R_B + \rho \left(l / A_C \right) . \tag{4.2}$$

The contact area (A_C) was assumed to be circular, thus, $A_C = \pi r^2$, $d = 2r$, where r and d were the radius and diameter of the contact area, respectively. Substituting the contact area in Eq. (4.2) we obtained,

$$R = R_T + R_B + \left(\rho\, l / \pi \right) r^{-2} . \tag{4.3}$$

In Eq. (4.3), only r changed with the applied weight (W). To simplify the calculation and find a tentative relationship between the applied weight and response of the touch location, a linear relationship between the applied weight and

the radius of contact area is assumed as, $r \propto W \Rightarrow r = \alpha W$, where α is the proportionality constant. The α was assumed to be dependent on the mechanical properties and associated parameters such as spacer distance, spacer height etc. of the touchpad material and geometry. Substituting the value of r, the Eq. (4.3) can be written as,

$$R = R_T + R_B + (\rho l/\pi) \times (\alpha W)^{-2}. \quad (4.4)$$

Eq. (4.4) provides a theoretical basis for the change in the resistance in a touch location upon pressing. The value of R_C from Eq. (4.4) has been plotted in the image (K) of Figure 4.1 as solid lines considering the order of the magnitude of α to be 10^{-6}.

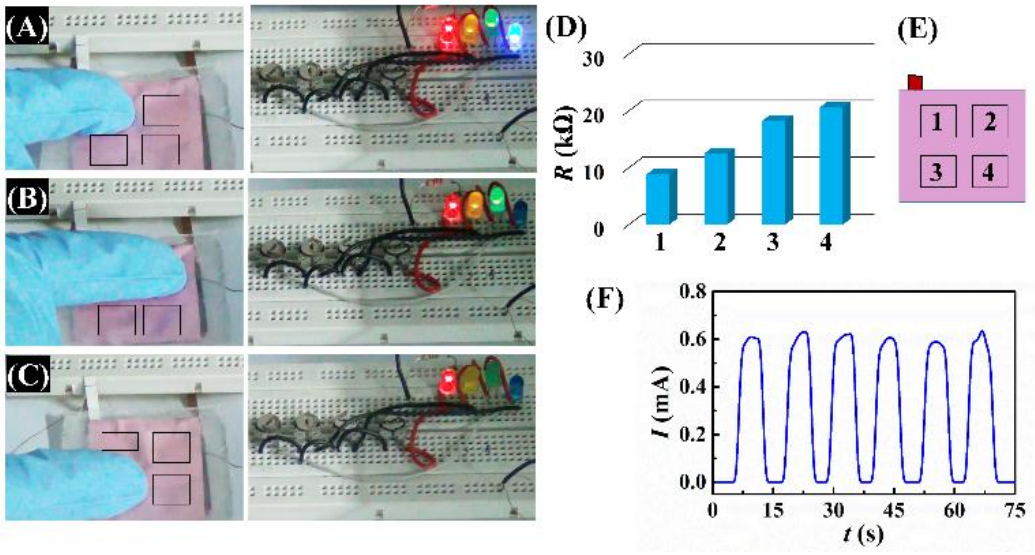

Figure 4.4: Experimental demonstration of the prototype. Images (A) – (C) show that the glowing of four, three and one LED(s) depending upon the touch location. Image (D) shows the output resistances of the different touch locations 1 to 4, as shown in the image (E). Image (F) shows the repetition of the output current for multiple touches made at location A.

The experimental values in symbols for touch layer thickness of 750 µm and 960 µm were also plotted where the value of $(R_T + R_B)$ was considered to be ~7.4 kΩ.

The plots showed an acceptable agreement between the theoretical and experimental values. Further, from the plots in the image (K) of Figure 4.1, it can be observed that the value for α reduces for a higher touch layer thickness.

Experimental images in Figure 4.4 show the turning on of the LEDs depending on 'touch' positions on the pad. Images (A) to (C) illustrates the experimental output of the proposed touchpad and image (D) shows the output resistance of different touch locations namely 1, 2, 3, and 4 as illustrated in image (E). In this case, all LEDs were turned on once touch was made in first location "1". Similarly, only 3 LEDs were turned on when touch was made in the second location "2" and only 1 LED was turned on once the touch is made in the third location "3". The image (F) shows that the output signal was stable for 6 repeated touch signals in the location 1, highlighting the robustness of the prototype.

In order to illustrate the tuning of the resistances further, a simpler example of the touchpad having two touch locations was considered. We assumed that the minimum current to turn on an LED was 0.3 mA. The circuit, shown in Figure 4.2(F), was designed in such a manner that when the touch area S_1 was pressed only the LED L_1 glowed. On the other hand, both the LEDs glowed when touch area S_2 was pressed, as shown in Figure 4.2(G).

To achieve this, the resistances R_1 and R_2 were tuned in such a manner that, $R_1 =$ 5 kΩ and $R_2 =$ 10 kΩ. The resistances of the different touch locations were, $R_A =$ 10 kΩ, $R_B =$ 5 kΩ, and the supply voltage was $V_S =$ 9 V. It was assumed that the LEDs did not have any internal resistance in order to reduce the complexity associated with the calculations. From circuit theory, when S_1 was pressed, the total current

through R_A was evaluated as, $I_1 = V_S(R_1R_2(R_1 + R_2)^{-1} + R_A)^{-1}$, which led to $I_1 =$ 0.675 mA, $I_{11} =$ 0.45 mA, and $I_{12} =$ 0.225 mA. Thus, only the L_1 LED was turned on. Again, if the S_2 was pressed we obtained, $I_2 =$ 1.08 mA, $I_{21} =$ 0.72 mA, and $I_{22} =$ 0.36 mA. Thus, in this case, both the LEDs were turned on.

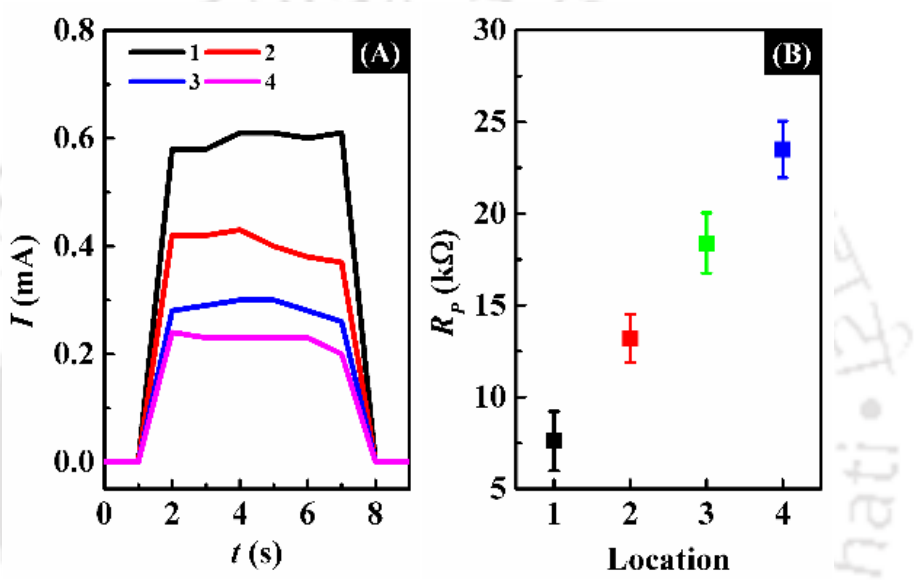

Figure 4.5: Electrical response of the different locations of the resistive touchpad. Image (A) shows the variation in the output current (I) of the touchpad with time (t) during a touch incident in the locations 1 to 4. The image (B) shows the variation in the peak output resistance (R_P) after 600 trials in the locations 1 to 4.

The output current due to the touch was also measured experimentally. The experiments showed that the output current (I) of the touchpad with time (t) during a touch incident in the locations 1 to 4 was different as illustrated in image (A) of Figure 4.5. The output resistance corresponding to the peak current, namely the peak output resistance (R_P), was also measured for 600 trials to confirm the stability of the proposed prototype. The variation in R_P at the locations 1 to 4 is shown in image (B) of Figure 4.5. Briefly, Figures 4.1 and 4.2 show the assemblage

of a paper-based low-cost flexible touchpad while the Figures 4.4 and 4.5 shows the operating principle and performance of the same.

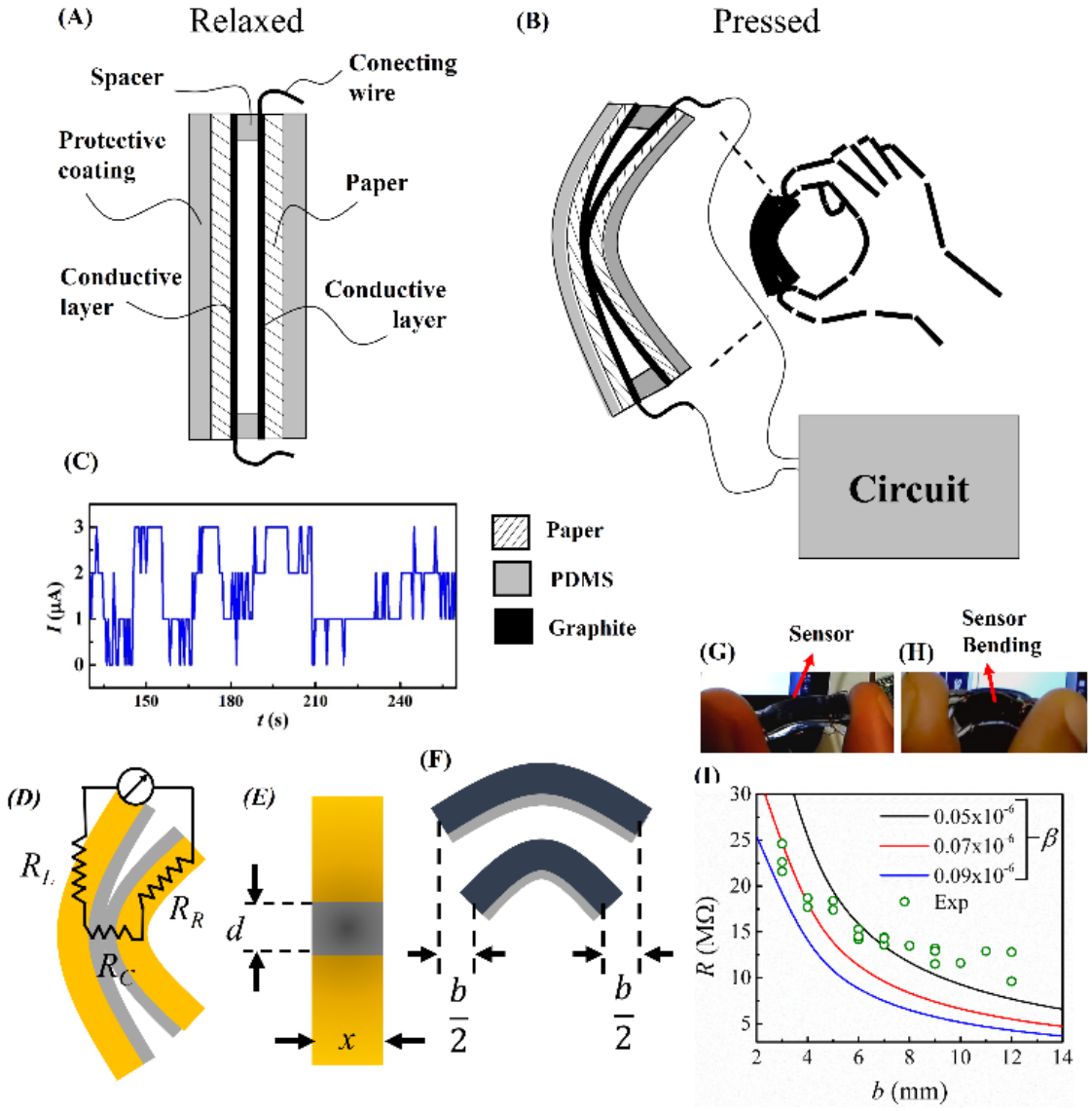

Figure 4.6: Detection of hand-tremor using the resistive pad. Image (A) shows the sensor that detects the hand tremor. Image (B) shows the mechanism of the sensor. Image (C) shows the fluctuation of the current due to hand tremors which can be used for quantification of tremors. Images (D) and (E) show the circuit model and front view of the sensor in a bent condition. Image (F) illustrates the quantification of bending schematically. The images (G) and (H) shows the real images of sensors in related and bent condition, respectively. Image (I) shows the theoretical (solid line) and experimental (scattered points) response of the sensor with the bending. The theoretical data in the image (I) are plotted for different values of β .

4.3.2 Hand Tremor Detector

Interestingly, the resistive touchpad could be employed to detect the hand tremors[57] linked to the neurological diseases like Parkinson's disease with some minor adjustments in the design. Images (A) and (B) Figure 4.6 show that when the touchpad was held vertically and pressed in such a manner that the entire embodiment bent, it could also generate electrical responses as shown in the image (C). Images (D) – (F) show the schematic illustration of the working along with a simplified circuit model and the quantification of bent in this case. Once the sensor was bent by index and thumb fingers, as shown in images (B), (G), and (H), the graphite layers came in contact and allowed the current to flow. Since the resistance depended upon the area of contact, a fluctuation in the force of bending due to the tremors in hand also varied the flow of current, which was detected by a digital multimeter (MASTECH M92A(H)), as shown in the image (C).

Similar to the previous section, image (D) shows the side view and a simplified circuit model for this sensor. This sensor also works based on the change in touch area due to bending. Image (E) shows the touch area from the front side. To understand the resistive response of a touch location upon bending, a simplified circuit model, similar to touchpad has been introduced where the output electrical resistance (R) of a pressed touch location has three major components, such as (i) left electrode resistance (R_L), (ii) contact resistance (R_C), and (iii) right electrode resistance (R_R). The resistances were connected in series to obtain the output resistance as,

$$R = R_L + R_C + R_R . \quad (4.5)$$

As the left and right electrode materials and positions were fixed during bending, the change in the resistance upon bending was assumed due to the contact resistance (R_C) only. Thus, the resistance can be rewritten as.

$$R = R_L + R_R + \rho\left(l/A_C\right). \quad (4.6)$$

As the contact area (A_C) in this situation was assumed to be rectangular as the spacers in this case were only in the top and bottom side of the sensor. Thus, $A_C = (x \times d)$, where x and d are the width and height of the contact area, respectively. We assumed that the width was constant while the height changed with bending, b. Image (F) shows the measurement of the bending, b, of the sensor in this study. Substituting the contact area in Eq. (4.6),

$$R = R_L + R_R + \rho l/(x \times d). \quad (4.7)$$

In Eq. (4.7), all the parameters are constant, however, only d changes with b. To simplify the calculation and find a correlation between the bending and response of the sensor, a linear relationship between the bending and the height of contact area was assumed, $d \propto b \Rightarrow d = \beta b$, where β is the proportional constant. Substituting the value of d, the Eq. (4.7) can be written as,

$$R = R_L + R_R + (\rho l/x) \times (\beta b)^{-1}. \quad (4.8)$$

Eq. (4.8) gives a theoretical basis for the change in the resistance in a sensor upon bending. Images (G) and (H) show the real images of the sensor in relaxed and bent condition, respectively. The value of R_C from Eq. (4.8) has been plotted as the solid lines in the image (I) of Figure 4.6 considering the order of the magnitude of β to be 10^{-8}. The experimental resistance values for a sensor with different bending were

also plotted as symbols where the value of $(R_L + R_R)$ was considered to be ~10 kΩ. From the plots in the image (I), it can be observed that the values are well aligned with the theoretical response.

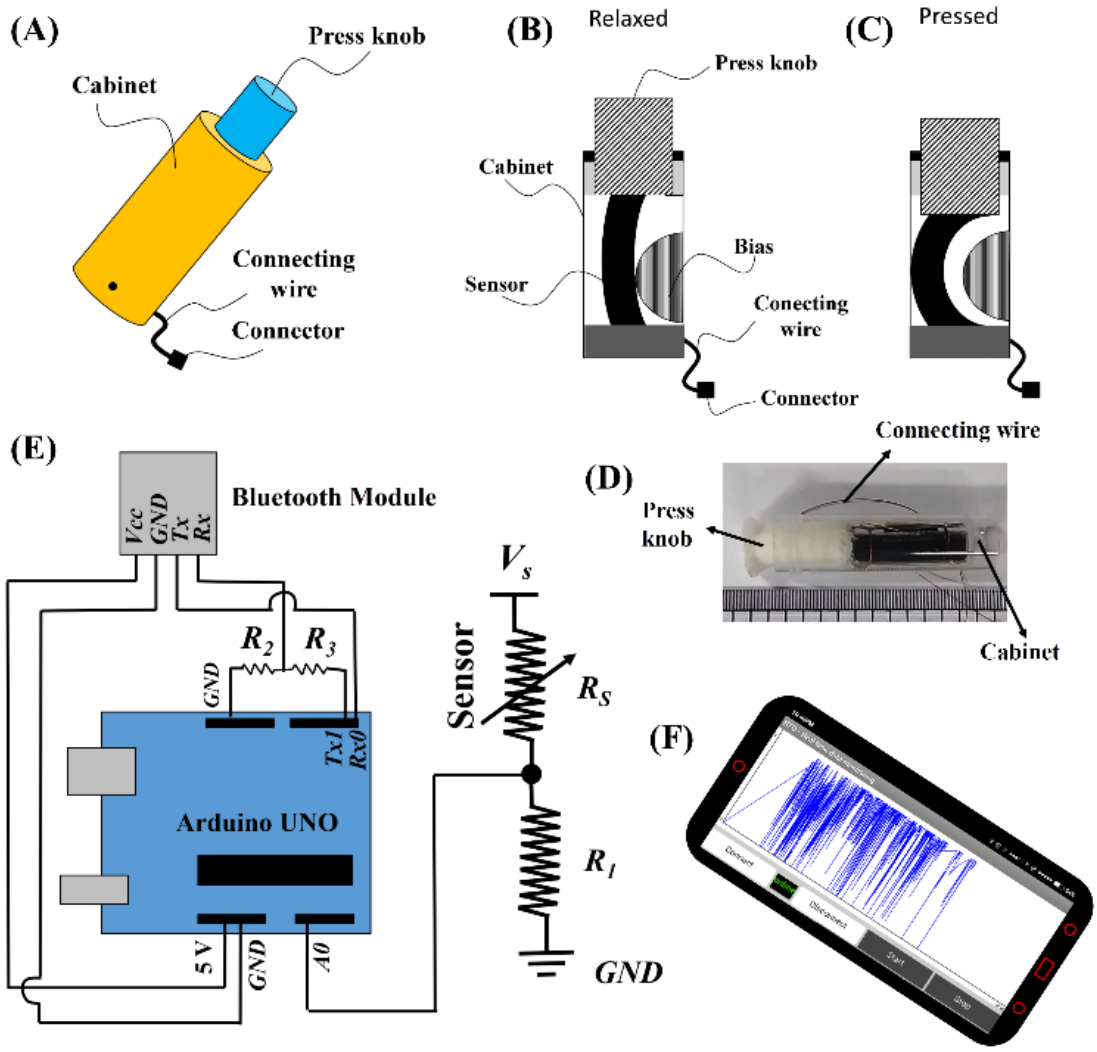

Figure 4.7: The device plan of the prototype. Image (A) shows the outside getup of the proposed device. The images (B) and (C) show the cross-sectional image of the prototype under relaxed and pressed conditions. The mechanical 'bias' in the embodiment ensures that the sensor bend towards left when the 'knob' at the top is pressed. Image (D) shows an image of the prototype. The electrical connect at the bottom connects the sensor to the controller unit, as shown in the image (E). Image (F) shows the fluctuation of the current due to hand tremors are transferred to the mobile interface with the help of the Bluetooth module integrated to the controller unit.

The fluctuations of current could easily be quantified and correlated to the hand tremors. For this purpose, a proof-of-concept prototype was developed which includes a grasping mean for holding by the user with a resiliently biased sensing unit to put pressure through fingers. The grasping mean contained a press-knob having an operative communication with a pressure sensitive sensor. The pressure sensor was configured to translate applied force on the pressing unit through the user's fingers to generate an electronic signal. With the variation in the applied pressure on the pressing unit by the user's fingers during the hand, tremor caused a change in the translated electronic signal, which was correlated in a connected processing unit with the hand tremor level of the user.

Image (A) in Figure 4.7 shows a schematic illustration of the handheld detection unit. The cross-sectional images under relaxed and pressed condition are shown in images (B) and (C), respectively. The press-knob was pressed by the user for detection of the tremor with the help of the flexible resistive sensor for detection of the change in bending. The images (B) and (C) show that the prototype contained a mechanical bias in the form of a hump structure, which ensured the flexible pressure sensor to bent always towards the left side. A freely movable support was provided on top of the housing while the press-knob was fixed with the support. The entire arrangement of press-knob with the movable support was attached to the top of the detection unit. When the knob was pressed, the flexible sensor was compressed to bend it leftwards, as shown in the image (C). During the release of the pressure, the knob to go back to its original position due to the upward force released by the flexible bent sensor, as shown in the image (B). The leftward bend

of the sensor caused a variation in the output electrical resistance of the sensor as an indication of the hand tremor. Image (D) shows the real image of the detection unit. Image (E) illustrates a preferred circuit representation of the processing unit.

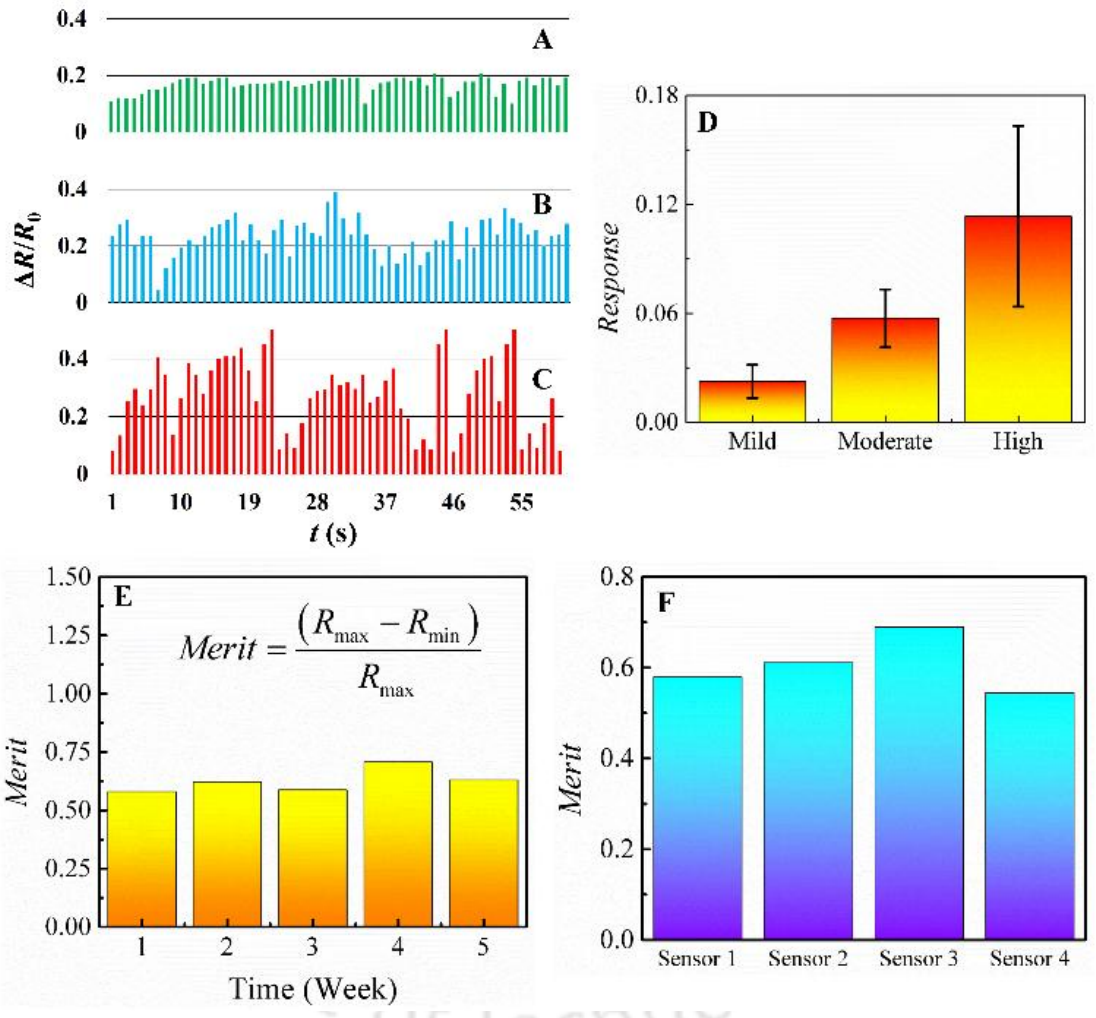

Figure 4.8: The images show the variations in the normalized resistance [$\Delta R/R_0 = (R - R_0)/R_0$] with time ($t$) for (A) mild, (B) moderate, and (C) high hand tremors. Here R_0 refers to the base resistance of the sensor and ΔR is the variation in the resistance. Image (D) shows the response of the sensor for mild, moderate and high tremor. Images (E) and (F) shows the sensor stability analysis. Image (E) shows the stability of the sensor with time and image (F) shows the merit of the four different sensors.

The detection circuit comprises a network of passive resistors comprising a supporting resistor (R_1) and contact area resistor of the sensor (R_s) biased with the

supply voltage. The output electronic signal i.e. the voltage across R_1 and R_S was transmitted to the SPU. The SPU comprised of an Arduino UNO board, a Bluetooth module, and resistors R_2, and R_3. The resistance R_1, R_2, and R_3 are calibrated according to the sensor (R_S) response. The output electronic signal from the detection circuit went to the analog input pin A0 of the Arduino UNO. The signal was then transmitted by the Bluetooth module and was further received by the Android mobile application, which displayed the results on the mobile screen, as shown in the image (E). Image (F) shows a typical display on the mobile interface of the current signal from the present system generated due to hand tremor.

In order to illustrate the working of the detection circuit, the following exemplary situation was considered. For a supply voltage V_S of 5 V and R_1 of 10 kΩ, the resistance of the sensor R_S was expected to change with the variation in pressure produced due to the tremor. For example, in a particular condition, the value of the R_S changed from 15 kΩ to 8 kΩ due to the increase in surface area between the two conductive layers. Thus, the voltage across the sensor R_S, $(R_S/(R_S + R_1)) \times V_S$, varied from 3 V to 2.22 V. This fluctuation of the voltage went to the analogue input A0 before converted to a digital signal and displayed on the mobile interface.

The prototype developed in Figure 4.7 was employed to measure the mild, moderate, and high hand tremors, as described in plots (A), (B), and (C) of Figure 4.8. In case of mild tremor, the normalized resistance ($\Delta R/R_0$) values were found to be less than 0.2 whereas $\Delta R/R_0$ values went beyond 0.2 in case of the moderate tremor. However, for the higher hand tremors, $\Delta R/R_0$ values went well beyond 0.4.

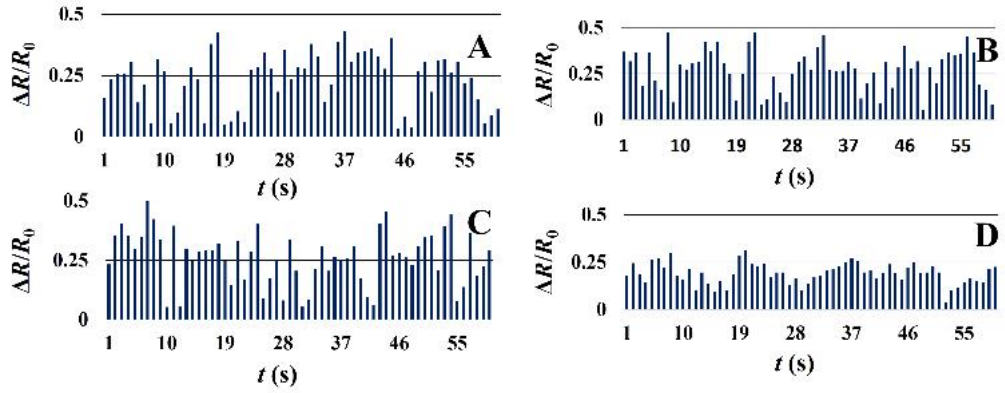

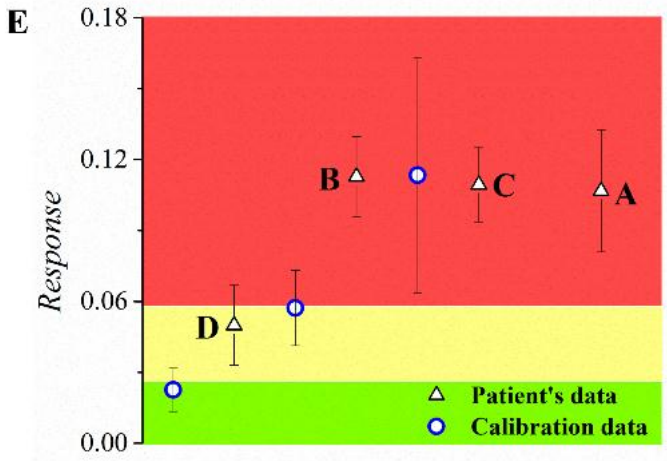

F

Response, $\sigma = \sqrt{\frac{\sum_{i=1}^{n}(R_N - \overline{R_N})^2}{n-1}}$	Severity $= \sqrt{\frac{\sum_{i=1}^{n}(\sigma - \overline{\sigma})^2}{n-1}}$	Implication
Low	Low	Healthy
Low	High	Initial Stage
High	Low	Severe
High	High	Very Severe

Figure 4.9: This images (A – D) show the variation in $\Delta R/R_0$ with time *t* for four different patients (A – D) having a hand tremor. Plot (E) shows the calculated response of the sensor for patients (A – D). Table (F) shows the descriptions of response and corresponding implications.

The plots indicated that the magnitude of $\Delta R/R_0$ could be one crucial parameter to differentiate the levels of tremor. It may be noted here that the tremor

characterizations reported in Figure 4.8 were of the hands of healthy peoples around the laboratory.

The tremors were generated by stressing the hand with different types of exercises to develop the mild, moderate, and high tremors. Image (D) summarizes the responses of the sensor for mild, moderate and high tremors. The response was calculated by taking the average of standard deviations of the $\Delta R/R_0$ values in the image (A), (B), and (C) for each 10 s as shown in Eq. 4.9. Further, the severity of the response represents the standard deviation of 6 consecutive response values as shown in Eq. 4.10.

$$\mathrm{Response}, \sigma = \sqrt{\frac{\sum_{i=1}^{n} \left(R_N - \overline{R_N}\right)^2}{n-1}}, \tag{4.9}$$

$$Severity = \sqrt{\frac{\sum_{i=1}^{n} \left(\sigma - \overline{\sigma}\right)^2}{n-1}}. \tag{4.10}$$

To understand the performance and quality of a fabricated sensor, the merit of the sensors was calculated using the following formula, $Merit = (R_{max} - R_{min})/R_{max}$, where R_{max} and R_{min} is the maximum and minimum resistance of the sensor during bending, respectively. Image (E) and (F) show the stability analysis of the sensor. The stability of the sensor was tested by comparing the merit of the sensor with time and different batches of sensors as shown in images (E) and (F), respectively. The images confirmed the stability and repeatability of the sensor signals in measuring the different types of hand tremors.

The results obtained in Figure 4.8 prompted us to test the prototype to detect the hand tremors of the real-life patients. Figure 4.9 shows the response of the sensor for four different patients (A – D). The detection, determination, and differentiation of tremor the levels were quantified by response and severity, as shown in the image (E). The calibration was performed by measuring the response and severity of the sensor as indicated in image (D) of Figure 4.8. The color of the image (E) shows three different stages of a user, where red signifies a severe condition, yellow signifies a condition that needs medical attention, and green signifies healthy condition. In this image (E), the higher value of response and severity was found to be an indication of a medical emergency. In principle, a higher error bar indicated more change in resistances at every 10 s interval and thus corresponded to even a higher severity. However, a lower error bar in this regard indicated a relatively steady tremor level. Table F summarizes a typical healthy, early stage, severe, and very severe stages of hand tremors obtained from the data analysis of the proposed prototype.

4.4. Conclusions

An economic and flexible resistive touchpad was fabricated employing pencil graphite and polymer-coated paper substrates. The pad could detect and differentiate touch or press locations based on the variation in the contact area of the inner graphitic layers, which generated different output electrical resistance based signals at the different touch locations. A simplified circuit model was shown to uncover the theoretical basis of the working principle, which was found to be very similar to the experimentally obtained values. The stability, repeatability, and reliability of the touch sensations were demonstrated based on a large number of trials.

A minor adjustment of the design of the pad led to a POCT device to detect the hand tremors of the neurological disorders such as the Parkinson's disease. The handheld prototype contained a paper-pad sensor, a signal processing unit, and a mobile display. The variation in the response of the resistive sensor was able to differentiate mild, moderate and high hand tremor levels at the human fingers. The response and severity analysis from the device were correlated to the different stages, namely, emergency, moderate, and healthy tremors for the real-life patients. While the working principle was explained in a similar manner as the touchpad, the stability and reliability were studied for a large number of data set.

The proposed proof-of-concept prototype has shown significant potential in the development of the POCT device for the early and chronic stage detections of various neurological disorders such as Parkinson's or Wilson's disease.

References

1. F. McGlone and D. Reilly, *Neuroscience & Biobehavioral Reviews*, 2010, **34**, 148-159.
2. R. N. Aguilar and G. C. M. Meijer, Proceedings of IEEE Sensors, 2002.
3. R.-Z. Li, A. Hu, T. Zhang and K. D. Oakes, *ACS Applied Materials & Interfaces*, 2014, **6**, 21721-21729.
4. M. Segev-Bar, A. Landman, M. Nir-Shapira, G. Shuster and H. Haick, *ACS Applied Materials & Interfaces*, 2013, **5**, 5531-5541.

5. R. Wimmer and P. Baudisch, presented in part at the Proceedings of the 24th annual ACM symposium on User interface software and technology, Santa Barbara, California, USA, 2011.

6. A. D. Mazzeo, W. B. Kalb, L. Chan, M. G. Killian, J.-F. Bloch, B. A. Mazzeo and G. M. Whitesides, *Advanced Materials*, 2012, **24**, 2850-2856.

7. C.-C. Kim, H.-H. Lee, K. H. Oh and J.-Y. Sun, *Science*, 2016, **353**, 682.

8. L. Viry, A. Levi, M. Totaro, A. Mondini, V. Mattoli, B. Mazzolai and L. Beccai, *Advanced Materials*, 2014, **26**, 2659-2664.

9. M. Bhattacharjee, V. Pasumarthi, J. Chaudhuri, A. K. Singh, H. Nemade and D. Bandyopadhyay, *Nanoscale*, 2016, **8**, 6118-6128.

10. C.-T. Wang, K.-Y. Huang, D. T. W. Lin, W.-C. Liao, H.-W. Lin and Y.-C. Hu, *Sensors*, 2010, **10**, 5054.

11. A. C. Siegel, S. T. Phillips, B. J. Wiley and G. M. Whitesides, *Lab on a Chip*, 2009, **9**, 2775-2781.

12. L. Yang, A. Rida, R. Vyas and M. M. Tentzeris, *IEEE Transactions on Microwave Theory and Techniques*, 2007, **55**, 2894-2901.

13. H. Zhu, Z. Fang, C. Preston, Y. Li and L. Hu, *Energy & Environmental Science*, 2014, **7**, 269-287.

14. J. Lessing, A. C. Glavan, S. B. Walker, C. Keplinger, J. A. Lewis and G. M. Whitesides, *Advanced Materials*, 2014, **26**, 4677-4682.

15. L. Nyholm, G. Nyström, A. Mihranyan and M. Strømme, *Advanced Materials*, 2011, **23**, 3751-3769.

16. Z. Fang, H. Zhu, C. Preston, X. Han, Y. Li, S. Lee, X. Chai, G. Chen and L. Hu, *Journal of Materials Chemistry C*, 2013, **1**, 6191-6197.

17. A. Darwish and A. E. Hassanien, *Sensors*, 2011, **11**.

18. *United States Pat.*, US2002/0101407A1, 2001.

19. S. Takahashi, B. J. Lee, J. H. Koh, S. Saito, B. H. You, N. D. Kim and S. S. Kim, *SID Symposium Digest of Technical Papers*, 2009, **40**, 563-566.

20. *United States Pat.*, US2009/0114457A1, 2007.

21. M. Céline, C. Caroline, M. Eléonore, M. Jean-François, C. Alexandre and S. Jean-Pierre, *Nanotechnology*, 2013, **24**, 215501.

22. D.-K. Kim, J.-H. Kim, H.-J. Kwon and Y.-H. Kwon, *ETRI Journal*, 2010, **32**, 722-728.

23. C. Conte, A. Ranavolo, M. Serrao, A. Silvetti, G. Orengo, S. Mari, F. Forzano, S. Iavicoli and F. Draicchio, *International Journal of Industrial Ergonomics*, 2014, **44**, 413-420.

24. J. M. Crow, *New Scientist*, 2010, **208**, 40-43.

25. A. K. Leeper, *SID Symposium Digest of Technical Papers*, 2002, **33**, 187-189.

26. D. Kelaher, T. Nay, B. Lawrence, S. Lamar and C. M. Sommerich, *Applied Ergonomics*, 2001, **32**, 101-110.

27. M. H. Ahn, E. S. Cho and S. J. Kwon, *Vacuum*, 2014, **101**, 221-227.

28. *United States Pat.*, US8253710B2, 2009.

29. M. Bhattacharjee, H. B. Nemade and D. Bandyopadhyay, *Biosensors and Bioelectronics*, 2017, **94**, 544-551.

30. S. Bae, H. Kim, Y. Lee, X. Xu, J.-S. Park, Y. Zheng, J. Balakrishnan, T. Lei, H. Ri Kim, Y. I. Song, Y.-J. Kim, K. S. Kim, B. Özyilmaz, J.-H. Ahn, B. H. Hong and S. Iijima, *Nature Nanotechnology*, 2010, **5**, 574.

31. D. S. Hecht, D. Thomas, L. Hu, C. Ladous, T. Lam, Y. Park, G. Irvin and P. Drzaic, *Journal of the Society for Information Display*, 2009, **17**, 941-946.

32. M. Layani, A. Kamyshny and S. Magdassi, *Nanoscale*, 2014, **6**, 5581-5591.

33. L. Chico, V. H. Crespi, L. X. Benedict, S. G. Louie and M. L. Cohen, *Physical Review Letters*, 1996, **76**, 971-974.

34. P. L. McEuen, *Nature*, 1998, **393**, 15.

35. S.-H. Hur, O. O. Park and J. A. Rogers, *Applied Physics Letters*, 2005, **86**, 243502.

36. M. Dragoman, E. Flahaut, D. Dragoman, M. A. Ahmad and R. Plana, *Nanotechnology*, 2009, **20**, 375203.

37. N. Kurra, D. Dutta and G. U. Kulkarni, *Physical Chemistry Chemical Physics*, 2013, **15**, 8367-8372.

38. N. Kurra and G. U. Kulkarni, *Lab on a Chip*, 2013, **13**, 2866-2873.

39. Y.-L. Tai and Z.-G. Yang, *Journal of Materials Chemistry*, 2011, **21**, 5938-5943.

40. *India Pat.*, 201631017054A, 2016.

41. N. Kurra, J. Park and H. N. Alshareef, *Journal of Materials Chemistry A*, 2014, **2**, 17058-17065.

42. B. Scrosati, *Nature Nanotechnology*, 2007, **2**, 598.

43. S. K. Mahadeva, K. Walus and B. Stoeber, *ACS Applied Materials & Interfaces*, 2015, **7**, 8345-8362.

44. H. Sirringhaus, T. Kawase, R. H. Friend, T. Shimoda, M. Inbasekaran, W. Wu and E. P. Woo, *Science*, 2000, **290**, 2123.

45. R. R. Kamath and M. J. Madou, *Analytical Chemistry*, 2014, **86**, 2963-2971.

46. X. Qiu, J. Zhang, Y. Li, C. Zhang, D. Wang, W. Zhu, F. Li, S. Ge, N. Xia and S. Qian, *Microsystem Technologies*, 2018, **24**, 2007-2015.

47. K. Chen, W. Gao, S. Emaminejad, D. Kiriya, H. Ota, H. Y. Y. Nyein, K. Takei and A. Javey, *Advanced Materials*, 2016, **28**, 4397-4414.

48. J. H. Chin and N. Vora, *Neurology*, 2014, **83**, 349.

49. M. F. Brin, K. E. Lyons, J. Doucette, C. H. Adler, J. N. Caviness, C. L. Comella, R. M. Dubinsky, J. H. Friedman, B. V. Manyam, J. Y. Matsumoto, S. L. Pullman, A. H. Rajput, K. D. Sethi, C. Tanner and W. C. Koller, *Neurology*, 2001, **56**, 1523.

50. R. J. Elble and J. E. Randall, *Electroencephalography and Clinical Neurophysiology*, 1978, **44**, 72-82.

51. D. J. Brooks, *Journal of Neurology, Neurosurgery & Psychiatry*, 2002, **72**, i10.

52. D. A. Bennett, L. A. Beckett, A. M. Murray, K. M. Shannon, C. G. Goetz, D. M. Pilgrim and D. A. Evans, *New England Journal of Medicine*, 1996, **334**, 71-76.

53. J. Jankovic, F. Cardoso, R. G. Grossman and W. J. Hamilton, *Neurosurgery*, 1995, **37**, 680-687.

54. Y.-J. Hong, I.-J. Kim, S. C. Ahn and H.-G. Kim, *Simulation Modelling Practice and Theory*, 2010, **18**, 446-455.

55. *United States Pat.*, US8994657, 2004.

56. H. Dai, P. Zhang and T. C. Lueth, *Sensors (Basel, Switzerland)*, 2015, **15**, 25055-25071.

57. *India Pat.*, 201731018530A, 2017.

II. Paper Based Electronic Sensors

CHAPTER 5

Nano-Enabled Paper Humidity Sensor for Mobile Based Point-of-Care Lung Function Monitoring

Contents

ABSTRACT 131
5.1. Introduction 132
5.2. Experimental Section 136
5.2.1 Materials 136
5.2.2 Synthesis and Characterizations of Nanoparticles 136
5.2.3 Fabrication of the Sensor, Micro-heater and their Integration 139
5.2.4 Experiments to Create Environment with different relative humidity 140
5.2.5 Description of Circuits for Heating and LEDs 141
5.2.6 Methods 144
5.3. Results and Discussion 145
5.3.1 Response of Paper Humidity Sensor 145
5.3.2 Response of LFM-POCT Device 149
5.3.3 LFM-POCT Device Architecture 152
5.3.4 Experimental and Simulation to Study the Dependence of Flowrate 153
5.3.5 Computational Analysis of Adsorption 154
5.3.6 Effect of Adsorption on CdS 157
5.4. Conclusions 161
References 162

भारतीय प्रौद्योगिकी संस्थान गुवाहाटी
Indian Institute of Technology Guwahati

ABSTRACT

The frequency of breathing and peak flow rate of exhaled air are necessary parameters to detect chronic obstructive pulmonary diseases (COPDs) such as asthma, bronchitis, or pneumonia. We developed a lung function monitoring point-of-care-testing device (LFM-POCT) consisting of a mouthpiece, paper-based humidity sensor, micro-heater, and real-time monitoring unit. The mouthpiece of optimal length was ensured that the exhaled air was focused on the humidity-sensor. The resistive relative humidity sensor was developed using a filter paper coated with nanoparticles, which could easily follow the frequency and peak flow rate of the human breathing. Adsorption followed by condensation of the water molecules of the humid air on the paper-sensor during the forced exhalation reduced the electrical resistance of the sensor, which was converted to an electrical signal for sensing. A micro-heater composed of a copper-coil embedded in a polymer matrix helped in maintaining an optimal temperature of the sensor, which ensured that water condensed only during forcible breathing and the sensor recovered rapidly after the exhalation was complete by desorption of water molecules. Two types of real-time monitoring units were integrated into the device based on light emitting diodes (LEDs) and smartphones. The LED-based unit displayed the diseased, critical, and fit conditions of the lungs by flashing LEDs of different colors. In comparison, for the mobile-based monitoring unit, an application was developed employing an open source software, which established a wireless connectivity with the LFM-POCT device to perform the tests.

This chapter is published in *Biosens. Bioelectron.* **94**, 544-551 (2017).

5.1. Introduction

Point-of-care testing (POCT) devices have become an integral part of modern life because of their role in improving the life expectancy through early detection of many irreversible health hazards. For example, monitoring of blood pressure,[1] body-mass-index, body-weight,[2] blood sugar,[3] or pregnancy[4] is now possible during the daily activities employing these gadgets. In particular, the aged, children, and the disabled persons have been immensely benefitted by the POCT devices because of their utility in evaluation and stabilization of health conditions during the critical hours before consulting the physicians. Although the development of the POCT gadgets has been rapid,[5] still there are numerous biomarkers, which require immediate attention. For example, a reliable, portable, economical, and a user-friendly POCT device capable of monitoring the lung condition can be one important addition.[6] Herein we report the development of a paper-based Lung-Function-Monitoring POCT (LFM-POCT) device. We employ a long-standing knowledge that the exhaled air from a human breath contains ~90 % – 100 % humidity[7] and then exploit the specialties of nanoparticles in high-precision sensing of the moisture to develop the device. The device can be operated with the help of a smartphone for immediate test and analysis of lung condition at the patient site.

In general, pulmonary function tests (PFT) are performed for the prognosis of the chronic obstructive pulmonary diseases (COPD) such as asthma, bronchitis, or pneumonia.[8] Reversible airway obstruction is the most common symptom of COPD,[9] which are estimated employing the peak flow meter[10] or spirometer.[11] The linear or in-line peak flow meter consists of a cylindrical housing, which has a restrictor near the inlet and an indicator that moves with the force of exhaled air, which is evaluated employing a piston-spring arrangement inside the housing.[12] For the rotary peak flow meters, a vane

arrangement attached to a torsion-spring inside a rectangular housing helps in measuring the lung function parameters through an indicator.[13] The digital peak flow meters are battery powered, relatively more accurate, and user-friendly.[14] Alternatively, spirometers are employed to evaluate the volume of air inhaled or exhaled, length of breathing, contaminants in breathing, length of obstructive and restrictive ventilation patterns, and effects of medication, among others. Presently, different varieties of spirometers[11] are available such as (a) plethysmograph – suitable for measuring the lung volume; (b) pneumo-tachometer – measures the flow rate of breathing; and (c) digital spirometers – electronically compute air flow rates. Apart from the peak flow meters, different other spirometric techniques are also available, which face the limitations associated with portability or economy or reliability or stability, essential for the development of any POCT device.[11]

In the present scenario, although efforts have been made to commercially develop some POCT versions of peak flow meters[10] and spirometers,[11] they are either costly or time-consuming or not very accurate or require medical experts for operation and analysis. Importantly, most of the reliable techniques to monitor the lung condition are available through centralized agencies to the large section of the patients. In many situations, at the time of diagnosis, the natural airway obstructions go unnoticed for a patient because COPD can take place during the critical hours of the day when the facilities are unavailable. Consequently, more intensive bronchial challenge tests (BCT) are performed[15] in which the patients are nebulized with methacholine or histamine to artificially provoke bronchial constriction, which is then quantified by the peak flow meter or spirometry.

In view of the above, we report the development of a paper-based LFM-POCT device, which can perhaps stage a paradigm shift in the lung fitness measurement. In the recent past, exploiting the variations in the size-dependent properties of the nanomaterials, many sensors suitable for the healthcare devices have been developed.[16] In the recent years, the sensors for the healthcare appliances have also been rapidly extended to the newer domains such as microfluidics,[17-21] micro-propellers,[22-25] a thin film based,[26] lab-on-a-chip,[27, 28] and MEMS,[29-31] Diverse nanoscale particles,[32, 33] wires,[34, 35] tubes,[36] or rods[37] of different types of materials such as semiconductors,[34] carbon,[36] graphene,[38] graphene oxide,[39, 40] metal oxides,[35, 38] polymers,[41] and nanocomposites[39] have been employed to fabricate high-precision humidity sensors by measuring the variations in electrical parameters such as resistance,[42] impedance,[43] and capacitance[44, 45] with humidity. In this direction, cadmium sulfide (CdS) nanoparticles (CdSNPs) have been found to be a wonder material,[46] which is not only capable of humidity sensing[32, 33] but also extensively employed in photovoltaics[47, 48], optoelectronics,[49] bio-sensing,[50] and gas[51-53] or alcohol[54, 55] detection.

In the present work, we developed a humidity sensor, which could follow the moisture content of the exhaled air issuing out of human breathing. The proposed LFM-POCT device comprised of four components, (i) a mouthpiece to focus exhaled air on the sensor, (ii) a resistive paper-sensor integrated to the mouthpiece for moisture detection, (iii) a micro-heater integrated with the sensor to maintain an optimal temperature, and (iv) a real-time monitoring unit to display lung condition. Figure 5.1 shows the humidity sensor in which a paper-substrate was initially coated with gold nanoparticles (AuNPs) to make it thermally and electrically conducting before depositing the CdSNPs. The CdSNPs could rapidly adsorb water molecules from the moisture,[56] which enabled rapid humidity

sensing. The patch of CdSNPs on the paper-surface was connected to a pair of silver (Ag) electrodes, which were integrated with an external electrical circuit to measure the change in the electrical conductivity with the variation in relative humidity (*RH*). The sensor was integrated with a micro-heater, which improved the recovery time of the sensor during humidity sensing.[57] We developed two different types of monitoring units based on, (a) light emitting diodes (LEDs) – where the illumination of LEDs indicated the lung condition and (b) mobile interface – where an application was developed using an open source software, which helped in the operation of the LFM-POCT device through the wireless connection with a smartphone. The integration of the LFM-POCT device and application in the mobile phone helped with real-time testing, monitoring, analysis, and data storage of the lung function parameters through smartphones.

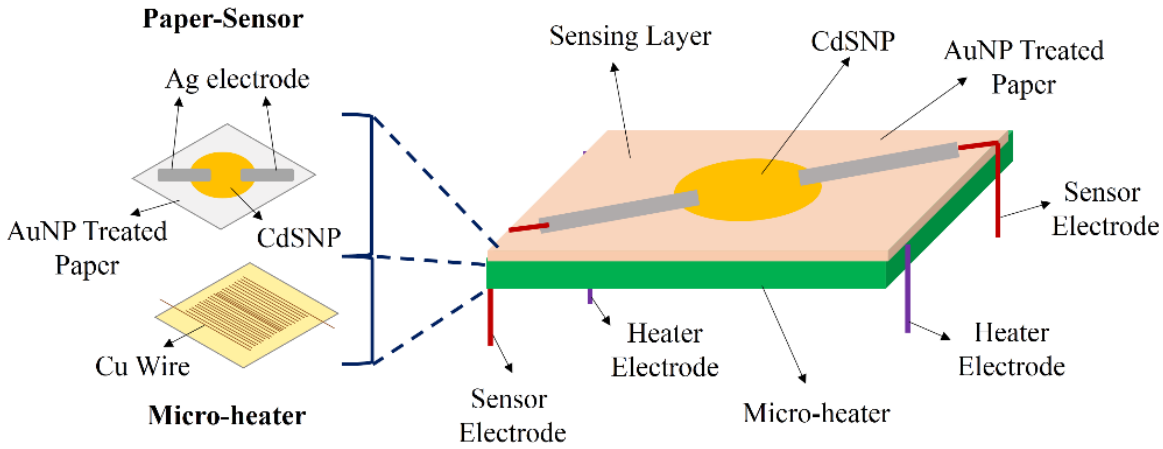

Figure 5.1: Schematic diagram showing the components of the paper-based humidity sensor. The image shows the coating of the CdSNPs and Ag electrodes, which was integrated with the micro-heating arrangement. The micro-heater composed of a Cu coil embedded inside a PDMS matrix is shown in the side.

5.2. Experimental Section

5.2.1 Materials

Cadmium chloride ($CdCl_2$), sodium sulphide (Na_2S) pellets, and methanol (99.5 %) were procured from Merck (India). Poly-dimethylsiloxane (PDMS) was obtained from Dow Corning, India (SYLGARD® 184 kit). We purchased Cu and double-sided tapes from the local vendors. The chemicals were of analytical grade and employed in the experiments without further purification. The Milli-Q grade water was used for cleaning and also to prepare the solutions.

5.2.2 Synthesis and Characterizations of Nanoparticles

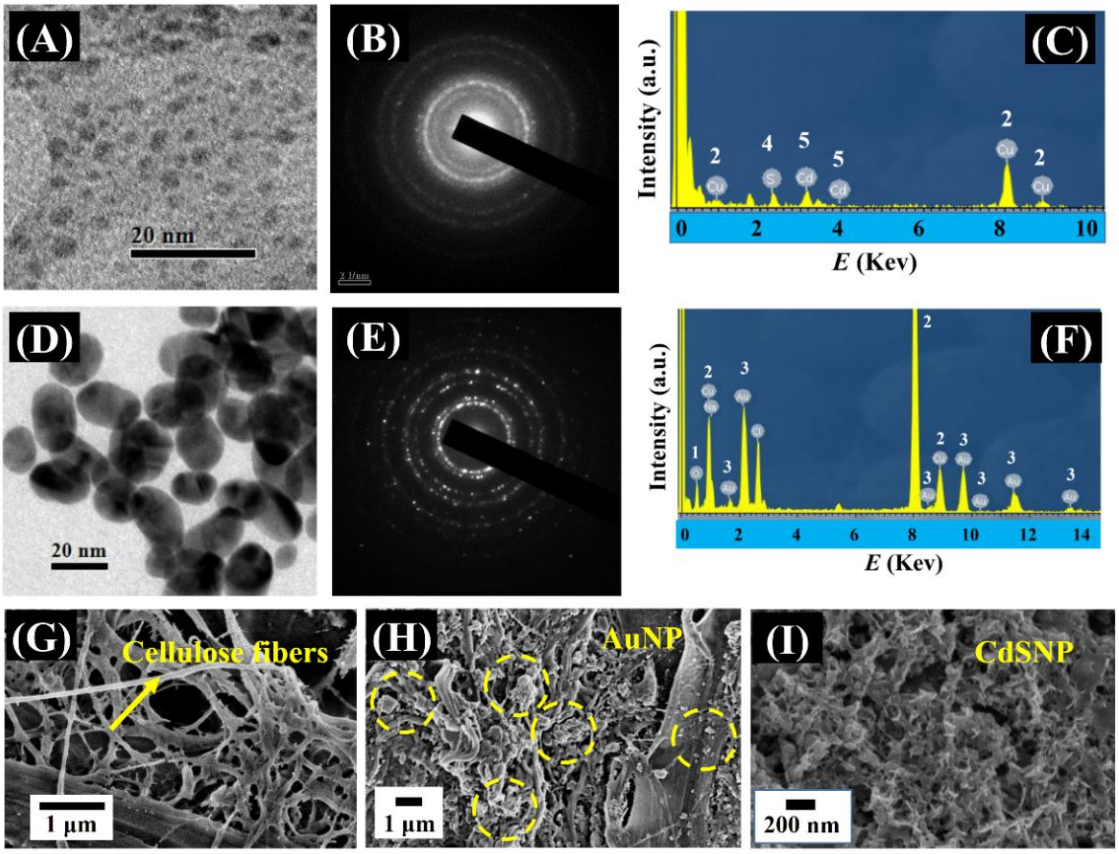

Figure 5.2: The images (A) – (C) show the TEM snapshot, SAED patterns, and EDS of the CdSNPs. The images (D) – (F) show the TEM snapshot, SAED patterns, and EDS of the synthesized AuNPs. Images (G) and (H) show the FESEM snapshot of the paper surface and AuNPs embedded on the paper surface, respectively and image (I) shows the FESEM image of the CdSNPs deposited on the AuNP treated paper surface.

The CdS nanoparticles (CdSNP) were synthesized using the chemical pathway[58] avoiding the other costly chemical vapor or bath deposition techniques[33-35] to keep the fabrication cost to the lower side. The $CdCl_2$ salt was used as the source for Cd^{2+} ions, the $Na_2S.9H_2O$ salt was used as the source for S^{2-} ions and methanol was the capping agent. In the beginning, 20 ml of 0.1M NaOH solution was prepared, which was then slowly added to 2.5 ml of methanol. The resultant solution was sonicated for 1 h in the ultra-sonication bath. Thereafter, the freshly prepared 0.1M Na_2S solution was added to the solution drop by drop with vigorous stirring. Then, 0.1M freshly prepared $CdCl_2$ solution was added to the previous solution with vigorous stirring, which turned the colorless solution to a yellowish one.

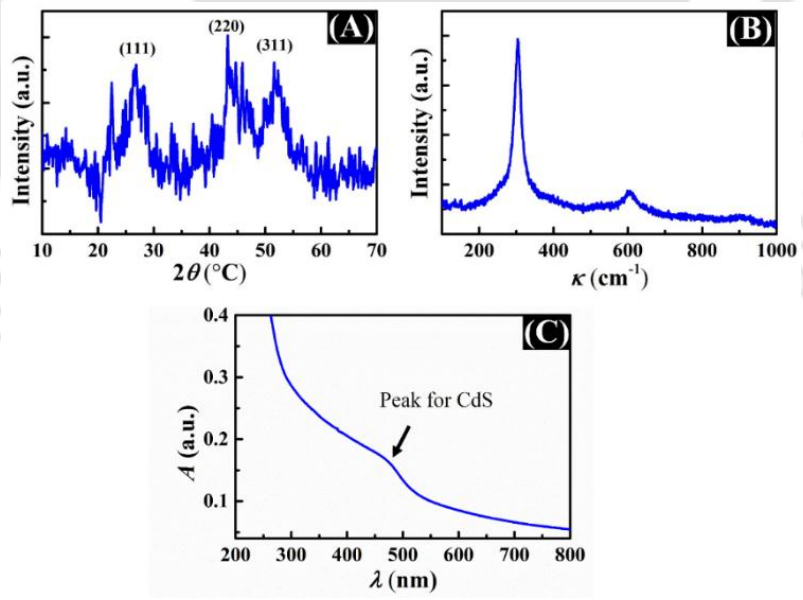

Figure 5.3: Images (A) and (B) show the XRD analysis and Raman spectroscopy of CdSNPs with the characteristics peaks of CdS and image (C) shows the typical UV-Vis spectroscopy data of CdSNPs.

Figures 5.2A – 5.2C show the transmission electron microscope (TEM) image, selected area electron diffraction (SAED) patterns, and energy dispersive spectroscopy (EDS) of the CdSNPs, which confirmed that the sizes were ~5 nm. Figure 5.3 shows the x-ray diffractometer (XRD), Raman and UV-Vis spectroscopy characterizations of the CdSNPs synthesized here.

The gold (Au) nanoparticles (AuNPs) were synthesized by reduction of the salt $HAuCl_4.3H_2O$.[59] Initially, a 50mM aqueous solution of the salt was prepared (solution I) by mixing the salt and HCl in the equal molar ratio. Thereafter, we prepared another 50mM of $NaBH_4$ solution (solution II) by mixing $NaBH_4$ with 1mM NaOH in the equal molar ratio. A 100 µl of the solution I was then diluted with water to 0.5mM before 300 µl of solution II was added to the diluted solution I with continuous stirring. The change in color from light yellow to orange indicated the formation of AuNPs inside the solution, which turned red after a few minutes of stirring. Figures 5.2D – 5.2F show the TEM image, SAED patterns, and EDS of the AuNPs, which confirmed that the sizes were ~20 nm.

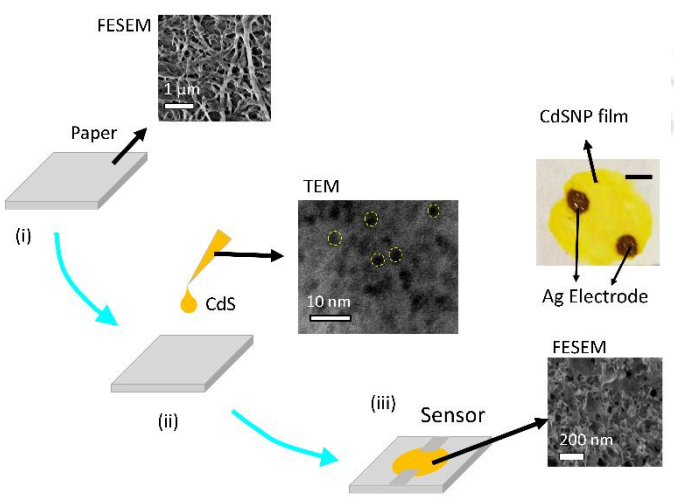

Figure 5.4: This figure shows the fabrication steps (i – iii) of the sensor along with the FESEM image of the paper surface, TEM image of CdSNPs, a photographic image of the fabricated

sensor, and a FESEM image of the paper embedded with CdSNPs. The scale bar in the sensor image is of 1.5 mm.

5.2.3 Fabrication of the Sensor, Micro-heater and their Integration

The filter paper (Whatman catalogue number – 1001 125 grade 1) used for sensor fabrication was pre-treated with AuNP solution for 2 h before drying in hot-air oven. Figure 5.4 shows the step-wise (i-iii) fabrication process of the sensor along with the corresponding FESEM and TEM images. Figures 5.2G and 5.2H show the field emission scanning electron microscope (FESEM) images of the surface morphology of the bare paper-substrate and paper-substrate embedded with AuNPs. Deposition of AuNPs on the paper surface improved the thermal and electrical conductivities, which helped in improving the recovery time of the paper-sensor. Following this, a 50 µl of freshly prepared CdSNPs was dispensed on a piece (1 cm × 1 cm) of an AuNP deposited paper surface using a micropipette before drying for 12 h. A lower volume of CDSNP drop could not make a proper film on the substrate whereas a higher volume forms cracks on the film surface. Figure 5.2I shows the FESEM image of the surface of CdSNP coated paper-substrate embedded with AuNPs. The Ag paste was used to make the electrodes around CdSNP coated paper surface for electrical measurements. The Ag paste was dried for 24 h after coating. Figure 5.1 in the main manuscript shows the arrangement of the paper piece coated with Ag electrodes, which was employed to measure the variation in the electrical resistance across the CdS patch using a multimeter, as described later. The FESEM image of paper substrate shows the cellulose fiber network having ~31 – 38% of porosity with average fiber width of ~150±30 nm. The synthesized CdSNPs of size ~3±2 nm, as shown in TEM image, were then drop casted on the filter paper. A photographic image of the fabricated sensor is shown in the step (iii) of image (A). The effective length between the electrodes in the sensor was ~2±0.6 mm and the electrodes were of circular

shape having diameter of ~1±0.3 mm. The FESEM micrograph of the CdSNPs coated on the paper surface shows a surface having scattered pore size of ~120±20 nm. The thickness of the CdSNP-layer was measured by placing a cross-section of the sensor under optical microscope, which uncovered the average thickness to be ~10-15 µm. The base resistance of the sensor was found to be of the order of 100 MΩ.

The micro-heater was fabricated using copper (Cu) wire of diameter 180 µm and the polymer PDMS. A long Cu wire was coiled in a 1 cm^2 area having 80 turns before embedding it into a PDMS matrix of size 1 cm (length) × 1 cm (width) × 2 mm (height) through replica molding method.[60] The micro-heater was then integrated with the paper with the help of an adhesive, as shown in the Figure 5.1 in the main manuscript. Integrating a battery through an external circuit to the Cu connects of the micro-heater helped in supplying current for joule heating. The heat supplied by the micro-heater was optimized by connecting a DC power supply (Testronix 93C) to flow a known amount of current through it and then evaluating the required surface temperature through the sensor of a hot plate (IKA RCT basic). The effect of different volatile organic compounds such as alcohols were found to be very less in presence of the micro heater as the compounds evaporated at a higher temperature.

5.2.4 Experiments to Create Environment with different relative humidity

In these experiments the relative humidity (*RH)* ranging from 5%, 30%, 48%, 76% to 85% was artificially created around the paper-sensor employing a standard technique.[61] A number of 250 ml of beakers was filled with 50 ml solutions of 96% H_2SO_4, 54% H_2SO_4, 44% H_2SO_4, saturated NaCl, saturated KCl. The beakers were then sealed with paraffin wax tape and kept for 24 h. These solutions provide constant relative humidity (*RH)* about 5%, 30%, 48%, 76%, and 85%, respectively at 30°C.

5.2.5 Description of Circuits for Heating and LEDs

The heating circuit as shown in Figure 5.5 was a square pulse generator, which helped in maintaining the micro-heater temperature to a constant value for long duration. The square wave was generated using the timer IC 555 while the frequency and duty cycles of the generated pulse were maintained by adjusting the values of resistors R_1 and R_2 and the capacitor *C*. A negative temperature coefficient (NTC) thermistor having electrical resistance, R_T, was connected in series to the resistor having electrical resistance, R_1, as a feedback to maintain the temperature of the heating element of electrical resistance, R_h. The resistance of the feedback NTC thermistor decreased with increase in temperature and the duty cycle of the square pulse was adjusted. The 'on' and 'off' times of the square pulse were estimated by, $t_{ON} = 0.693 \times (R_1 + R_2) \times C$ and $t_{OFF} = 0.693 \times R_2 \times C$. The duty cycle was estimated as, $D_c = t_{ON}\left(t_{ON} + t_{OFF}\right)^{-1} = (R_1 + R_2)(R_1 + 2R_2)^{-1}$. Tuning the R_1 and R_2, we could maintain a constant temperature for a long duration when the terminal voltage V_T was applied through a battery.

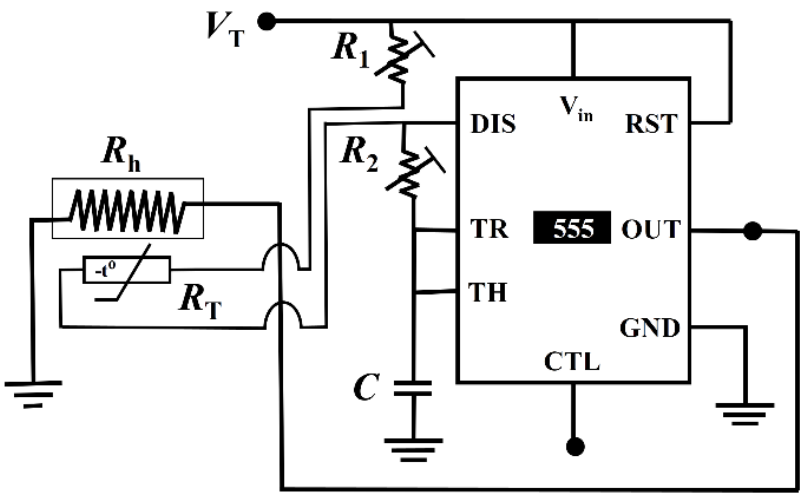

Figure 5.5: The image shows the circuit employed to ensure continuous supply of heat to the paper-sensor while experiments are performed.

The circuit shown in Figure 5.6 had three parts: (I) sensor (R_S) – at the center of the device; (II) heating circuit – in the right side of the sensor, which was associated with the micro-heater (R_h); (III) monitoring circuit – in the left side of the sensor, which helps in displaying the LEDs. Three indicators LEDs (L_R, L_Y, and L_G) are connected to the sensor (R_S) via three variable resistances (R_R, R_Y, and R_G), respectively, in the display circuit, as shown in Figure 5.6. The heating circuit was explained previously in the experimental section, which was a square pulse.

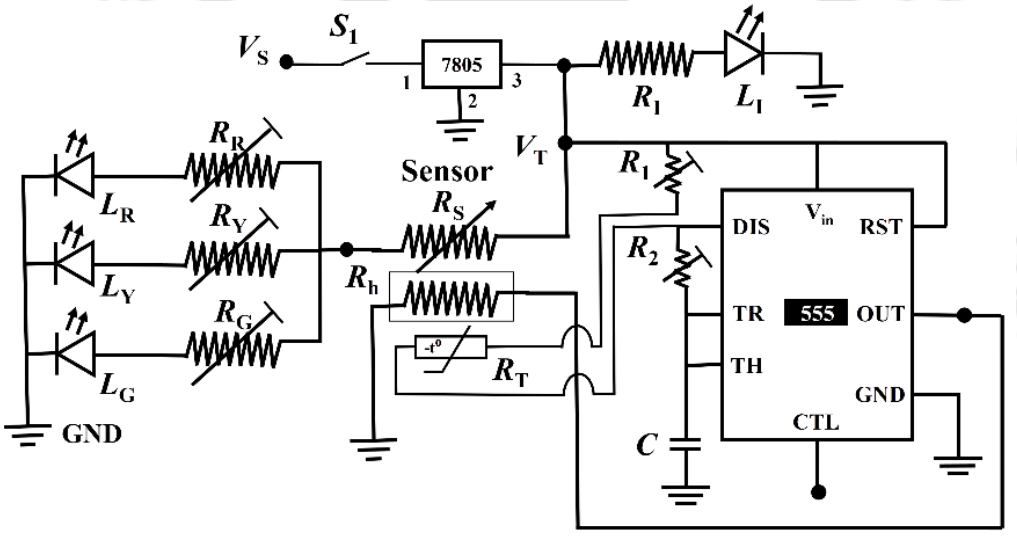

Figure 5.6: The image shows the circuit arrangement for the LED-based real-time monitoring unit.

The frequency and duty cycle of the micro-heater was maintained by adjusting the values of resistors R_1, R_2, and a capacitor *C*. A voltage regulator 7805 was also connected to the supply voltage in order to maintain the constant 5 V supply. The notation S_1 belonged to the place for the ON-OFF switch while L_1 the ON-OFF indicator LED. The notations V_S, V_T and GND denote the supply voltage, terminal voltage, and ground terminal, respectively.

To illustrate the operation of the LFM-POCT device, it was assumed that R_{SA} = 10 kΩ, which was the resistance value of R_S in case of Figure 5.7A and R_{SB} = 5 kΩ, which was the resistance value of R_S in case of Figure 5.7B. If we assumed the minimum current to illuminate an LED was 0.3 mA (3 mm LED LT004), the circuit shown in the Figure 5.7A was designed in such a manner that when the F_R was below safety level, then red LED L_R glowed while the green LED, L_G, remained off. In comparison, when F_R was above safety level, both red and green LEDs glowed. To achieve this, the resistances were tuned to have, R_1 = 5 kΩ and R_2 = 10 kΩ for a terminal voltage V_T = 9 V. We assumed that the LEDs have negligible internal resistance in order to reduce the complexity. From circuit theory, when F_R was below the safety level, the total current through R_{SA} was be given by, $I_1 = V_T(R_1R_2(R_1 + R_2)^{-1} + R_{SA})^{-1}$.

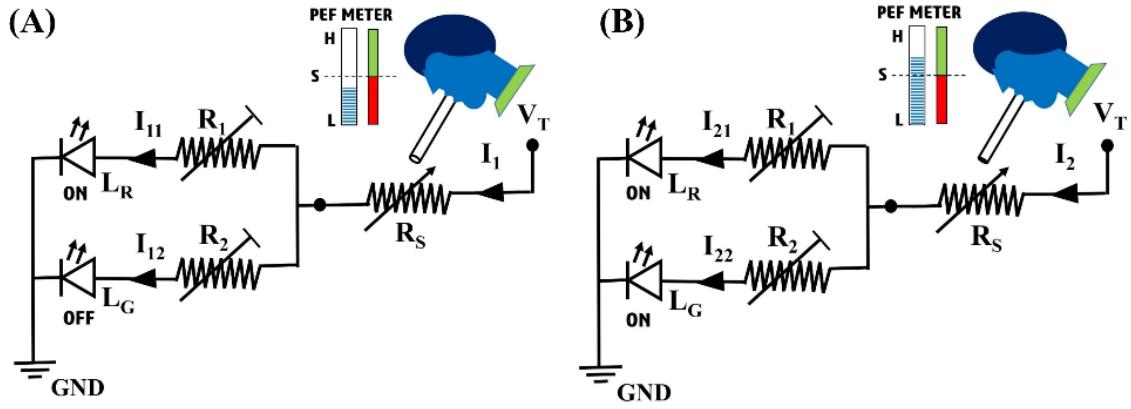

Figure 5.7: Images (A) and (B) show description and illustration of the detection circuit of the control assembly for two different situations of the illumination of the red and green LEDs. In case of the image (A), the F_R is below the desired level (*S*) as shown in the imaginary scale peak expiratory flow (PEF) meter. In contrast, image (B) shows the situation where F_R is above the

safety level (*S*). It may be noted here that the ΔR is more in case of the image (B) than that of the image (A).

Similarly, when F_R was above safety level, the current was, $I_1 = V_T(R_1R_2(R_1 + R_2)^{-1} + R_{SB})^{-1}$. When, F_R was below safety level, the total current was I_1 and the current through R_1 was, $I_{11} = I_1 \times (R_2(R_1 + R_2)^{-1})$ and the current through R_2 was, $I_{12} = I_1 \times (R_1(R_1 + R_2)^{-1})$. If all the values of the resistances were put in the I_1 = 0.675 mA, I_{11} = 0.45 mA, and I_{12} = 0.225 mA, which confirmed that in this case only the red LED (L_R) would be turned on to indicate the necessity of medical assistance required. In contrast, if the F_R was above safety level, then I_2 = 1.08 mA, I_{21} = 0.72 mA, and I_{22} = 0.36 mA, which ensured both the green and red LEDs (L_G and L_R) were turned on to confirm fitness of the lungs. In Figure 5.7 we showed a simpler model where two LEDs were used, whereas in the main device shown in the Figure 5.5 of the main manuscript, we employed a similar principle, but a more complex circuit to ensure three different types of signals were obtained to ensure diseased, onset of disease, and fitness conditions, as mentioned previously.

5.2.6 Methods

The characteristics of micro-heater is shown in Figure 5.8. Image (A) shows the temperature (*T*) response of micro-heater with time (*t*). In this experiment, the current source was turned on for 60 s, which ensured a temperature rise with time. The source was turned off after 60 s and therefore, a decrease in temperature was observed. Since the mechanism was based on Joule heating, we could generate high temperature with an increase in the current and time, as shown in images (A) and (B). Image (C) shows the

input current flowing through the electrical circuit to maintain a constant temperature on the micro-heater surface at ~30 °C.

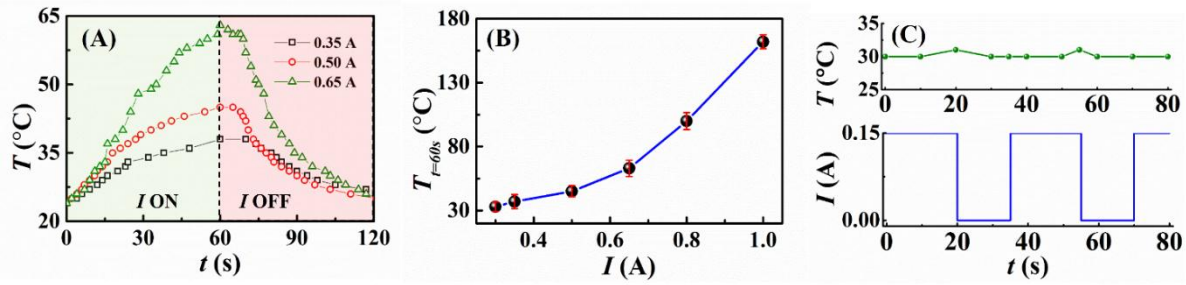

Figure 5.8: Image (A) shows the variation in temperature (*T*) with time (*t*) for different current (*I*) inputs to the micro-heater. The current source was turned on for first 60 s before turned off. Image (B) shows the temperature ($T_{t=60s}$) generated on the micro-heater surface after 60 s at different current flow (*I*). Image (C) shows the current input (*I*) and temperature output (*T*) employed for the micro-heater.

5.3. Results and Discussion

5.3.1 Response of Paper Humidity Sensor

When the humidity sensor was exposed to human exhalation, the water molecules progressively adsorbed on the CdSNPs to reduce the electrical resistance. The variation in the flow rate of the exhaled air could be correlated with the variation in the electrical resistance across the sensor, which helped in evaluating the frequency and the peak flow rate of human breathing. Figure 5.9A schematically illustrates a three-step process in which the step I shows the dry sensor having high electrical resistance; step II shows the adsorption followed by condensation of the water molecules on the sensor [3] when the humid air was concentrated, leading to the reduction in the electrical resistance; and step III shows the desorption of the water molecules from the paper-surface after the exhalation was complete, which led to the increase in the electrical resistance.

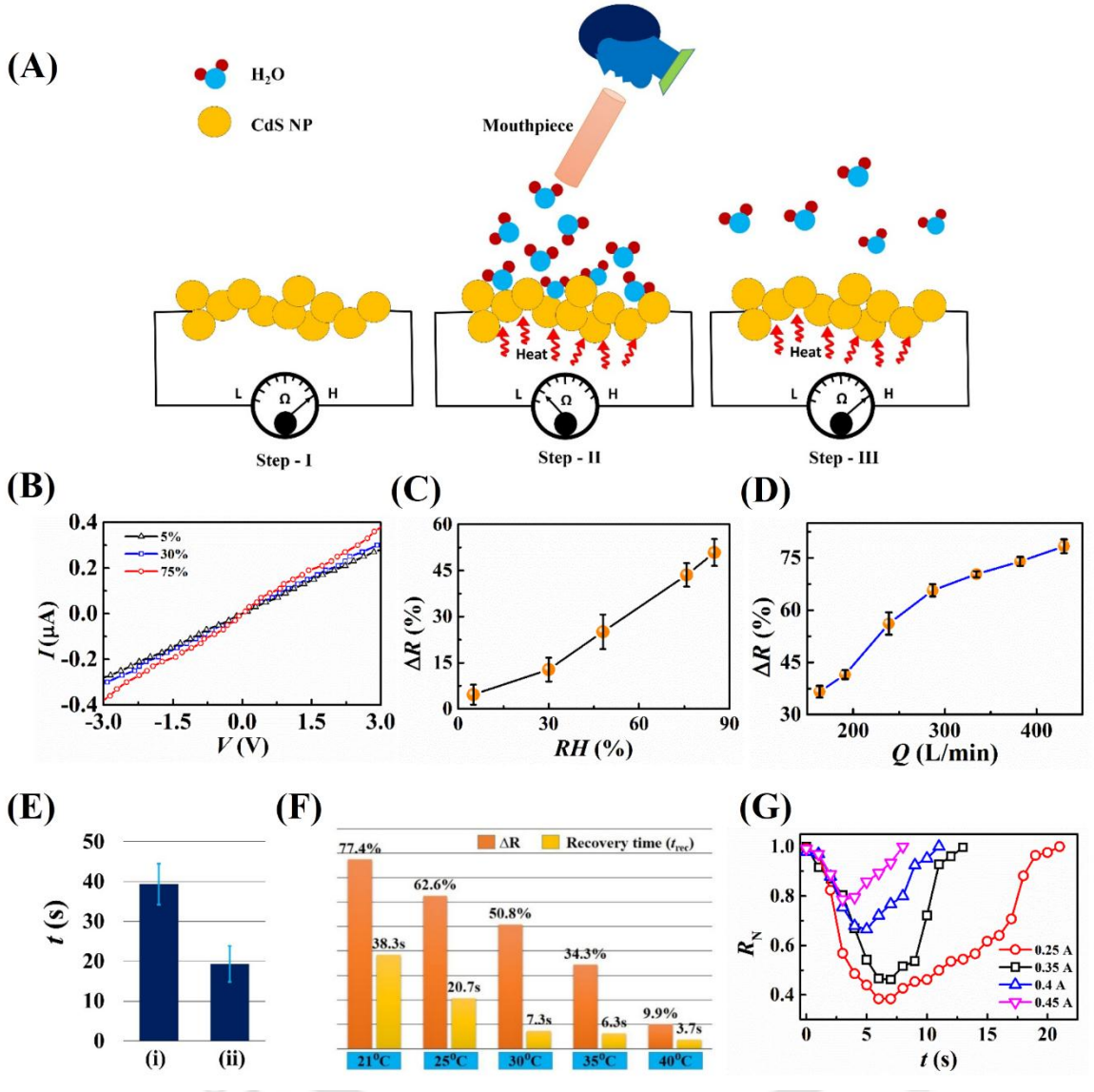

Figure 5.9: Image (A) schematically illustrates the step by step adsorption and desorption processes of the sensing mechanism. Image (B) shows the current-voltage (I-V) characteristics of the sensor for different relative humidity conditions. Image (C) shows the change in resistance (ΔR) of the sensor at different *RH*. Image (D) shows the change in ΔR of the sensor due to the pulsed exposure of ~97 % humid air at different *Q*. Image (E) shows the time taken by a paper substrate to reach 50ºC when the paper was, (i) devoid of AuNPs and (ii) embedded with AuNPs while the paper substrate was kept on a heated surface at 65°C. Image (F) shows the change in ΔR and recovery time (t_{rec}) at different temperatures of the paper-sensor. Image (G) shows the response of the sensor with time for different magnitudes of current (*I*) flown through the micro-heater when air flow rate was ~450 L/min.

The paper-sensor illustrated in Figure 5.1 was connected to a digital multimeter (MASTECH M92A(H)) to verify the electrical response in presence of different humidity conditions. Figures 5.9B and 5.9C show the I-V characteristics and change in resistance ($\Delta R = R_i - R$) of the humidity sensor with the variation in the external *RH* where R and R_i are the variables and initial electrical resistance of the wet and dry sensors. The I-V curves in the Figure 5.9B were recorded after the sensor was placed in the closed beaker of different *RH* for 1 h. The plots suggest that with the increase in *RH* the resistance of the paper-sensor reduced and current flow increased.

Figure 5.9C suggests that the increased conductance of the paper-sensor in the presence of humid air led to a linear increase in ΔR with *RH*. In these experiments, an air of different *RH* was blown artificially on the sensor before measuring the change in ΔR. Previous studies indicated that the electrical resistance of CdSNPs could decrease exponentially at higher levels of *RH* in the surrounding [32-34]. Experiments suggested that when *RH* was relatively low (~5 %), a monolayer of water molecules formed on the surface of the CdSNPs did not change the electrical resistance significantly [33]. However, condensation of water molecules on the CdSNP surface due to multilayer physical adsorption at relatively higher *RH* (> 60 %) could lead to an exponential decrease in the electrical resistance. In such a scenario, the reduction in the electrical resistance could be attributed to the production of ionic hydroxyl groups from the water molecules when the current is flown across the CdSNPs.

Figure 5.9D illustrates the effect of flow rate (Q) of ~96 % humid air on the sensor. In this experiment, the fluid was introduced using a cylindrical silicone tube of length 4 in with an inner diameter of 1/16 in for ~2 s. The pressure drop was measured using digital manometer (HTC PM-6205), *RH* was measured using an HTC-1 digital hygrometer, and

the flow rate was calculated using the standard Hagen-Poiseuille equation. We observed that the change in electrical resistance was higher in case of higher *Q* of the air.

The AuNPs on the sensor, improved the thermal and electrical conductance. Figure 5.9E shows that the presence of the AuNPs could rapidly heat up and cool down the sensors. Figures 5.9F and 5.9G show the typical variation in ΔR and the subsequent recovery time of the paper-sensor at different temperature (*T*) and current flow (*I*) through the micro-heater for a flow rate ~450 L/min, which was very close to the average peak flow rate of adult human breathing, ~424 L/min. The optimal condition for a faster response and recovery time of the paper-sensor was found to be at ~30 ºC and 0.35 A because under these circumstances large variation in ΔR at high *RH* and the fast recovery time were observed, as shown in the Figure 5.9F.

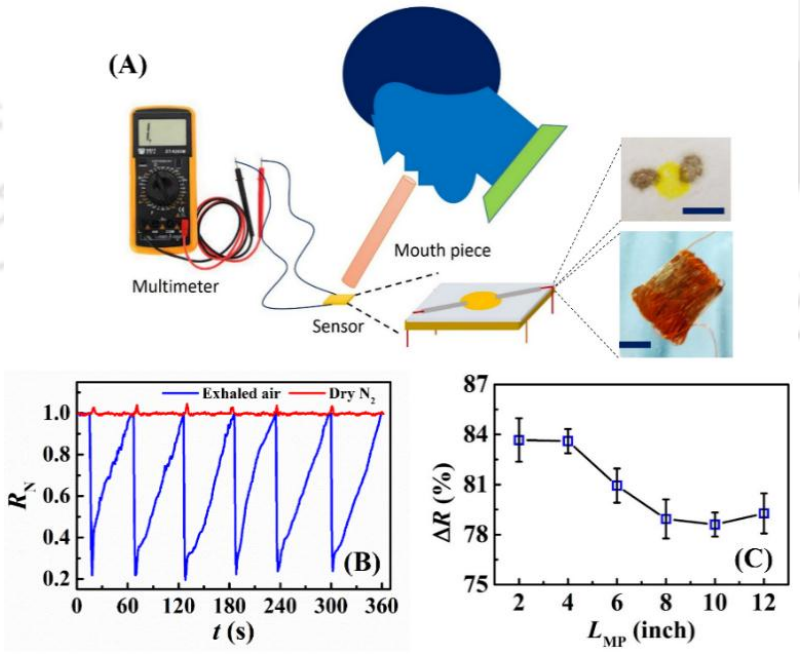

Figure 5.10: Image (A) schematically shows the experimental set up composed mouthpiece, paper-sensor, micro-heater, and multimeter to measure the various parameters during exhalation. The insets show the real images of paper-sensor and micro-heater where the scale bars are of 5 mm. Image (B) shows the variation in the normalized resistance ($R_N = R/R_i$) with time (*t*) for six cycles of breathing alongside a control experiment with dry N_2 gas. Image (C) shows the variation in the ΔR for different length of the mouthpiece (L_{MP}).

5.3.2 Response of LFM-POCT Device

Image (A) in the Figure 5.10 schematically shows the experimental set up employed to standardize the LFM-POCT device. In this setup, when the exhaled air issuing out of a human breathing was focused on the paper-sensor, we observed a rapid decrease in the normalized resistance ($R_N = R/R_i$) with time (t) during the breath-out cycle, as shown in the image (B). In order to focus the exhaled air from human breathing on the paper-sensor we employed the mouthpiece of optimized length (4 in) and diameter (1.2 in), as shown in the image (C). The image suggested that smaller mouthpieces equal or smaller than 4 in showed better response. We also observed a quick recovery of the paper-sensor to its initial state because of the rapid desorption of the water molecules at 30^0C, as previously discussed in Figure 5.9.

The control experiment with dry N_2 gas showed no change in resistance, as shown in image (B). However, during the exhalation cycle, the electrical resistance of the paper-sensor progressively decreased to a minimum value due to the adsorption followed by condensation and ionization of the water molecules on the sensor. Thus, repeated inhalation and exhalation could be captured through the prototype, as shown by the three repeated cycles in the image (B). The plots shown in the image (B) suggest that the paper-sensor was capable of detecting the breathing frequency, which is one of the important parameters to detect various COPD.[62]

Another control experiments with a paper surface devoid of CdSNP and having only the AuNPs also showed no response, which highlighted the importance of CdSNPs for the device. In the presence of the micro-heater, the elevated temperature of the paper-sensor did not allow easy condensation of the water molecules and only after forceful exhalation could change the resistance. Once the exhalation was complete, the micro-heater helped in

maintaining an elevated temperature to rapidly desorb the water molecules from the surface and restore the initial electrical resistance of the dry sensor.

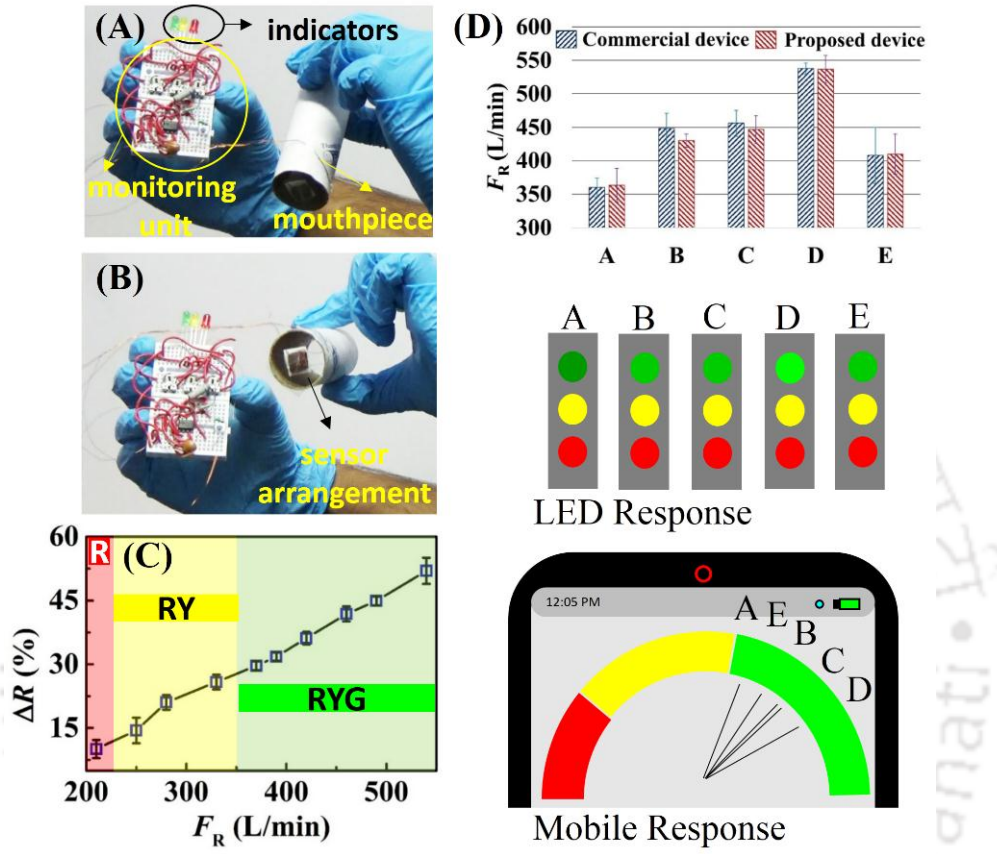

Figure 5.11: Images (A) and (B) show the photographs of the device. Image (C) shows the variation in ΔR because of different peak flow rate (F_R) of the exhaled air. Image (D) shows the comparison of results between a commercial device, JSB N02 peak flow meter and the proposed device along with a schematic illustration of the corresponding LED and mobile response.

Figure 5.11 summarizes the performance of the LFM-POCT prototype proposed with respect to commercially available peak flow meter JSB N02. The images (A) and (B) show the photographs of the device assembled, having a mouthpiece, a paper-sensor, and an LED-based real-time monitoring unit. The sensor in the mouthpiece acted as an obstruction to the exhaled air, whereas the opening beside the sensor let the air flow out. The experiments suggest that a forced exhalation on the sensor could turn on either the red LED – signifying alarming condition; red and yellow LEDs – signifying the onset of the

diseased condition; red, yellow, and green LEDs – signifying the non-diseased state of lungs.

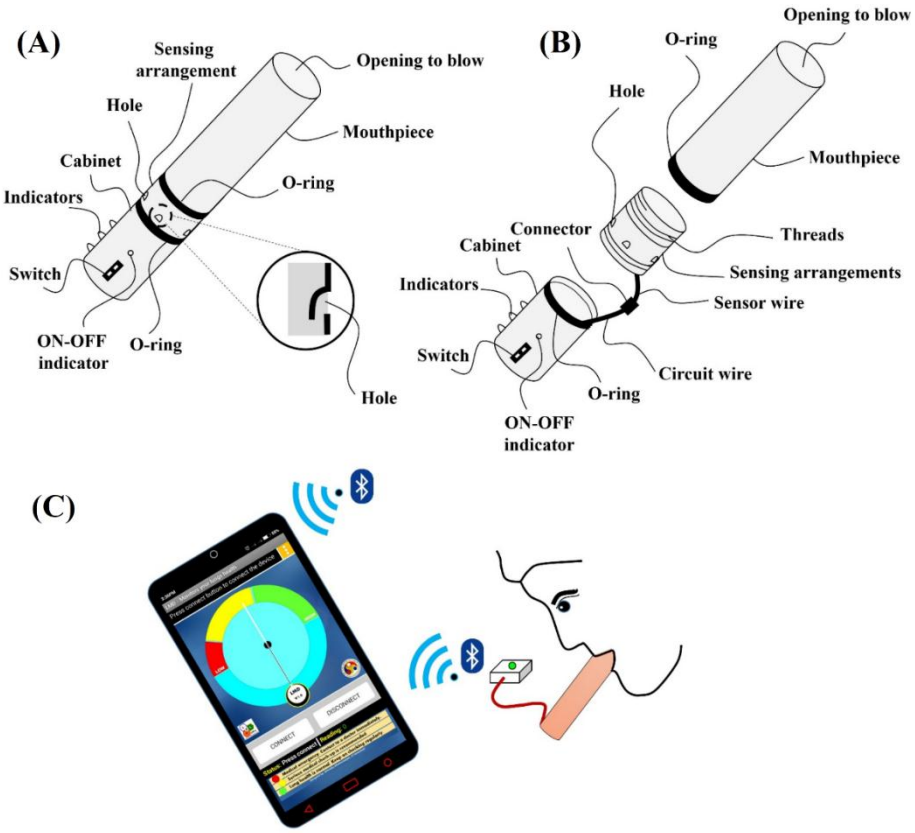

Figure 5.12: Images (A) and (B) schematically show the components of the mobile-based LFM-POCT device. Image (C) illustrates the device connected to a smartphone through Bluetooth and perform a wireless lung function test through the open standard software (***Patent filed***).[63]

The typical circuits employed to integrate the sensor with LED indicators are provided in the Figures 5.5 and 5.6. Importantly, we employed a commercial peak flow meter to obtain the peak flow rate (F_R), which was then correlated back to the change in electrical resistance (ΔR) of the paper sensor, as shown in Figure 5.11C. The resistances in the circuit of the LFM-POCT device was then attuned with the calibration plot shown in the Figure 5.11C. Thereafter, we compared the result of commercially available peak flow meter with the proposed LFM-POCT device for five different volunteers, as illustrated in

the Figure 5.11D. The experiments suggested that the performance of the proposed device was comparable to the commercially available one.

5.3.3 LFM-POCT Device Architecture

In order to make the device more user-friendly, we also developed a mobile application, which could be interfaced with the LFM-POCT device in order to operate with the help of a smartphone. Figures 5.12A and 5.12B show the components of the device having a mouthpiece with the opening to blow air, threads for assemblage, indicator cabinet, on-off-switch, and sensor placement, among others. The smartphone had a wireless connection with the LFM-POCT through Bluetooth.

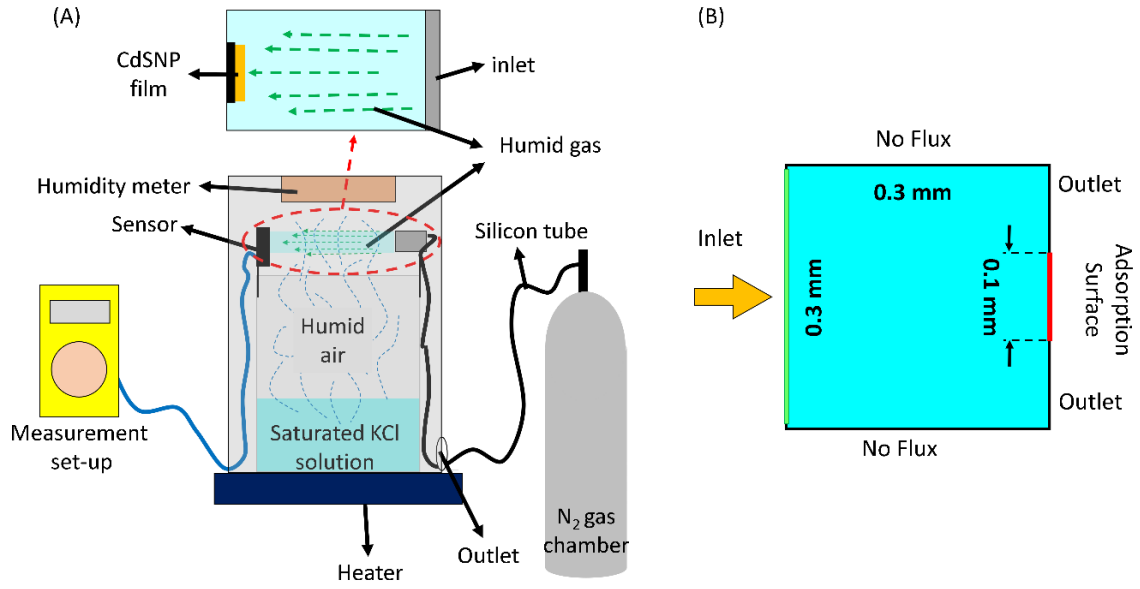

Figure 5.13: Image (A) shows the experimental set-up for measuring the response of the sensor. The experimental section, which is considered as the computational domain is marked with a red dotted line and magnified above. The inlet, flow of humid gas, and position of CdSNP adsorption surface are indicated in the magnified figure. The equivalent 2D computational geometry is illustrated in the image (B).

We developed an open standard 'Android' based application, which was employed to follow the tests of the LFM-POCT device on the mobile display. The application had a

virtual needle on the mobile display, which moved towards the red (diseased), yellow (onset of disease), and green (fit) zones reflecting the conditions of lung functions, as shown in the Figure 5.12C. Figure 5.12C shows the typical steps of operation of the LFM-POCT device. The Figure 5.12 suggested that the LFM-POCT device was initially connected to the mobile phone through Bluetooth. Then the software interface available on the mobile screen helped in displaying the performance of lung function test.

5.3.4 Experimental and Simulation to Study the Dependence of Flowrate

Figure 5.13A illustrates the experimental set-up. The experimental section associated with computational study is also magnified in the figure, which is described in Figure 5.13B**.** The experiments were performed in a closed environment to maintain a relative humidity of ~97%. The chamber contained 250 ml container with 50 ml saturated KCl solution kept on a heater for 12 h. The temperature was adjusted by the heater between 25 – 40^0C to maintain a relative humidity of ~97% during the experiments. A digital humidity meter (HTC-1) was kept inside the chamber to monitor the relative humidity. In order to flow humid gas in the chamber, one end of a 4 in silicon tube (Sigma Aldrich, inner diameter 1/16 in) was connected to nitrogen (N_2) gas cylinder (99% pure, compressed) whereas the other end was placed in front of the sensor, at a distance of ~3 cm to study the effect of flowrate of humid gas. The sensor and silicone tube was fixed with the arrangement with glass slides and double-sided tape and the silicon tube was positioned in such a way so that the humid gas directly strikes the sensor. The flowrate of the humid gas was maintained using the flow of N_2 gas through the silicon tube at a specific pressure. The usage of compressed N_2 gas, in this case, eliminated the possibility of interference of ambient humidity, which was the limitation of using a compressed air. The pressure drop across the tube was measured using digital manometer (HTC PM-6205). The flowrate was

then calculated using the standard Hagen-Poiseuille equation. The typical flowrate associated with this experiment was found to be in the range of ~200 – 600 L/min, which could be comparable to many physical or biological systems such as the peak flowrate of human lungs. The sensor was connected to a digital multimeter (MASTECH M92A(H)), which was kept outside the chamber to measure the electrical response of the sensor. Each measurement was taken in a pulsed mode where the compressed N_2 gas was blown for ~2 s and at least 5 readings were taken for each flowrate.

5.3.5 Computational Analysis of Adsorption

The Figure 5.13B shows 2-D domain used in the simulations schematically. In this geometry, the left-side was modeled as the inlet, the top and bottom sides were modeled as no-flux walls, and a part of the outlet boundary to the right-side was the sensor. The finite element method (FEM) modeling of the governing equations and boundary conditions was performed with the assumption that the adsorbate behaved as an ideal gas under an isothermal condition. The adsorption and desorption on the sensor was expressed as, $A \rightleftharpoons A_S$, where the rate constants were denoted by k_a and k_d. The notations A and A_S stand for the molecules in the gas and adsorbed on active sites on the surface, respectively. According to the Langmuir model,[64, 65] the rate of desorption of molecules, $r_d = k_1\theta_s$, where the fraction of active sites occupied by adsorbed molecules is θ_s, and k_1 is the rate constant. The rate of adsorption of molecules, $r_a = k_2 P_A (1 - \theta_S)$, where the fraction of free sites on the surface is, $(1 - \theta_S)$, k_2 is the rate constant, and the rate at which the molecules strike the surface is proportional to the partial pressure of the species adsorbing, P_A.

Subsequently, with some rearrangements the rate equations, r_d and r_a, can be expressed in terms of the surface concentration (c_S) in the following forms,[64, 65]

$$r_d = k_d c_S \text{ and } r_a = k_a c (\Gamma_S - c_S). \quad (5.1)$$

where, $\theta = c_S / \Gamma_S$, $P_A = cRT$, $k_d = k_1 / \Gamma_S$, and $k_a = (k_2 RT) / \Gamma_S$. In these expressions, the bulk adsorbate concentration is c, Γ_S is the total surface concentration of active sites (mol/m^2), R is the universal gas constant (J/(mol·K)) and T is temperature (K). Further, the redefined rate constant for desorption, k_d has the unit of, (1/s) while the rate constant for adsorption, k_a has the unit of, (m^3/mol·s).

When a material, A, adsorbed and desorbed on the surface, the material balance equation for the transport and reaction was described by,[64, 65]

$$\partial c_S / \partial t + \nabla \cdot (-D_S \nabla c_S) = k_a c (\Gamma_S - c_S) - k_d c_S. \quad (5.2)$$

In the Eq. (5.2), D_S denotes the surface diffusivity of the reacting species. The initial condition employed to solve the Eq. (2) was, $c_S = 0$ at $t = 0$. The transport of the material, A, in the bulk of the sensor was described by the equation,[64, 65]

$$\partial c / \partial t + \nabla \cdot (-D \nabla c) = 0. \quad (5.3)$$

In the Eq. (5.3), D denotes the diffusivity of the reacting species and c is the bulk concentration of the adsorbate molecule. The initial condition employed to solve the Eq. (5.3) was, $c = c_0$ at $t = 0$ in the bulk. The boundary condition, $\mathbf{n} \cdot (-D \nabla c) = 0$, was enforced to the outlet and no flux boundaries at the top and bottom. The adsorption-desorption at the sensor surface was modeled as a boundary condition,

$\mathbf{n}\cdot(-D\nabla c) = -k_a c(\Gamma_S - c_S) + k_d c_S$, where $\mathbf{n}$ is the unit vector. The governing Eqs. (5.1) – (5.3) with the initial and boundary conditions were solved employing FEM based COMSOL^{TM} multiphysics software.

In the experiments, increase in the flowrate of the humid gas effected the inflow of water molecules on the sensor. Thus, the flowrate of the humid gas was modeled by correlating the concentration of water at the inlet, c_{0c} as a function of time (t) and maximum flowrate (F_R). This was done by linearly approximating the increase in concentration per unit volume to, c_{0a} = 1000 mol/m^3 while the c_{0c} was considered as, $c_{0c} = c_0 + (F_R \times t \times c_{0a})$. Other than the linear approximation, a logarithmic approximation was also employed to model the variation in the concentration as, $c_{0c} = c_0 + \ln\left[(F_R \times t \times c_{0a})/c_0 + 1\right]$. In a way, the approximations were taken to find the best suit with the results of experimental investigations.

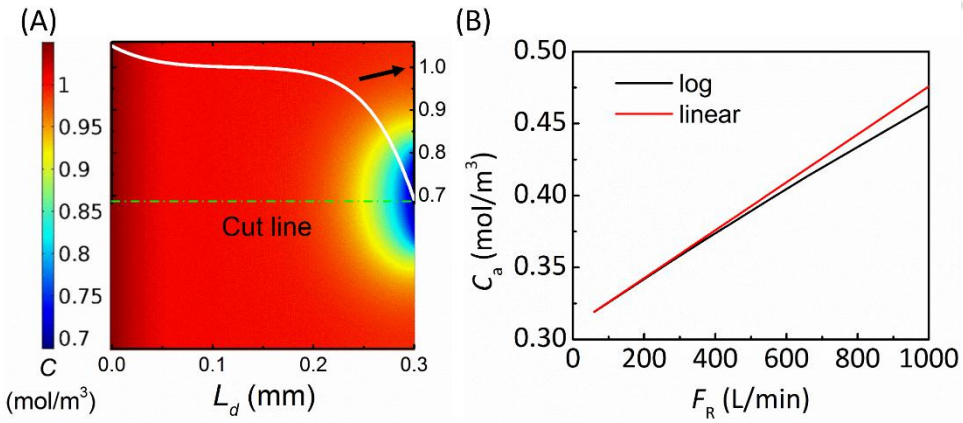

Figure 5.14: Image (A) shows the contour plot of the concentration of adsorbate molecule (C) in the pipe for 300 L/min in linear approximation. The white curve shows the concentration of molecules measured along the cut-line (broken line) with distance (L_d). Image (B) shows the variation of adsorbed molecule concentration (c_a) under linear and logarithmic approximation with different flowrates (F_R).

In the beginning, we assumed that the molecules inside the computational domain increased linearly or logarithmically with the increase in flowrate. Figure 5.14A shows the contour plot along with the curve of adsorbate molecule concentration (C) along the length (L_d) of the computational domain for the flowrate of 300 L/min considering the linear approximation. The plot show that the concentration of the molecules decreased sharply near the sensor due the adsorption which in turn led to the change in electrical conductance. Figure 5.14B shows the adsorbed molecule concentration (c_a) for different F_R following the linear and logarithmic approximations. In both the flowrates the logarithmic approximation suggested a lower adsorption of water molecules as compared to the linear one. Adsorption of the water molecules was directly related to the change in electrical conductance as described in the later section with the help of semiconductor physics analysis.

5.3.6 Effect of Adsorption on CdS

In order to understand the change in electrical resistance of the semiconducting sensor due to the adsorption of water molecules, we explored the variation in the space charge effects. It is well known that CdS is an n-type semiconductor[66] and under equilibrium the Fermi energy E_F is same in the bulk and surface, which is illustrated in Figure 5.15A. Thus, we assumed that on surface there could a layer of negative charge of density, Q_{ss}, which was balanced by the positive charges of equal amount. These positive charges were the ionized donors in the space charge layer, $Q_{SS} = -Q_{SC} \approx eN_D d$, where, N_D was the positive charge density and d was the thickness of space charge layer, as shown in the Figure 5.15A.

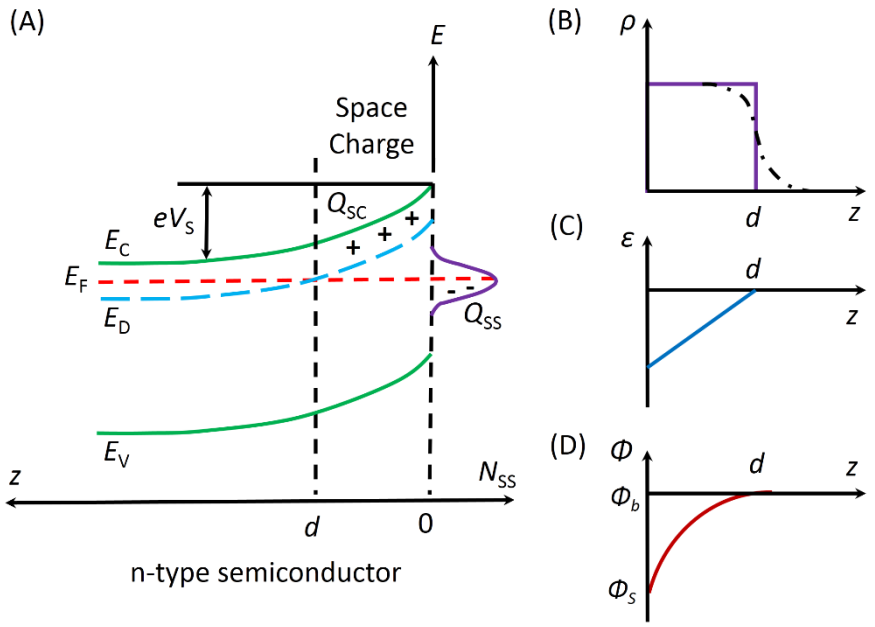

Figure 5.15: The plot (A) schematically shows the band energy *E* vs. *z*-coordinate normal to sensor-surface to illustrate band bending of the n-type CdSNPs near the surface of the sensor (left-side) due to the space charge layer. The notations N_{SS}, E_V, E_D, E_F and E_C show the surface charge density and the energies corresponding to valance band, donor level, Fermi level and conduction band of the sensor. Plots (B) to (D) show the volume charge density (ρ), electric field (ε) in the space charge layer and the electric potential (φ) characteristics with *z*-coordinate, respectively. The surface and bulk electric field potentials are denoted by φ_s and φ_b and the thickness of space charge layer is denoted by *d*. The notations Q_{SS}, Q_{SC}, N_{SS}, and eV_S denotes surface state charge, space charge, surface state charge density, and band bending at the surface.

Under these circumstances, we defined the electric field potential φ and band deformation V to be,[67]

$$e\varphi(z) = E_F - E_i(z) \text{ and } eV(z) = e[\varphi_b - \varphi(z)], \tag{5.4}$$

where the position dependent potential energy, $e\varphi(z)$ was the difference between Fermi energy E_F and the intrinsic level E_i. The term φ_b denoted the value of $\varphi(z)$ in the bulk. Therefore, the total band bending was given by, $eV_S = e[\varphi_b - \varphi(0)] = e[\varphi_b - \varphi_s]$, where φ_s denotes the value of $\varphi(z)$ in the surface.

The governing equation that illustrated the band bending and space charge layer formation was the Poisson's equation. In full-depletion approximation, i.e. $Q_{SS} = -Q_{sc} \approx eN_D d$, the equation could be written as,[67] $d^2\varphi/dz^2 = -(eN_D)/(\varepsilon_r\varepsilon_0)$. (5.5)

Where ε_r and ε_0 are the relative and absolute permittivity and $\varepsilon = d\varphi/dz$, denotes the electric field. Integrating Poisson's equation once, we obtained the electric field in the space charge region as,[67]

$$\varepsilon(z) = \left[(eN_D)/(\varepsilon_r\varepsilon_0)\right](z-d), \qquad 0 \le z \le d \ . \tag{5.6}$$

A further integration of electric field ε(z) led to the electric field potential as,

$$\varphi(z) = \varphi_b - \left[(eN_D)/(2\varepsilon_r\varepsilon_0)\right](z-d)^2, \ 0 \le z \le d \ . \tag{5.7}$$

Subsequently, total band bending was obtained as,[67]

$$|eV_S| = |e(\varphi_b - \varphi_s)| = (e^2 N_D d^2)/(2\varepsilon_r\varepsilon_0). \tag{5.8}$$

Here, V_S shows the maximum potential at the surface. The typical nature of the volume charge density (ρ), the electric field (ε), and electric field potential (φ) near the sensor surface is shown in the plots (B), (C) and (D) of Figure 5.15, respectively.

Sensor Response: During the adsorption of water molecules on the surface of CdSNP layer a negatively charged layer of OH^- ions was formed.[68] This negatively charged layer of OH^- ions acted as the surface charge as described by the term Q_{SS} in the previous section. Thus, the adsorption of the water molecules, as illustrated in the Figure 5.13, directly influenced the positive charge density (N_D), in the space charge layer and hence the band bending happened amounting the value obtainable from the Eq. (5.8). The formation of negative surface charge layer led to change the electrical conductance of the

semiconductor, which was defined in terms of band bending.[67, 69] The change in the conductivity due to the band bending was evaluated as,

$$\Delta\sigma/\sigma_0 = 2(L/l)\exp(|eV_S|/2). \quad (5.9)$$

Where, the thickness of the semiconductor was assumed to be, $2l$, much larger than the length of screening L. The notation σ_0 is the base conductivity of the sensor and the band bending $|eV_S|$ is in kT units.

The experimental variation in the electrical conductivity ($\Delta\sigma$) with the flowrate of humid gas (F_R) is illustrated by symbols in the Figure 5.16. The plot helped in obtaining a calibrated variation, which can easily be employed to develop a humidity or a flowrate sensor. It may be noted here that the experiments were performed at room temperature. It was observed that at a lower temperature (less than 12°C), the water molecules condensed on the sensor surface leading to ~8% fluctuations in the sensor response after 4-5 times of reuse.

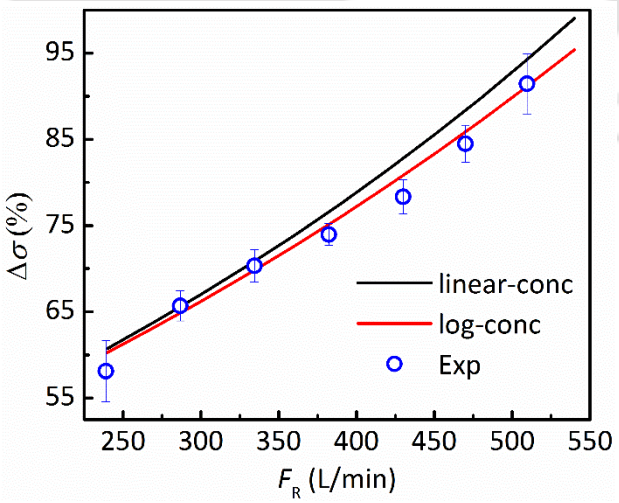

Figure 5.16: The variation in the electrical conductivity ($\Delta\sigma$) with the flowrate of humid gas (F_R) due to the variation in the adsorption of water molecules on the sensor. The solid lines show the

simulated values for the linear (black) and logarithmic (red) variations in F_R of the humid gas with the concentration of the adsorbed molecules. The scattered circular symbols show the experimental results.

The solid lines in the plot show the variation in $\Delta\sigma$ for linear and logarithmic variations in F_R of the humid gas with the concentration of the adsorbed molecules, obtained from the FEM simulations in the Figure 5.13. The computational and experimental study together show that the conductivity of the semiconducting material increased with flowrate. It is very evident from the Figure 5.16 that the experiments showed a better agreement with the simulated logarithmic variations in F_R of the humid gas with the loading of the adsorbed molecules.

5.4. Conclusions

An economic, fast, reliable, portable, biocompatible, and user-friendly LFM-POCT device consisting of mouthpiece, paper-sensor, micro-heater assemblage, and monitoring unit has been developed. The device was capable of measuring the frequency of breathing and peak flow rate of human exhalation, which could be necessary to detect COPDs such as asthma, bronchitis, or pneumonia. The sensor was developed by depositing AuNPs and CdSNPs on a paper-surface in which the former enhanced the electrical and thermal conductivities while the latter infused the capacity of high precision humidity sensing. Adsorption followed by condensation of the water molecules on the CdSNPs during the forced exhalation reduced the electrical resistance of the sensor, which was then converted to an electrical signal for sensing. The micro-heater embodiment integrated with the sensor helped in maintaining an optimal temperature, which allowed condensation of the water molecules only during forced breathing and facilitated rapid desorption and evaporation of the molecules once the exhalation was complete. Two types of real-time monitoring units were integrated with the device. The LED-based unit displayed the diseased, critical, and

fit conditions of the lungs by flashing LEDs of different colors. The mobile-based monitoring unit was developed employing an open source software, which helped in the operation of the LFM-POCT device on a smartphone interface by establishing a wireless connection. The device was found to be equally efficient as some of the commercially available ones. The LFM-POCT device envisioned to stage a paradigm shift in test, transfer, and storage of lung-fitness data for facile prognosis, diagnosis, and therapeutics at the patient site.

References

1. S. Gong, W. Schwalb, Y. Wang, Y. Chen, Y. Tang, J. Si, B. Shirinzadeh and W. Cheng, *Nature Communications*, 2014, **5**, 3132.
2. *United States Pat.* US20160349104A1, 2011.
3. S. Ding and M. Schumacher, *Sensors*, 2016, **16**, 589.
4. X. Li, S. Weng, B. Ge, Z. Yao and H.-Z. Yu, *Lab on a Chip*, 2014, **14**, 1686-1694.
5. S. K. Vashist, P. B. Luppa, L. Y. Yeo, A. Ozcan and J. H. T. Luong, *Trends in Biotechnology*, 2015, **33**, 692-705.
6. C. J. L. Murray et al., *The Lancet*, 2012, **380**, 2197-2223.
7. V. Ruzsanyi and J. Baumbach, *International Journal of Ion Mobility Spectrom*, 2005, **8**, 5-7.
8. M. Nishimura, H. Makita, K. Nagai, S. Konno, Y. Nasuhara, M. Hasegawa, K. Shimizu, T. Betsuyaku, Y. M. Ito, S. Fuke, T. Igarashi, Y. Akiyama and S. Ogura, *American Journal of Respiratory and Critical Care Medicine*, 2012, **185**, 44-52.
9. J. C. de Groot, H. Storm, M. Amelink, S. B. de Nijs, E. Eichhorn, B. H. Reitsma, E. H. D. Bel and A. ten Brinke, *ERJ Open Research*, 2016, **2**.

10. G. X. Ayala, C. Gillette, D. Williams, S. Davis, K. B. Yeatts, D. M. Carpenter and B. Sleath, *Journal of Asthma*, 2014, **51**, 84-90.

11. K. R. Jat, *Primary Care Respiratory Journal*, 2013, **22**, 221.

12. K. J. Klingman, J. Castner and A. H. Titus, *Nursing Research*, 2016, **65**, 238-248.

13. R. P. Marcotte, W. Manchester, D. Henton, D. Parent and T. Gehan, *Journal*, 2005.

14. *United States pat.*, US8034002B2, 2005.

15. I. Ojanguren, M. J. Cruz, A. Villar, M. Sanchez-Ortiz, F. Morell and X. Munoz, *BMC Pulmonary Medicine*, 2015, **15**, 109.

16. J. Xu, Q. Pan, Y. a. Shun and Z. Tian, *Sensors and Actuators B: Chemical*, 2000, **66**, 277-279.

17. M. Bhattacharjee, V. Pasumarthi, J. Chaudhuri, A. K. Singh, H. Nemade and D. Bandyopadhyay, *Nanoscale*, 2016, **8**, 6118-6128.

18. M. M. Aeinehvand, F. Ibrahim, S. W. Harun, I. Djordjevic, S. Hosseini, H. A. Rothan, R. Yusof and M. J. Madou, *Biosensors and Bioelectronics*, 2015, **67**, 424-430.

19. X. Qiu, S. Ge, P. Gao, K. Li, S. Yang, S. Zhang, X. Ye, N. Xia and S. Qian, *Microsystem Technologies*, 2016, DOI: 10.1007/s00542-016-2979-z, 1-6.

20. K. Mondal, M. A. Ali, S. Srivastava, B. D. Malhotra and A. Sharma, *Sensors and Actuators B: Chemical*, 2016, **229**, 82-91.

21. M. A. Ali, K. Mondal, Y. Jiao, S. Oren, Z. Xu, A. Sharma and L. Dong, *ACS Applied Materials & Interfaces*, 2016, **8**, 20570-20582.

22. S. Kumar, A. K. Singh, A. K. Dasmahapatra, T. K. Mandal and D. Bandyopadhyay, *Carbon*, 2015, **89**, 31-40.

23. K. K. Dey, X. Zhao, B. M. Tansi, W. J. Méndez-Ortiz, U. M. Córdova-Figueroa, R. Golestanian and A. Sen, *Nano Letters*, 2015, **15**, 8311-8315.

24. S. Kumar, M. R. Ali Faridi, A. K. Dasmahapatra and D. Bandyopadhyay, *RSC Advances*, 2016, **6**, 107049-107056.

25. A. K. Singh, K. K. Dey, A. Chattopadhyay, T. K. Mandal and D. Bandyopadhyay, *Nanoscale*, 2014, **6**, 1398-1405.

26. B. Ravi, S. Chakraborty, M. Bhattacharjee, S. Mitra, A. Ghosh, P. S. Gooh Pattader and D. Bandyopadhyay, *ACS Applied Materials & Interfaces*, 2016, DOI: 10.1021/acsami.6b12182.

27. B. Roy, G. Chattopadhyay, D. Mishra, T. Das, S. Chakraborty and T. K. Maiti, *Biomicrofluidics*, 2014, **8**, 034107.

28. E. Roy, G. Stewart, M. Mounier, L. Malic, R. Peytavi, L. Clime, M. Madou, M. Bossinot, M. G. Bergeron and T. Veres, *Lab on a Chip*, 2015, **15**, 406-416.

29. O. Parlak, S. Beyazit, B. Tse-Sum-Bui, K. Haupt, A. P. F. Turner and A. Tiwari, *Nanoscale*, 2016, **8**, 9976-9981.

30. S. Dutta, N. Mandal and D. Bandyopadhyay, *Biosensors and Bioelectronics*, 2016, **78**, 447-453.

31. N. Pal, S. Sharma and S. Gupta, *Biosensors and Bioelectronics*, 2016, **77**, 270-276.

32. R. Demir, S. Okur and M. Şeker, *Industrial & Engineering Chemistry Research*, 2012, **51**, 3309-3313.

33. R. Demir, S. Okur, M. Şeker and M. Zor, *Industrial & Engineering Chemistry Research*, 2011, **50**, 5606-5610.

34. L. Du, Y. Zhang, Y. Lei and H. Zhao, *Materials Letters*, 2014, **129**, 46-49.

35. S.-P. Chang, S.-J. Chang, C.-Y. Lu, M.-J. Li, C.-L. Hsu, Y.-Z. Chiou, T.-J. Hsueh and I. C. Chen, *Superlattices and Microstructures*, 2010, **47**, 772-778.

36. J.-W. Han, B. Kim, J. Li and M. Meyyappan, *The Journal of Physical Chemistry C*, 2012, **116**, 22094-22097.

37. Y. Zhang, K. Yu, D. Jiang, Z. Zhu, H. Geng and L. Luo, *Applied Surface Science*, 2005, **242**, 212-217.

38. W.-D. Lin, C.-T. Liao, T.-C. Chang, S.-H. Chen and R.-J. Wu, *Sensors and Actuators B: Chemical*, 2015, **209**, 555-561.

39. D. Zhang, J. Tong and B. Xia, *Sensors and Actuators B: Chemical*, 2014, **197**, 66-72.

40. S. Borini, R. White, D. Wei, M. Astley, S. Haque, E. Spigone, N. Harris, J. Kivioja and T. Ryhänen, *ACS Nano*, 2013, **7**, 11166-11173.

41. P. Pattananuwat, M. Tagaya and T. Kobayashi, *Sensors and Actuators B: Chemical*, 2015, **209**, 186-193.

42. A. Erol, S. Okur, B. Comba, Ö. Mermer and M. Ç. Arıkan, *Sensors and Actuators B: Chemical*, 2010, **145**, 174-180.

43. R.-J. Wu, Y.-L. Sun, C.-C. Lin, H.-W. Chen and M. Chavali, *Sensors and Actuators B: Chemical*, 2006, **115**, 198-204.

44. R. K. Nahar, V. K. Khanna and W. S. Khokle, *Journal of Physics D: Applied Physics*, 1984, **17**, 2087.

45. K. Uksong and K. D. Wise, *Electron Devices, IEEE Transactions on*, 2000, **47**, 702-710.

46. F. Atay, V. Bilgin, I. Akyuz and S. Kose, *Materials Science in Semiconductor Processing*, 2003, **6**, 197-203.

47. S. Kumazawa, S. Shibutani, T. Nishio, T. Aramoto, H. Higuchi, T. Arita, A. Hanafusa, K. Omura, M. Murozono and H. Takakura, *Solar Energy Materials and Solar Cells*, 1997, **49**, 205-212.

48. R. S. Singh, V. K. Rangari, S. Sanagapalli, V. Jayaraman, S. Mahendra and V. P. Singh, *Solar Energy Materials and Solar Cells*, 2004, **82**, 315-330.

49. R. R. Ahire, N. G. Deshpande, Y. G. Gudage, A. A. Sagade, S. D. Chavhan, D. M. Phase and R. Sharma, *Sensors and Actuators A: Physical*, 2007, **140**, 207-214.

50. J. Travas-Sejdic, H. Peng, R. P. Cooney, G. A. Bowmaker, M. B. Cannell and C. Soeller, *Current Applied Physics*, 2006, **6**, 562-566.

51. V. A. Smyntyna, V. Gerasutenko, S. Kashulis, G. Mattogno and S. Reghini, *Sensors and Actuators B: Chemical*, 1994, **19**, 464-465.

52. L. Yadava, R. Verma and R. Dwivedi, *Sensors and Actuators B: Chemical*, 2010, **144**, 37-42.

53. B. K. Miremadi, K. Colbow and Y. Harima, *Review of Scientific Instruments*, 1997, **68**, 3898-3903.

54. T. Gao and T. Wang, *Chemical Communications*, 2004, DOI: 10.1039/b411018h, 2558-2559.

55. T. Gao, Q. Li and T. Wang, *Chemistry of Materials*, 2005, **17**, 887-892.

56. V. Ladizhansky, G. Hodes and S. Vega, *The Journal of Physical Chemistry B*, 2000, **104**, 1939-1943.

57. Q. Zhou, A. Sussman, J. Chang, J. Dong, A. Zettl and W. Mickelson, *Sensors and Actuators A: Physical*, 2015, **223**, 67-75.

58. L. Qi, H. Cölfen and M. Antonietti, *Nano Letters*, 2001, **1**, 61-65.

59. M. N. Martin, J. I. Basham, P. Chando and S.-K. Eah, *Langmuir*, 2010, **26**, 7410-7417.

60. Y. Xia, J. J. McClelland, R. Gupta, D. Qin, X.-M. Zhao, L. L. Sohn, R. J. Celotta and G. M. Whitesides, *Advanced Materials*, 1997, **9**, 147-149.

61. Q. Kuang, C. Lao, Z. L. Wang, Z. Xie and L. Zheng, *Journal of the American Chemical Society*, 2007, **129**, 6070-6071.

62. R. L. Dellacà, P. Santus, A. Aliverti, N. Stevenson, S. Centanni, P. T. Macklem, A. Pedotti and P. M. A. Calverley, *European Respiratory Journal*, 2004, **23**, 232.

63. *India Pat.*, 201631033190 A, 2016.

64. I. Langmuir, *Journal of the American Chemical Society*, 1918, **40**, 1361-1403.

65. R. I. Masel, *Principles of Adsorption and Reaction on Solid Surfaces*, Wiley, 1996.

66. W. Jingjin, F. Ang, Z. Cezhou and J. S. Smith, Proceedings of the 20th IEEE International Symposium on the Physical and Failure Analysis of Integrated Circuits (IPFA), 2013.

67. H. Lüth, *Solid Surfaces, Interfaces and Thin Films*, Springer International Publishing, 2014.

68. H. Farahani, R. Wagiran and M. Hamidon, *Sensors*, 2014, **14**, 7881.

69. S. M. Kogan and V. B. Sandomirskii, *Bulletin of the Academy of Sciences of the USSR, Division of chemical science*, 1959, **8**, 1771-1773.

II. Paper Based Electronic Sensors

CHAPTER 6

Paper Based GMR Nanobiosensor for α-Amylase Estimation under Impulse Magnetic Field

Contents

ABSTRACT 171
6.1. Introduction 172
6.2. Materials and Methods 175
6.2.1 Materials 175
6.2.2 Ni-Ag Core Shell Nanoparticle Synthesis 176
6.2.3 Sensor Fabrication and Experimental method 178
6.2.4 Computational Details 179
6.3. Results and Discussion 181
6.3.1 Magnetoresistance in Impulse Magnetic Field 181
6.3.2 α-Amylase Detection 186
6.4. Conclusions 189
References 190

ABSTRACT

In giant magnetoresistance (GMR) phenomenon, the resistance of the layers of alternate ferromagnetic and non-magnetic materials significantly varies under the influence of an externally applied magnetic field. In the last few decades, GMR biosensors have shown immense potential in clinical diagnosis for their high sensitivity, output, and cost-effectiveness. In this chapter, we report the development of a GMR nanobiosensor using paper as a substrate and silver-nickel (Ag/Ni) nanoparticles as the sensing materials to detect levels of α-amylase in human blood serum. The Ag/Ni nanoparticles capped with starch was synthesized and deposited on filter papers to fabricate the paper nanobiosensor, which was then placed between an electromagnet. The paper nanobiosensor showed a variation in the electrical resistance under an impulse magnetic field. The maximum magnetoresistance achieved was more than 50% at room temperature. Dispensing amylase of known quantities led to the depletion of the equivalent amount of starch coated on the nanoparticles, which led to the variation in the magnetoresistance with the change in the amylase loading in the analyte. A calibration plot obtained from the known amount of amylase in analyte was employed to evaluate the actual amount of amylase in real life blood samples. A computational analysis was performed by numerically solving the governing equations with appropriate boundary conditions to determine the change in magnetization in ferromagnetic material, which uncovered that the applied magnetic field created a transient switching in magnetization direction for few nanoseconds. The transient switching was found to be a function of the size of the nanoparticle agglomerates. An atomistic model was developed to explain the GMR behavior observed in the experiments.

Manuscript is under preparation.

6.1. Introduction

The giant magnetoresistance (GMR) is a very uncommon quantum mechanical phenomena known to happen in the multilayer of electrically conductive thin films composing alternating ferromagnetic and non-magnetic layers. After the discovery in 1988,[1] GMR has been employed extensively in the fields of sensor and magnetic hard drive applications, which led to the 2007 Nobel Prize in Physics to Prof. Albert Fert and Prof. Peter Grünberg. The first GMR effect[1] has been observed in a multilayer iron (ferromagnetic) and chromium (nonmagnetic) in which the magnetic moment of the ferromagnetic material is found to depend on the dimensionality of the material.[4] The spin dependent scattering of electrons in the multilayer structure is found to be the main source of magnetoresistance in presence of an externally applied magnetic field.[2] Later on, various groups fabricated different types of multilayers to improve the effects associated with GMR.[3-5] For example, Lenssen et al. has shown that a GMR multilayer, which can withstand high temperature and high magnetic field.[6] A recent report demonstrated a wheatstone bridge-giant magnetoresistance (GMR)[7] sensor for the detection of biomaterial such as α-amylase . The sensor was fabricated using $[Co(1.5nm/Cu(1.0nm)]_{20}$ multilayer structures and Fe_2O_3 was employed as a magnetic tag for the biomolecules. In the similar line, a nanowire based GMR sensor was developed pressure sensing application.[8]

Apart from multilayer structure, granular GMR embodiments have also opened up another avenue to fabricate GMR sensors where instead of films ferromagnetic granules or nanoparticles are used.[9] For example, granular GMR has been reported by Xiong et al. and Xiao et al.[10, 11] at very low temperature. A more recent study by Gu et al. has shown the GMR effects employing the granular polymeric composites.[12] Further, nanostructures like

nanowire and nanoparticles of different materials have also been used to fabricate conventional and granular GMR sensors.[13-17]

Importantly, in the recent past the printable and stretchable GMR device have also been developed employing Co/Cu as components.[5, 18, 19] The MR effects have also been studied in highly pulsed magnetic field[20-22] where most of the studies are carried throughout a range of magnetic field. Recently, GMR effect has been uncovered using multilayer graphene in between Ni and Ag metal layers at room temperature.[23] The GMR effects are also found to be pronounced when a topological insulator has been sandwiched in between ferromagnets.[24, 25] In this situation, the device was fabricated by depositing ferromagnets on the diffusive surface of the topological insulator.

Of late, the GMR biosensors have shown immense potential in clinical diagnosis for their high sensitivity, output, and cost-effectiveness. Further, rapid, selective, low-cost, and highly sensitive point-of-care-testing (POCT) has become one of the major focus of research owing to its necessity in the detection of multifarious diseases at the user's site. In this direction, in the present chapter, we report the development of a GMR based biosensor using paper as a substrate and silver-nickel (Ag/Ni) nanoparticles as sensing materials to detect levels of α-amylase in human blood serum, suitable for POCT applications.

Typically, a nanobiosensor has five basic parts namely a receptor, an interface architecture, the transducer element, computer software, and an interface to human operator.[26-29] The recently invented bio-nanomaterials are found to be suitable for the biosensors for the detection of various biomarkers in the analytes.[30, 31] Of late, scientists have developed GMR sensors to be used as biosensors for various healthcare applications.[32, 33] For example, GMR biosensors have been employed to detect urinary[34], pulmonary,[35] and other[36-38] biomarkers alongside the detection of DNA target[39], quantification of cancer cells,[40] interleukin-6

protein,[41] hepatitis B virus,[42] and biological warfare agents,[43] among others. Multiple biomarkers like human immunoglobulin G and M can now be detected in a single chip using GMR sensors which is also incorporated in a smartphone interface.[44] At present, there is an increasing demand of lab-on-chip as well as POCT devices, which can improve health facilities where a patient can detect a biomarker without the help of any operator.[45, 46]

In this regard, the efficacies of the nanoscience and nanotechnology has shown their immense potential in the development of the proof-of-concept POCT prototypes,[47, 48] for the detection of multifarious biomarkers.[49-52] Further, the microelectromechanical systems (MEMS) integrated with the specialties of nanoscience and nanotechnology have also been in extensive use to fabricate miniaturized POCT devices.[53-55] The commonly available detection kits such as polymerase chain reaction (PCR) or enzyme-linked immunosorbent assay (ELISA) are to be replaced by the nano-enabled microfluidic POCT devices such as urine test strips, pregnancy kits, blood pressure meters, glucometer, and pH strips.[56-60] For example, in glucometers the material poly (3, 4-ethylenedioxythiophene) is found to efficiently trap glucose oxidase, which senses the varying current at different glucose concentrations. A colorimetric biosensor based on smartphone interface has been developed for the detection of diabetes in human saliva.[61] However, there are numerous biomarkers that require immediate attention in terms of the development of the POCT devices.

For example, the enzyme α-amylase (1,4-α-D-glucanglucanohydronase) is one such biomarker, which helps in the diagnosis of pancreatic disease.[62, 63] This enzyme is produced in salivary and pancreatic glands to break down starch into sugars like maltose and glucose.[64, 65] The hydrolysis of starch in presence of amylase is a saccharogenic approach, which has been widely employed for detection of α-amylase in human blood or saliva.[66] A normal human can have α-amylase in the range of 25-85 Units/Liter.[63] Previously, graphene

based immunosensors,[62] potentiometric sensors,[67] magneto-elastic sensors,[68] or colorimetric[61] have been employed to detect this enzyme in blood serum shown greater potential. However, there is hardly any study, which employ the GMR platform for the rapid and sensitive detection of α-amylase suitable for a portable POCT device.

In this chapter, we attempt to develop a GMR based nanobiosensor for the POC detection of α-amylase in human blood serum. Initially we report the fabrication of the GMR sensor composed of Ni-Ag core-shell nanoparticles deposited on a paper surface. The GMR effect is found to be active only when there a magnetic impulse is present. In order to corroborate the experimental observations, the variation in magnetization inside a ferromagnetic material with external magnetic field is also explored numerically solving the governing equations with appropriate boundary conditions.[69] Further, the spin transport mechanism in Ni-Ag particles has also been investigated computationally employing an atomistic model. Finally, the granular structured starch stabilized Ag/Ni nanoparticle core-shell GMR biosensor has been employed to detect α-amylase in human blood serum of different concentrations from 10-110 Units/L. In this regard, a calibration plot has been initially developed by dispensing known amount of amylase n the sensor and then noting down the change in the electrical resistance of the sensor. The calibration plot has been employed to detect the unknown amount of the amylase in the human blood serum. The reported GMR sensor has shown the potential to develop into a portable, inexpensive, easier to fabricate and miniaturized POCT device for the amylase detection.

6.2. Materials and Methods

6.2.1 Materials

Starch $(C_6H_{10}O_5)_n$ and Sodium Hydroxide (NaOH) pellets were procured from Merck (India). Porcine α-amylase enzyme, Nickel (II) Chloride ($NiCl_2$), 98% Hydrazine

Monohydrate ($H_4N_2.H_2O$) and Silver Nitrate ($AgNO_3$) were procured from Sigma-Aldrich (India). 10 x Phosphate buffer, D-Glucose ($C_6H_{12}O_6$) were obtained from SRL (India). Filter papers (Φ, 125 mm) were obtained from Whatmann (India). Ethyl alcohol was procured from Tedia (India). The chemicals mentioned above were of analytical grade and used in the experiments without any further treatment. Milli-Q grade water was used in cleaning and for preparing solutions.

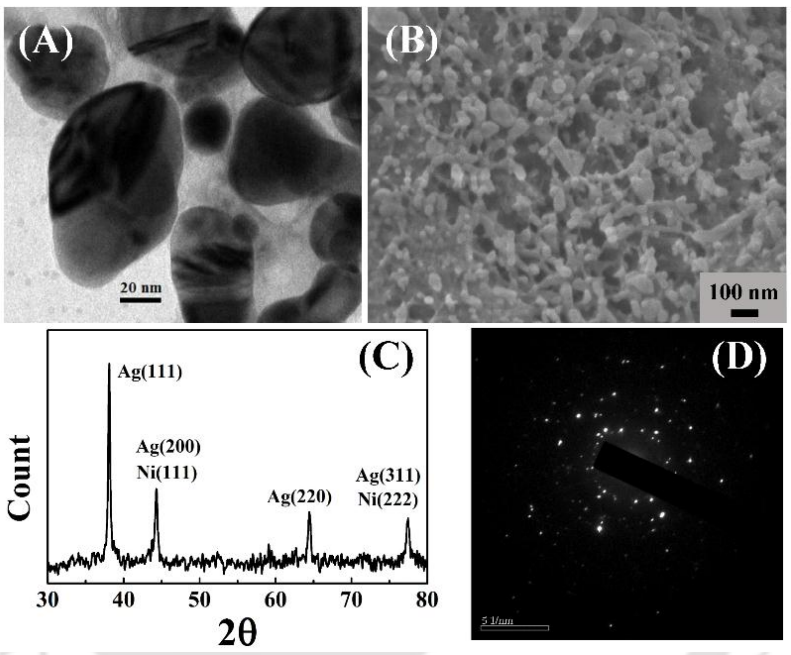

Figure 6.1: Image (A) shows the TEM image of Ni-Ag core shell nanoparticles. Image (B) shows the FESEM image of Ni-Ag core shell nanoparticles deposited on a paper substrate. Image (C) shows the XRD of Ni-Ag core shell nanoparticle. Image (D) shows the SAED pattern of Ni-Ag nanoparticles.

6.2.2 Ni-Ag Core Shell Nanoparticle Synthesis

In order to obtain Ni-Ag core shell nanoparticles, Ni nanoparticles were prepared with hydrazine reduction[70] of $NiCl_2$. 5mM $NiCl_2$ and 0.1M hydrazine was added in ethanol. Then NaOH (0.1M) was added (10 µl per 1 ml) to the above solution as a catalyst. Ni nanoparticles were formed after 1 h continuous stirring at 60ºC. The Ni nanoparticles were magnetically recovered and re-dispersed in fresh ethanol for synthesis of Ni-Ag core shell

nanoparticles. 2.5mM Silver nitrate ($AgNO_3$) and 0.05mM hydrazine were added to the above solution. Ni-Ag core shell nanoparticles were formed after 0.5 hr stirring at room temperature. The characterization of synthesized nanoparticles and prepared sample is shown in Figure 6.1 where Figure 6.1(A) shows the TEM image and the FESEM image in Figure 6.1(B) shows the morphology of the prepared film. Moreover, characteristics peaks at 2θ = 38.2, 44.4, 64.6 and 77.6 in XRD data of nanoparticles in Figure 6.1(C) confirms the presence of face centered cubic (FCC) Ag (111), (200), (220) and (311) planes and the characteristics peaks of FCC Ni (111) and (222) planes at 2θ = 44.5 and 76.4 were overlapped with FCC Ag (200) and (311) planes.[70] Typical SAED pattern in Figure 6.1(D) also shows the prepared nanoparticles were polycrystalline in nature.

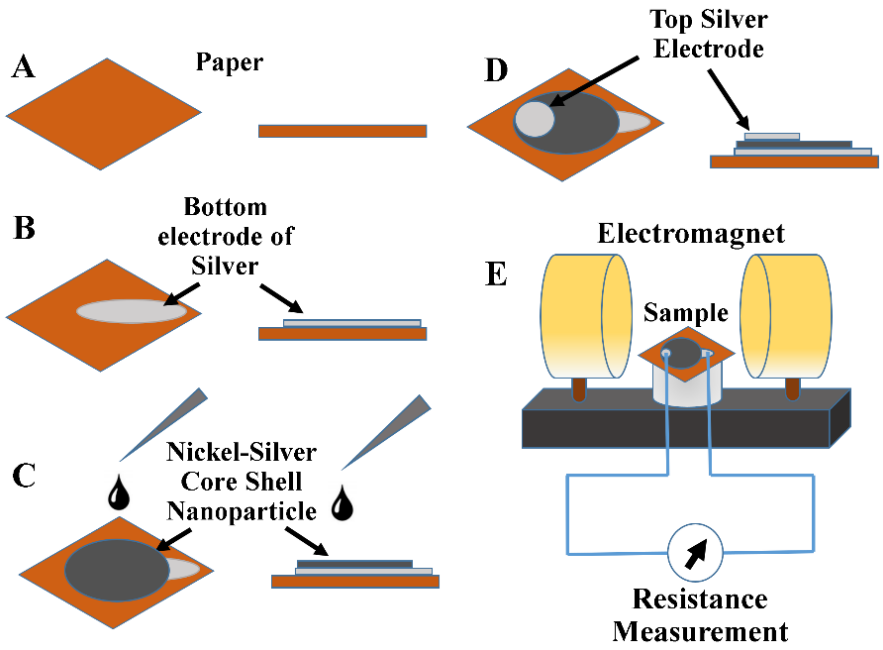

Figure 6.2: Images (A) to (D) show the steps of fabrication of the magnetoresistive sensor on a paper substrate. Image (E) schematically shows the experimental set-up employed for the magnetoresistance experiment where the sensor was kept in between two electromagnets, which produces pulsed magnetic field.

A part of Ni nanoparticles was used to synthesize silver capped-nickel nanoparticles. The α-amylase solutions of 10, 30, 50, 80, 100, and 110 U/L concentrations were prepared by dissolving the specific amount of enzyme into 1× phosphate buffer solution.

6.2.3 Sensor Fabrication and Experimental method

A bottom silver electrode was made on a 1 cm × 1 cm filter paper (Whatman cat no. 1001 125 grade 1) with silver paste and kept it for 12 hour to get it dried. Prepared Ni-Ag core-shell nanoparticles were magnetically accumulated at the bottom of the container and 50 µl Ni-Ag core shell nanoparticle was dropped on the filter paper using micropipette. The prepared sample was kept again for 24 hour in order to get dried. Top contacts was made on the sample with conductive silver paste. Again the sample kept for 12 hour after silver contact was made.

Measurement was taken using electromagnet (EMU-50, DPS-50 Model from SES Instruments Pvt. Ltd.) and digital multimeter (MASTECH M92A(H)). The prepared sample was placed in between the electromagnet and the contacts were connected to a digital multimeter using copper electrodes. Magnetic impulse was given using the electromagnet and the data was recorded. The magnetic field applied is in the range of 0-2 kGauss. The sensor fabrication steps are given in Figure 6.2 (A – D), whereas the experimental set-up is illustrated in image (E). The normalized MR is calculated in impulse magnetic field using the Eq. 6.1.

$$MR = \frac{R(0) - R(H)}{R(H)}. \qquad (6.1)$$

where *R(H)* and *R(0)* indicates the resistance of the sample with and without magnetic field.

6.2.4 Computational Details

In this study, a Matlab based micromagnetic computational model M3[71, 72] is employed to understand the physics inside ferromagnetic materials, which is governed by the Landau-Lifshitz-Gilbert equation as shown below,

$$\frac{\partial M}{\partial t} = -\gamma M \times H_{eff} + \frac{\alpha}{M_s} M \times \frac{\partial M}{\partial t}. \quad (6.2)$$

where M_s is saturation magnetization which is material property, α is damping constant and γ is the gyromagnetic ratio. The effective magnetic field H_{eff} expression is given in the later section of this chapter. It is found that if an impulsive external magnetic field is applied to a ferromagnetic particle then the magnetization switches from one direction to other depending on the direction of external magnetic field. The transition takes few nanoseconds to come to the steady state. Since the magnetization vector M has a rotational effect with H_{eff} , the magnetization vector oscillates before comes in equilibrium and such a oscillations cause a low positive MR.

In order to calculate the magnetostatic interaction field, a Fast Fourier transform (FFT) method is employed, utilizing Newell's demagnetizing tensor formulation[73] at short distances and a dipole approximation for the far field. For the exchange interaction six neighbor method is implemented with Neumann boundary conditions having non-periodic boundaries.[74] Interlayer exchange coupling is implemented using modified boundary conditions for the layers next to the interlayer. The dynamics of a 50 × 50 × 50 nm cubical Ni are calculated. The parameters of the material are as follows: A = 0.86 × 10^{-11}J/m, Ms = 484.1 kA/m, α = 1, γ = 2.21x10^5 m/As (1.7595 × 10^7 Hz/Oe).[75, 76] The parameters were selected based on the reports in literature. A three layered structure can be used to understand some basic mechanisms of the experimental results. Atomistic Toolkit is used

to study the spin-transport simulation after optimizing the geometry. The whole system is described by a spin polarized density functional theory[77] (DFT) with the non-equilibrium Green's function (NEGF) technique.[77, 78] The exchange correlation has been taken as spin polarized generalized gradient approximation (SGGA) in the form of Perdew-Burke-Ernzerhof (PBE) functional. A single-polarized basis is set for Nickel atoms and double polarized is set for the other atoms. The Monck Horst-Pack grid with (6, 6, 100) k-points is applied in the 3D Brillouin zone.

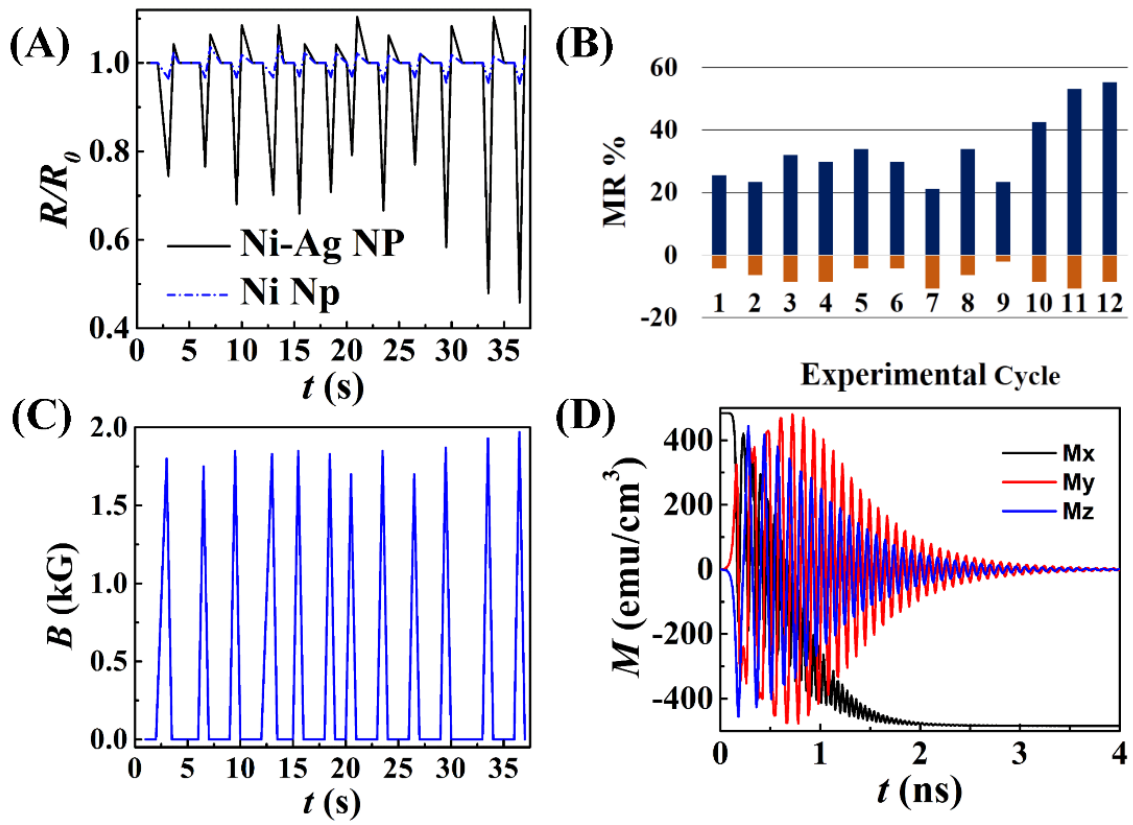

Figure 6.3: Image (A) shows the change in normalized resistance with time due to applied impulse magnetic field. Image (B) shows the magnetoresistance percentage (MR%) due to applied magnetic impulse. The applied magnetic impulse is shown in plot (C). Image (D) shows the computational result of the change in magnetization in X, Y, and Z direction after applying an external magnetic field in X-direction in a Ni nanoparticle.

6.3. Results and Discussion

6.3.1 Magnetoresistance in Impulse Magnetic Field

GMR effect in a multilayer or granular system is because of the spin dependent scattering of electrons. In ordinary MR the resistance of a metal increases with external magnetic field.[79] A layer of Ag-Ni core shell nanoparticles were formed on a paper. The effect of pulsed magnetic field was studied and the change in resistance is shown here in Figure 6.3(A). The normalized MR is calculated in impulse magnetic field using the Eq. (6.1).

The MR study here was done in room temperature and we got a maximum of 50-55% of MR for current perpendicular to plane (CPP) geometry. The bar graph in Figure 6.3(B) shows the percentage of MR for different cycles of experiments. The corresponding magnetic field pulses are shown in image (C). However, Figure 6.3(D) shows a computational study of change in X, Y, and Z direction magnetizations inside a ferromagnetic Ni nanoparticle when a magnetic field of 200 Oe was applied in X-direction. The reason behind the magnetoresistive response can be attributed to the oscillation of the magnetization which took place in each nearby magnetic Ni nanoparticles separated by an Ag layer.

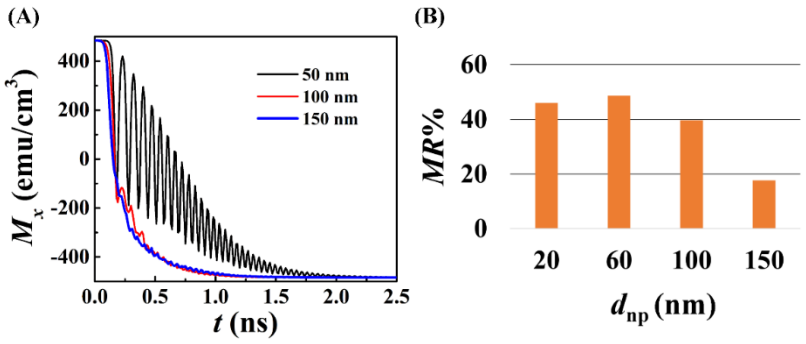

Figure 6.4: Image (A) shows the computational result of the switching of X-directional magnetization for different sized Ni nanoparticles. Image (B) shows the experimental magnetoresistance (MR%) values of fabricated magnetoresistive sensor for different sized Ni-Ag nanoparticle.

The oscillation in the magnetization produced parallel magnetization condition which led to a decrease in the resistance. However, only nickel nanoparticles showed substantially less magnetoresistance in presence of magnetic field. In case of, Ni nanoparticles the change was due to the colossal magnetoresistance which increased heavily in the Ni-Ag particles due to the effect of giant magnetoresistance.

With the decrease in the particle size, a higher switching time from one magnetization to the other was observed in the simulation as shown in Figure 6.4(A). Hence, a similar consequence was observed in experimental magnetoresistance as illustrated in image (B) of Figure 6.4. The magnetoresistance was higher in case of small particles due to the increase in the oscillation of magnetizations. It was observed that the response was highest for ~50 nm particle size. The magnetization distribution in a ferromagnetic material is governed by the following Landau-Lifshitz-Gilbert[80] equation as described previously,

$$\frac{\partial M}{\partial t} = -\gamma M \times H_{eff} + \frac{\alpha}{M_S} M \times \frac{\partial M}{\partial t}. \qquad (6.2)$$

Where M_s is saturation magnetization which is material property, α is damping constant and γ is the gyromagnetic ratio. The first term in right hand side of the Eq. (6.2) represents the rotation of magnetization vector around an effective magnetic field. The second term contains the local damping mechanism. The magnetization vector M gains equilibrium with magnetic field alignment. The effective magnetic field H_{eff} expression is shown in Eq. 6.3

$$H_{eff} = \frac{2A}{\mu_0 M_S} \Delta \hat{m} - \frac{1}{\mu_0 M_S} \frac{\partial f_{ani}(\hat{m})}{\partial \hat{m}} + H_d + H_{ex}. \qquad (6.3)$$

The first term in Eq. (6.3) is due to exchange coupling where A is the exchange constant which is the measure for magnetic stiffness of ferromagnetic material. The second term refers the magneto-crystalline anisotropy where f_{ani} gives the angular dependency. The parameter H_d is the demagnetization field and all other external magnetic field effect is given by H_{ex}. Figure 6.3(C) is a simulation result that explains how the magnetization in X, Y, Z direction changes in applied magnetic field and the system reaches equilibrium after few ns. That explains Figure 6.3(A), where the change in resistance took place only at impulse magnetic field. Here a small amount of negative magnetoresistance was also observed as there exists an oscillation in magnetization as shown in Figure 6.3(C). Moreover, Figure 6.3(D) shows a dependency of magnetization (M_X) switching time with average magnetic particle size. Experimentally the MR was measured for different sized Ni-Ag nanoparticles and it was observed that percentage of MR decreases with size of nanoparticles as shown in Figure 6.4 as discussed earlier.

In order to understand the quantum mechanical phenomenon in a silver-nickel-silver multilayer structure an atomistic simulation was also performed. micromagnetic simulation shows that there is oscillation in the magnetization in the all three direction and the oscillation in the X-direction (direction of external magnetic field) depends largely on the size of the nanoparticle. The ~50 nm particle showed the highest oscillation and this was reflected in the experimental results where the MR response was maximum for ~50 nm particle. However, the quantum transport for the similar structure was yet to be studied up to this point and hence the atomistic simulation was intended. The puposeof this simulation was to study the transmission spectra, density of states, and current in the device for both spin-up and spin-down electron.

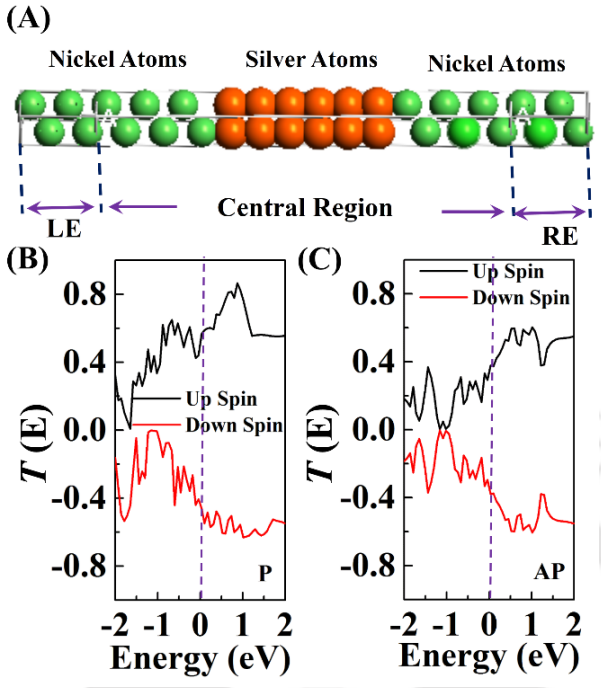

Figure 6.5: Image (A) shows the computational geometry of the atomistic system under consideration. The left electrode (LE), central scattering region and right electrode (RE) of the system are demarcated using vertical dotted lines. In this image, the green spheres represent Ni atoms and orange spheres represent Ag atoms. Images (B) and (C) show the transmission spectrum of up and down spin electrons for parallel (P) and anti-parallel (AP) configuration respectively. The Fermi energy E_F of the system is denoted by the broken lines in images (B) and (C).

The three-layer structure as discussed in the computational details section is illustrated in image (A) of Figure 6.5, where silver layer is sandwiched between two nickel layers. An atomistic simulation was carried out to understand the spin dependent transport of electron. The details of the simulations are already discussed earlier in the computational details section. It is important to note that the geometry as shown in the image is divided in to three different layers. The left side represents left electrode which is connected with the central region where the transport and other parameters will be calculated and the right side represents the right electrode. The transmission spectrum was first calculated for both spin-up and spin-down electron to study the quantum conductance, $G = G_0 T(E)$ where $G_0 = 2e^2/h$ and T(E) is the transmission spectrum.

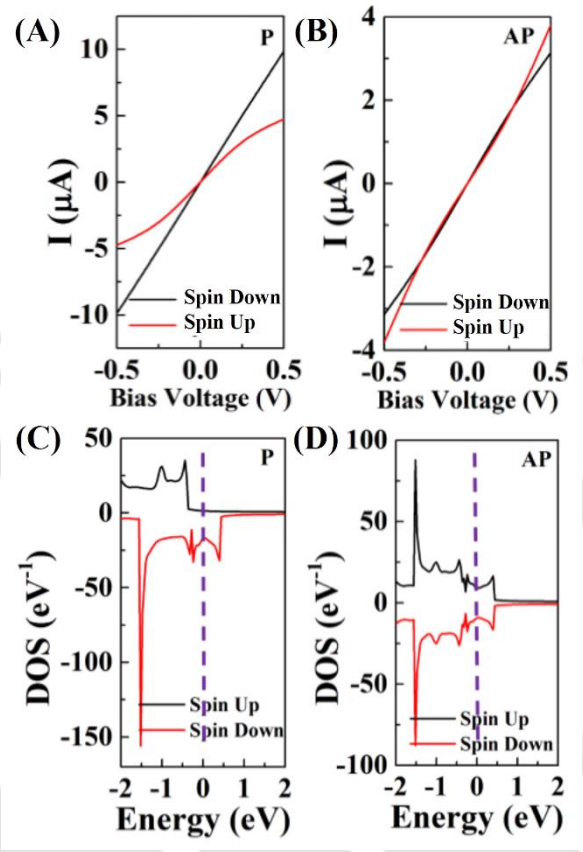

Figure 6.6: Image (A) shows the spin polarized current for spin up and spin down electrons in parallel (P) configuration, whereas image (B) shows the spin polarized current for spin up and spin down electrons for anti-parallel (AP) configuration. Images (C) and (D) show the density of states (DOS) of electron for parallel and anti-parallel configuration, respectively. Dotted lines in images (C) and (D) represents the Fermi energy E_F of the system.

Electron transmission spectra of spin-up and spin-down electrons are shown in Figure 6.5(B) and 6.5(C) for both parallel (P) and anti-parallel (AP) magnetizations, respectively. It is clear from Figure 6.5(B) that the spin-up and spin down electron have a broad peak around fermi level (E_F) but the spin up electron has more transmission coefficient than that of spin down which indicates the ease of spin up electron transport through the device, however, anti-parallel configuration have similar transmission spectrum for both spin up and down electron as shown in Figure 6.5(C).

The asymmetric spin up and spin down current in Figure 6.6(A) and 6.6(B) indicate spin polarization in both the parallel and anti-parallel case, though the spin polarization in antiparallel case is very less. We also discuss the device density of states (DOS) to understand the spin polarization in P and AP configurations. The DOS, shown in Figure 6.6(C) and 6.6(D), suggests only spin down electrons have a peak near the Fermi energy at ±1.5eV in parallel configuration. However, the DOS looks similar for both spin-up and spin-down electrons in case of anti-parallel configurations. Thus, the parallel configuration have considerable amount of spin polarization, which lead to a magnetoresistive response.

6.3.2 *α*-Amylase Detection

The sensor for the detection of α-amylase was prepared using the starch coated Ni-Ag nanoparticles. 0.2% w/v of starch solution was taken in freshly prepared nickel nanoparticles. The solution was sonicated for 15 min followed by the addition of 0.001M solution of $AgNO_3$ which was again kept in the sonication bath for 10mins at room temperature. 0.1 M Glucose and 0.1 M NaOH was then added to the solution. The formation of silver nanoparticles was confirmed when the solution turned orange after an hour in the sonicator. After the preparation, a series of characterization experiments were performed to confirm the attachment of starch molecule to the Ag surface.

Characterizations: UV-Vis spectroscopy confirmed the formation of Ni-Ag, Ag-starch, and Ni-Ag-starch NPs as shown in Figure 6.7. The absorption band at 414 nm depicts the characteristics absorption peak of silver nanoparticles and the narrow range indicates the fine size distribution. The hydroxyl groups of starch facilitate combination of silver ions in the molecular matrix while the aldehyde groups ease the reduction. The peak for the Ni-Ag nanoparticles was broadened as expected due the presence of Ni nanoparticles and the peak shifted to its left after being attached to the starch molecules as illustrated in literature.

The FTIR spectra of starch capped silver nanoparticles and pure starch is given in Figure 6.8. Pure starch exhibited characteristic peaks at 3301 cm^{-1} assigned to -OH stretching, 1639 cm^{-1} to -OH bending of water, 2920 cm^{-1} to C-H stretching, 1338 cm^{-1} to –CO stretching of primary alcoholic groups and 1018 cm^{-1} to C-O-C symmetrical stretching. The FTIR spectra of starch capped silver nanoparticles show a similar pattern with slight shift in frequencies showing interaction of –OH groups.

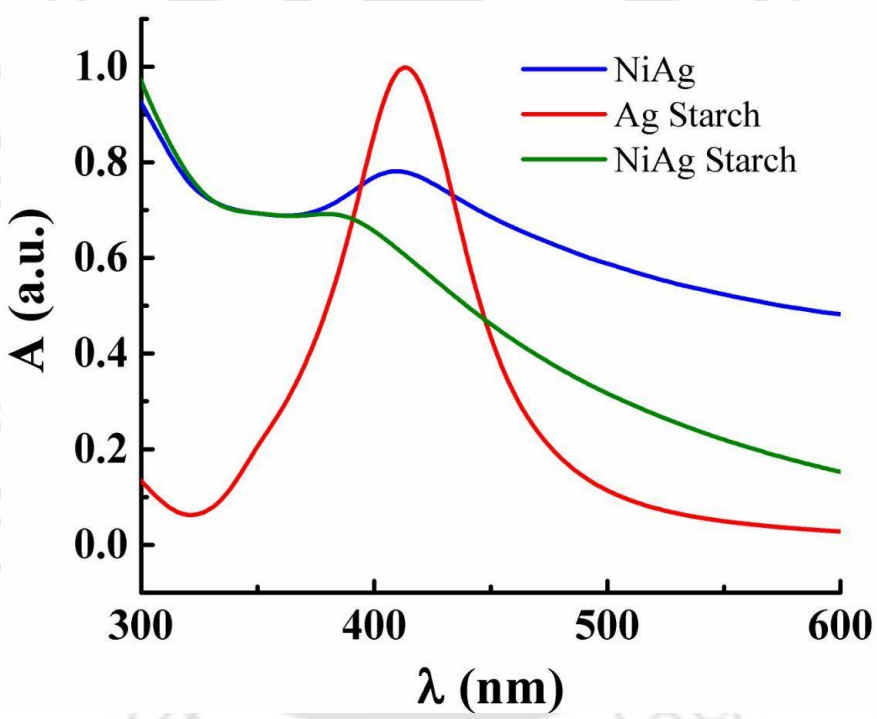

Figure 6.7: This figure shows the UV-Vis spectra of the synthesized Ni-Ag nanoparticles, Ag-starch and Ni-Ag starch nanoparticles.

The UV-Vis spectroscopy study was not sufficient although a shift in the peak of absorption spectra was clearly visible in the plot. Thus, the FTIR study of the same composite was carried out followed by an EDS study of the same. In both the cases, the attachment of starch was indicated and hence it was confirmfed.

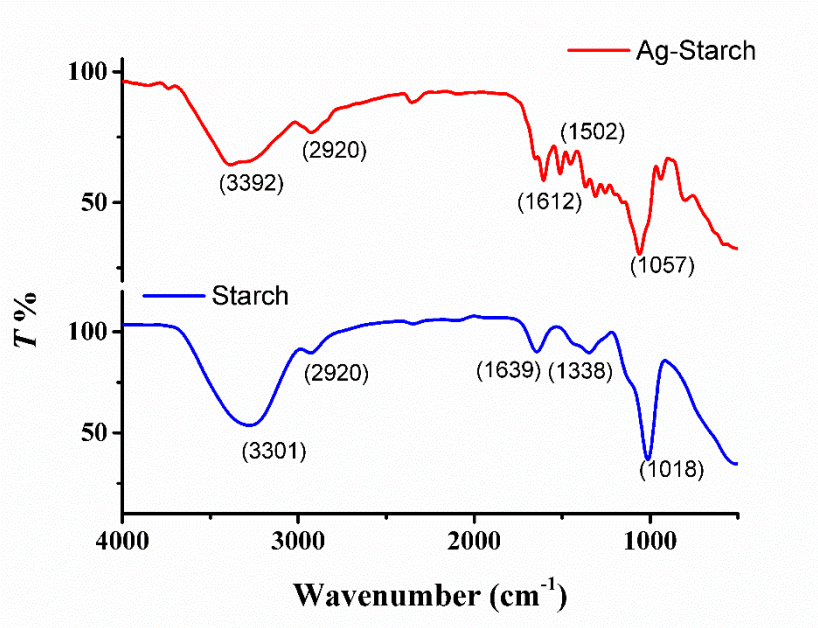

Figure 6.8: This figure shows the FTIR spectra for the starch and Ag-starch composite to confirm the attachment of starch to the Ag surface.

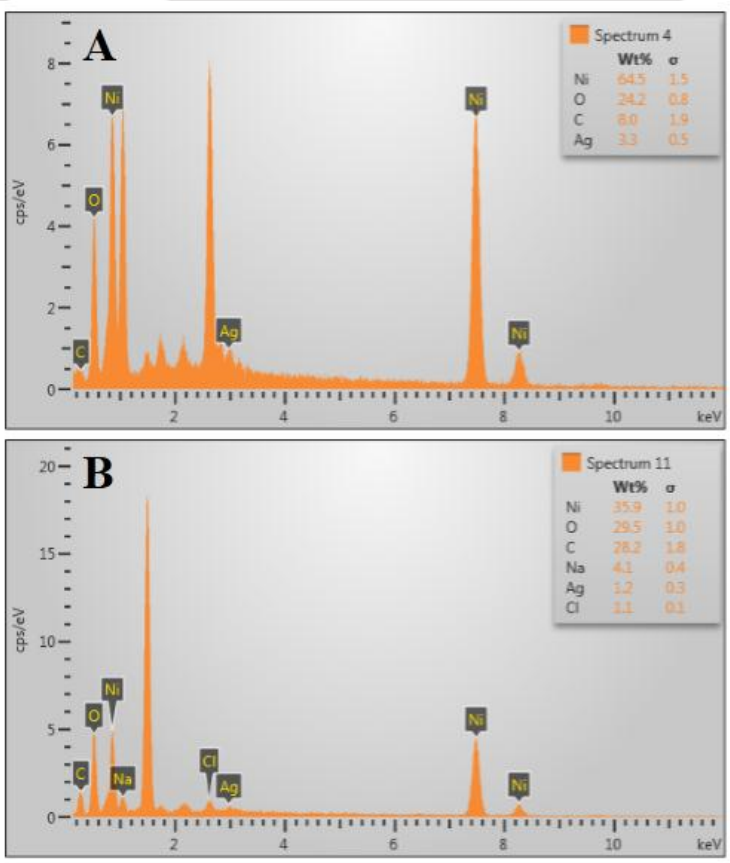

Figure 6.9: This figure shows the EDS spectra for (A) Ni-Ag and (B) Ni-Ag-starch composite to confirm the presence of elements in the prepared samples.

The EDS spectra of Nickel-Silver nanoparticles and Nickel-with starch coated silver nanoparticles in Figure 6.9 (A) and (B) shows distinct peaks of Nickel and Silver thus confirming their presence.

Detection: The experiments to detect the α-amylase was performed using the same set-up explained in Figure 6.1. The base response of the sensor was measured initially before performing the tests with amylase sample. The difference between responses before and after amylase introduction was then calibrated with the concentration of the amylase. A calibration curve was formed using the known concentrations of the amylase. Thereafter, experiments were performed using human blood-serum sample and it was found that the response of the sensor was similar to that of the readings received from hospitals. Figure 6.10 shows the calibration curve and the readings for bio samples are scattered in the plot.

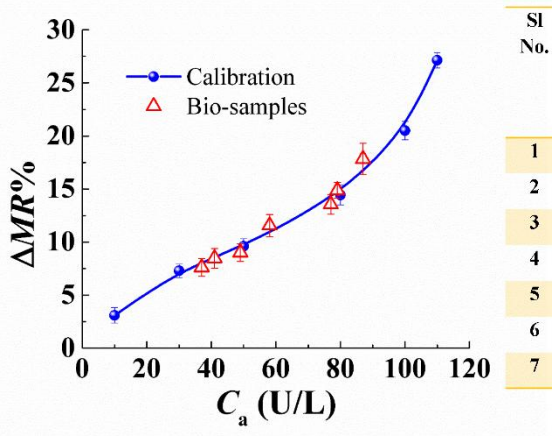

Sl No.	Amylase level in blood serum from clinically approved method (U/L)	Calibration curve (ΔMR%)	Associated standard deviation	Amylase concentration from the sensor (U/L)
1	49	9.003333	0.810514	**45.0±3**
2	41	8.473333	0.932863	**40.5±3.5**
3	58	11.56	1.050857	**61±4**
4	79	14.87333	0.749689	**78.5±2.5**
5	87	17.83	1.468094	**90.0±4**
6	77	13.55	0.9219	**75.5±3**
7	37	7.606667	0.820508	**34.6±2**

Figure 6.10: This figure shows the calibration plot for the detection of α-amylase. The red scattered points in the graph are indicating the bio-sample values. The table shows the comparison of values obtained from the Dimension RxL Max Integrated Chemistry System, SIEMENSTM, for human serum and the response of the proposed sensor.

6.4. Conclusions

In summary, the MR effect in granular structure with core shell nanoparticles in impulse magnetic field was discussed and it was significantly as high as ~50% even at room

temperature. The computational study indicated a relation of magnetization switching with the size of ferromagnetic nanoparticle. It was observed that the response of the sensor increases with the decrease in the nanoparticle size. However, at 50 nm, the magnetoresistance response saturates as the magnetization oscillation was found to be highest at that dimension.

A paper-based sensor using GMR phenomena has been fabricated to detect the concentration of α-amylase in human blood serum for the diagnosis of pancreatitis. We observed that with different concentrations of α-amylase, the magnetoresistance increased which was then plotted accordingly. In order to validate the results, the sensors were experimented with human blood samples. The results with human blood samples were similar to that of the results from the standard pathological testing of the α-amylase samples.

References

1. M. N. Baibich, J. M. Broto, A. Fert, F. N. Van Dau, F. Petroff, P. Etienne, G. Creuzet, A. Friederich and J. Chazelas, *Physical Review Letters*, 1988, **61**, 2472-2475.
2. G. A. Prinz, *Science*, 1998, **282**, 1660-1663.
3. J. Daughton, J. Brown, E. Chen, R. Beech, A. Pohm and W. Kude, *IEEE Transactions on Magnetics*, 1994, **30**, 4608-4610.
4. J. C. Rife, M. M. Miller, P. E. Sheehan, C. R. Tamanaha, M. Tondra and L. J. Whitman, *Sensors and Actuators A: Physical*, 2003, **107**, 209-218.
5. M. Melzer, D. Makarov, A. Calvimontes, D. Karnaushenko, S. Baunack, R. Kaltofen, Y. Mei and O. G. Schmidt, *Nano Letters*, 2011, **11**, 2522-2526.

6. K. M. H. Lenssen, D. J. Adelerhof, H. J. Gassen, A. E. T. Kuiper, G. H. J. Somers and J. B. A. D. van Zon, *Sensors and Actuators A: Physical*, 2000, **85**, 1-8.

7. G. Antarnusa, P. E. Swastika and E. Suharyadi, *Journal of Physics: Conference Series*, 2018, **1011**, 012061.

8. J. J. Park, K. S. M. Reddy, B. Stadler and A. Flatau, *IEEE Sensors Journal*, 2017, **17**, 2015-2020.

9. H. Gu, J. Guo, X. Yan, H. Wei, X. Zhang, J. Liu, Y. Huang, S. Wei and Z. Guo, *Polymer*, DOI: http://dx.doi.org/10.1016/j.polymer.2014.05.024.

10. P. Xiong, G. Xiao, J. Q. Wang, J. Q. Xiao, J. S. Jiang and C. L. Chien, *Physical Review Letters*, 1992, **69**, 3220-3223.

11. J. Q. Xiao, J. S. Jiang and C. L. Chien, *Physical Review Letters*, 1992, **68**, 3749-3752.

12. H. Gu, J. Guo, X. Yan, H. Wei, X. Zhang, J. Liu, Y. Huang, S. Wei and Z. Guo, *Polymer*, 2014, **55**, 4405-4419.

13. B. Cox, D. Davis and N. Crews, *Sensors and Actuators A: Physical*, 2013, **203**, 335-340.

14. G.-T. Jose, V. Elisa and G. Elvira, *Nanotechnology*, 2012, **23**, 405701.

15. A. B. Granovsky, M. Ilyn, A. Zhukov, V. Zhukova and J. Gonzalez, *Phys. Solid State*, 2011, **53**, 320-322.

16. R. P. Tan, J. S. Lee, J. U. Cho, S. J. Noh, D. K. Kim and Y. K. Kim, *Journal of Physics D: Applied Physics*, 2010, **43**, 165002.

17. I. Enculescu, M. E. Toimil-Molares, C. Zet, M. Daub, L. Westerberg, R. Neumann and R. Spohr, *Appl. Phys. A*, 2007, **86**, 43-47.

18. D. Karnaushenko, D. Makarov, C. Yan, R. Streubel and O. G. Schmidt, *Advanced Materials*, 2012, **24**, 4518-4522.

19. Y.-f. Chen, Y. Mei, R. Kaltofen, J. I. Mönch, J. Schumann, J. Freudenberger, H.-J. Klauß and O. G. Schmidt, *Advanced Materials*, 2008, **20**, 3224-3228.

20. T. Stankevič, L. Medišauskas, V. Stankevič, S. Balevičius, N. Žurauskienė, O. Liebfried and M. Schneider, *Review of Scientific Instruments*, 2014, **85**, -.

21. E. Broide and M. Yakunin, *J Supercond Nov Magn*, 2008, **21**, 161-162.

22. J. Freudenberger, N. Kozlova, A. Gaganov, L. Schultz, H. Witte and H. Jones, *Cryogenics*, 2006, **46**, 724-729.

23. S. C. Bodepudi, A. P. Singh and S. Pramanik, *Nano Letters*, 2014, **14**, 2233-2241.

24. K. Taguchi, T. Yokoyama and Y. Tanaka, *Physical Review B*, 2014, **89**, 085407.

25. Z.-Y. Quan, L. Zhang, W. Liu, H. Zeng and X.-H. Xu, *Nanoscale Res Lett*, 2014, **9**, 1-7.

26. L. Setti, C. Piana, S. Bonazzi, B. Ballarin, D. Frascaro, A. Fraleoni-Morgera and S. Giuliani, *Analytical Letters*, 2004, **37**, 1559-1570.

27. A. Ibraheem and R. E. Campbell, *Current Opinion in Chemical Biology*, 2010, **14**, 30-36.

28. S. Cherukuri, K. K. Venkatasubramanian and S. K. S. Gupta, 2003.

29. J. R. North, *Trends in Biotechnology*, 1985, **3**, 180-186.

30. A. W. Martinez, S. T. Phillips, G. M. Whitesides and E. Carrilho, *Analytical Chemistry*, 2010, **82**, 3-10.

31. A. Poghossian and M. J. Schöning, *Electroanalysis*, 2014, **26**, 1197-1213.

32. J. Llandro, J. J. Palfreyman, A. Ionescu and C. H. W. Barnes, *Medical & Biological Engineering & Computing*, 2010, **48**, 977-998.

33. R. S. Gaster, L. Xu, S.-J. Han, R. J. Wilson, D. A. Hall, S. J. Osterfeld, H. Yu and S. X. Wang, *Nature Nanotechnology*, 2011, **6**, 314.

34. O. Liangos, H. Tighiouart, M. C. Perianayagam, A. Kolyada, W. K. Han, R. Wald, J. V. Bonventre and B. L. Jaber, *Biomarkers*, 2009, **14**, 423-431.

35. S. A. Kharitonov and P. J. Barnes, *Biomarkers*, 2002, **7**, 1-32.

36. J. Skog, T. Würdinger, S. van Rijn, D. H. Meijer, L. Gainche, W. T. Curry Jr, B. S. Carter, A. M. Krichevsky and X. O. Breakefield, *Nature Cell Biology*, 2008, **10**, 1470.

37. C. R. Jack, D. S. Knopman, W. J. Jagust, L. M. Shaw, P. S. Aisen, M. W. Weiner, R. C. Petersen and J. Q. Trojanowski, *The Lancet Neurology*, 2010, **9**, 119-128.

38. S. S. Sehnert, L. Jiang, J. F. Burdick and T. H. Risby, *Biomarkers*, 2002, **7**, 174-187.

39. G. Rizzi, J.-R. Lee, P. Guldberg, M. Dufva, S. X. Wang and M. F. Hansen, *Biosensors and Bioelectronics*, 2017, **93**, 155-160.

40. G. Kokkinis, S. Cardoso, F. Keplinger and I. Giouroudi, *Sensors and Actuators B: Chemical*, 2017, **241**, 438-445.

41. Y. Li, B. Srinivasan, Y. Jing, X. Yao, M. A. Hugger, J.-P. Wang and C. Xing, *Journal of the American Chemical Society*, 2010, **132**, 4388-4392.

42. X. Zhi, M. Deng, H. Yang, G. Gao, K. Wang, H. Fu, Y. Zhang, D. Chen and D. Cui, *Biosensors and Bioelectronics*, 2014, **54**, 372-377.

43. R. L. Edelstein, C. R. Tamanaha, P. E. Sheehan, M. M. Miller, D. R. Baselt, L. J. Whitman and R. J. Colton, *Biosensors and Bioelectronics*, 2000, **14**, 805-813.

44. J. Choi, A. W. Gani, D. J. B. Bechstein, J.-R. Lee, P. J. Utz and S. X. Wang, *Biosensors and Bioelectronics*, 2016, **85**, 1-7.

45. L. Syedmoradi, M. Daneshpour, M. Alvandipour, F. A. Gomez, H. Hajghassem and K. Omidfar, *Biosensors and Bioelectronics*, 2017, **87**, 373-387.

46. C. D. Chin, V. Linder and S. K. Sia, *Lab on a Chip*, 2007, **7**, 41-57.

47. T. Kubik, K. Bogunia-Kubik and M. Sugisaka, *Current Pharmaceutical Biotechnology*, 2005, **6**, 17-33.

48. M. M.-C. Cheng, G. Cuda, Y. L. Bunimovich, M. Gaspari, J. R. Heath, H. D. Hill, C. A. Mirkin, A. J. Nijdam, R. Terracciano, T. Thundat and M. Ferrari, *Current Opinion in Chemical Biology*, 2006, **10**, 11-19.

49. A. Maria de Souza Antunes, M. Simone de Menezes Alencar, C. Henrique da Silva, J. Nunes and F. Maria Lins Mendes, *Recent Patents on Nanotechnology*, 2012, **6**, 29-43.

50. N. Sozer and J. L. Kokini, *Trends in Biotechnology*, 2009, **27**, 82-89.

51. S. Singh and H. S. Nalwa, *Journal of Nanoscience and Nanotechnology*, 2007, **7**, 3048-3070.

52. J. Safari and Z. Zarnegar, *Journal of Saudi Chemical Society*, 2014, **18**, 85-99.

53. C. H. Ahn, C. Jin-Woo, G. Beaucage, J. H. Nevin, L. Jeong-Bong, A. Puntambekar and J. Y. Lee, *Proceedings of the IEEE*, 2004, **92**, 154-173.

54. B. Robert, *Sensor Review*, 2007, **27**, 7-13.

55. Y. Huang, E. L. Mather, J. L. Bell and M. Madou, *Analytical and Bioanalytical Chemistry*, 2002, **372**, 49-65.

56. E. M. Fenton, M. R. Mascarenas, G. P. López and S. S. Sibbett, *ACS Applied Materials & Interfaces*, 2009, **1**, 124-129.

57. Y. Du, A. Pothukuchy, J. D. Gollihar, A. Nourani, B. Li and A. D. Ellington, *Angewandte Chemie International Edition*, 2017, **56**, 992-996.

58. E. O'Brien, R. Asmar, L. Beilin, Y. Imai, J.-M. Mallion, G. Mancia, T. Mengden, M. Myers, P. Padfield, P. Palatini, G. Parati, T. Pickering, J. Redon, J. Staessen, G. Stergiou, P. Verdecchia and o. b. o. t. E. S. o. H. W. G. o. B. P. Monitoring, *Journal of Hypertension*, 2003, **21**, 821-848.

59. L. V. Rao, F. Jakubiak, J. S. Sidwell, J. W. Winkelman and M. L. Snyder, *Clinica Chimica Acta*, 2005, **356**, 178-183.

60. Y. Takahashi, H. Kasai, H. Nakanishi and T. M. Suzuki, *Angewandte Chemie*, 2006, **118**, 927-930.

61. A. Soni and S. K. Jha, *Analytica Chimica Acta*, 2017, **996**, 54-63.

62. S. R. Teixeira, C. Lloyd, S. Yao, G. Andrea Salvatore, I. S. Whitaker, L. Francis, R. S. Conlan and E. Azzopardi, *Biosensors and Bioelectronics*, 2016, **85**, 395-402.

63. S. Dutta, N. Mandal and D. Bandyopadhyay, *Biosensors and Bioelectronics*, 2016, **78**, 447-453.

64. G. J. Tortora and B. H. Derrickson, *Principles of Anatomy and Physiology*, John Wiley & Sons, 2008.

65. J. Singh, A. Dartois and L. Kaur, *Trends in Food Science & Technology*, 2010, **21**, 168-180.

66. L. Zajoncová, M. Jílek, V. Beranová and P. Peč, *Biosensors and Bioelectronics*, 2004, **20**, 240-245.

67. N. Sakač, M. Sak-Bosnar, M. Horvat, D. Madunić-Čačić, A. Szechenyi and B. Kovacs, *Talanta*, 2011, **83**, 1606-1612.

68. S. Wu, Y. Zhu, Q. Cai, K. Zeng and C. A. Grimes, *Sensors and Actuators B: Chemical*, 2007, **121**, 476-481.

69. P. Khunkitti, A. Siritaratiwat, M. Leeprakobboon, A. Kruesubthaworn and A. Kaewrawang, *Proceedings of The 2013 International Electrical Engineering Congress (iEECON2013)*, 2013.

70. D.-H. Chen and S.-R. Wang, *Materials Chemistry and Physics*, 2006, **100**, 468-471.

71. W. H. Butler, T. Mewes, C. K. A. Mewes, P. B. Visscher, W. H. Rippard, S. E. Russek and R. Heindl, *IEEE Transactions on Magnetics*, 2012, **48**, 4684-4700.

72. L. D. Muiznieks and F. W. Keeley, *Biochimica et Biophysica Acta (BBA) - Molecular Basis of Disease*, 2013, **1832**, 866-875.

73. A. J. Newell, W. Williams and D. J. Dunlop, *Journal of Geophysical Research: Solid Earth*, 1993, **98**, 9551-9555.

74. M. J. Donahue and D. G. Porter, *Physica B: Condensed Matter*, 2004, **343**, 177-183.

75. H. M. Lu, W. T. Zheng and Q. Jiang, *Journal of Physics D: Applied Physics*, 2007, **40**, 320-325.

76. A. Michels, J. Weissmüller, A. Wiedenmann and J. G. Barker, *Journal of Applied Physics*, 2000, **87**, 5953-5955.

77. M. Brandbyge, J.-L. Mozos, P. Ordejón, J. Taylor and K. Stokbro, *Physical Review B*, 2002, **65**, 165401.

78. J. Taylor, H. Guo and J. Wang, *Physical Review B*, 2001, **63**, 245407.

79. I. Ennen, D. Kappe, T. Rempel, C. Glenske and A. Hütten, *Sensors (Basel, Switzerland)*, 2016, **16**, 904.

80. A. Regtmeier, A. Weddemann, I. Ennen and A. Hutten, *Proceedings of COMSOL Conference Boston*, 2011.

III. Other Electronic Sensors and POC Devices

CHAPTER 7

A Nano-BG-FET for Point-of-Care Estimation of Ammonia and Urea in Human Urine

Contents

ABSTRACT 199
7.1. Introduction 200
7.2. Materials and Methods 205
7.2.1 Materials 205
7.2.2 Fabrication of BG-FET 206
7.2.3 Synthesis and Characterization of Nanocomposite 207
7.2.4 Material Characterization of the CdS-TiO_2 Composite Nanoparticles 207
7.2.5 Calibration 208
7.3. Results and Discussion 208
7.3.1 Electrical Characterization 208
7.3.2 Ammonia Sensing 212
7.3.3 Mechanism for Ammonia Detection 214
7.3.4 Selectivity of BG-FET 215
7.3.5 Sensing of Human Urine Samples 217
7.3.6 Calculation of Ammonia and Urea in Human Urine Samples 219
7.4. Conclusions 221
References 222

ABSTRACT

The cleaners, farmers, or industrial workers everyday come under the exposure of hazardous and pyrophoric ammonia gas or vapor, which cause severe health disorders in them. However, there is hardly any point-of-care-testing (POCT) device, which can detect the level of ammonia in real-time. Further, activity of ammonia and urea the body fluids such as breath, urine, and blood are the biomarkers for kidney or liver functions. Herein a highly sensitive and reusable back-gate-field-effect-transistor (BG-FET) has been developed to selectively detect ammonia in air together with ammonia and urea in a human urine. The BG-FET was prepared on a p-type Si substrate with a n-type channel material of CdS-TiO_2 nanocomposite and a poly-methyl methacrylate (PMMA) film as the dielectric layer. In order to make the sensor reusable, it was employed as a cover to a chamber where the ammonia gas or the urine sample was placed. The response of the BG-FET was analyzed by measuring the I-V characteristics, which showed increase in the drain current with ammonia release from the chamber. The underlying principle of the BG-FET enabled the creation of more (fewer) charge carriers for the reducing (oxidizing) gases such as ammonia upon adsorption on the nanostructures of the CdS-TiO_2 as the channel material. Control experiments with different gases/vapors suggested that the change in the current-to-voltage response of the BG- FET could be calibrated to selectively measure the activity of diverse hazardous gases. The lowest concentration of ammonia which could be detected was ~0.85 ppm at a response time of 30 s with an operating gate voltage of less than 0.5 V, which were significantly superior than the previously reported any ammonia sensor. Urease enzyme was added to the urine sample to liberate ammonia proportionately, which could also be detected employing the same sensor. The urea-urease lock-and-key enzyme catalysis reaction made the sensor specific in detecting the biomarker. The performance of the calibrated BG-FET was also compared and contrasted with the standard clinical urea detection methodologies. The reliability, accuracy, reusability, and fast response time of the device could be employed to develop a point-of-care biomedical-device for ammonia and urea detection.

The manuscript is under review.

7.1. Introduction

Low-cost, portable, and reusable point-of-care testing (POCT) devices have been designed and developed in the recent times with the vision to improve the quality of human lives and their expectancy.[1] In one direction, they are expected to keep a track of blood pressure,[2] amylase,[3] COPD,[4] virus infection,[5] diabetes and blood sugar,[6, 7] or pregnancy[8] at the user site on a regular basis. On the other hand, they are likely to detect pollutants present in air,[9] water,[10] or soil and promote awareness to prevent environmental hazards. Although the technological progress has been very rapid in this regard, the number of pollutants and biomarkers that require urgent attention is perhaps increasing every day.

For example, the environmental pollutions associated with inflammable and toxic ammonia (NH_3) gas, due to the rapid industrialization of the fertilizer or pesticide synthesis and their large-scale use, have influenced the ecological stability,[11] human health,[12] and animal life.[13, 14] The sewage cleaners of nitrogenous liquid or solid wastes everyday come under the exposure of ammonia gas/vapor, which cause irritation to skin, eyes, throat, and lungs if not blindness or reduction in life expectancy, in many of the severe cases.

Importantly, in the present scenario, the technologies associated with ammonia gas detection using spectroscopic techniques are rather costly[15] and time consuming. There is hardly any POCT device, which can detect the level of ammonia issuing out of wastes, urinals, pesticides, or fertilizers. In view of the above, the present study reports the design and development of a portable and reusable back-gated-field-effect-transistor (BG-FET) employing the specialities of nanoscale science and technology for the real-time detection of ammonia gas/vapor present in the atmosphere. The sensors are designed in such a

manner that they can also be integrated to POCT devices to determine the activity of ammonia and urea in the human urine samples.

The amount of ammonia and urea in the body fluids such as breath or blood or urine are considered to be important biomarkers to judge the quality of the health and fitness.[16-18] It is well known that in the human body both ammonia and urea originate from protein metabolism wherein the proteins are initially broken down to toxic ammonia before converted into rather non-toxic urea.[19] While ammonia has an immediate relation to the acid-base imbalance in the human body, urea is not directly responsible for the same.[20] A high urinary/plasma nitrogen ratio indicate the onset of azotemia while a low value is indicative of acute tubular necrosis.[18] Clinically, less than 50 μM of ammonia content is considered to be the normal in the human blood.[21] Kidney dysfunction or enzymatic deficiencies may lead to endogenous ammonia intoxication or hyperammonemia,[22] responsible for hepatic encephalopathy.[23, 24] In addition, ammonium ion, a significant constituent of urine, is volatile at alkaline pH and release ammonia.[25] Further, presence of NH_3 in the human breath is also considered to be an indicator for renal failure and amino acid deficiency.[26, 27]

The prior art suggests that the regular detection of ammonia in human breath, blood, and urine can provide an insight into several important health disorders, for example, liver dysfunction (cirrhosis),[28] ovulation in women,[29] protein digestion, deposition of creatinine in joints during arthritis, or regulation of protein intake,[30] among others. Apart from ammonia, regular monitoring of the amount of urea in the body fluids can also help in the early diagnosis and prevention of renal failure,[18] tubular necrosis,[17] heart failure,[31] or dehydration, among others. However, the presently available POCT urine strips do not

include urea detection. A few commercially available devices such as iSTAT™ from Abbott Healthcare employ electrochemical sensing to detect blood urea nitrogen, electrolytes, and glucose. However, this process is not only expensive but also involve cartridges that are not reusable.

In view of the above, of late, the real-time detection of ammonia gas present in air and also the detection of ammonia, urea, and nitrogen in the biological fluids have attracted a lot of scientific and technological attentions.[15] In particular, the focus has shifted to the development of the diagnostic tools[32] leveraging on the efficacies of the nanoscience and nanotechnology.[33] For example, conducting polymer based resistive ammonia sensors have been reported recently in the literature.[34-36] Conductometric metal oxides sensors composed of ZnO, and TiO_2 or metal chalcogenides like CdS have also been developed.[15, 37-43] Nanocomposites of different metal oxides[42, 44] along with polymers are designed and developed with the aim to exploit the special properties of materials and enhance the efficiency of the sensors under ambient condition. The different other schemes of ammonia sensing include quartz crystal microbalance,[45] gas chromatography,[46] colorimetry[47, 48] or amperometry,[35] among others. Gas sensors, in general, has also been demonstrated with graphene.[49] A dual conductometry cum colorimetry sensor using dye coupled reduced graphene oxide has also been reported very recently.[50]

In this direction, as the transduction platform, the FETs have shown significant potential due to their excellent sensitivity, selectivity, and compatibility with the existing label-free detection methodologies.[51] Their real time response, ease of miniaturization qualifies them for POC applications.[52] For example, the accurate but costly chromatographic or spectroscopic methods require time and expertize for the detection and analysis, not

suitable for real time monitoring. Further, as compared to the two-electrode chemiresistor or conductometric sensors, the presence of the third gate electrode in the FETs improve the performance by providing more control over the response. In addition, FETs offers a multi-parametric attribute while sensing because apart from the current, the threshold voltage or the sub-threshold current swing can also change.[53]

Importantly, the use of nanotechnology in the FET sensors composed of ZnO,[54] In_2O_3[55] and Si[56] has improved the performance. The use of the nanoscale films of polymers as the gate or active channel materials have also reduced their production cost suitable for POCT devices.[57-59] For example, FET composed of TiO_2 has been used previously to detect ammonia, harnessing the phenomenon of partial reduction of the oxide in presence of the reducing ammonia gas leading to an increased current response.[41, 42, 44] Oxygen defects in TiO_2 make it an n-type semiconductor. Thus, adsorption the electron deficient oxidizing gases like oxygen extract electrons from these materials to develop a depletion layer near the adsorbed interface, which creates a potential barrier at the grain boundary to increase the electrical resistance.[60] In contrast, in presence of an electron donating reducing gas such as the ammonia the resistance of the channel material reduces after absorbing electons.[61] However, the voltage of operation for most of the previously reported FETs are ~60-80 V,[57, 62] which is perhaps one of the major roadblock behind the commercial use of the FETs as gas sensors suitable for the POCT devices.

In this chapter, a BG-FET sensor has been developed suitable for POCT of the activity of ammonia vapor/gas in atmosphere as well as the detection of ammonia and urea in human urine samples. The n-type nanocomposite of CdS-TiO_2 semiconductor has been employed as a channel material for the highly sensitive detection of ammonia gas at lower voltages.

The nanoparticles of CdS-TiO_2 composites are used to improve the gas sensitivity with the reduction in the grain size.[63] In fact, the study shows that the extent of reduction in resistance with the adsorption of different types of gases/vapors on the channel nanomaterial show distinctive I-V characteristics, which help in distinguishing different gases/vapors. We achieve this type of sensitivity and selectivity at an exceptionally low operating voltage and gate potentials, as compared to the ones reported in the literature.[52, 58, 62] An inexpensive closed chamber has been designed to perform the real-time measurements using the same BG-FET at room temperature to showcase its reusability. The ability of the BG-FET to quantitatively and selectively sense ammonia in human urine samples has also been demonstrated. This has been achieved by estimating the activity of ammonia issuing out of a lock and key enzymatic urea and urease reaction. Once calibrated, the sensitivity of the same sensor can be exploited for selective detection of different other gases/vapors based on the distinctive reduction or increase in the electrical resistance during the adsorption of the gases/vapors on the grain boundaries of the nanostructures present in the channel.

7.2. Materials and Methods

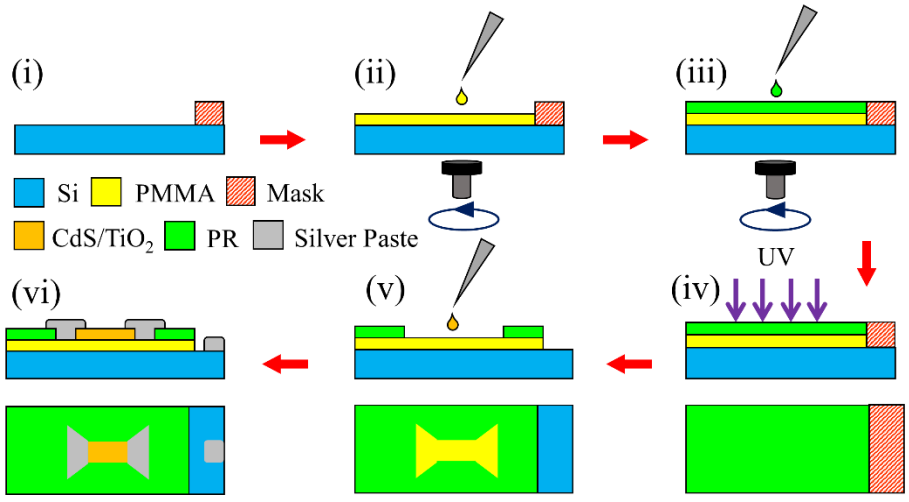

Figure 7.1: Schematic steps to fabricate the BG-FET device. Side views - (i) masking of the Si wafer; (ii) coating of PMMA on the Si Wafer; (iii) Coating of the photoresist (PR) on the PMMA layer; (iv) UV exposure through photo lithography and development of the patters; (v) CdS-TiO_2 deposition through drop casting; and (vi) electrode deposition through silver paste. The bottom row in the images (iv) - (vi) show the top schematic views.

7.2.1 Materials

Poly-methyl methacrylate (PMMA) was obtained from Alresist GmbH, Germany. Silicon wafers (<100> P-type, Boron doped, Resistivity 0.01-0.02 ohm.cm) were procured from N.J. International Corporation, India. Microposit S1813 positive photoresist was purchased from MicroChem, USA. Titanium dioxide (TiO_2) was obtained from Qualigens Fine Chemicals, India. Cadmium chloride ($CdCl_2$), sodium sulphide (Na_2S) pellets, and methanol (Ch_3OH, 99.5%) were procured from Merck, India. Concentrated ammonia solution (NH_3), hydrochloric acid (HCl, 37%), ethanol, anisole, and toluene were also procured from Merck, India. Poly-dimethylsiloxane (PDMS - SYLGARD® 184 kit) was obtained from Dow Corning, India. Urease enzyme extracted from *Canavalia ensiformis* (jack bean) was obtained from Sigma Aldrich, India. The Cu wires and double sided tapes were

procured from the local vendors. The chemicals were of analytical grade and employed in the experiments without further purification. The Milli-Q grade water was used for cleaning the glassware and also while preparing the fresh solutions.

7.2.2 Fabrication of BG-FET

The fabrication process of the BG-FET has been outlined in Figure 7.1. Initially 2 cm × 2 cm pieces of Si wafer were cut and cleaned in piranha solution (3:1 mixture of concentrated H_2SO_4 and H_2O_2). After thorough cleaning in acetone and isopropyl alcohol, the wafers were dried by a nitrogen jet before placing on a hotplate for ~10 min. A portion of each wafer was initially covered with a mask as shown in the Figure 7.1(i). Following this, a PMMA dielectric layer was spin-coated twice with a spin-speed of 1000 (Figures 7.1(i) and 7.1(ii)) on the unmasked region. The PMMA coated Si wafer was soft-baked at 135°C for ~3 min on a hotplate followed by hard-baking at 150°C for ~1 min. The film thickness was found to be ~200 nm, measured by an Imaging Ellipsometer (EP3, Nanofilm, Accurion Scientific Instruments Pvt. Ltd). After that a 3.5 µm thick positive photoresist, S1813, was spin-coated twice with a spin-speed of 1000 RPM on the PMMA layer, as shown in the Figure 7.1(iii). The channel region was defined (Figure 7.1(iv)) by a laser writer, Dilase 250 (KLOE, France) using a 1.5 mW UV laser exposure of wavelength 375 nm. Thereafter, about 2 µl of the aqueous CdS-TiO_2 composite was drop casted on the channel (Figure 7.1(v)) and left to dry overnight. Drain and source electrodes were defined on either sides of the CdS-TiO_2 channel with silver paste, as shown in the Figure 7.1(vi). The gate electrode was fabricated by depositing the silver paste on the masked portion of the Si substrate, after removing the mask, as shown in the Figure 7.1(vi).

7.2.3 Synthesis and Characterization of Nanocomposite

The CdS-TiO_2 composite nanoparticles were synthesized chemically as previously reported in literature.[64] Cadmium chloride ($CdCl_2$) and sodium sulphide ($Na_2S.9H_2O$) salts were used as the sources for Cd^{2+} and S^{2-} ions, respectively. Initially, 20 ml of 0.1M TiO_2 solution was prepared and sonicated for 1 h in the ultra-sonication bath. Freshly prepared 0.1M Na_2S solution was then added to the solution drop by drop with vigorous stirring. Subsequently, a freshly prepared 0.1M $CdCl_2$ solution was added to the above-mentioned solution with continuous stirring, which turned the previous white solution into a yellowish-white.

7.2.4 Material Characterization of the CdS-TiO_2 Composite Nanoparticles

The nanocomposite was characterized by Raman spectroscopy and X-Ray diffraction (XRD) analysis. A micro-Raman spectrometer, Jovin Horiba, LabRam HR800, with a 532 nm Ar laser was used for the purpose. The XRD was carried out in a Bruker, Model-D8-Advance powder X-ray diffraction equipment. The results are shown in Figure 7.2.

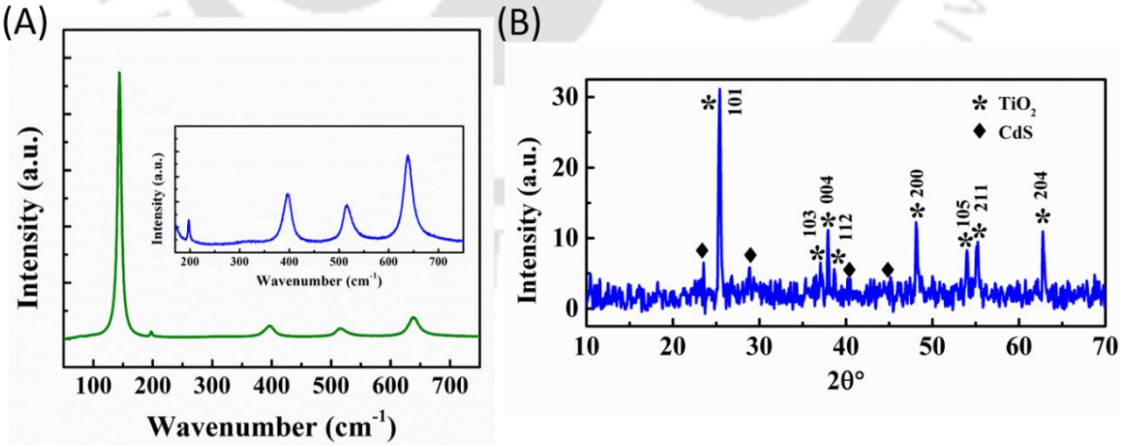

Figure 7.2: Material characterization of CdS-TiO_2. (A) Raman spectra of the CdS-TiO_2 nanocomposite in which the inset shows the magnified view of the same. (B) X-Ray diffraction analysis of the composite nanoparticles.

The peaks in the Raman spectra correspond to the Raman active modes of TiO_2: E_g (~140 cm^{-1}), B_{1g} (~390 cm^{-1}), A_{1g} (~520 cm^{-1}) and E_g (~630 cm^{-1}) and a multi-proton process (~200 cm^{-1}). The weak and broadened peak around 320 cm^{-1} corresponds to CdS nanoparticles. However, its signature Raman active mode around 600 cm^{-1} was not observed due to the dominant TiO_2 peak in the vicinity. In the XRD pattern, the strong peaks at 2θ ~25° and ~48° confirms the anatase phase of TiO_2. The peak at 2θ ~28° corresponds to reflection from (101) planes of hexagonal CdS while, reflection from (220) planes is represented by the peak at 2θ ~41°. As it was expected for nanocrystals, the peaks in general are weak and broadened.

7.2.5 Calibration

The electrical measurements were carried out using a power supply (Testronix 11A) and digital multimeter (Mashtech 32(H)9A) in ammeter configuration. Initially, the sensor's response to different known concentrations of NH_3 solutions were recorded. These measurements were used to calibrate the device for the testing of 10 times diluted urine samples which followed next. All experiments were conducted with a liquid volume of 50 µl. Testing of urine samples were carried out in two steps, before and after the addition of urease. The first reading correspond to the ammonia concentration present in urine by default while the second corresponds to the combined concentration of ammonia already present in urine and that released by the urea hydrolysis in presence of urease.

7.3. Results and Discussion

7.3.1 Electrical Characterization

The FET was fabricated in a back-gate- top-contact configuration, as schematically shown in Figure 7.3(A) with PMMA as dielectric, CdS-TiO_2 nanocomposite as the

channel material with silver paste as electrode. Here, the acceptor p-type Si substrate of resistivity 0.01-0.02 ohm.cm acted as the gate electrode. A negative voltage at the gate terminal repelled the majority carrier electrons of n-type CdS-TiO_2 nanocomposite towards the surface of the channel. The charge distribution in the channel under negative gate potential and the electrical connections for measurements are illustrated in the Figure 7.3(A).

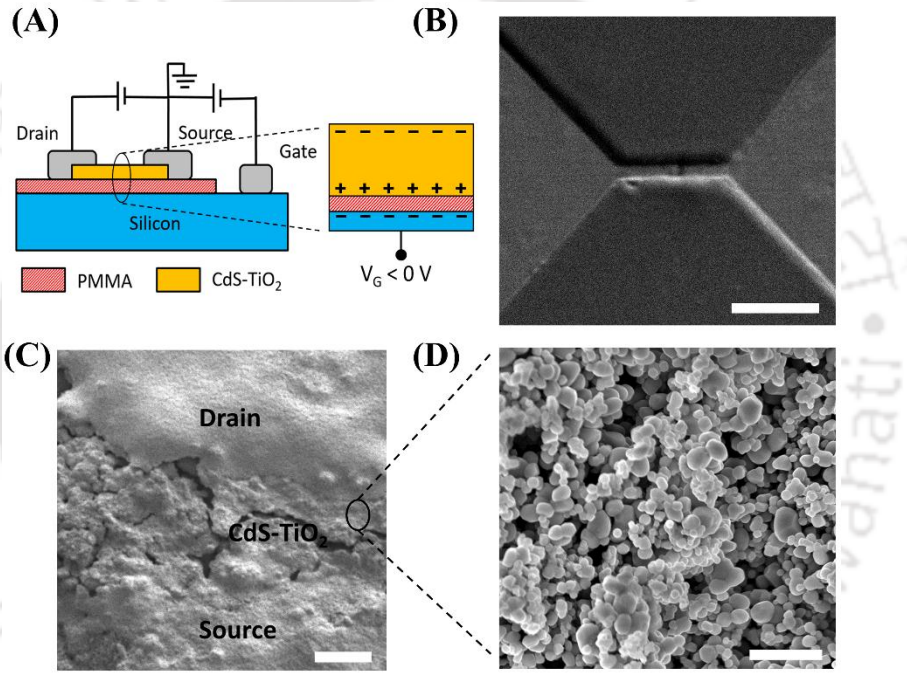

Figure 7.3: Image (A) shows the schematic diagram of the BG-FET device and the electrical connections. The magnified inset shows the effect of applying a negative bias at the gate electrode (V_G < 0 V). Image (B) shows FESEM image of the 100 µm x 20 µm channel region on the photoresist after photolithography. Image (C) is the FESEM image of the active region and drain-source electrodes. Image (D) shows a magnified view of the active region depicting the surface morphology of the CdS-TiO_2 nanostructures. Scale bar for (B) and (C) is 100 µm and 1 µm for (D).

The channel region before and after the deposition of the active composite material of CdS-TiO_2 is illustrated in FESEM images Figure 7.3(B) and 2(C), respectively. The active CdS-TiO_2 region bounded on the upper and lower sides by the drain and source electrodes of conductive silver-paste. Figure 7.3(D), a FESEM image of the

sample shown in the Figure 7.3(C), depicts the details of the channel where the CdS-TiO_2 nanostructures are clearly visible.

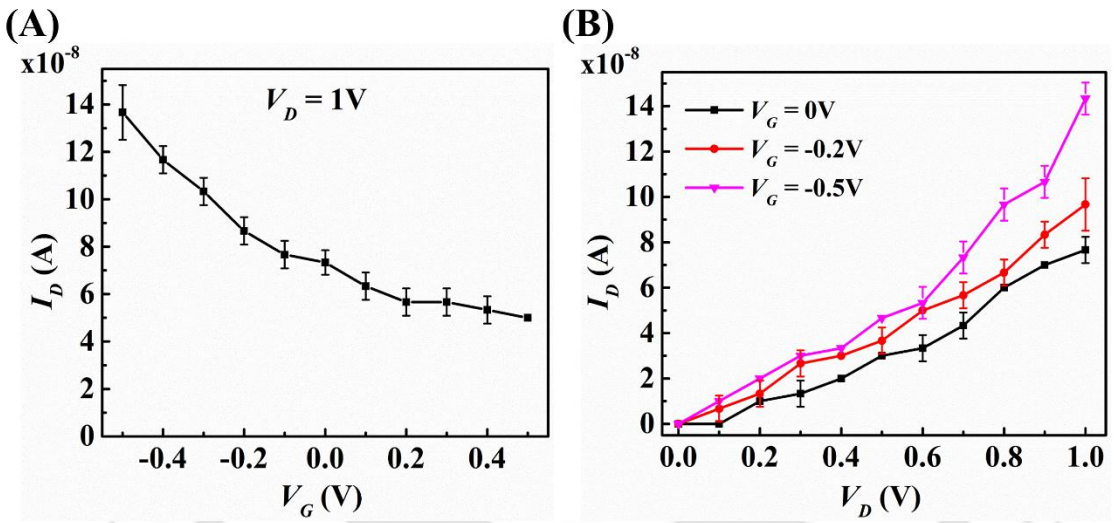

Figure 7.4: Electrical characterization of the FET in absence of ammonia. (A) I_D vs V_G characteristics of the FET at a constant drain bias, V_D = 1 V. (B) I_D vs V_D response of the FET at different gate biases, V_G = 0 V, –0.2 V, and –0.5 V.

The electrical characterization suggested that the channel of the FET conducted at zero gate bias (V_G = 0 V), as shown in the drain current (I_D) versus gate voltage (V_G) plot at a drain-source voltage (V_D) of ~1 V in the Figure 7.4(A). In such a situation, the application of negative V_G could enhance the I_D whereas a positive V_G did not show any significant change in the I_D, as illustrated in Figure 7.4(A). The electronic properties of CdS-TiO_2 nanocomposite helped in describing these behaviors. In general, TiO_2 is known to be an n-type semiconductor due to the presence of oxygen vacancies[65] and undoped CdS films also exhibit n-type behavior.[66] Thus, the composite of CdS-TiO_2 could exhibit n-type characteristics with electrons as majority carriers. Application of a negative V_G induced positive charges near the dielectric, which repelled the negative majority carriers and enriched the surface of the active layer with electrons. In consequence, significant

conduction through the surface was observed as the I_D increased. Figure 7.4(B) illustrates that increasing magnitude of V_G shifted the I_D vs. V_D plots towards higher I_D values, suggesting a better sensing performance at a higher V_G.

However, voltages beyond V_G = –0.5 V resulted in high gate current resulting from the dissociation of thin dielectric layer. Hence, for this study, V_G = –0.5 V was chosen as the suitable gate bias for all subsequent experiments, while V_D was swept from 0 V to 1 V for obtaining the device characteristics.

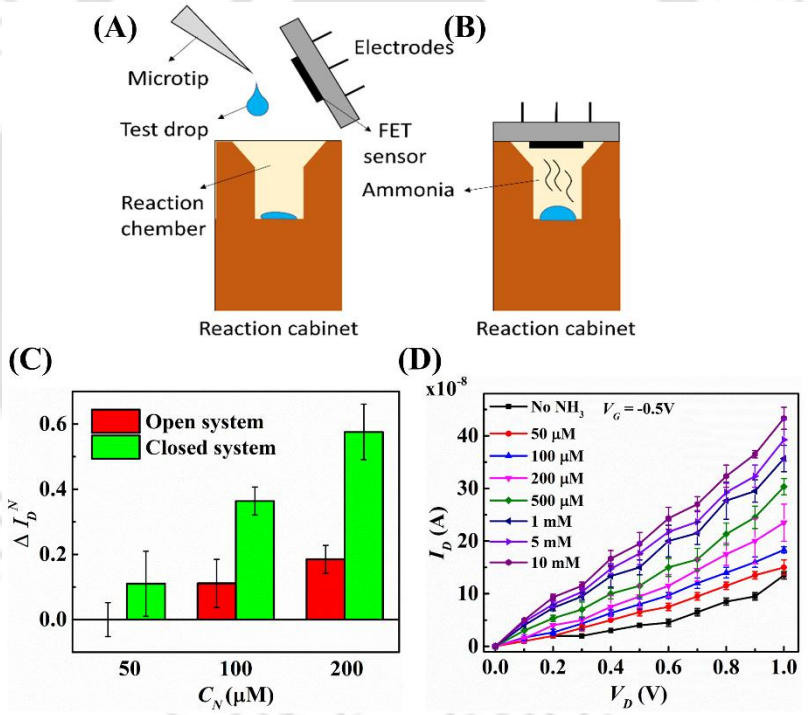

Figure 7.5: (A, B) Schematic diagram of the closed setup for ammonia sensing. (C) Comparison between current responses in the open and the closed system for 3 different concentrations, 50μM, 100μM, and 200μM. (D) I_D vs V_D characteristics of the FET at a fixed gate voltage, V_G = –0.2 V, for different concentrations of aqueous ammonia solution in the closed system.

Unlike conventional curves, the characteristics of the proposed device did not saturate at V_D up to 1 V due to high contact resistance and significant conduction at the surface of the active layer. A voltage higher than 1 V would have showed the saturation. However, at a higher voltage led to high currents, which damaged the

channel material and reduced the life time of the sensor. The conduction of electrons in this case through the surface and bulk due to thick layer of drop casted nanoparticles and thus the effect of gate is somewhat opposite. The typical gate current observed was of the order of 10^{-11} A.

7.3.2 Ammonia Sensing

The BG-FET was tested for ammonia sensing in room temperature. For this purpose, aqueous ammonia solutions were prepared by adding different amount of 13.4M stock ammonia solution into water. During the test, initially, the experiments were carried in the open environment where the sensor was kept under ambient condition. A 50 µl drop of the respective solution was kept at a distance of around 3 cm from the device. Once the drop was dispensed, the measurements were recorded by a digital multimeter after an interval of ~30 s.

A time interval of 5 min was allowed between two consecutive experiments to ensure the restoration of electrical and physical characteristics of BG-FET to its native state in order to avoid cross responsivity between successive measurements. Further, we also performed these experiments in closed system with an objective to improve the sensitivity. The enclosed setup is illustrated in images (A) and (B) of Figure 7.5. In this set-up, the reaction chamber was created by casting PDMS in a cylindrical vessel and the sensor was attached as the lid to the vessel. The test drop was dispensed into the reaction chamber before the lid with the BG-FET confine the chamber, as illustrated in Figure 7.5(B). The I_D vs V_D characteristics at V_G = – 0.5 V were subsequently measured with 3 different concentrations of ammonia solution 50 µM, 100 µM and 200 µM. The open and closed systems were evaluated

in terms of the normalized change in drain current, ΔI_D^N, determined as per the following expression:

$$\Delta I_D^N = \frac{\Delta I_D}{\Delta I_{D0}}. \quad (7.1)$$

Where, ΔI_D is the change in drain current in presence of the samples and ΔI_{D0} is the drain current in absence of ammonia gas/vapour at, V_G = -0.5 V and V_D = 1 V.

Table 7.1: Summary of different notable FET based sensors for NH_3 detection and a comparison with the sensor reported in this work.

Material	Type	Configuration	ppm Range	$\|V_{ds}\|$ (V)	$\|V_g\|$ (V)	t_{Res}	refs
P3HT	NF	BGBC	0.1-25	60	30	5-25 sec	[57]
P3HT	NF	BGBC	100	100	85	400 sec	[71]
P-29-DPP-SVS	NF	BGTC	29-1000	5	5	5 min	[72]
Polyaniline	NW	BGBC	1-20	8	10	10 sec	[73]
PBTTT	NF	BGTC	10-100	30	30	40 sec	[74]
P3HT/PS	Blend	BGTC	5-50	40	40	5-10 min	[75]
In_2O_3	NW	BGTC	200-10000 *	0.3	60	0.5-2 min	[55]
Si	NW	BGTC	-	1-5	20	-	[56]
CdS/TiO_2	**NC**	**BGTC**	**0.85-170 #**	**1**	**0.5**	**30 sec**	**This work**

t_{Res} = Response time, BGBC - Back gate back contact, BGTC - Back gate top contact, NF – Nano-film, NW – Nano-wire, NC – Nano-composite.
*1 ppm = 10^4 % (v/v)
#1 ppm = 58.82 µM/L (for NH_3 solution)

Figure 7.5(C) compares the ΔI_D^N for the open and closed systems for 3 of the lowest concentrations of ammonia (C_N). It was observed that the response of the closed system was at least 3 times better than the open environment, as shown in Figure 7.5(C). At a particular V_G and V_D, the concentration was related to the current by a one-to-one correlation, which was used for the measurements. Moreover, it was also observed that the closed system could detect 50 µM of NH_3 solution, which was almost undetectable in the open system. These experiments suggested that the sensitivity of the close system was significantly high and all further experiments were carried employing this closed setup. The device responses at the same V_G = -0.5 V with different concentrations of ammonia solution ranging from 50 µM to 10 mM were compiled in the Figure 7.5(D).

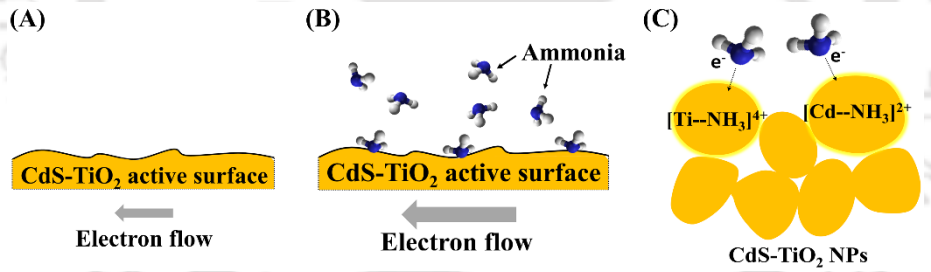

Figure 7.6: Schematic representation of ammonia sensing: (A) Small current flowing through CdS-TiO_2 active surface in absence of ammonia. (B) Adsorption of ammonia molecules on the surface and resultant enhancement of current. (C) Electron transfer process between the ammonia molecules and CdS-TiO_2 nanoparticles (NPs) leading to the formation of weak coordinate-covalent bonds.

7.3.3 Mechanism for Ammonia Detection

The sensing with CdS-TiO_2 can be explained by the partial reduction of the nanostructures in presence of ammonia. As discussed earlier, several metal oxides and chalcogenides exhibit gas sensing property because of the pronounced or reduced electron transport owing to the partial reduction or oxidation of the active material. For example, Figure 7.6(A) shows the lower current response of the virgin BG-FET in presence of fewer

carriers on the CdS-TiO_2 nanostructures. In comparison, the exposure of ammonia led its adsorption on the CdS-TiO_2 nanostructures through the donation of the lone pair of electrons, as shown in Figure 7.6(B). Subsequently, the weak coordinate-covalent bonds were formed on the CdS-TiO_2 nanostructures, as illustrated in Figure 7.6(C).[43] In the process, the active channel material was enriched with electrons, which increased the number of charge carriers and current response. The higher porosity of the nanoparticle based active materials showed a better response through more efficient adsorption of the gas, as compared to the continuous films of the same material.

A comparison of the present work with previously fabricated FET based sensors is illustrated in Table 7.1. The data suggests that, most of the back gated FET based sensors fabricated for detection of ammonia were found to be operated at higher voltage compared to the FET sensor device fabricated in this work. Moreover, the response time of our device was ~30 s, which was less than most the FET devices for detection of ammonia. Further, the lowest concentration detected was found to be 50 µM, which was equivalent to ~0.85 ppm, comparable to some of the previously reported results. Concisely, the proposed BG-FET combined all the features of low operation voltage, high sensitivity, reusability, and low response time to qualify for the integration with a real time POCT device.

7.3.4 Selectivity of BG-FET

The selectivity of BG-FET for ammonia was investigated based on the comparison of the responses from 3 volatile solvents, 500 µM hydrochloric acid (HCl), ethanol, and toluene, other than ammonia. The ΔI_D^N for the different solvent vapors (C_{vap}) exposures are shown in the Figure 7.7. When 500 µM ammonia was present in the

solution, the increase in current (about 1.2 times) was almost 4 times higher compared to the case of HCl (about 0.3 times). Toluene showed a negligible variation in I_D and the response in case of ethanol was found to be negative.

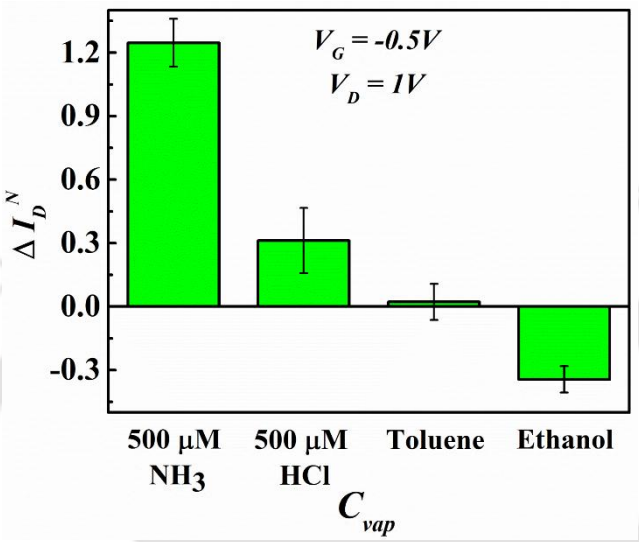

Figure 7.7: Comparison of the normalized change in I_D for different volatile samples, 500 µM NH_3, 500 µM HCl, toluene and ethanol.

Selectivity of nanostructured TiO_2 and its composites towards ammonia at room temperature has been investigated earlier.[67, 68] For example, the chloride ions from HCl can undergo oxidation by the surface adsorbed oxygen and in the process, contribute electrons to the composite as:

$$Cl^- + O^- \xrightarrow{CdS/TiO_2} ClO^- + e^- \qquad (7.2)$$

This might be the reason behind, $\Delta I_D^N > 0$ for the proposed BG-FET in presence of HCl vapors. In comparison, ethanol, in small concentration is also known to undergo oxidation and increase conductivity according to the following equation:[69]

$$C_2H_5OH + 6e^- \xrightarrow{CdS/TiO_2} 2CO_2 + 3H_2O + 6e^- \qquad (7.3)$$

Since this is typically reported at elevated temperatures (greater than 100°C),[70] it is imperative that room temperature was not sufficient to provide the activation energy for the reaction. Again, in a humid environment, adsorption of H_2O molecules further lowers the possibility for the oxidation of ethanol.[37] The combined effect manifests as, $\Delta I_D{}^N < 0$, response in presence of ethanol vapor. In case of toluene, it is understandable that being an aromatic compound, it would show minimal electron donating behavior and consequently result in a feeble response.

Concisely, the Figure 7.7 shows the capacity of the BG-FET for the real-time and highly-sensitive and selective detection of different gases. The underlying principle of the proposed BG-FET enable the creation of fewer (more) charge carriers for the oxidizing (reducing) gases upon adsorption on the nanostructure of the channel material. Subsequent change in the current-to-voltage response can be calibrated easily to selectively measure the activity of diverse hazardous gases.

7.3.5 Sensing of Human Urine Samples

The BG-FET was tested with human urine samples to validate its capability to sense urea. Random urine samples of both male and female were obtained from a hospital having ages ranging from 45 to 68 years. The samples were diluted 10 times and 50 µL of the diluted samples was used for testing. It is well known that hydrolysis of urea by the enzyme urease selectively produce ammonium ions. This enzymatic reaction was utilized to convert urea into highly volatile ammonia which in turn was sensed by the BG-FET. A highly concentrated urease solution (~40,000 Units/L) was prepared in dilute phosphate buffer of pH 7.4 to ensure a quick reaction. As urine itself contained some amount of dissolved NH_3, the urea content

in urine could not be directly correlated to the device response. In such a situation, the amount of dissolved ammonia was quantified before the urease was introduced. Thus, initially, the response of the sensor for a drop of collected urine sample was measured to detect the amount of ammonia in urine. Thereafter, the urease solution was introduced to the same urine drop and the response of the BG-FET was recorded again. The response measured in first step corresponded to the dissolved ammonia while the increase in the response in second step was due to the ammonia generated from urea-urease reaction as mentioned earlier.

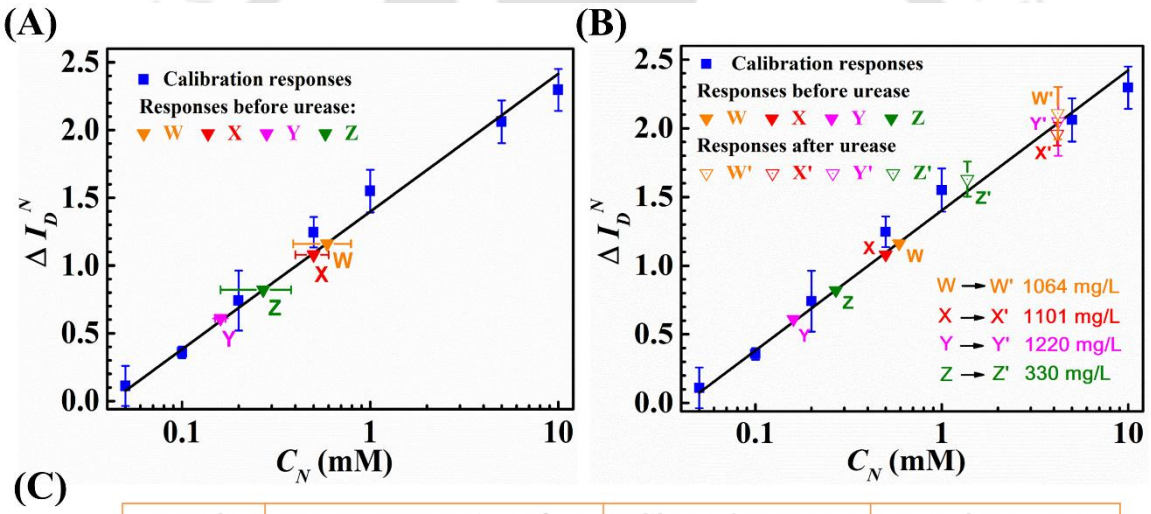

(C)

Sample	NH_3 Concentration After Urease ($C_{N,2}$) (mM)	Calibrated Response ($\Delta I_{D,2}^{N,C}$)	Actual Response ($\Delta I_{D,2}^{N}$)
W	4.19	2.035	2.11 ± 0.19
X	4.16	2.027	1.958
Y	4.22	2.038	2.05 ± 0.25
Z	1.36	1.539	1.63 ± 0.13

Figure 7.8: Sensor response for human urine samples. (A) Normalized device responses for urine samples before the introduction of urease (represented by filled triangles W, X, Y and Z) along with the linear fitted responses for known calibration samples. (B) Normalized device responses before (filled triangles) and after (unfilled triangles) the introduction of urease, superposed with liner fitted responses for known calibration samples. W', X', Y' and Z' are the modified responses after urease was introduced. (C) Comparison between the actual and calibrated responses for 4 different urine samples W, X, Y and Z.

The sensor responses were measured in terms of normalized change in I_D (ΔI_D^N) as before. The ΔI_D^N values corresponding to different known concentrations of aqueous NH_3 were extracted from the V_D vs I_D responses to construct a calibration plot illustrated in Figure 7.8(A). The initial responses of the samples ($\Delta I_{D,1}^N$), in absence of urease indicates the inherent ammonia content of urine ($C_{N,1}$). Quantitatively, it can be obtained from the calibration plot of Figure 7.8(A). The notations W, X, Y and Z denote the 4 different urine samples prior to urease injection. Following this, 10 µL of urease solution was introduced into the reaction chamber and subsequent responses were recorded between 2 and 3 min.

Figure 7.8(B) shows the NH_3 concentrations in presence of urease ($C_{N,2}$) and the corresponding responses ($\Delta I_{D,2}^N$). Since the urea concentrations found in the clinical pathology tests do not relate directly to the observed ΔI_D^N values, the equivalent $C_{N,2}$ values were obtained after multiple adjustments for dilution, stoichiometry of the enzyme reaction and $C_{N,1}$. The calculations are discussed in details here-in-below.

7.3.6 Calculation of Ammonia and Urea in Human Urine Samples

Urease hydrolyses urea in aqueous medium to produce ammonium hydroxide. The gas/vapour NH_3 being highly volatile, is released from the solution. Urine in itself contain some amount of dissolved NH_3. Hence the response of the BG-FET sensor corresponds to the net NH_3 content comprising of both inherent NH_3 as well as the NH_3 derived from urea hydrolysis. For the experiments, the diluted working samples were named as W, X, Y and

Z. The initial response of the device in absence of urease ($\Delta I_{D,1}^{N}$) represents the amount of NH_3 already present in diluted urine samples ($C_{N,1}$). The $C_{N,1}$ values were measured from the calibration plot with known samples. The C_U^R (mg/L) denotes the urea concentrations in the undiluted samples obtained from standard pathology test. Following this, the C_U^R values were converted to its equivalent NH_3 concentration (C_N^R) by considering urea-urease reaction stoichiometry and the dilution ratio. It is well known that each mole of urea would produce 2 moles of NH_4^+. Again, C_U^R values were measured for the actual undiluted samples. Since the working samples were prepared by a 10 times dilution, an adjustment factor of 0.1 was required for the calculations.

Table 7.2: Details of calculations of the urea equivalent NH_3 concentration in the presence of urease.

Sample	**Response before urease** ($\Delta I_{D,1}^{N}$)	**NH3 conc. before urease** ($C_{N,1}$) **(mM)**	**Clinical report of urea content** (C_U^R) **(mg/L)**	**Corresponding NH3 conc.** (C_N^R) **(mM)** $C_N^R = \frac{C_U^R \times 2 \times 0.1}{60.06^*}$	**NH3 conc. after urease** ($C_{N,2}$) **(mM)** $C_{N,2} = C_N^R + C_{N,1}$
W	1.16 ± 0.19	0.59 ± 0.2	1064	3.543	4.19
X	1.08 ± 0.12	0.5 ± 0.1	1101	3.666	4.16
Y	0.61 ± 0.09	0.16 ± 0.01	1220	4.062	4.22
Z	0.82 ± 0.25	0.27 ± 0.11	330	1.098	1.36

* Molecular Weight of Urea = 60.06 g/mole

The calculation is shown in the 5th column of Table 7.2. The net NH_3 concentration ($C_{N,2}$) was obtained by adding C_N^R and $C_{N,1}$ as illustrated in 6th column of Table 7.2. The value of $C_{N,2}$ was considered as the abscissa while plotting the responses of the devices in presence of urease ($\Delta I_{D,2}^N$).

The notations W', X', Y' and Z' are the respective counterparts of W, X, Y and Z depicting the changes in ΔI_D^N after introduction of urease. The horizontal shift from $C_{N,1}$ to $C_{N,2}$ in each case corresponds to the urea concentration of the particular undiluted samples. The results of standard pathological urea tests are also shown in Figure 7.8(B). The Table shown in the Figure 7.8(C) compares and contrasts the results with the calibrated responses ($\Delta I_{D,2}^{N,C}$). In summary, the Figure 7.8 showed the capacity of the BG-FET for the real-time and highly-sensitive detection of ammonia and urea in the human urine sample suitable for POCT detection. The results shown here suggest that the same BG-FET can be calibrated easily to measure the nitrogen, ammonia, and urea content of different body fluids such as breath, blood serum, and urine.

7.4. Conclusions

In summary, a CdS-TiO_2 nanocomposite based BG-FET sensor was fabricated, which was operated at a small negative gate voltage of <-0.5 V. The operating voltage of proposed FET was significantly low compared to the previously reported FET based sensors. The BG-FET was found to be suitable for real-time point-of-care (POC) detection of hazardous and inflammable ammonia gas present in the atmosphere in a closed set-up. The lowest concentration of ammonia which could

be detected was ~0.85 ppm at a response time of 30 s. The response time and sensitivity of the present BG-FET was found to be superior than other similar FET based ammonia sensors[71-75] reported earlier. The underlying principle of the BG-FET enabled the creation of fewer (more) charge carriers for the oxidizing (reducing) gases upon adsorption on the nanostructure of the channel material. Thus, the change in the current-to-voltage response can be calibrated easily to selectively measure the activity of other hazardous gases.

The BG-FET could also be utilized for the real-time and highly-sensitive detection of ammonia and urea in the human urine sample suitable for POCT detection. It can be calibrated and integrated to a POCT biomedical-device to detect nitrogen, ammonia, and urea content of different body fluids such as breath, blood serum, and urine, which could lead us to diagnose abnormalities and diseases like urea-cycle disorder, Reye syndrome, and acute tubular necrosis, among others.

References

1. A. St John and C. P. Price, *The Clinical Biochemist Reviews*, 2014, **35**, 155-167.
2. L. M. Lopez and J. R. Taylor, *Annals of Pharmacotherapy*, 2004, **38**, 868-873.
3. S. Dutta, N. Mandal and D. Bandyopadhyay, *Biosensors and Bioelectronics*, 2016, **78**, 447-453.
4. M. Bhattacharjee, H. B. Nemade and D. Bandyopadhyay, *Biosensors and Bioelectronics*, 2017, **94**, 544-551.
5. X. Qiu, S. Zhang, F. Xiang, D. Wu, M. Guo, S. Ge, K. Li, X. Ye, N. Xia and S. Qian, *Sensors and Actuators, B: Chemical*, 2017, **243**, 738-744.

6. S. R. K. Vanjari, N. Bhat, S. Srinivasan, B. Amrutur, C. Kalapu and A. K. Mandal, *Journal*, 2012.

7. M. Taguchi, A. Ptitsyn, E. S. McLamore and J. C. Claussen, *Journal of Diabetes Science and Technology*, 2014, **8**, 403-411.

8. J. R. L. Ehrenkranz, *Epidemiology*, 2002, **13**, s15-s18.

9. B. K. Weis, D. Balshaw, J. R. Barr, D. Brown, M. Ellisman, P. Lioy, G. Omenn, J. D. Potter, M. T. Smith, L. Sohn, W. A. Suk, S. Sumner, J. Swenberg, D. R. Walt, S. Watkins, C. Thompson and S. H. Wilson, *Environmental Health Perspectives*, 2005, **113**, 840-848.

10. U. Kim, S. Ghanbari, A. Ravikumar, J. Seubert and S. Figueira, *IEEE Transactions on Engineering in Health and Medicine*, 2013, **1**, 3700207-3700207.

11. E. S. Wilkins and M. G. Wilkins, *Journal of Environmental Science and Health . Part A: Environmental Science and Engineering*, 1985, **20**, 149-175.

12. R. A. Michaels, *Environmental Health Perspectives*, 1999, **107**, 617-627.

13. W. J. Visek, *Journal of Dairy Science*, 1968, **51**, 286-295.

14. J. A. Camargo and Á. Alonso, *Environment International*, 2006, **32**, 831-849.

15. B. Timmer, W. Olthuis and A. Van Den Berg, *Sensors and Actuators, B: Chemical*, 2005, **107**, 666-677.

16. R. F. Butterworth, J.-F. Giguère, J. Michaud, J. Lavoie and G. P. Layrargues, *Neurochemical Pathology*, 1987, **6**, 1-12.

17. C. P. Carvounis, S. Nisar and S. Guro-Razuman, *Kidney International*, 2002, **62**, 2223-2229.

18. T. R. Miller, R. J. Anderson, S. L. Linas, W. L. Henrich, A. S. Berns, P. A. Gabow and R. W. Schrier, *Annals of internal medicine*, 1978, **89**, 47-50.

19. D. L. Nelson, *Lehninger principles of biochemistry*, Fourth edition. New York : W.H. Freeman, 2005., 2005.

20. P. A. Wright, *The Journal of experimental biology*, 1995, **198**, 273-281.

21. R. J. Barsotti, *Journal of Pediatrics*, 2001, **138**, S11-S20.

22. A. Auron and P. D. Brophy, *Pediatric Nephrology*, 2012, **27**, 207-222.

23. M. Holecek, *Nutrition*, 2015, **31**, 14-20.

24. J. P. Ong, A. Aggarwal, D. Krieger, K. A. Easley, M. T. Karafa, F. Van Lente, A. C. Arroliga and K. D. Mullen, *The American Journal of Medicine*, 2003, **114**, 188-193.

25. J. A. Cunarro and M. W. Weiner, *Kidney International*, 1974, **5**, 303-305.

26. C. Popa, M. Petrus and A. M. Bratu, *Journal of Biomedical Optics*, 2015, **20**, 57006-57006.

27. S. Davies, P. Spanel and D. Smith, *Kidney International*, 1997, **52**, 223-228.

28. G. Tarantino, V. Citro, P. Esposito, S. Giaquinto, A. de Leone, G. Milan, F. S. Tripodi, M. Cirillo and R. Lobello, *BMC gastroenterology*, 2009, **9**, 21-21.

29. A. M. Diskin, P. Spanel and D. Smith, *Physiological Measurement*, 2003, **24**, 191-191.

30. A. M. Dawson, *Gut*, 1978, **19**, 504-509.

31. R. D. Thomas, A. Newill and D. B. Morgan, *Postgraduate Medical Journal*, 1979, **55**, 10-14.

32. B. D. Malhotra and A. Chaubey, *Sensors and Actuators B: Chemical*, 2003, **91**, 117-127.

33. X. Liu, S. Cheng, H. Liu, S. Hu, D. Zhang and H. Ning, *Sensors*, 2012, **12**, 9635-9665.

34. A. L. Kukla, Y. M. Shirshov and S. A. Piletsky, *Sensors and Actuators, B: Chemical*, 1996, **37**, 135-140.

35. K. Crowley, E. O'Malley, A. Morrin, M. R. Smyth and A. J. Killard, *The Analyst*, 2008, **133**, 391-391.

36. U. V. Patil, N. S. Ramgir, N. Karmakar, A. Bhogale, A. K. Debnath, D. K. Aswal, S. K. Gupta and D. C. Kothari, *Applied Surface Science*, 2015, **339**, 69-74.

37. C. Wang, L. Yin, L. Zhang, D. Xiang and R. Gao, *Sensors*, 2010, **10**, 2088-2106.

38. G. N. Dar, A. Umar, S. A. Zaidi, S. Baskoutas, S. W. Hwang, M. Abaker, A. Al-Hajry and S. A. Al-Sayari, *Talanta*, 2012, **89**, 155-161.

39. S. J. Chang, W. Y. Weng, C. L. Hsu and T. J. Hsueh, *Nano Communication Networks*, 2010, **1**, 283-288.

40. J. M. Tulliani, A. Cavalieri, S. Musso, E. Sardella and F. Geobaldo, *Sensors and Actuators, B: Chemical*, 2011, **152**, 144-154.

41. B. Karunagaran, P. Uthirakumar, S. J. Chung, S. Velumani and E. K. Suh, *Materials Characterization*, 2007, **58**, 680-684.

42. V. G. Bairi, S. E. Bourdo, N. Sacre, D. Nair, B. C. Berry, A. S. Biris and T. Viswanathan, *Sensors (Switzerland)*, 2015, **15**, 26415-26429.

43. T. Fu, *Materials Research Bulletin*, 2013, **48**, 1784-1790.

44. Y. Wang, W. Jia, T. Strout, A. Schempf, H. Zhang, B. Li, J. Cui and Y. Lei, *Electroanalysis*, 2009, **21**, 1432-1438.

45. Y. Ogimoto, R. Selyanchyn, N. Takahara, S. Wakamatsu and S.-W. Lee, *Sensors and Actuators B: Chemical*, 2015, **215**, 428-436.

46. R. W. Jenkins, C. H. Cheek and V. J. Linnenbom, *Analytical Chemistry*, 1966, **38**, 1257-1258.

47. T. Wang, W. Yasukochi, S. Korposh, S. W. James, R. P. Tatam and S.-W. Lee, *Sensors and Actuators B: Chemical*, 2016, **228**, 573-580.

48. J. N. Hao and B. Yan, *Nanoscale*, 2016, **8**, 2881-2886.

49. S. Kumar, S. Kaushik, R. Pratap and S. Raghavan, *ACS Applied Materials and Interfaces*, 2015, **7**, 2189-2194.

50. L. T. Duy, T. Q. Trung, V. Q. Dang, B.-U. Hwang, S. Siddiqui, I.-Y. Son, S. K. Yoon, D. J. Chung and N.-E. Lee, *Advanced Functional Materials*, 2016, **26**, 4329-4338.

51. P. Feng, F. Shao, Y. Shi and Q. Wan, *Sensors (Basel, Switzerland)*, 2014, **14**, 17406-17429.

52. A. de Moraes and L. Kubota, *Chemosensors*, 2016, **4**, 20-20.

53. L. Torsi, A. Dodabalapur, L. Sabbatini and P. G. Zambonin, *Sensors and Actuators B: Chemical*, 2000, **67**, 312-316.

54. R. Ahmad, N. Tripathy, M. Y. Khan, K. S. Bhat, M.-s. Ahn and Y.-B. Hahn, *RSC Adv.*, 2016, **6**, 54836-54840.

55. C. Li, D. Zhang, X. Liu, S. Han, T. Tang, J. Han and C. Zhou, *Applied Physics Letters*, 2003, **82**, 1613-1615.

56. A. A. Talin, L. L. Hunter, F. Leonard and B. Rokad, *Applied Physics Letters*, 2006, **89**, 153102-153102.

57. H. W. Zan, W. W. Tsai, Y. r. Lo, Y. M. Wu and Y. S. Yang, *IEEE Sensors Journal*, 2012, **12**, 594-601.

58. K. Besar, S. Yang, X. Guo, W. Huang, A. M. Rule, P. N. Breysse, I. J. Kymissis and H. E. Katz, *Organic Electronics*, 2014, **15**, 3221-3230.

59. S. Tiwari, A. K. Singh, L. Joshi, P. Chakrabarti, W. Takashima, K. Kaneto and R. Prakash, *Sensors and Actuators B: Chemical*, 2012, **171**, 962-968.

60. N. Yamazoe and K. Shimanoe, *Sensors and Actuators, B: Chemical*, 2008, **128**, 566-573.

61. S. Kanan, O. El-Kadri, I. Abu-Yousef and M. Kanan, *Sensors*, 2009, **9**, 8158.

62. Y. Yang, G. Zhang, H. Luo, J. Yao, Z. Liu and D. Zhang, *ACS Applied Materials and Interfaces*, 2016, **8**, 3635-3643.

63. S. B. L. F. L. M. J. Y. L. Z. J. L. T. K. Y.F Sun and J. H. Liu, *Sensors*, 2012, **12**, 2610-2631.

64. L. Qi, H. Cölfen and M. Antonietti, *Nano Letters*, 2001, **1**, 61-65.

65. J. M. Coronado, F. Fresno, M. D. Hernández-Alonso and R. Portela, *Design of Advanced Photocatalytic Materials for Energy and Environmental Applications*, 2013.

66. V. Bilgin, S. Kose, F. Atay and I. Akyuz, *Materials Chemistry and Physics*, 2005, **94**, 103-108.

67. Q. Wang, X. Dong, Z. Pang, Y. Du, X. Xia, Q. Wei and F. Huang, *Sensors (Switzerland)*, 2012, **12**, 17046-17057.

68. Y. Liu, L. Wang, H. Wang, M. Xiong, T. Yang and G. S. Zakharova, *Sensors and Actuators, B: Chemical*, 2016, **236**, 529-536.

69. O. Lupan, V. Cretu, V. Postica, N. Ababii, O. Polonskyi, V. Kaidas, F. Schütt, Y. K. Mishra, E. Monaico, I. Tiginyanu, V. Sontea, T. Strunskus, F. Faupel and R. Adelung, *Sensors and Actuators, B: Chemical*, 2016, **224**, 434-448.

70. P. Hu, G. Du, W. Zhou, J. Cui, J. Lin, H. Liu, D. Liu, J. Wang and S. Chen, *ACS Applied Materials and Interfaces*, 2010, **2**, 3263-3269.

71. A. Klug, M. Denk, T. Bauer, M. Sandholzer, U. Scherf, C. Slugovc and E. J. W. List, *Organic Electronics: physics, materials, applications*, 2013, **14**, 500-504.

72. G. S. Ryu, K. H. Park, W. T. Park, Y. H. Kim and Y. Y. Noh, *Organic Electronics*, 2015, **23**, 76-81.

73. D. Chen, S. Lei and Y. Chen, *Sensors*, 2011, **11**, 6509-6516.

74. S. H. Yu, J. Cho, K. M. Sim, J. U. Ha and D. S. Chung, *ACS Applied Materials & Interfaces*, 2016, **8**, 6570-6576.

75. S. Han, X. Zhuang, W. Shi, X. Yang, L. Li and J. Yu, *Sensors and Actuators, B: Chemical*, 2016, **225**, 10-15.

III. Other Electronic Sensors and POC Devices

CHAPTER 8

A Prototype for Point-of-Care Stress Detection at Different Body Parts

Contents

ABSTRACT 231
8.1. Introduction 232
8.2. Experimental Section 238
8.2.1 Materials 238
8.2.2 Fabrication 238
8.2.3 Optimization and Characterization of Patterned Electrode 240
8.2.4 Experimental Method 241
8.3. Results and Discussion 243
8.4. Conclusions 249
References 250

भारतीय प्रौद्योगिकी संस्थान गुवाहाटी
Indian Institute of Technology Guwahati

ABSTRACT

Design and development of an affordable, user-friendly, and portable proof-of-concept prototype for the detection of the physical stress at different parts of the body has been reported. The prototype is composed of three major parts, namely, a sensor arrangement, a signal processing unit, and a power supply. The sensor arrangement consists of a flexible and soft substrate made of polydimethylsiloxane (PDMS) coated with electrically conducting aluminum (Al) and reduced graphene oxide (RGO) layers. The conductive layer on the flexible PDMS substrate helps in detecting the raw surface electromyogarphic (RSEMG) potential of the different parts a human body such as finger-tip, tip-toe, wrist, or tongue, once they come in contact with the sensor. The array of high density microstructures of Al/RGO decorated on the PDMS substrate generates an electrical signal, which can be correlated to the stress level of the body parts with a very high-precision. In particular, the physically heterogeneous Al/RGO microstructures fabricated on the polymer surface helps in the development of a better adhesion between the sensor and the epidermal surface of the body part for a superior sensor response as compared to their homogeneous counterparts. The electrical signal generated by the sensor is sent to the signal processing unit, which is further transmitted wirelessly to an open source mobile application for the display of the results. The prototype can useful for the early detection of many disorders related to heart, nerves and muscles, which can be correlated with the symptom of increase in the levels of stress at different body parts.

The manuscript is under preparation.

8.1. Introduction

Regular monitoring of diverse health parameters in real time has become one of the basic necessities of the contemporary human life.[1-3] In particular, the busy and compact schedules in the professional and personal spaces of the individuals have led to the onset of various lifestyle related diseases, which are rather unheard of about a century back. The stressful daily routines of the children to adults have been taking a big toll on all the functional organs, which often go unnoticed owing to the lack of measurement tools. Recent studies indicate that the chronic health issues involving heart, muscles, and nervous disorders have their origin in the accumulation of such stresses for a longer duration.[4] These disorders have become common not only among the elderly peoples but also among the youths across the globe.[5]

In this situation, a portable and economic detection technique is required to keep a track of the stress related abnormalities of human body in real time. Presently, the available techniques like electromyography (EMG), electrocardiography (ECG), or electroencephalography (EEG) are the most common methods for monitoring of these health parameters associated with muscle, heart, and brain, respectively.[1] However, they are not only costly and non-portable techniques but also available in the centralized health agencies. Most of these instruments need medical experts or professional to operate as well as analyze the data. Thus, a user-friendly and portable device with an artificial intelligence based data analytical tool for the real time monitoring of the stress accumulations parameters is perhaps the need of the hour.

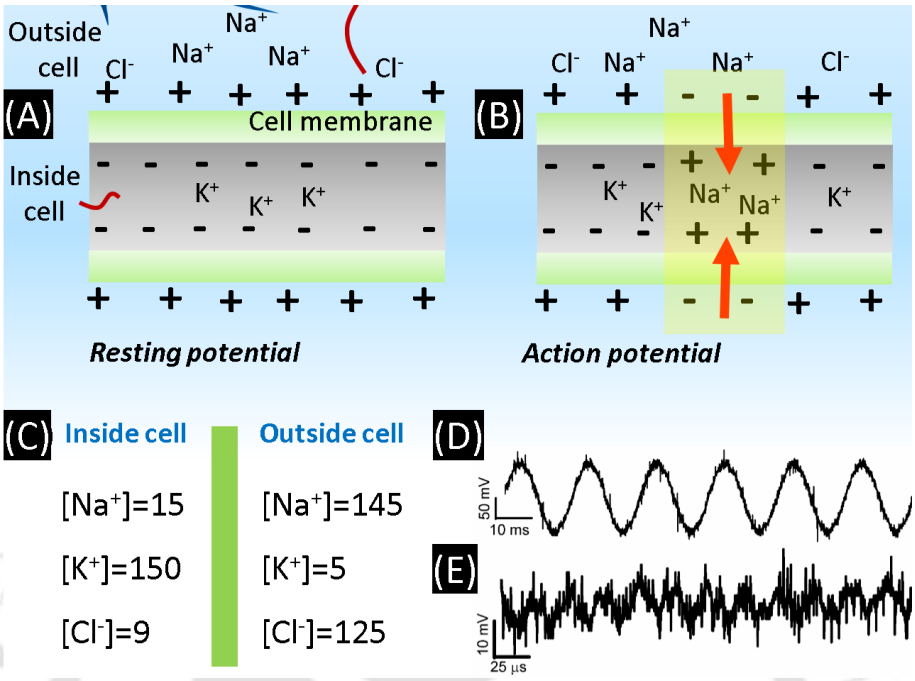

Figure 8.1: The figure shows mechanism of resting and action potential formation on cell membrane. Images (A) and (B) shows the formation of resting and action potential on the cell membrane, respectively. Image (C) shows the concentration of three majorly contributing ions Na^+, K^+, and Cl^- in during resting potential condition, inside and outside the cell. The concentrations are in mmol/l. Images (D) and (E) show the recorded low and high frequency voltage signals, respectively from the surface of index finger.

Among the existing methodologies, EMG generates equivalent electrical signal to diagnose stiffness or strain of the muscles of different body parts such as heart, nerve, and muscles.[6-8] The muscles are constantly monitored under EMG scanner to identify the trigger point[9-11] by analyzing the spontaneous 'EMG-activity' in a muscle location as compared to the other 'EMG-quite' zones.[12-15] Once the trigger point is identified for the muscle spasm and pain, the treatment is provided to eradicate the movement disorder, recurrent muscular pain and muscle degeneration or degradation issues.[14, 16]

However, the previous studies report that to detect the body potential[17] a group of muscle needs to be separated by the use of support or restrain device arrangement.[18] This limits the patient's movement and not a feasible option to be used in public places. Moreover,

use of a multiple electrode system coupled with a computing device makes the instrument non-portable.[19-23] In some of the EMG devices,[24-27] electrodes are placed across the spine in order to detect the pattern of body electric potential[28] where the pattern of the potential helps in determining the health condition of the patient. In the other existing devices,[29] there is a necessity to generate a range of motions with respect to a particular group of muscles before the pattern of potential are compared and contrasted with a standard by the medical experts.[30] Clearly, the processes involved with the EMG based diagnosis are costly, non-portable, complex, and require medical experts.

On the other hand, ECG and EEG are other two methodologies, which have been employed in detecting the heart-wave and brain activities of a human in order to diagnose heart and brain related diseases.[31-33] The currently available EMG and ECG devices comprise of multiple electrodes to track the potentials of the related muscles.[34-36] The electrodes in these devices are generally coupled to an external computer integrated with the signal processing circuits for the accurate detection and analysis of the symptoms. Prior art show the use of specialized electrodes and signal processing patterns in order to detect the electric field potentials near the heart or brain muscles.[37-39] Apart from the measurement of electric field potential, electrodynamic sensors have also been employed to detect the electrical signal from human body for diagnosis purpose.[40, 41]

However, a point-of-care-testing (POCT) device for the early detection of stress related abnormalities of a human body parts by measuring its electric field potential is yet to make appearance in the research arena or market. In the present study we show a simple paper based sensor coated with an array of aluminium (Al) and graphene oxide (RGO) microstructure can measure electric field potential of different body parts at the patients

site. We show that the integration of this sensor with a signal processing unit and a power supply can lead to the development of a POCT device useful for the regular monitoring of the stress accumulations at the different body parts such as finger-tip, tip-toe, wrist, or tongue.

It is well known that the surface of a human skin or a muscle carries some electrostatic charges owing to the nature of the skin tissues.[42] The reason behind this electrostatic potential is as follows. The human tissues are composed of cells, joining the extracellular matrix[43, 44] and they communicate with each other through the exchange of electrical signals through neurons and muscles.[45] In general, the cell-membranes possess a resting electrical potential of about -40 to -80 mV.[46, 47] The concentration gradient of different ions, inside and outside the cell, such as, sodium (Na^+), potassium (K^+) and chloride (Cl^-) play vital roles in maintaining potential difference between the inner and outer part of the cells. Since the cell membrane is semi-permeable, these ions undergo a potential dependent transport across it in order to respond to various triggers.[48] For example, during rest the concentration of K^+ is found to be higher inside the cell while the concentration of Na^+ is higher outside the cell, which allows a natural chemical potential gradient for transport of various materials across the membrane, as shown in image (A) of Figure 8.1.[49, 50] In addition, the negatively charged Cl^- ions are also found in higher concentration outside the cell.

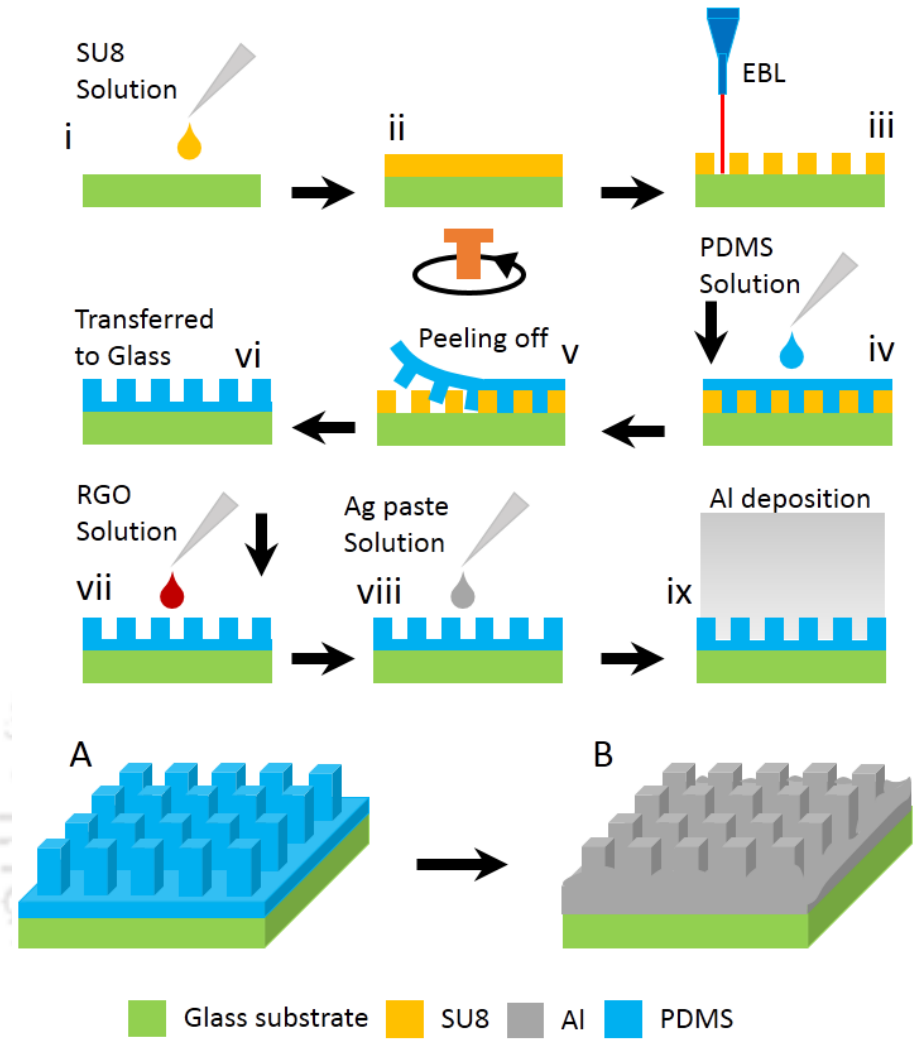

Figure 8.2: The figure shows fabrication steps and the schematic diagram of the patterned electrode. Images (i) to (ix) are the different steps of fabrications. Image (A) shows the schematic isometric view of the pattern on PDMS. Image (B) shows the final electrode schematically after Al deposition.

Thus, at rest, the skin tissues possess a 'resting' potential, which is the sum of the potentials of all the cells present on the surface. The cells communicate with each other based on the change in the concentration of the ions, inside and outside the cells. The typical concentration of Na^+, K^+, and Cl^- ions during rest condition are tabulated in image (C) where the concentrations are in mmol/l.[51] The resting potential are often disturbed by various external stimuli, neuronal excitement, or muscle movement to a higher or lower

value based on depolarization and hyperpolarization, respectively.[52] In depolarization mechanism, a channel opens for Na^+ ions to move inside the cell, resulting in a rise in outside cell potential whereas during hyperpolarization, channel for K^+ opens up, resulting in decrease in outside cell potential.[53] Figure 8.1(B) schematically shows the generation of action potential and an open channel for Na^+ ions.

Thus, the voltage signal from the skin surface are often utilized for diagnosing the health of diverse tissues and organs. For example, EMG gives information about the health of muscles.[54, 55] The EMG can be recorded by two different techniques, (i) putting a needle electrode inside the muscle or (ii) taking signals from the surface of a skin.[35] Most of these techniques record low frequency signals, e.g. ~30 Hz or less, to determine the medical conditions.[56] However, the electrode used in these techniques often experience issues related to skin-contact and noise reception from muscle contraction.[57]

In view of this background, herein we target to detect the high frequency components of the electrostatic signals on the skin tissues to diagnose the health of muscle or skin. For this purpose, we develop a specialized micro/nano patterned electrode for a seamless contact with the human body parts. The electrodes help us in the analyses of combined neuronal and muscle signals of RSEMG to diagnose the abnormalities associated with the muscle or neuronal activities. Figures 8.1(D) and 8.1(E) show low and high frequency signals from an index finger detected by the proposed device. The results reported here can be of significance in the development of futuristic EMG, ECG, and EEG electrodes employing the proposed methodology.

8.2. Experimental Section

8.2.1 Materials

Sodium hydroxide (NaOH) pellets, Hydrochloric acid (HCl), sodium chloride (NaCl), potassium permanganate ($KMnO_4$), 50% hydrogen peroxide (H_2O_2), 98% sulfuric acid (H_2SO_4), 125 mm filter paper (grade 1), acetone (CH_3COCH_3), and 84% ortho-phosphoric acid (H_3PO_4) were procured from Merck (India). Phosphorous pentoxide (P_2O_5), 98% hydrazine monohydrate (N_2H_4) were obtained from Sigma–Aldrich (India). Graphite flakes (99.99%) and anhydrous barium chloride ($BaCl_2$) were procured Alfa Aesar and Fisher Scientific, respectively. PDMS Sylgrad 184 was procured from Dow Corning, India. SU8 was procured from Microchem, Germany. Graphite flakes was obtained from Sigma Aldrich, India. Aluminum wire (99%) utilized for vapor deposition was procured from Alfa Aesar, India. Glass slide, Cu wire, and other electrical components were obtained from local vendor.

8.2.2 Fabrication

The patterned electrodes were prepared by making a negative pattern on SU-8 (on glass substrate) and transferring it on PDMS as shown in Figure 8.2. First, a 1.5 cm x 1.5 cm glass piece was cut and cleaned. Next, a 2 µm thick SU-8 layer was applied by spin coating followed by baking at 90^0C for 2 mins on a hot plate. Rectangular patterns of different dimensions were defined on SU-8 by electron beam lithography (Xenos XeDraw 2) at an acceleration voltage of 30 kV. Post exposure, the samples were baked again for 3 mins at 90^0C on a hot plate.

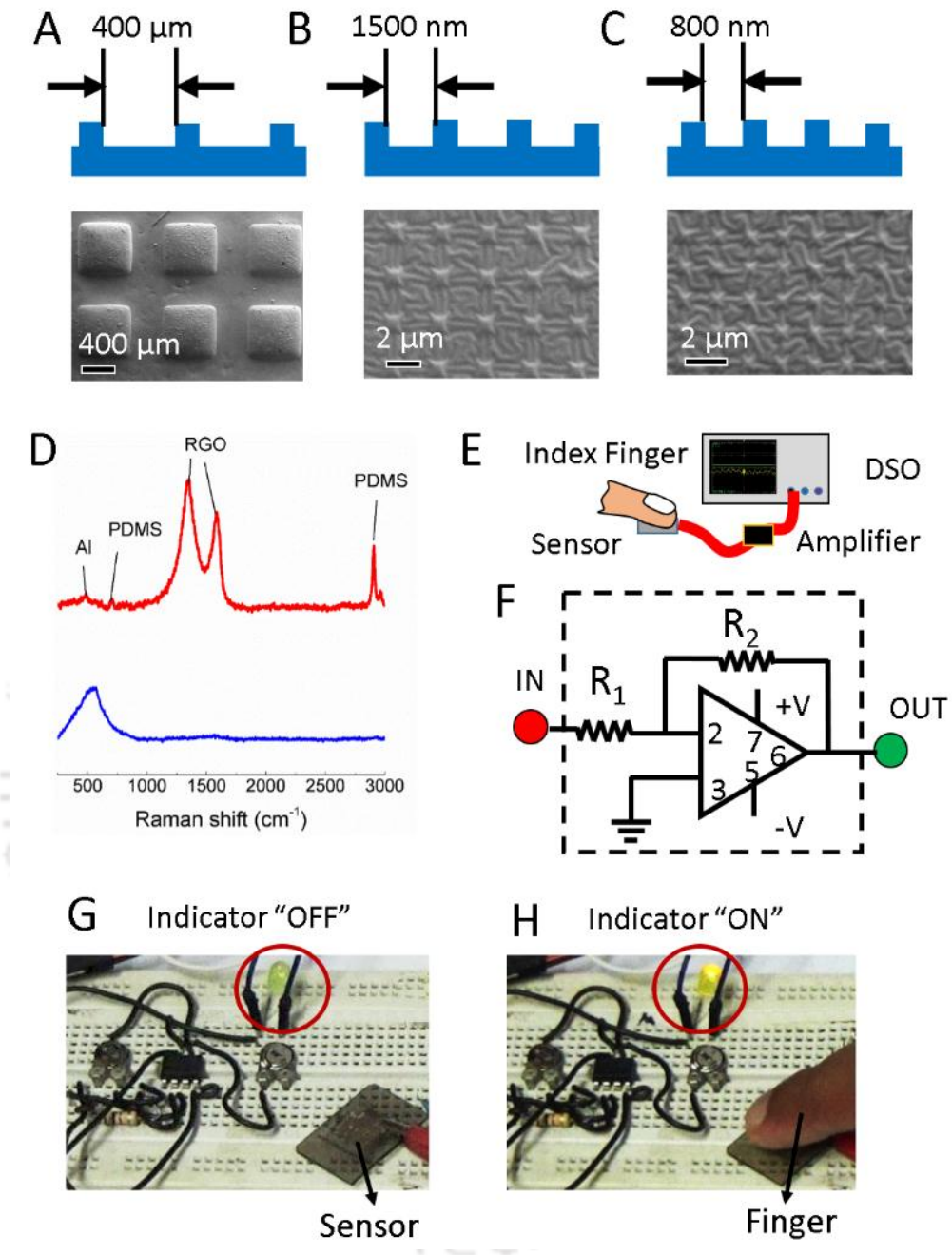

Figure 8.3: This figure shows the sensor optimization, characterization, and experimental set-up. Images (A)-(C) shows the fabricated patterns for the sensor electrode along with the FESEM images. Image (D) shows the Raman spectroscopy of the fabricated metal electrode of Al coated glass substrate (blue) and patterned electrode based on RGO, Al, and PDMS. Image (E) shows the experimental set-up to record the surface electrical potential of a body part. Image (F) shows the associated amplifier circuit employed to detect the surface potential. Images (G) and (H) shows the real experimental image with an indicator LED to demonstrate the generation of surface electric potential.

They were subsequently developed in a developer solution followed by rinsing in DI water. The substrates were dried in a nitrogen stream and re-heated. Thus the SU-8 master was prepared. However, for creating larger patterns, electron beam lithography was not preferred. Instead, square patterns were defined on a photoresist (S1818) coated glass substrate by direct UV laser exposure (Mask writer, Dilase 250) followed by etching in 20% aqueous HF solution.

In order to transfer the pattern on a soft substrate, a ~1.5 mm thick PDMS (monomer: cross-linker = 10:1) was cast on the master and left to cure overnight at ambient temperature. After peeling off the cured PDMS, aqueous dispersion of GO was drop cast on the patterned PDMS surface and reduced to RGO by hydrazine vapor in a closed system.

This was followed by a drop cast of Ag paste solution on the pattern. RGO had been pre-prepared by a modified Hummers' method. Finally, an aluminium layer was deposited on the RGO coated PDMS by thermal evaporation in order to achieve a conducting surface.

The fabrication steps are illustrated schematically in images (i) to (ix) of Figure 8.2. Images (A) and (B) shows the schematic diagram of patterned electrode before and after metal deposition, respectively. Different spacing and size of the pattern were fabricated in order to optimize the sensor electrode. The optimization and characterizations are discussed in the next section.

8.2.3 Optimization and Characterization of Patterned Electrode

Multiple patterned electrodes were fabricated with different spacing between the square patterns as shown in FESEM images (A) to (C) in Figure 8.3. It was found

400 µm spacing was optimum in this case because smaller patterns led to the development of surface wrinkles during the development phase as shown on the images. Image (D) shows the Raman spectroscopy of the Al deposited electrode and electrode with Al-RGO coating on PDMS. The corresponding peaks as indicated in the image confirms the presence of the materials.

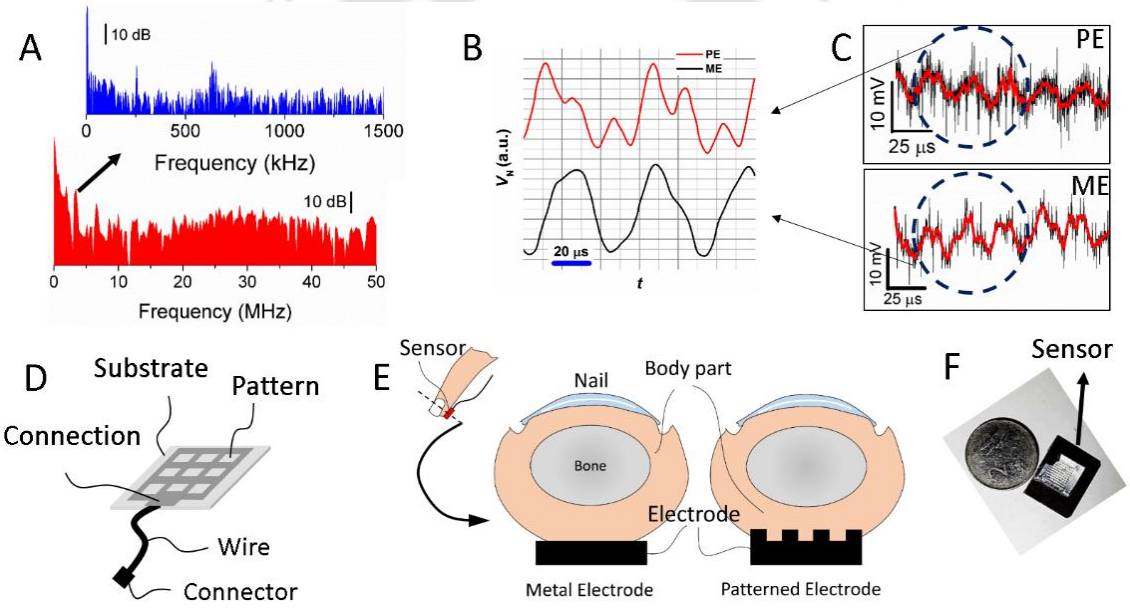

Figure 8.4: This figure shows sensor results. Image (A) shows the power spectrum of the RSEMG signal received from the index finger. Image (B) shows the smoothed signal received by patterned electrode (PE) and metal electrode (ME) whereas image (C) shows the signal as received by the electrode. Image (D) and (E) shows the schematic representation of the patterned electrode and the arrangement of placing the electrode on index finger. Image (F) shows the real image of the fabricated sensor.

8.2.4 Experimental Method

The experiments were performed in ambient condition. The electrodes after fabrication was connected to an amplifier circuit, as shown in the Figure 8.3F before the sensor was brought in contact with different body parts such as index finger, wrist, toe, and tongue. Figure 8.3E of the Figure 8.3 shows the experimental

set-up schematically. The output of the sensor was measured using a digital oscilloscope. The data were then collected and analyzed for understanding.

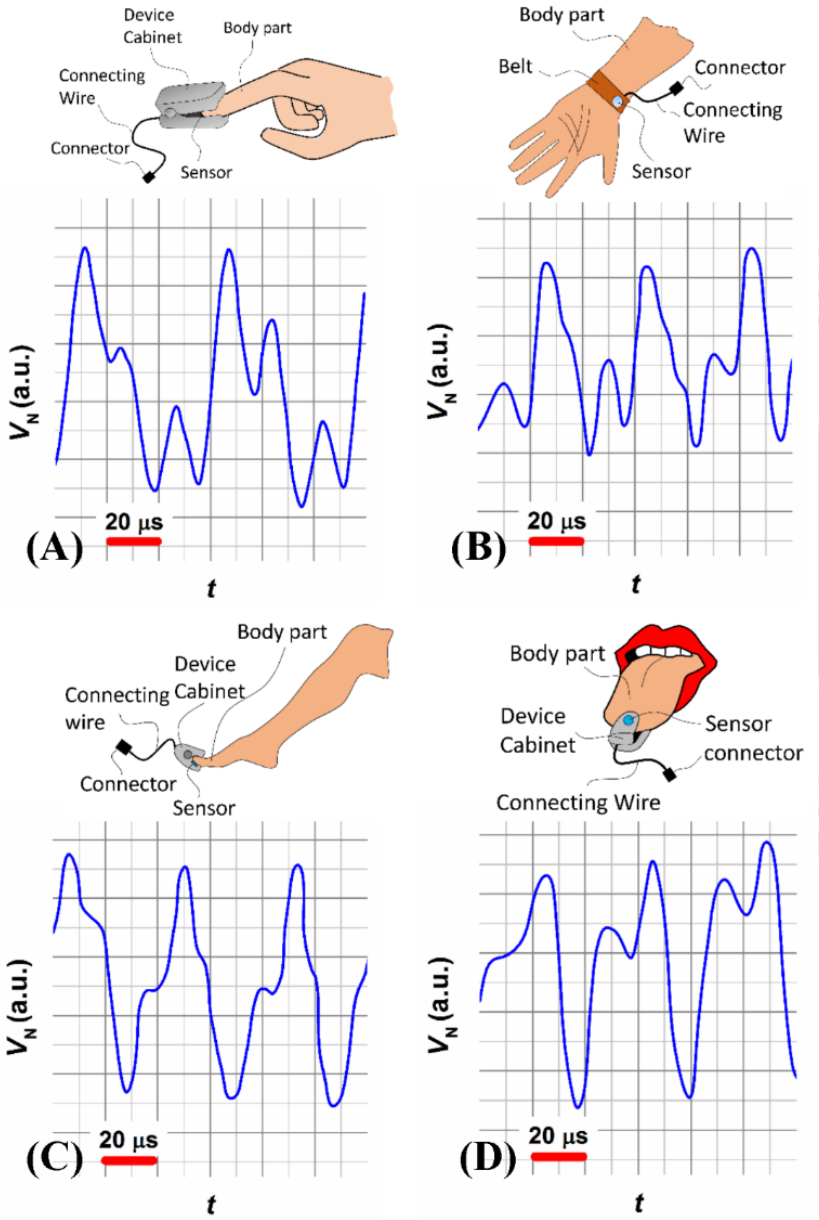

Figure 8.5: The figure shows the response of the PE sensor at rest for index finger (A), wrist (B), big toe (C), and tongue (D). Here, V_N refers to the normalized voltage signal from the respective organs in arbitrary units (a.u.) and t is the time.

8.3. Results and Discussion

In this chapter, we are targeting the high frequency signal of the RSEMG signal. To understand the power distribution, a power spectrum study was performed as illustrated in image (A) of the Figure 8.4, where the signal in kHz range was targeted. The power distribution suggests the existence of the high components which can be used for further analysis. Image (B) and (C) shows the RSEMG signal received from index finger by a metal electrode (ME) and patterned electrode (PE). It was observed that the patterned electrode signal carried much detailed information. The reason behind this was the contact between the electrode and the skin surface. The sensor geometry is described in image (D).

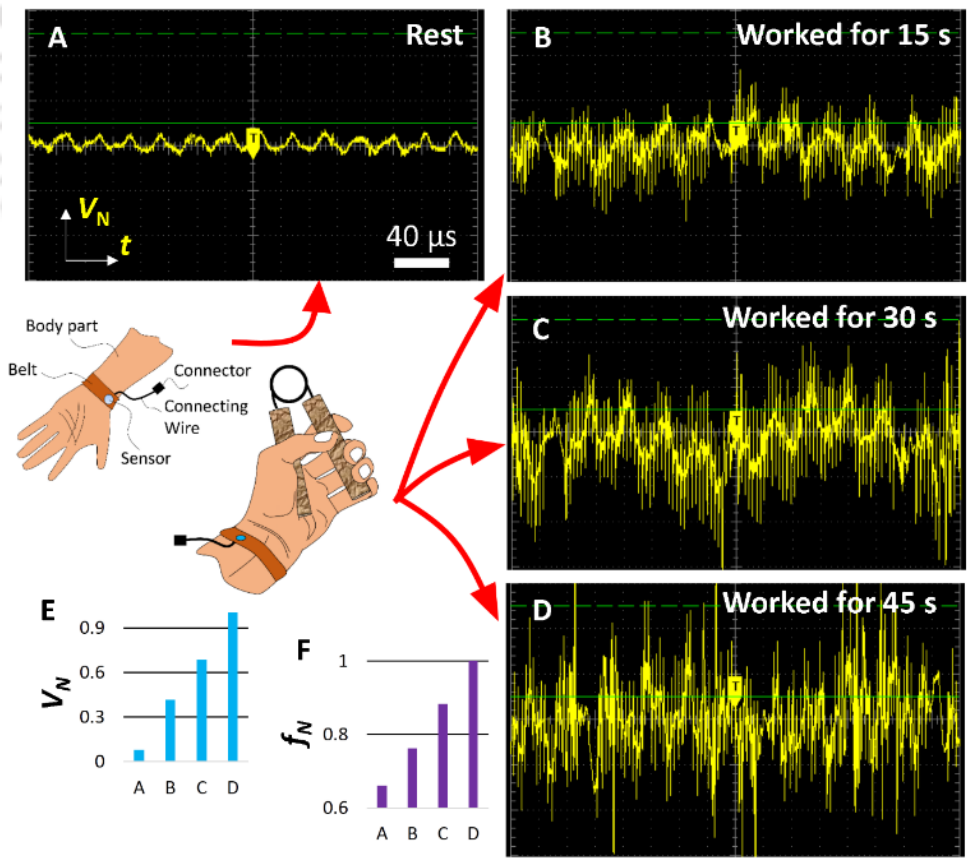

Figure 8.6: The figure shows the response of the PE sensor attached to the wrist at rest condition (A) and while working (B-D) for different time. Plot (E) and (F) show the change in normalized

voltage (V_N) and frequency (f_N) of the body potential signal, respectively, for the cases described in images (A-D). Here, V_N refers to the normalized voltage and f_N stands for normalized frequency of the signal from the respective organs in arbitrary units (a.u.) and t is the time.

The sensor was fabricated on a flexible or soft substrate of PDMS. The sensor also consisted of conductive layers of aluminium (Al) and RGO. The sensor has micro/nano-patterns on the surface which ensures a large contact area and the softness of the sensor helps in adjusting the surface according to the shape of the skin and muscle. The schematic illustration in image (E) shows how the contact area for a patterned electrode increases compared to a plane metal electrode. Image (F) shows a real image of the fabricated sensor electrode.

Figure 8.5 shows the signal received from different body parts. Images (A)-(D) shows the RSEMG signal for index finger, wrist, toe, and tongue respectively. It Is important to observe that the pattern of the signals are slightly different in different body parts which confirms that the depolarization and hyperpolarization of the Na^+/K^+ ion in the epidermal layer of skin happen at a different rate depending upon the body parts. The high frequency response in this case also suggests that there is continuous movement of ions in the epidermal layers and muscle layers as there is a regular movement of muscle throughout the body even at a rest condition due different physiological activities.

It is well known that the signals received from the skin is generally influenced by three components of our body, namely, muscle, fat, and neuron.[58] The received signals in Figure 8.5 has the mentioned three components, however, the contribution of fat would be very small as the fat accumulation in the selected body parts are significantly less. Moreover, the high frequency neuronal activity often get

interfered by the muscle activity as per prior art,[59] but in this study the major aim is to identify whether the high frequency RSEMG signals can be used for the primary diagnosis of muscle health, neurological disorders or not. Hence, the combination of the muscle and neuronal activity was recorded simultaneously.

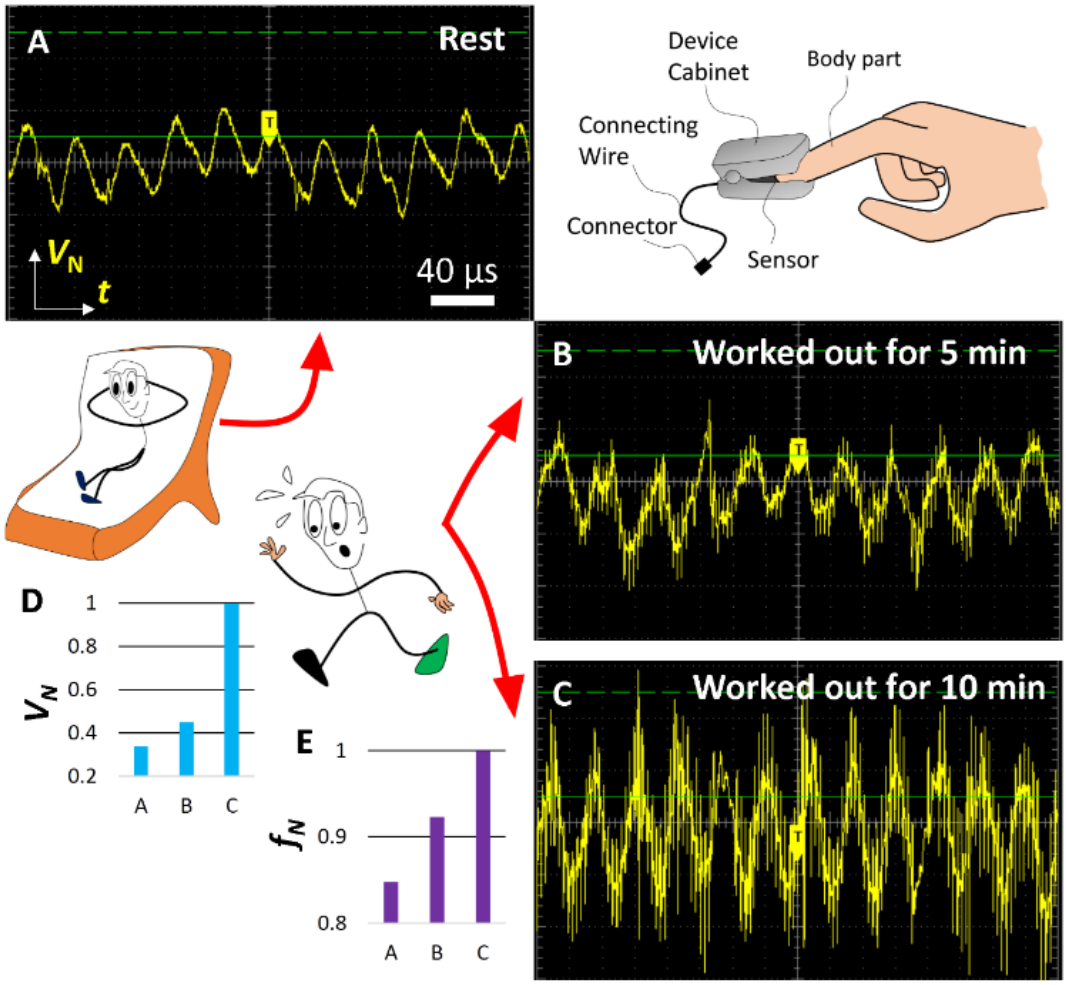

Figure 8.7: The figure shows the response of the PE sensor attached to index finger (A) at rest condition and after working out for (B) 5 min and (C) 10 min. Plot (D) and (E) show the change in normalized voltage (V_N) and frequency (f_N) of the body potential signal, respectively for the cases described in images (A-C). Here, V_N refers to the normalized voltage and f_N stands for normalized frequency of the signal from the respective organs in arbitrary units (a.u.) and t is the time.

Figure 8.6 shows a response from the wrist during the physical activity. The sensor in this case was attached in the left side of the left wrist in order to detect the RSEMG signal. During rest condition as shown in image (A) of Figure 8.6, the signal was similar as described in image (B) of Figure 8.5.

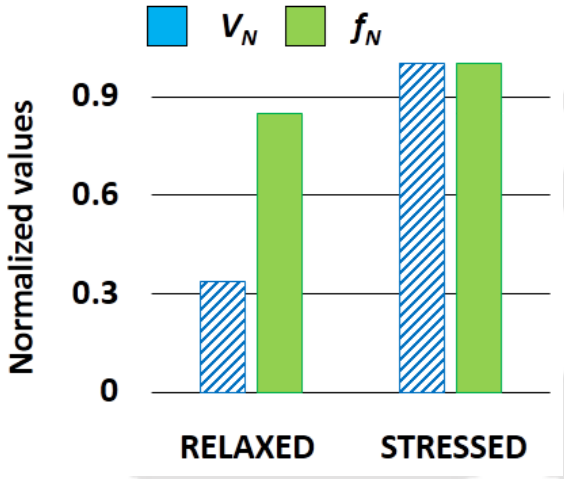

Figure 8.8: The figure shows the change in normalized voltage (V_N) and frequency (f_N) of the body potential signal detected by a PE sensor attached to index finger for relaxed and stressed body condition due to work out of 10 min.

However, the amplitude and frequency was found to increase at a considerably higher value while performing hand exercise as shown in images (B)-(D) of Figure 8.6. The plots (E) and (F) shows the variation in the normalized magnitude of voltage amplitude (V_N) and frequency (f_N). During exercise, the contraction and expansion in the muscle and skin effected the ion transport in the skin and neuron which created an action potential of higher magnitude. The change in the RSEMG can be utilized to detect the activity of the muscle, skin, and neuron. In many cases, the potential fluctuation during the rest condition, indicating a health issue related to muscle, skin, or neuron, can be detected at the early stages.

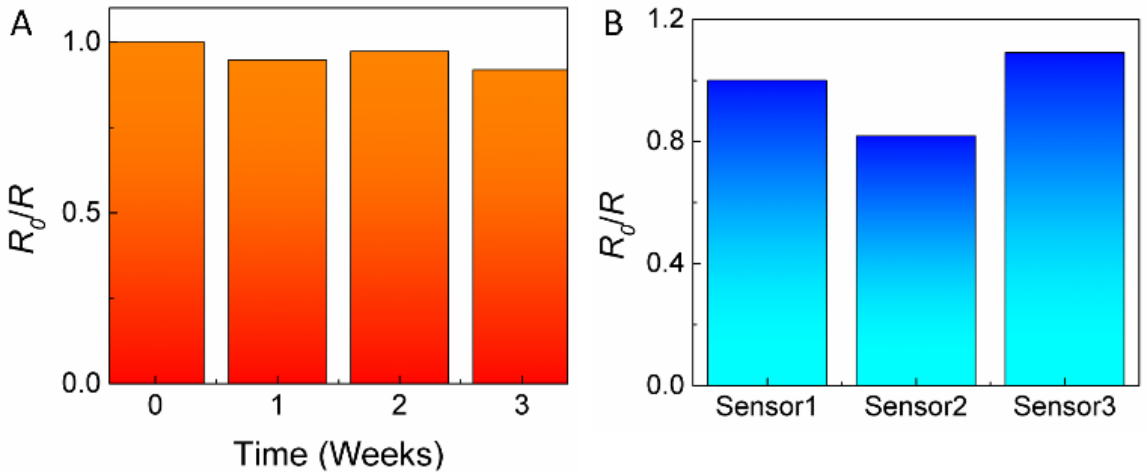

Figure 8.9: This figure shows the stability analysis of the sensor electrode. Image (A) shows the stability of the sensor with time. Image (B) shows the comparison between different sensors.

Figure 8.7 shows the similar experiment as described, previously, but, in this case the RSEMG signal was recorded from the index finger at a regular time interval during a physical exercise. In this situation, the response was taken after performing physical activity for a given time interval. Image (A) of Figure 8.7 shows the response at the rest condition. It was found that the RSMG showed a higher response in terms of voltage amplitude and frequency after higher amount of physical exercise as shown in images (B) and (C) of Figure 8.7. Images (D) and (E) show the normalized voltage and frequency response for three different time intervals as shown in images (A) to (C).

Figure 8.8 summarizes the responses received in this situation as RSEMG signal. It was found that during physical stressed situation the voltage of the RSEMG signal rises significantly compared to a relaxed situation. A rise in the frequency was also observed due to the physical stress or exercise.

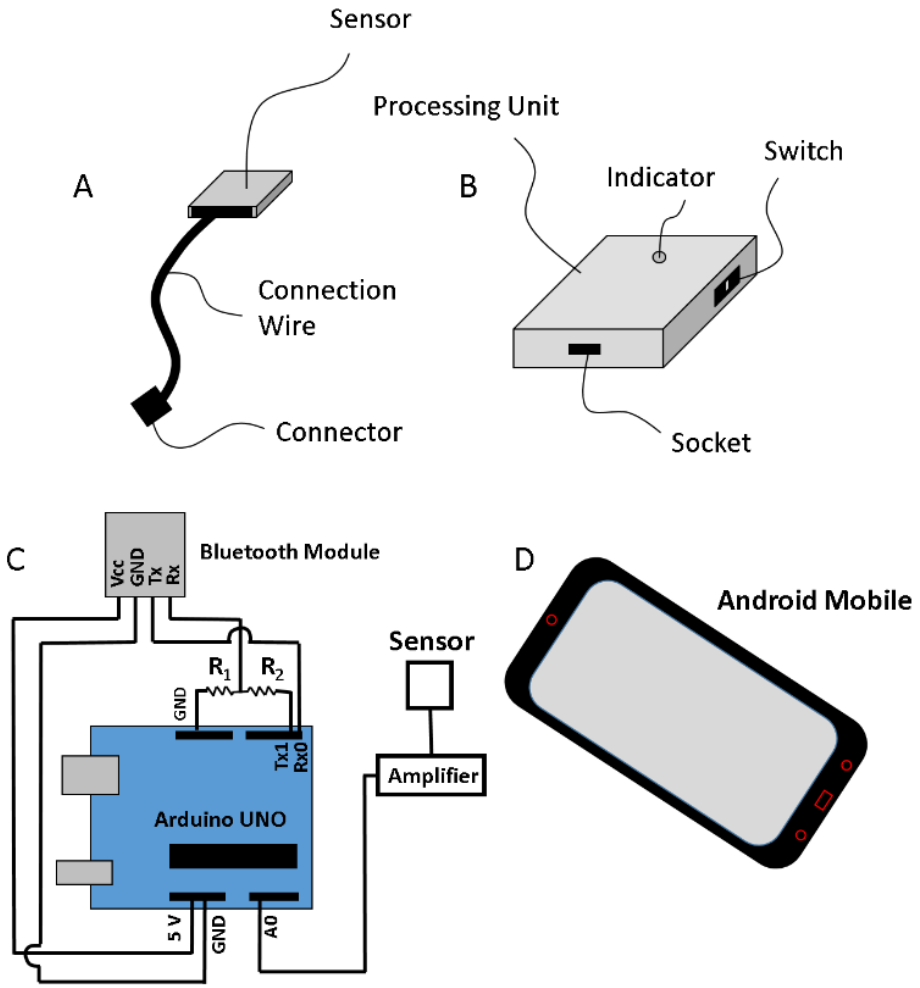

Figure 8.10: This figure shows the sensor arrangement and processing unit. The sensor is fabricated on a flexible or soft substrate of say PDMS. The processing unit contains a socket for connecting the connector of the sensor. The processing unit also contains an indicator LED and an ON-OFF switch.

Figure 8.9 shows a stability study of the fabricated sensor electrode. The stability was measured by taking the resistance value across the sensing electrode over time and dividing the base resistance value with the resistance values obtained at different time interval. Image (A) shows the stability of the sensor with time. Further, different batches of sensor electrodes were also prepared and a comparison with different batches of sensor was performed as shown in image (B) of Figure 8.9. It was found that the sensor electrodes were stable for a considerable amount of time.

The idea of this work was to analyze the RSEMG signal and to understand the effect of different body conditions on the RSEMG signal so that the signal can be utilized in primary healthcare for detection of muscle, nerve, and heart related issues at early stages. The sensor here was a patterned electrode which comes in contact with the muscle under diagnosis. Images (A) and (B) show the possible sensor arrangement and processing unit. The processing unit of the prototype has a socket for connecting the plug. The device also contains a LED indicator and an ON-OFF switch. Image (C) shows the associated circuit of the processing unit of the prototype. The circuit diagram consists of an open source development board, Arduino UNO, a commercial Bluetooth module (HC-06/05), and electrical passive components.

The symbols R_1 and R_2 are the resistors with fixed resistance value which were calibrated according to the sensor response. The sensor is connected to an amplifier which amplifies the received signal and then transmit it to the analog input pin A0 of the Arduino UNO. The signal is then transmitted by the Bluetooth module and is further received by the android mobile application as shown in image (D) which displays it on the mobile screen.

8.4. Conclusions

A user-friendly, and portable proof-of-concept prototype for the detection of the physical stress at different parts of the body has been developed using a micro-nano pattern based sensor. The sensor is flexible and made of a polymer PDMS, which has been patterned using replica molding technique followed by a RGO and Ag-paste solution treatment. The conductive layer coated on the flexible PDMS substrate helps in detecting the electric field

potential of a part of a living body such as finger-tip, tip-toe, wrist, or tongue, once they come in contact with the sensor. The received signal has been further amplified and send to detection unit for analysis. It has been observed that the magnitude and frequency of the received electric potential has a relation with the stress of that muscle. Hence, the prototype is useful for the early detection of many diseases or disorders related to heart, nerves and muscles, which can be correlated with the symptom of increase in the stress at different body parts such as finger-tip, tip-toe, wrist, or tongue, among others.

References

1. S. Patel, H. Park, P. Bonato, L. Chan and M. Rodgers, *Journal of NeuroEngineering and Rehabilitation*, 2012, **9**, 21.
2. R. Ogawa and T. Togawa, 1st Annual International IEEE-EMBS Special Topic Conference on Microtechnologies in Medicine and Biology. Proceedings (Cat. No.00EX451), 2000.
3. U. Varshney, *Mob. Netw. Appl.*, 2007, **12**, 113-127.
4. G. P. Chrousos, *Nature Reviews Endocrinology*, 2009, **5**, 374.
5. F. W. Booth, C. K. Roberts and M. J. Laye, in *Comprehensive Physiology*, John Wiley & Sons, Inc., 2011, DOI: 10.1002/cphy.c110025.
6. O. Vasseljen, B. M. Johansen and R. H. Westgaard, *Scand J Rehabil Med*, 1995, **27**, 243-252.
7. S. F. Bensamoun, S. I. Ringleb, L. Littrell, Q. Chen, M. Brennan, R. L. Ehman and K.-N. An, *Journal of Magnetic Resonance Imaging*, 2006, **23**, 242-247.
8. M. van Tulder, A. Malmivaara and B. Koes, *The Lancet*, 2007, **369**, 1815-1822.

9. C. J. De Luca, *Muscle & Nerve*, 1993, **16**, 210-216.

10. G. Sjøgaard, U. Lundberg and R. Kadefors, *European Journal of Applied Physiology*, 2000, **83**, 99-105.

11. *United States Pat.*, US5722420A, 1995.

12. W. H. McNulty, R. N. Gevirtz, D. R. Hubbard and G. M. Berkoff, *Psychophysiology*, 1994, **31**, 313-316.

13. C. R. Carlson, J. P. Okeson, D. A. Falace, A. J. Nitz and J. E. Lindroth, *Pain*, 1993, **55**, 397-400.

14. T. M. Cummings and A. R. White, *Archives of Physical Medicine and Rehabilitation*, **82**, 986-992.

15. *United States Pat.*, US20120065538A1, 2010.

16. *United States Pat.*, US20080064977, 1999.

17. *United States Pat.*, US5318039, 1989.

18. *United States Pat.*, US5086779A, 1990.

19. B. G. Lapatki, D. F. Stegeman and I. E. Jonas, *Journal of Neuroscience Methods*, 2003, **123**, 117-128.

20. H. Onishi, R. Yagi, K. Akasaka, K. Momose, K. Ihashi and Y. Handa, *Journal of Electromyography and Kinesiology*, 2000, **10**, 59-67.

21. D. T. Westwick, E. A. Pohlmeyer, S. A. Solla, L. E. Miller and E. J. Perreault, *Neural Computation*, 2006, **18**, 329-355.

22. C. Anders, S. Patenge, K. Sander, F. Layher, U. Biedermann and R. W. Kinne, *PLOS ONE*, 2017, **12**, e0178957.

23. *United States Pat.*, US20160151626, 2013.

24. M. Alizadeh, G. G. Knapik, J. S. Dufour, C. Zindl, M. J. Allen, J. Bertran, N. Fitzpatrick and W. S. Marras, *Journal of Electromyography and Kinesiology*, 2017, **32**, 101-109.

25. J. Hwang, G. G. Knapik, J. S. Dufour, T. M. Best, S. N. Khan, E. Mendel and W. S. Marras, *Journal of Electromyography and Kinesiology*, 2017, **33**, 1-9.

26. A. Rainoldi, G. Melchiorri and I. Caruso, *Journal of Neuroscience Methods*, 2004, **134**, 37-43.

27. S. McGill, D. Juker and P. Kropf, *Journal of Biomechanics*, **29**, 1503-1507.

28. *United States Pat.*, US5058602, 1988.

29. *United States Pat.*, US7420472, 2005.

30. *United States Pat.*, US5513651, 1994.

31. D. Kurian, L. J. J. P, K. Radhakrishnan and A. A. Balakrishnan, 2014.

32. J. S. Paiva, D. Dias and J. P. S. Cunha, *PLOS ONE*, 2017, **12**, e0180942.

33. J. Werth, L. Atallah, P. Andriessen, X. Long, E. Zwartkruis-Pelgrim and R. M. Aarts, *Sleep Medicine Reviews*, **32**, 109-122.

34. E. A. Clancy, E. L. Morin and R. Merletti, *Journal of Electromyography and Kinesiology*, 2002, **12**, 1-16.

35. C. De Luca, in *Encyclopedia of Medical Devices and Instrumentation*, John Wiley & Sons, Inc., 2006, DOI: 10.1002/0471732877.emd097.

36. A. Kubacki and A. Milecki, Cham, 2017.

37. M. B. I. Reaz, M. S. Hussain and F. Mohd-Yasin, *Biological Procedures Online*, 2006, **8**, 11-35.

38. S. Sanei and J. A. Chambers, *EEG Signal Processing*, Wiley, 2013.

39. C. J. De Luca, *Journal of Applied Biomechanics*, 1997, **13**, 135-163.

40. C. J. Harland, T. D. Clark and R. J. Prance, *Measurement Science and Technology*, 2002, **13**, 163.

41. C. J. Harland, T. D. Clark and R. J. Prance, *Measurement Science and Technology*, 2003, **14**, 923.

42. R. M. Fish and L. A. Geddes, *Eplasty*, 2009, **9**, e44.

43. L. D. Muiznieks and F. W. Keeley, *Biochimica et Biophysica Acta (BBA) - Molecular Basis of Disease*, 2013, **1832**, 866-875.

44. P. M. Crapo, T. W. Gilbert and S. F. Badylak, *Biomaterials*, 2011, **32**, 3233-3243.

45. B. Alberts, D. Bray, K. Hopkin, A. Johnson, J. Lewis, M. Raff, K. Roberts and P. Walter, *Essential Cell Biology, Fourth Edition*, Taylor & Francis Group, 2013.

46. R. R. Kamath and M. J. Madou, *Analytical Chemistry*, 2014, **86**, 2963-2971.

47. R. Dey, S. Kar, S. Joshi, T. K. Maiti and S. Chakraborty, *Microfluidics and Nanofluidics*, 2015, **19**, 375-383.

48. F. M. Ashcroft, *Ion Channels and Disease*, Elsevier Science, 1999.

49. R. Lewis, K. E. Asplin, G. Bruce, C. Dart, A. Mobasheri and R. Barrett-Jolley, *Journal of Cellular Physiology*, 2011, **226**, 2979-2986.

50. C. Hammond, in *Cellular and Molecular Neurophysiology (Fourth edition)*, Academic Press, Boston, 2015, DOI: https://doi.org/10.1016/B978-0-12-397032-9.00003-0, pp. 39-54.

51. K. Chen, W. Gao, S. Emaminejad, D. Kiriya, H. Ota, H. Y. Y. Nyein, K. Takei and A. Javey, *Advanced Materials*, 2016, **28**, 4397-4414.

52. L. G. Brock, J. S. Coombs and J. C. Eccles, *The Journal of Physiology*, 1952, **117**, 431-460.

53. X. Qiu, J. Zhang, Y. Li, C. Zhang, D. Wang, W. Zhu, F. Li, S. Ge, N. Xia and S. Qian, *Microsystem Technologies*, 2018, **24**, 2007-2015.

54. K. A. Nyni, L. K. Vincent, L. Varghese, V. L. Liya, A. N. Johny and C. V. Yesudas, 2017.

55. S. M. Felipe, D. J. Marcelino, P. L. Maxwell, M. B. Fles, L. Steven, R. Jim and C. J. Rosa, *Muscle & Nerve*, 2017, **55**, 28-34.

56. S. Gabriel, R. W. Lau and C. Gabriel, *Physics in Medicine & Biology*, 1996, **41**, 2251.

57. L. Mesin, R. Merletti and A. Rainoldi, *Journal of Electromyography and Kinesiology*, 2009, **19**, 719-726.

58. R. Chowdhury, M. Reaz, M. Ali, A. Bakar, K. Chellappan and T. Chang, *Sensors*, 2013, **13**, 12431.

59. *India Pat.*, 201631017054A, 2016.

III. Other Electronic Sensors and POC Devices

CHAPTER 9

Conversion of Observed Speed of a Moving Object to Diagnose Tunnel Vision

Contents

ABSTRACT 257
9.1. Introduction 259
9.2. Experimental Section 263
9.2.1 Materials 263
9.2.2 Characterization Techniques 263
9.2.3 Methods 263
9.3. Results and Discussion 264
9.3.1 Visual Plane 264
9.3.2 Effect of Recording Angle 266
9.3.3 Effect of Other Parameters 267
9.3.4 Concept of Observed Speed 268
9.3.5 Detection of Tunnel Vision 273
9.4. Conclusions 276
References 277

ABSTRACT

We discuss a simple method to measure the distance of a moving object and subsequently the angle of view of the viewer employing the concept of the variation in the observed speed with distance of a moving object. It is well known that when an object moves at a real speed, the observed speed appear to reduce with the increase in the distance between the object and the observer. In this study, we employ this simple concept to measure the distance of the moving objects. We provide a geometrical argument to employ this variation in the observed speed with the distance to measure the distance of multifarious distant objects moving with a finite speed. The very concept can be of significance in the facile measurements of the distance of moving celestial objects in the space, cars on the road, airplanes in the sky, or ships in the ocean. Furthermore, employing the same concept, a virtual motion picture based point-of-care-testing (POCT) device has been developed where the angle of view of a viewer suffering from tunnel vision can be determined. While the virtual motion picture arrangement generates a virtual moving object on the screen, the patient under test is supposed to track the movement of the same from one side-end to the other on the screen. The patient is equipped with a hand held on-off stopwatch, which enable him/her to 'start' the tracking of the movement of the virtual object on its appearance on one side of the screen until its disappearance to the other to mark the 'end'. Based on the patient's response to the virtual moving object on the screen the angle of view of the patients suffering from tunnel vision, retinitis pigmentosa, or hypovolemia can be detected with the help of the proposed POCT device.

Manuscript under preparation.

भारतीय प्रौद्योगिकी संस्थान गुवाहाटी
Indian Institute of Technology Guwahati

9.1. Introduction

Dynamic measurement of the distance of a moving object with the progress in time is an important activity in multifarious fields which include astronomy, construction engineering, navigation, and surveillance, among others. While the instruments like scale or measuring tapes are popular for short distance static measurements, for long distance ones, radio frequency,[1,2] ultrasound,[3-6] radio network,[7-9] polarized light,[10] frequency modulated wave,[11] capacitive or inductive remote sensing,[12] microwaves,[13-15] and lasers[16, 17] have been frequently employed. For example, in the radio frequency technique,[1,2] the measurement of distance is carried out using a frequency hopping scheme where the relative phase offset between various signals of different frequencies received are distinguished to obtain the physical distance. In this regard, the slope of the phase offset is correlated with the frequency to evaluate the distance between the objects. However, most these techniques are based on the detection of the reflected signal of the electromagnetic wave, which suffer from the issues like scattering, background noise, signal loss, fabrication complexity, and cost. A cost-effective and simpler method to measure time varying long distances between the observer and objects is certainly the need of the hour.

In this direction, we report a method to determine the distance between a moving object and an observer employing the concept of observed speed of a moving object. When an object moves at a real speed, the observed speed appear to reduce with the increase in the distance from the observer. We employ this simple concept to measure the distance of the moving objects. We provide a geometrical argument to employ this variation in the observed speed with the distance to measure the distance of multifarious distant objects. The proposed concept can be of significance in the facile measurements of the distance of

moving celestial objects in the space, cars on the road, airplanes in the sky, or ships in the ocean, among others.

Employing the same concept, a virtual motion picture based point-of-care-testing (POCT) device has been designed and developed where the angle of view of the patients suffering from tunnel vision is determined. In this regard, it is important to note here that the regular monitoring eye health has become important in the modern human life owing to the excessive use of display devices such as computers, mobile phones, or television sets. Different eye diseases such as the tunnel vision have become common even among the children and middle aged people. In this disorder, the angle of view of a person starts contracting from the periphery. However, owing to the lack of regular monitoring facilities, in most of the cases the disorder is detected when it becomes chronic.

Presently, there are different devices to diagnose eye using visual eye test,[18-20] a fundus imaging test[21-24] or optical tomography[25-27] test. In the visual eye testing[28-30] charts of different patterns with predetermined shapes, positions, and colors are kept in front to note the response of the patients and detect the disorders with the help of optometrists or ophthalmologists. On the other hand, the fundus imaging technique[23, 31-33] includes a scanning system, a light source and a receiver. The scanning system scans the fundus, which is the interior line of eye ball with light from a light source. The scanner receives the reflected light from the fundus using a receiver to create an image based on the light received. This image is further analyzed by medical experts for diagnosis. Optical coherence tomography technique[34-38] consists of at least one eye piece through which light incidents on the patient's eye. An interferometer creates optical interference using the

light reflected from the patient's eye. An optical detector senses the optical interference and sends the digital data to a computerized system for further analysis.

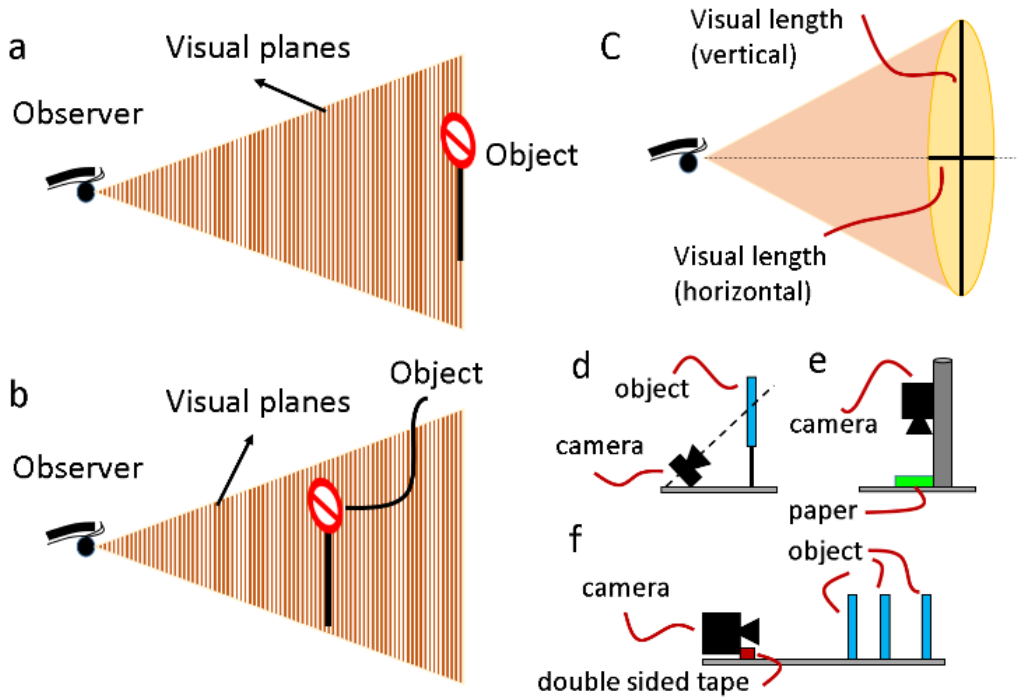

Figure 9.1: This figure shows the concept of visual planes. Images (a) shows the imaginary visual planes in between the object and observer. Image (b) shows how an object enters in a narrower visual plane with respect to the observer, when it comes closer to the observer. Image (c) shows the concept of visual lengths. Image (d – e) shows the different experimental set-up employed in the experiments.

However, all the aforementioned techniques face limitations associated with higher cost of installation and operation, involvement of medical experts, non-portability of the devices, and complex data analysis, among others. In view this, herein we report a method of detecting angle of view of a patient employing the concept of observed speed of a moving object for the POCT of the tunnel vision. In this device, while the virtual motion picture arrangement generates a virtual moving object on the screen, the patient under test is supposed to track the movement of the same from one side-end to the other end of the

screen. The patient is equipped with an on-off stopwatch, which enable him/her to 'start' the tracking of the movement of the virtual object on its appearance on one side of the screen until its disappearance to the other side to mark the 'end'. The angle of view of the patients suffering from tunnel vision, retinitis pigmentosa or hypovolemia can be detected based on the patient's response to the virtual moving object on the screen with the help of the proposed POCT device.

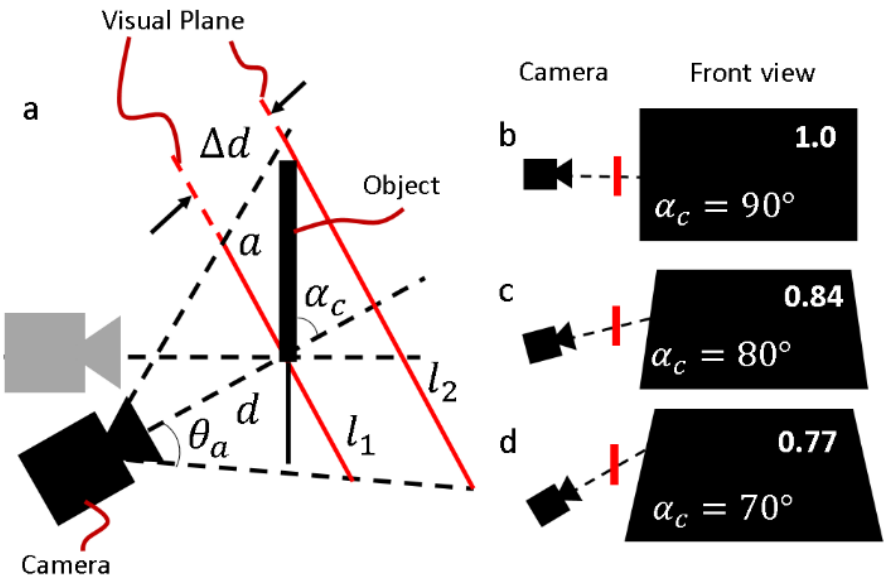

Figure 9.2: This figure shows the effect of angle between the camera-axis with the object. Image (a) shows the schematic illustration of the situation where the angle between the camera-axis with the object is denoted by α_c. The distance between the object and camera is denoted by d while a is the length of the object. The visual planes corresponds to two edges of the object, which is denoted by l_1 and l_2. The distance between the visual planes is denoted by Δd and $2\theta_a$ denotes the angle of view of the camera. Images (b) – (d) show the experimental observation with different values of α_c such as, 90^0, 80^0, and 70^0 and the corresponding ratio (l_r) of the upper side of the quadrilateral to the lower side as indicated in the top right corner.

9.2. Experimental Section

9.2.1 Materials

Digital camera (13 megapixel Redmi 5A) was used to perform the experiments. ImageJ, IrfanView, and Adobe photoshop softwares were used to analyze the captured images and videos. Double sided tapes were procured from local vendors.

9.2.2 Characterization Techniques

The experiments are based on image and video analysis. To perform the experiments in order to determine the distance, motion pictures were taken using a digital camera. Different frames were extracted from the motion picture using an open source software. The frames were then characterized using different image processing softwares as listed in previous section.

9.2.3 Methods

Digital camera was employed to perform the experiments as discussed earlier. An experiment was performed to understand the concept of the visual planes, which determines the observed measurement of an object. In this experiment, multiple images of a rectangular object was analyzed for different camera-angle (α_c) i.e. the angle between the camera-axis with the object. In this case, images of a rectangular object (~ 46 cm x 28 cm) was taken by tiling the camera at different angles as shown in image (d) of Figure 9.1. The images were then post processed to analyze the results.

To find the effect of camera velocity, distance, and angle of view on the observed distance between two objects an experimental setup was made using paper and a solid stand. Three sets of a pair of circular dots were drawn on a piece of paper. The first, second, and third pair of dots were separated by a distance of 1 cm, 2 cm and 3 cm, respectively. A

cylindrical stand was marked with distance with a measuring scale. The paper was kept at the end of a cylindrical stand while the cylindrical stand was kept perpendicular to the ground with circular cross-section touching the ground. The camera was moved upwards manually to get a motion picture and image of the dots drawn on the paper as shown in image (e) of Figure 9.1. The angle of view of the camera was changed by increasing the optical zoom of the camera and the motion picture width was varied by varying the width of display during analysis.

Another experiment was performed to determine the distance of three objects A, B, and C kept at three different distances of 30 cm, 40 cm, and 60 cm from the digital camera. A line was made on the table using double sided tape to maintain the distance constant during the experiment and the camera was kept behind that line and was moved along the line manually. The average speed of the camera was taken in to consideration for the calculation of distance. The set-up is illustrated in image (f) of Figure 9.1. Similarly, a motion picture of full moon at a night sky was taken into consideration for calculating the distance of the moon.

9.3. Results and Discussion

9.3.1 Visual Plane

The distant object appears smaller whereas the same appears bigger when it is closer to the observer as illustrated in Figure 9.1(a) and 1(b). Thus, two objects placed at different distances can be compared in terms of size. To explain the fact in a simple manner, we can assume that there are infinite numbers of visual planes between the object and observer and due to the angle of view of an observer, the visual planes become bigger as the distance increases between the object and observer. The horizontal and vertical edge to

edge perpendicular length associated with the visual plane can be termed as visual length. Figure 9.1(a) shows a schematic illustration of the visual plane. When an object comes closer to an observer as shown in image (b), the object enters to a narrower visual plane with respect to the observer and thus with respect to the visual length the size of the object becomes larger.

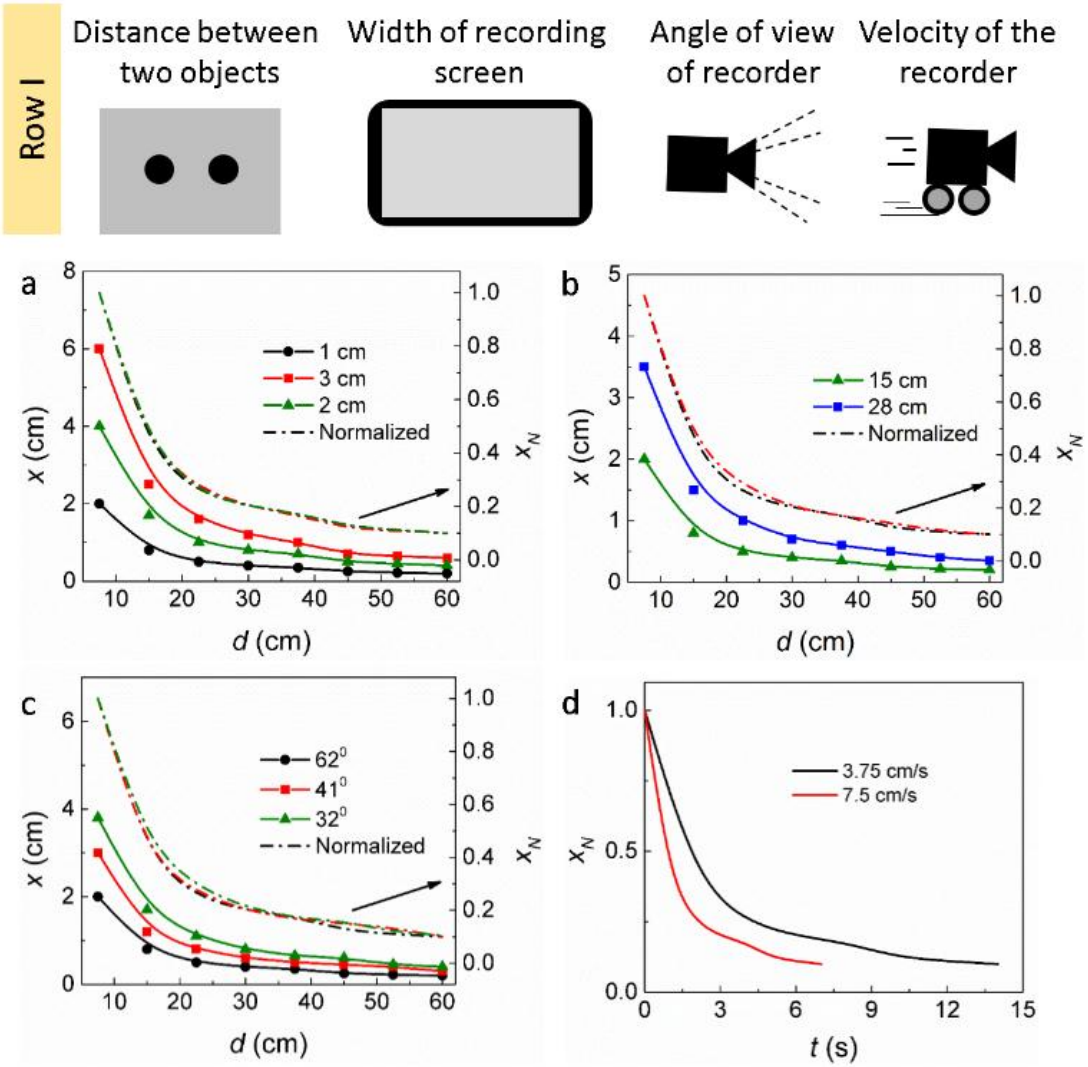

Figure 9.3: This figure shows the study of different parameters. Row I schematically shows the different parameters under considerations. Image (a) shows the change in the distance between two objects (*x*) and the normalized value (x_N) in a motion picture for three different set of objects having actual distances of 1 cm, 2 cm, and 3 cm between them with the distance between the

object and the camera (*d*). Image (b) and (c) show the same study for different motion picture width and angle of view, respectively for a set of objects having 1 cm distance between them. Image (d) shows the change in x_N with time (*t*) for two different average velocity of the camera.

9.3.2 Effect of Recording Angle

The effect of the visual plane appears even more significantly when the images of an object are taken in different angle with respect to axis of the camera and object. This angle can also be termed as camera-angle (α_C). To understand this, image (a) of Figure 9.2 shows a schematic illustration of the situation where the angle between the camera-axis with the object is denoted by α_C. The distance between the object and camera is denoted by d while a is the length of the object. The visual planes corresponds to two edges of the object is denoted by l_1 and l_2, the distance between the visual planes is denoted by Δd, and $2\theta_a$ denotes the angle of view of the camera. From image (A) the relation between α_C and Δd can be written as, $\Delta d = a\cos\alpha_C$. Similarly, the visual planes can be defined as, $l_1 = d\tan\theta_a$ and $l_2 = (d+\Delta d)\tan\theta_a$.

The variation in the visual length due to the change in distance between object and observer can be correlated to the variation in the observed length of an object. For example, if the visual length increases by a certain percent due to the increase in the distance between camera and observer, then the observed length of an object would reduce by the same percentage due to this change in distance. In this case, the variation in the visual length can be evaluated as, $\Delta l = (l_2 - l_1)/l_2 = \Delta d/(d+\Delta d)$. The ratio of upper side to the lower side of the rectangular object can be given as, $l_r = \left[x - x\left(\Delta d/(d+\Delta d)\right)\right]/x = d/(d+\Delta d) = d/(d+a\cos\alpha_C)$. Images (b) – (d) of Figure 9.2 show the experimental observation with different values of α_C such as, 90^0, 80^0, and

70^0. The corresponding ratio (l_r) of the upper side of the quadrilateral to the lower side is as indicated in the top right corner.

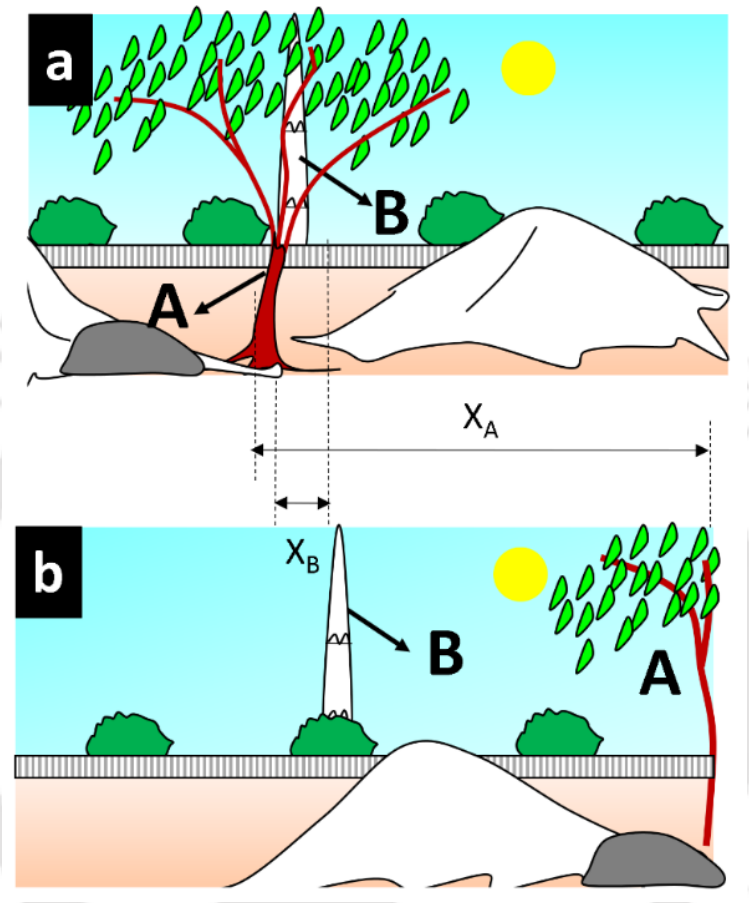

Figure 9.4: This figure shows the associated concept schematically. The two images are showing a photograph taken from the side window of a moving car in a certain time interval. Two of the objects are marked as A and B. The object A which is a tree is nearer to the observer compared to object B which is a tower situated at a larger distance. The displacement of object A and B in the photos are also marked as X_A and X_B, respectively.

9.3.3 Effect of Other Parameters

Different parameters were also studied in order to understand the concept, as shown in the row I of the Figure 9.3. Image (a) shows the change in the distance between two objects (x) and the normalized value (x_N) of the same in a motion picture for three different set of objects having actual distances of 1 cm, 2 cm, and 3 cm between them with the distance between the object and the camera (d). The width of the digital media screen was kept as

15 cm and the angle of view was 62^0. The Image (b) and (c) show the same study for different motion picture width and angle of view, respectively for a set of objects having 1 cm distance between them. Angle of view in case of image (b) was 62^0 and the width of media screen was 15 cm in case of image (c).

The image (a) – (c) suggest that there is almost 90% change or decrement in the observed separation between two points having different actual separation. The angle of view and the media screen length also had no significant effect on the same. However, the decrement in the separation was related to the change in the visual length due to the increase in the distance. There was almost 90% decrement in the visual planes at 60 cm distance and 7.5 cm distance and this was reflected in the observed length scale. Image (d) shows the change in x_N with time (t) for two different average velocity of the camera. This observation suggests that the rate of change in the observed length scale is also dependent on the velocity of the observer or the object.

9.3.4 Concept of Observed Speed

The observed speed of the object was found to depend upon the visual width of the motion picture screen length (l) at that distance (d). To make the concept clear let us consider two different frames of a motion picture taken from the side window of moving vehicle while running at a speed V. If one considers two images (a) and (b) taken at two different time interval as shown in Figure 9.4, the displacement of nearer object A is found to be higher than distant object B in the frames. The images suggest that the observed speed of nearer object A is larger than the same of the distant object B. The reason behind this is the visual length i.e. the length of

one's view at the position of object A is less than that of object B. Hence, the observed lateral displacement of A is higher than B for a given time interval.

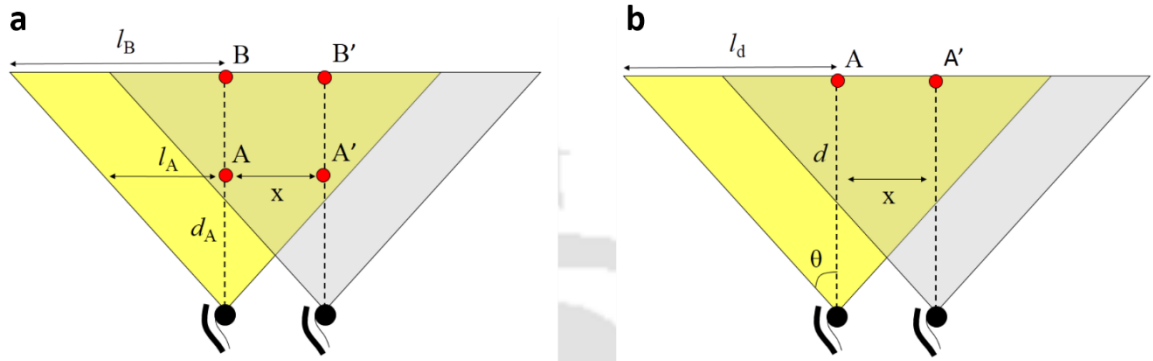

Figure 9.5: This figure shows the schematic illustration of the associated theory. Image (a) shows the displacement of moving objects A and B, situated at a distance d_A and d_B in our different vision length l_A and l_B.

The observed lateral displacement is a function of angle of view of the recording system such as the digital camera or eye. In the Figure 9.5(a), A and B are two objects at a distance d_A and d_B from the viewer having an angle of view $2\theta_a$. The visual length at a distance d_A and d_B are $2l_A$ and $2l_B$. Let us assume that the object A and B are in the middle of their vision and thus the normal line (AB) as shown in Figure 9.5(a) intersects the positions of the object. In this situation, if the viewer moves a distance x in time *t* then there can be an equal amount of displacement of the normal line with respect to the observer. However, for the viewer the observed displacement for A and B are $x/2l_A$ and $x/2l_B$ fraction of total visual length in the same time *t* and thus observed speed for A is higher than that of B because $l_A < l_B$.

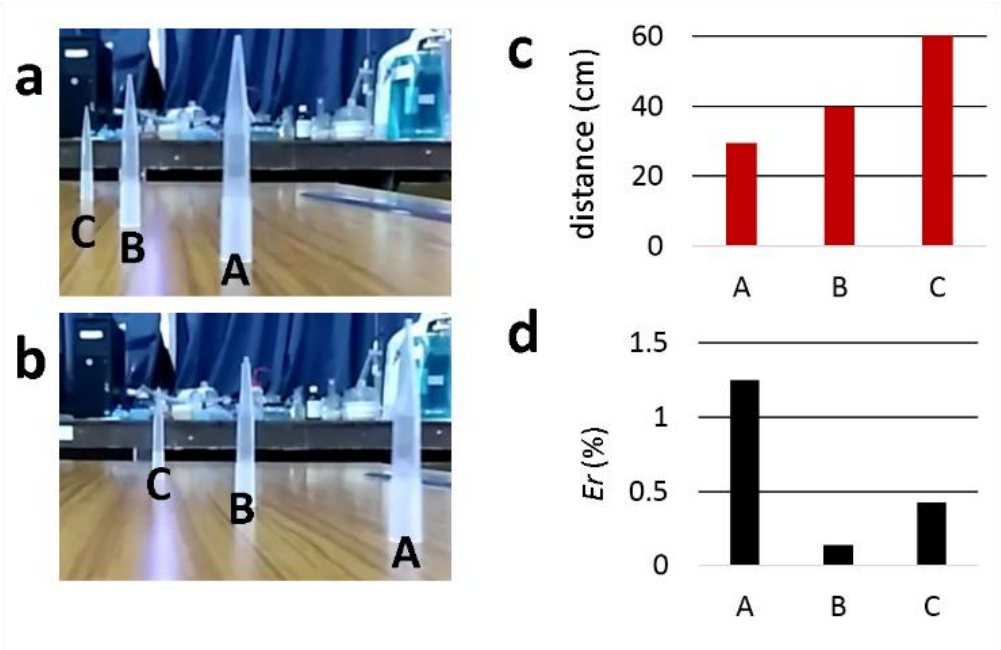

Figure 9.6: The figure shows the experimental images (a and b) for measuring the distance of three objects A, B, and C. The images were taken by a moving (at ~7.5 cm/s) digital camera at t = 0 s and t = 1 s, respectively. Image (c) shows the calculated distances of objects A, B, and C. Image (d) shows the associated error (*Er*) in measurement.

If one captures a video of the event using a digital camera and try to calculate the observed speed, the image width can represent the visual length of each point. To mathematically define the terms, a generic schematic has been made as shown in Figure 9.5(b) where the angle of view is $2\theta_a$, visual length at a distance d is $2l_d$, and the distance travelled by the viewer is x a time interval of, *t*. In this situation, the relation between l_d, d and θ_a is, $l_d = (d \times \tan\theta_a)$. Let us consider the camera display width to be w. Thus, in the image w represents $2l_d$ while x is represent by $(2l_d \times x_C)/w$ where x_C is the scaled distance in camera. The time taken by the camera to go from A to A' is *t* and the speed of the camera is, $V_C = x/t$. In order to represent the velocity in the reference frame of camera, we obtain,

$V_C = (2l_d \times x_C)/(w \times t)$ in which if we put the value of l_d then the speed of the camera is obtained as,

$$V_C = (2 \times d \times \tan\theta_a \times x_C)/(w \times t). \quad (9.1)$$

Here, the value of x_C can be measured in the image and value of t can be extracted from the frame rate and value of θ_a is fixed for a digital camera. Now, if one knows the value of d, the velocity V_C can be evaluated. For example, in this case, if $d = 0$ then, $V_C = 0$ which is because of assuming the observer as a point. In this calculation, $d = 0$ indicates the visual length $l_d = 0$ which means the observer or object is non-existent and hence $d = 0$ does not have any physical significance.

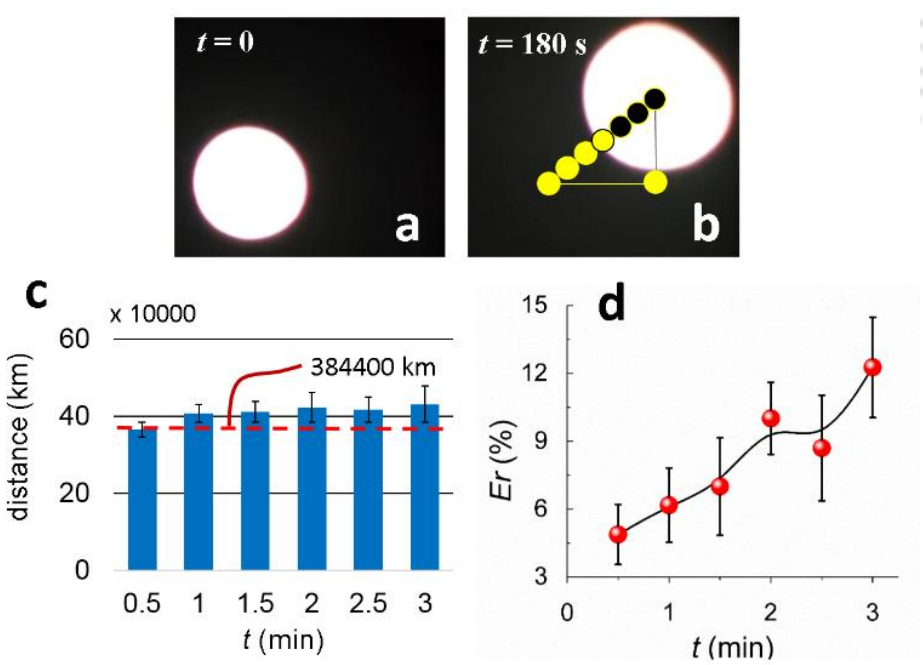

Figure 9.7: The figure shows the images (a) and (b) of moon at t = 0 s and t = 180 s, respectively. Image (c) shows the calculated distance of moon at different time intervals. The dotted red line shows the reported distance of moon from earth. Image (d) shows the associated deviation in terms of percentage error (*Er*) while measuring the distance between moon and earth for different time intervals using the proposed theory of observation.

Importantly, the same theory can also be extended for both moving observer and moving object. In such situation, the relative speed or velocity is expected to play the role in determining the distance and angle of view. Figure 9.6 shows a demonstration of measuring distance where the distances of three objects A, B, and C have been measured. Images (a) and (b) shows two consecutive frames taken at t = 0 and t = 1 s. Image (c) shows the calculated distances of objects A, B, and C. The error (*Er*) in calculated distance is shown in image (d). The error (*Er*) in the plot (d) represents the percentage deviation of original measured distance and the calculated distance using the above mentioned concept. This concept can also be applied to investigate the distance of celestial object on night sky, just by analyzing recorded motion pictures such as videos, the velocity of observer in this situation is the speed of earth. However, if we track a known distant celestial object like moon, we can also track the revolution speed of earth on daily basis and can explore different environmental and cosmic phenomenon. This probably is one of the easiest and economic concept to know the distance of other celestial objects and keeping track of speed of earth. Images (a) and (b) of Figure 9.7 shows the images of moon taken at t = 0 and t = 180 s. In image (b) the yellow and black dots denote the position of the moon at different timings at an interval of 30 s. In this case the displacement of moon along the green-line was taken into consideration for measuring the distance between the observer and the moon. Image (c) of Figure 9.7 shows the calculated distance of moon at different time intervals. The dotted red line shows the reported distance of moon from earth. The error (*Er*) in the calculated result is shown in image (d). The error shows the percentage deviation of

the distance from the reported distance. According to the plot, it is evident that a short-time measurement can yield more accurate result.

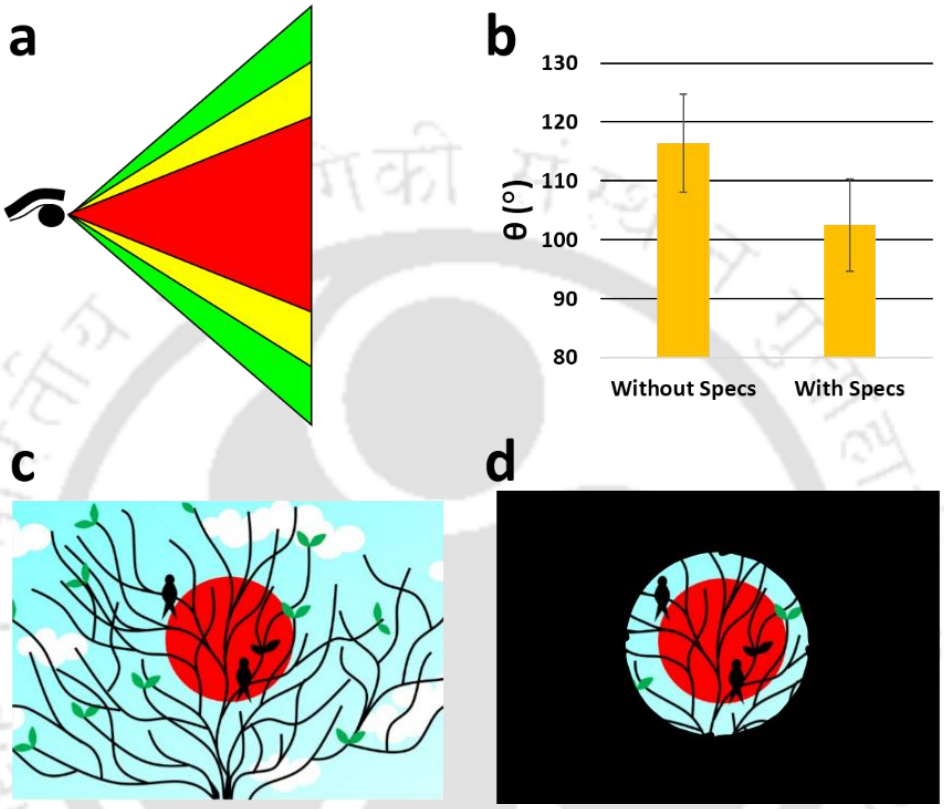

Figure 9.8: The figure shows the measurement of angle of view using the proposed methodology. Image (a) shows the concept of angle of view and image (b) shows the measured angle of view of a person with and without specs. Image (c) and (d) illustrates normal vision and tunnel vision effects, respectively in order to explain the biomedical importance of measuring angle of view. Thus, the proposed method can be useful in detection diseases associated with tunnel vision.

9.3.5 Detection of Tunnel Vision

The aforementioned concept can also be applied in medical diagnosis of tunnel vision, an outcome of different diseases like retinitis pigmentosa or hypovolemia. In this disorder, the patients of mentioned diseases suffer from a contraction of angle of view. Figure 9.8 shows the measurement of angle of view using the proposed methodology. Image (a) shows the concept of angle of view contraction in which green is normal, yellow indicates borderline while red is the onset of the disorder.

In the proposed method, we first plan to put forward a motion picture of an object moving horizontally from one side to other with a uniform speed (V_c) in front of a patient at a particular distance. In this case, V_C is the velocity of the object and the camera or observer is stationary. Further, the patient is equipped with a time measuring equipment e.g. stopwatch to record the time up to the point the patient can observe the moving object. Following this, the observed velocity, V_c can be calculated, which can help in evaluating the angle of view, θ_a, from the Eq. (1). In this measurement, we assume, $x_C = w$.

Image (b) shows the measured angle of view of a person with and without specs. In this experiment, the video was played in a screen in front of a user, who recorded the time. Generally, a person loses a portion of vision while wearing a power-eyeglasses as the vision becomes restricted up to the boundaries of eyeglasses. Image (c) and (d) illustrates normal vision and tunnel vision effects, respectively in order to explain the biomedical importance of measuring angle of view. Thus, the proposed method can be useful in detection diseases associated with tunnel vision.

Figure 9.9 shows a proof-of-concept prototype to measure the angle of view for the POCT of the eye diseases related to the tunnel vision. The device is composed of a display and time measuring unit. The headset contains a display and the belt to adjust the headset while the handheld stopwatch measures the time, as shown in the image (a). There are two eye-pieces that allows to watch a video in the display. Thus, when the headset is fit into the eyes of a patient and a moving object is created in the display to pass on through the display side by side, the patient turns on the stop watch immediately at its appearance at one side.

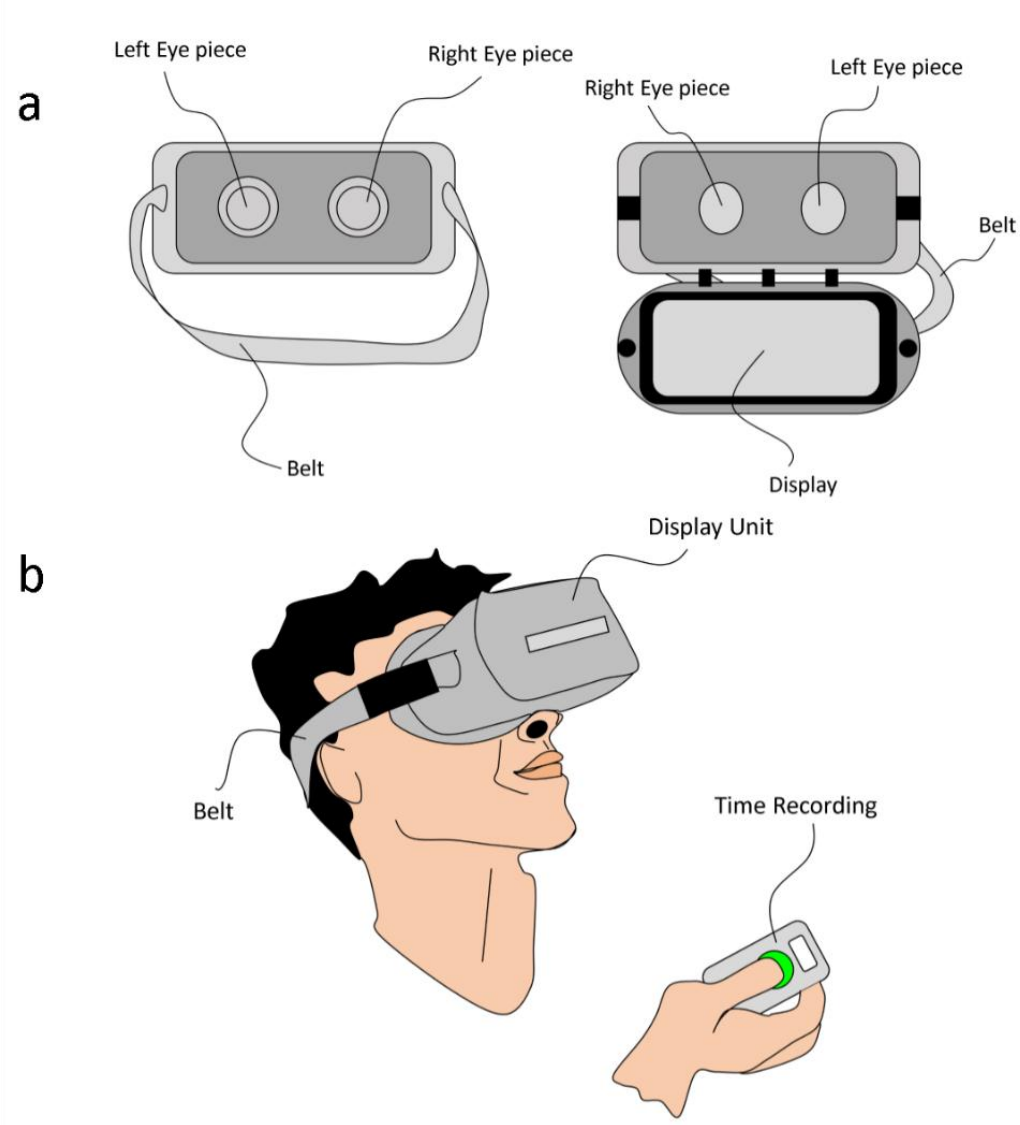

Figure 9.9: Image (a) shows the interior of the headset. The head-set consists of two eye-pieces that allow to watch a video in the display. Image (b) shows the method of detecting angle of view of a person. The system consists of a headset which contains a display and a belt to adjust the headset. There is an instrument similar to stopwatch which measures the time.

The patient is expected to turn off the stop watch once the motion picture disappears from the other side of the display, as shown in the image (b). Based on the response from the patient the angle of view (θ_a) of the viewer can be determined using Eq. (9.1). In this case, we expect to know the velocity of the moving object on the virtual motion picture to enable the calculation of, θ_a.

9.4. Conclusions

In summary, this work uncovers an entirely distinct pathway of measuring distance of a moving object employing the variation in the observed speed of a moving object with distance. Employing the well-known phenomenon of the reduction in the observed speed of an object with the increase in its distance from the viewer a geometrical argument has been developed to determine the speed of the moving object dynamically with time. Example cases are shown to measure the velocities of celestial objects or moving bodies employing the simple concept.

The study also shows that when an object goes away (closer) from (to) an observer, it enters in a new visual plane having a higher (lower) visual length and smaller (larger) appearance. Thus, following the same principle, a pair of objects appear as a single point if they are observed from an infinite distance. This very fact can be correlated to determine the angle of view of a viewer. In it well known that the angle of view of eyes of a human being is a potential parameter to detect many diseases like tunnel vision due to retinitis pigmentosa, or hypovolemia, among others. The aforementioned principle has been employed to design and develop a virtual motion picture based point-of-care-testing (POCT) device where the angle of view of a patient. A headset has been developed to generate a virtual moving object on the screen while the patient under test is supposed to track the movement of the same from one side-end to the other on the screen. The patient is equipped with a stopwatch to track the movement of the virtual object on its appearance on one side of the screen until its disappearance to the other to end. Based on the patient's response the angle of view of the patients suffering from tunnel vision can be detected with the help of the proposed POCT device.

The results reported can be of significance in the facile measurement of the distance of moving celestial objects in the space, cars on the road, airplanes in the sky, or ships in the ocean alongside its utility as a POCT device for tunnel vision detection.

References

1. S. Lanzisera, D. Zats and K. S. J. Pister, *IEEE Sensors Journal*, 2011, **11**, 837-845.
2. J. Rogowski, Xth International Scientific and Technical Conference "Computer Sciences and Information Technologies" (CSIT), 2015.
3. F. Gueuning, M. Varlan, C. Eugene and P. Dupuis, *IEEE Instrumentation and Measurement Technology Conference and IMEKO Tec*. 1996.
4. M. Parrilla, J. J. Anaya and C. Fritsch, *IEEE Transactions on Instrumentation and Measurement*, 1991, **40**, 759-763.
5. J. L. Crowley, International Conference on Robotics and Automation, 1989.
6. D. Webster, *IEEE Transactions on Instrumentation and Measurement*, 1994, **43**, 578-582.
7. P. Bahl and V. N. Padmanabhan, IEEE Computer and Communications Societies (Cat. No.00CH37064), 2000.
8. B. Alavi and K. Pahlavan, *IEEE Communications Letters*, 2006, **10**, 275-277.
9. A. H. Sayed, A. Tarighat and N. Khajehnouri, *IEEE Signal Processing Magazine*, 2005, **22**, 24-40.
10. N. Bobroff, *Measurement Science and Technology*, 1993, **4**, 907.
11. M.-C. Amann, T. M. Bosch, M. Lescure, R. A. Myllylae and M. Rioux, SPIE, 2001.

12. E. Sardini and M. Serpelloni, *Sensors*, 2009, **9**, 943.

13. K. D. Froome and R. H. Bradsell, *Journal of Scientific Instruments*, 1961, **38**, 458.

14. M.-G. Suh and K. J. Vahala, *Science*, 2018, **359**, 884.

15. X. Zheng, C. Zhao, H. Zhang, Z. Zheng and H. Yang, International Conference on Optical Instruments and Technology, 2018.

16. Y. Liu, L. Yang, Y. Guo, J. Lin, P. Cui and J. Zhu, *Optics and Lasers in Engineering*, 2018, **101**, 35-43.

17. X. Xiong, X. Qu and F. Zhang, International Conference on Optical Instruments and Technology, 2018.

18. J. S. Glaser, *Neuro-ophthalmology*, Lippincott Williams & Wilkins, 1999.

19. N. G. Congdon, H. A. Quigley, P. T. Hung, T. H. Wang and T. C. Ho, *Acta Ophthalmologica Scandinavica*, 1996, **74**, 113-119.

20. H. D. Perry and E. D. Donnenfeld, *Current Opinion in Ophthalmology*, 2004, **15**, 299-304.

21. A. E. Elsner, S. A. Burns, J. J. Weiter and F. C. Delori, *Vision Research*, 1996, **36**, 191-205.

22. L. A. Yannuzzi, M. D. Ober, J. S. Slakter, R. F. Spaide, Y. L. Fisher, R. W. Flower and R. Rosen, *American Journal of Ophthalmology*, **137**, 511-524.

23. R. Bernardes, P. Serranho and C. Lobo, *Ophthalmologica*, 2011, **226**, 161-181.

24. *United States Pat.*, US20150313467 A1, 2012.

25. S. R. Arridge, *Inverse Problems*, 1999, **15**, R41.

26. D. A. Boas, D. H. Brooks, E. L. Miller, C. A. DiMarzio, M. Kilmer, R. J. Gaudette and Z. Quan, *IEEE Signal Processing Magazine*, 2001, **18**, 57-75.

27. *United States Pat.*, US8410456 B2, 2009.

28. R. W. Beck, P. S. Moke, A. H. Turpin, F. L. Ferris, III, J. P. SanGiovanni, C. A. Johnson, E. E. Birch, D. L. Chandler, T. A. Cox, R. C. Blair and R. T. Kraker, *American Journal of Ophthalmology*, **135**, 194-205.

29. P. M. Livingston, C. A. Carson, Y. L. Stanislavsky, S. E. Lee and H. R. Taylor, *Ophthalmic Epidemiology*, 1994, **1**, 139-148.

30. *United States Pat.*, US20040207813, 2001.

31. J. I. Lim, L. LaBree, T. Nichols and I. Cardenas, *Ophthalmology*, **107**, 866-870.

32. G. K. Frampton, N. Kalita, L. Payne, J. L. Colquitt, E. Loveman, S. M. Downes and A. J. Lotery, *Eye*, 2017, **31**, 995.

33. Z. Kapsala, A. Anastasakis, D. Mamoulakis, I. Maniadaki and M. Tsilimbaris, *Journal Français d'Ophtalmologie*, 2018, **41**, 39-44.

34. H. Schulz-Hildebrandt, B. Sauer, F. Reinholz, M. Pieper, M. Mall, P. König and G. Huettmann, Conference Presentation in SPIE BiOS, 2017.

35. M. Wojtkowski, A. Kowalczyk, R. Leitgeb and A. F. Fercher, *Optics Letter*, 2002, **27**, 1415-1417.

36. M. R. Hee, J. A. Izatt, E. A. Swanson and et al., *Archives of Ophthalmology*, 1995, **113**, 325-332.

37. Y. Jia, S. T. Bailey, T. S. Hwang, S. M. McClintic, S. S. Gao, M. E. Pennesi, C. J. Flaxel, A. K. Lauer, D. J. Wilson, J. Hornegger, J. G. Fujimoto and D. Huang, *Proceedings of the National Academy of Sciences*, 2015, **112**, E2395.

38. *United States Pat.*, EP1858402 A1, 2005.

CHAPTER 10

Summary and Future Scope

Contents

10.1. Summary 283
10.2. Future Scope 287

भारतीय प्रौद्योगिकी संस्थान गुवाहाटी
Indian Institute of Technology Guwahati

10.1. Summary

In summary, the thesis uncovers different platforms with variety of applications such as sensing, energy harvesting, diagnostics, and therapeutics. The sensors have been developed employing different phenomenon such as microfluidics, spintronics, MEMS, and FET. In this regard, diverse smart and nano-materials have been employed to integrate the efficacies of nanoscience and nanotechnology into the microscale sensors. Apart from fabrications and experimentation, multiple computational studies have also been performed to understand underlying the physics and working principles of the devices.

After introducing the problems in the first chapter, in the second chapter, we discuss about a droplet based vapor sensor and energy harvester. The study unveils a microdroplet vapor sensor capable of harvesting energy while sensing. The surface tension gradient across the liquid-air interface of the droplet helps in creating a rotational motion inside the droplet. The experimental investigation suggested that the curved surface of a liquid droplet could set higher rotational motion compared to a flat surface of a water columns in petri dish. Moreover, the experiment demonstrated a liquid state electronic sensor employing a microfluidic phenomenon. The droplet system also was able to generated electrical energy while sensing the organic vapors due to the partial restoration of ζ-potential in the electrodes integrated with the same. Although the generation of power at its present stage is not sufficient to power a portable device, however, this experiment probably introduced the idea of self-powered microfluidic sensing technology. Interestingly, when the vapor stimuli has been replaced by heat, the same droplet system could sense amylase concentration in blood serum as discussed in the third chapter.

In the fourth chapter, we discuss a new fabrication technique of a resistive touchpad. The proposed resistive touchpad is paper based and flexible. The determination technique of a

particular location is based on the output electrical resistance of the system. The touchpad was fabricated in such a manner that it is flexible from both the sides, which enabled its use from either side. The one location of this touchpad was further engineered to make a system for the detection of hand tremor of a Parkinson's patient. The hand tremor detection was also based on resistive response where the fluctuation in the output resistance played the determining role for detection of hand tremor of a user.

In the fifth chapter, we introduced the design and development of a lung monitoring device for point-of-care-testing (POCT) of chronic obstruction pulmonary disease (COPD) such as asthma. The device was developed with the help of CdS nanoparticle based humidity sensor. The nanosensor was fabricated on a paper substrate. The experiments showed the dependency of flow rate of humid air issuing out of human breadth with the electrical conductivity of the of the paper nanosensor. A theoretical analysis was performed to uncover the underlying mechanism of humidity sensing of the paper nanosensor. The said humidity sensor was then applied to detect the peak flow rate of lungs and breathing frequency to determine the lung health of a person.

In the sixth chapter, we discuss about a nanoparticle based back-gated FET biosensor to detect ammonia and urea from urine sample to diagnose kidney related diseases. The FET was fabricated using CdS-TiO_2 nanocomposite as a channel material. Upon exposure with ammonia vapor the response of the FET changes due to the partial reducing nature of ammonia. The human urine sample was also tested to determine ammonia and urea. The result showed a close match with the hospital samples. The proposed back-gated FET showed superior performance in comparison with recently developed similar FET sensors.

In the seventh chapter we innovate a new magnetoresistance phenomenon. In this experiment, when the Ni-Ag core-shell nanoparticles were coated on a paper substrate, the

system showed magnetoresistance in presence of impulse magnetic field. The variation of nanoparticle size in experimental condition showed that below a critical size of ~50 nm, the magnetoresistance response saturated. A series of atomistic and numerical simulations of the governing equations with appropriate boundary conditions have been performed to uncover the underlying physics of the proposed system. The sensor was further employed to detect the concentration of amylase in blood serum, which showed a satisfactory performance when compared with the standard methodologies to detect amylase in the human blood serum samples.

The eighth chapter illustrates a body potential measuring method using micro-nano patterned electrodes. The electrode was developed with micro and nano patterning on a glass substrate. The patterning was done with a polymer named PDMS and the metal was deposited on top of the pattern. The pattern was treated with reduced graphene oxide (RGO) which acted as a filer to micro-nano defects in the patterned surface. Body-potential detection can be useful in determining diseases and disorders related to muscle degeneration, heart, and nerve.

We introduced a new concept of distance and angle of view measurement in the ninth chapter. The proposed invention discussed about a method of measuring distance of an object and angle of view of eyes employing concept of observed speed or velocity. The method can be useful in different fields such as astronomy, surveillance, or defense to measure the variable distance of a moving object. According to this method or concept, distance of any object can be determined if the velocity of observer or object, angle of view of the camera was known. This concept was applied to detect the angle of view of a user using some pre-defined motion picture played at a particular distance with a time

recording device to measure the time during the motion picture. This method can be useful early diagnosis of diseases and disorder associated with tunnel vision.

Concisely, this thesis has broadly covered different aspects of research, namely, (i) innovation of new scientific phenomena, (ii) identification of the underlying physics, chemistry, and engineering behind them, (iii) use of these phenomena for useful applications, and (ii) translation of the invented scientific phenomena into the proof-of-concept prototypes of devices. Scientifically, the findings can be listed out in the following ways. The thesis shows that Marangoni motion was prevalent in case of a curved liquid surface compared to a flat surface when the stimuli was different kind of vapors. Moreover, a liquid state sensor was demonstrated with energy harvesting capability which may be considered as the self-powered microfluidic device. A sensor to detect α-amylase was also developed employing the thermal Marangoni effect. The thesis also shows a novel pathway of fabricating a touchpad. A new spintronic phenomenon namely, impulse-magnetoresistance (IMR) has been suggested and demonstrated. A concept or theory of observed velocity also has been proposed which could be of higher significance or importance in other different fields such as defense, surveillance, astronomy etc. However, application of this concept has been demonstrated as a healthcare device to detect tunnel vision at early stages. Besides the mentioned points, the thesis also demonstrated a nanoparticle based back-gated FET sensor for the detection of ammonia and urea in human urine sample and a mico-nano patterned sensor to detect human body-potential for diagnosing disorders and diseases associated with muscle, brain, heart, and nerve. Apart from the scientific findings as discussed above, the thesis also proposes a few commercial healthcare methods and prototypes for diagnosing lung diseases, tunnel vision, pancreatitis, muscle degeneration, heart, brain or nerve related issues.

10.2. Future Scope

The work in the present thesis can be extended in the following ways,

(i) The droplet based microfluidic sensors can also be targeted for other biosensing application apart from the amylase sensor as discussed.

(ii) The droplet can be loaded with biomolecule functionalized nanoparticles in order to increase the sensitivity.

(iii) The CdS based humidity sensor can also be diversified using stabilized nanocposities in order to detect volatile organic compounds (VOC) and different microbes associated with lung and oral diseases.

(iv) Different geometries or configurations such as top gate FET sensor can be fabricated and the channel dimensions can be reduced to check the variation in the responses.

(v) The channel material can also be functionalized with biomolecules to detect different bio-markers.

(vi) The materials of the magnetoresistance based sensor can be replaced with other metals or polymers in order to improve the response.

(vii) The concept of observed speed/velocity can be tried out in different fields like defense and surveillance by creating an application which can measure distance from a video.

(viii) The micro-nano patterns can be varied to find out any possibility of improvement.

(ix) The body potential response can be analyzed in a more detailed manner to check whether any other body parameters like ECG, EEG etc can be exactly extracted from the present data or not.

भारतीय प्रौद्योगिकी संस्थान गुवाहाटी
Indian Institute of Technology Guwahati

Appendix - I

Comparison and Limitations

A. Microfluidic sensors

Comparison: Two types of microfluidic sensors have been developed, one is a droplet based vapour sensor and the other one is the thermal Marangoni based α-amylase sensor. There is rarely any commercial α-amylase sensor available at present. Moreover, the commercial organic vapour sensors are solid state metal oxide semiconductor based. Arguably, this thesis introduces first liquid state droplet based microfluidic vapour sensor with a possibility towards the development of self-powered sensor.

Limitations: One of the major limitation of the liquid-state device is the packaging and implementation of the sensor in a device. A proposed device model has been given below as a prospective solution to use the vapour sensor as a product.

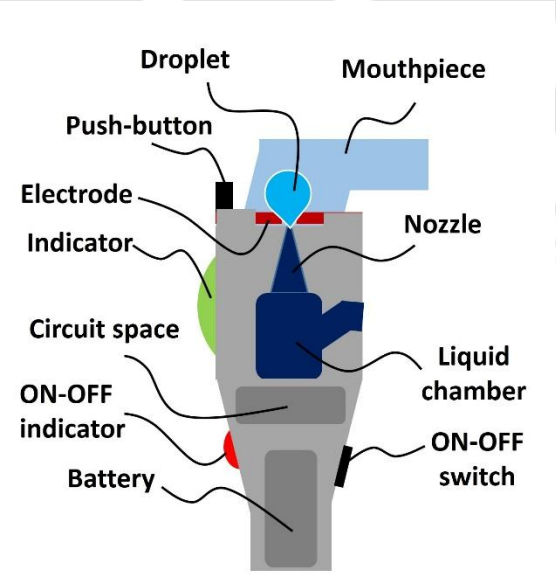

Figure A1.1: This image shows a prospective device model for the droplet based vapour sensor.

Another major problem is the ambient and atmospheric disturbance. However, a sufficiently smaller droplet typically at micro or nanoscale can get rid of this problem.

In principle, the droplet vapour system can be termed as an energy harvester as it is able to translate the mechanical energy i.e. Marangoni recirculation into an electrical one. This energy harvesting has been performed in a microfluidic droplet based system and arguably the first-step towards the droplet based microfluidic self-powered sensor system. Although a substantial improvement is required in this direction and this is kept a future scope of this work.

B. Paper based sensors

Comparison: There are three different types of paper based sensors as discussed in the thesis. Among those the paper based hand tremor detection device is arguably the one of its kind and thus comparison is not likely. However, the paper based magnetoresistive sensor have some counterparts which is mostly layered structure and works on constant magnetic field as discussed in the introduction section of Chapter 6. The proposed sensor only works at impulse magnetic field. Moreover, this is a paper based disposable MR sensor capable of detecting α-amylase in blood serum. Lastly, the paper based humidity sensor and lung monitoring device (LMD) has a few commercial counterparts. A detailed comparison and market study has been performed as shown below.

The initial medical, customer, market survey, and design reports for the lung monitoring device are as follows.

Figure A1.1: This image summarizes the initial survey report of the proposed innovation. This survey is done with the support of Department of Design, IIT Guwahati.

User survey and expert views: The initial survey as shown in Figure A1.1, illustrated the applicability of the present device. We have discussed with 3 doctors and 1 pulmonologist. We wanted to know the following details,

1. The need of the device.
2. The end users of the device.
3. Frequency of usage of device.
4. Popularity of the device among Asthma patients.
5. Behaviour of the patients towards the device.

According to the doctors the device is useful but addition of few more attributes such as detection of tidal volume, capacity of lungs would add more value to the present work. The patients and doctors themselves can be the end users of the device. However, the

mentioned attributes can make the device more acceptable and attractive to doctors.

For doctors, the usage of the device would be high as they generally treat a huge number of patients every day. However, patients or common people would like to use the device at least once a day.

We also have discussed with few patients, who has given a positive response but they also mentioned few points as listed below,

1. The existing devices are costly and hence not preferred. If the cost of the device can be reduced to say 500 INR, it would become popular among patients.
2. The patients do not trust the accuracy of such devices, however, the mobile phone display attracted their attention and similar devices for blood glucose monitoring are also becoming popular.
3. The patients do not find time in their hectic day to perform such a test, however the portability and ease of use of the present device are sounded promising for them.

Currently we are working on these mentioned issues to add attributes.

Market study: According to this report in Figure A1.2, it is evident that similar product is already in the market and doing very good business. However, the cost associated with these devices is high and thus most of the cases are not affordable or attractive for middle and lower middle class people. In our innovation, we incorporated a replaceable paper sensor and the device uses the mobile phone's display unit. These attributes are helpful to cut the price significantly, which in turn will lead to an affordable product.

We have surveyed four popular medical devices associated with COPD as listed below,

Philips Respironics - Personal Asthma Monitoring

- It costs 3000 Rs. It is a mechanical device in which the indicator covers a certain

distance depending on the peak flow. The accuracy of the device is around +/- 10 %. Its body is made of ABS plastic

Asthma MD- 3 Zone Management System

– It costs 13 $ and is not available in India. It creates digital overview of asthma activity using a mobile application. It helps doctors prescribe medicines by regular tracking. The QR Code is link to tutorials. The three zones helps to determine what the condition of current lung performance is.

Figure A1.2: This image summarizes the market survey report of the proposed innovation. This

survey is done with the support of Department of Design, IIT Guwahati.

Micro Life - Peak Flow Meter for Spirometry

- It is a digital monitoring device and costs 6000 Rs. It has USB port to upload storage to PC and stores 240 measurements. It measures PEF and FEV1 with high accuracy.

Rossmax

- Its costs 600 Rs.and is mechanical based. It does not allow storage of data and user has to log data on daily basis.

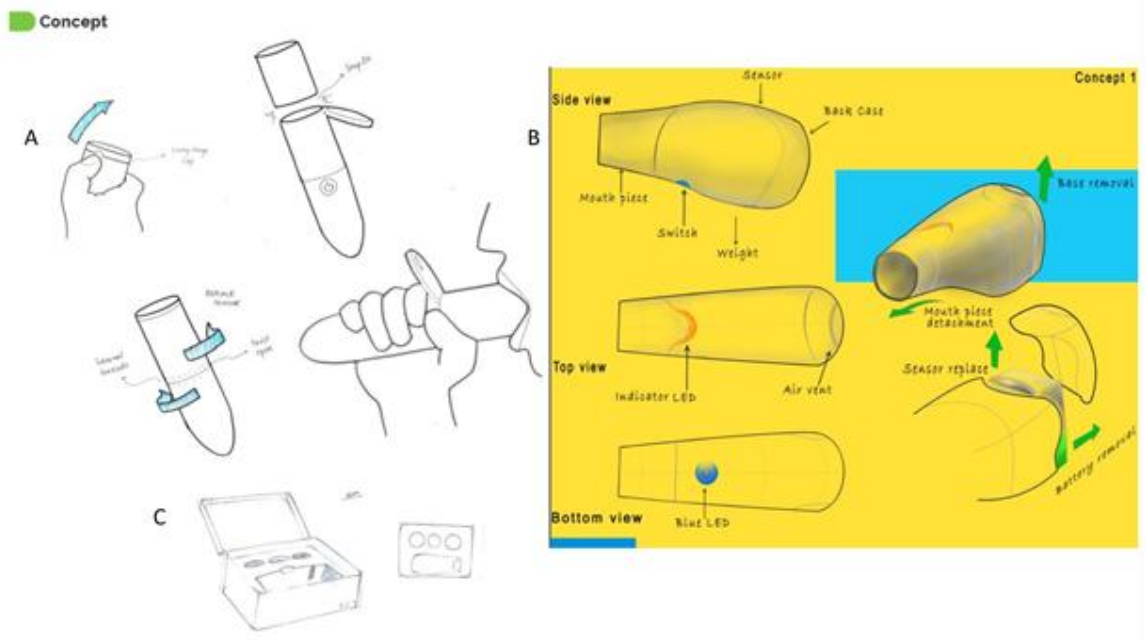

Figure A1.3: This image shows the concept and design of the proposed innovation. Image (A) shows the concept of the device and their different parts. Image (B) shows the aesthetic look of the device once it is ready for trial. Image (C) shows the proposed box and packaging of the device. This design part is done with the support of Department of Design, IIT Guwahati.

Initial design:

Contribution of Department of Design IIT Guwahati: The design and concept shown in Figure A1.3, are initially prepared by Department of Design. Image (A) shows the

concept of the device, where the mouth-piece is removable using a snap-fit. A screw fitting is also proposed in the concept. Further, image (B) shows the aesthetic initial design of the proposed device, where the battery cabinet is kept at the back side of the device. Image (C) shows the tentative box of the device. This image gives the idea of packaging of the proposed innovation. The designs were prepared keeping the estimated circuit space and battery space in mind. This design may change in future depending upon the feedback from industrial partner.

Contribution of industry partner: The industry partner, Forus Electric Pvt. Ltd. has given a design and PCB for the initial prototype development as shown in Figure A1.4 (A-C). Image (A) shows the initial prototype design similar to "d" shape, where the top part is the mouthpiece and the bottom part contains battery, circuit and other electronic component. The assembly of the component is shown in image (B) with the battery and PCBs. This gives an interior look of the device. Image (C) shows the initially prepared PCBs.

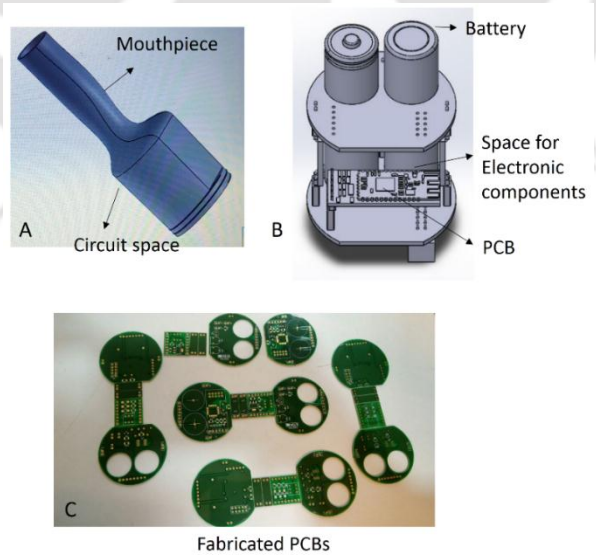

Figure A1.4: This image shows the design and PCB of the proposed innovation by the industry partner. Image (A) shows the initial design of the device. Image (B) shows the interior of the device. Image (C) shows fabricated PCBs of the proposed device. This design has been done and proposed by the Forus Electric pvt. Ltd.

Limitations: One of the major limitation in paper based sensor is to coating the material uniformly on the paper substrate. This can be solved using the screen printing method. A work on the coating procedure is in progress to solve this issue.

Durability of a sensor and stability of nanoparticles are another major concerns. However, experimental results suggests that the sensors are stable for approximately six months. Stability of the sensors for at least one month has been reported for almost all the sensors. However, the disposable sensors with moderate shelf-life is good for commercialization.

C. Other Electronic Sensors

Comparison: This section introduces three different sensors and methods for healthcare application, among which the tunnel vision detection mechanism is based on the concept of observed speed. The body potential detection system detects the electric potential associated with body parts in order to determine any abnormal muscle related issues or physical stress. Although myographic methods determines the body potential, but it is mostly invasive and sophisticated and thus costly. The BG-FET based ammonia sensor determines the urea and ammonia level in urine sample. Any such commercial device is not currently available and thus a comparison with similar FET sensors has been tabulated in the chapter.

Limitation: The fabrication of BG-FET is comparatively complicated and the synthesis of CdS-TiO_2 composite involves special care. Similarly, the patterned electrode design also require expertise in order to develop the sensor.

Currently, the use of urine sample needs some post processing before introducing them on the sensor. To make them usable for a POCT application a standard sample solution needs to be provided where the user will put a drop of urine sample before exposing it to the sensor. However, there is a possibility of making the system even more robust by integrating the solution reservoir directly to the device and connecting it to the reaction chamber using a micro-channel. I kept the development in this direction as a future scope of this research.

Appendix - II

Publications, Patents and Conferences

A1.1 International Publications

From the thesis -

1. **Mitradip Bhattacharjee**, Harshal Nemade and Dipankar Bandyopadhyay, "Nano-Enabled Paper Humidity Sensor for Mobile Based Point-of-Care Lung Function Monitoring", Biosens. Bioelectron., 2017. 94: p. 544-551. (DOI: 10.1016/j.bios.2017.03.049)
2. **Mitradip Bhattacharjee**, Viswanath Pasumarthi, Joydip Chaudhuri, Amit Kumar Singh, Harshal Nemade and Dipankar Bandyopadhyay, "Self-spinning Nanoparticle Laden Microdroplets for Sensing with Energy Harvesting", Nanoscale, 2016. 8(11): p. 6118 - 6128. (DOI: 10.1039/C6NR00217J)
3. **Mitradip Bhattacharjee** and Dipankar Bandyopadhyay, "Mechanisms of Humidity Sensing using CdS Nanoparticles", Sensors and Actuators A: Physical, (Major Revision Stage) 2018.
4. **Mitradip Bhattacharjee** and Dipankar Bandyopadhyay, "Flexible Paper Touchpad for Parkinson's Hand Tremor Detection", (Under Review) 2018.
5. Sagnik Middya, **Mitradip Bhattacharjee**, Dipankar Bandyopadhyay, "A Multipurpose Reusable Nano-BG-FET for Point-of-Care Estimation of Ammonia in Air and Urea in Human Urine", (Under Review) 2017.

Other publications -

6. Nilanjan Mandal, **Mitradip Bhattacharjee**, Arun Chattopadhyay, and Dipankar Bandyopadhyay, "Point-of- Care-Testing of Amylase Activity in Human Blood Serum", Biosensors and Bioelectronics, 2018. xx: p. xxx-xxx. (Accepted).
7. Sagnik Middya, **Mitradip Bhattacharjee**, Nilanjan Mandal, and Dipankar Bandyopadhyay, "RGO-Paper Sensor for Point-of-Care Detection of Lipase in Blood Serum." IEEE Sensors Letters, 2018. 4: p. 1-4. (DOI: 10.1109/LSENS.2018.2849418).
8. Tamanna Bhuyan, **Mitradip Bhattacharjee**, Amit Kumar Singh, Siddharth Sankar Ghosh and Dipankar Bandyopadhyay, "Boolean-Chemotaxis for Deciphering the

Motions of Microorganisms", Soft Matter, 2018. 14: p. 3182-3191. (DOI: 10.1039/C8SM00132D)

9. Bolleddu Ravi, Snigdha Chakraborty, **Mitradip Bhattacharjee**, Shirsendu Mitra, Abir Ghosh, Partho Sarathi Gooh Pattader, and Dipankar Bandyopadhyay, "Pattern Directed Ordering of Spin-dewetted Liquid Crystal Micro or Nanodroplets as Pixelated Light Reflectors and Locomotives", ACS Appl. Mater. Interfaces, 2017. 9(1): p. 1066–1076. (DOI: 10.1021/acsami.6b12182)
10. **Mitradip Bhattacharjee**, Seim Timung, Tapas Kumar Mandal and Dipankar Bandyopadhyay, "Microfluidic Schottky-Junction Photovoltaics with Superior Efficiency Stimulated by Plasmonic Nanoparticles", (Under Review) 2017.
11. Bolleddu Ravi, **Mitradip Bhattacharjee**, Abir Ghosh, and Dipankar Bandyopadhyay, "Fabrication of Liquid Crystal Nanolenses Employing the Contact Line Instabilities of Evaporating Films", (Under Review) 2017.
12. Siddharth Thakur, Saptak Rarotra, **Mitradip Bhattacharjee**, Gayatri Natu, Tapas Mandal, Ashok Dasmahapatra, and Dipankar Bandyopadhyay, "Self-Organized Large-Scale-Integration of Mesoscale Ordered Heterojunctions for Process-Intensified Photovoltaics", (Under Review) 2018.
13. Bolleddu Ravi, Snigdha Chakraborty, **Mitradip Bhattacharjee**, Nandini Bhandaru, Partho Sarathi Gooh Pattader, Rabibrata Mukherjee, and Dipankar Bandyopadhyay, "Pattern Directed Phase Transitions and Vapor Sensing of Liquid Crystals under Ambient Conditions." (Under Review) 2018.

A1.2 Book Chapters

1. **Mitradip Bhattacharjee** and Dipankar Bandyopadhyay, "Conductive Polymer Nanobiosensors", Springer (Accepted) 2018.
2. **Mitradip Bhattacharjee** and Dipankar Bandyopadhyay, "Optical Nanosensors for Water Quality Monitoring", Springer (Minor Revision Stage) 2018.

A1.3 International Patents

1. **Mitradip Bhattacharjee**, Dipankar Bandyopadhyay, and Sunny Kumar, "A POINT-OF-CARE HAND TREMOR DETECTION DEVICE", International patent status: PCT Appl.No. PCT/IN2017/050366 dated 29-08-2017.
2. **Mitradip Bhattacharjee**, Seim Timung, Dipankar Bandyopadhyay, and Tapas Kumar Mandal, "A MICROFLUIDIC ELECTRICAL ENERGY HARVESTER", International patent status: PCT Appl.No. PCT/IN2017/050364 dated 29-08-2017.
3. **Mitradip Bhattacharjee**, Dipankar Bandyopadhyay, and Harshal B. Nemade, "A LUNG CONDITION MONITORING DEVICE.", International patent status: PCT Appl.No. PCT/IN2017/050363 dated 29-08-2017.
4. **Mitradip Bhattacharjee**, Sagnik Middhya, and Dipankar Bandyopadhyay, "A POINT-OF-CARE SYSTEM FOR DETECTION OF THE PHYSICAL STRESS AT DIFFERENT PARTS OF BODY", International patent status: under processing.
5. **Mitradip Bhattacharjee**, and Dipankar Bandyopadhyay, "A MOBILE RF RADIATION DETECTION DEVICE", International patent status: under processing.

A1.4 National Patents

1. **Mitradip Bhattacharjee**, Siddharth Thakur, and Dipankar Bandyopadhyay, "ACOUSTIC DIAGNOSTIC POINT-OF-CARE TESTING DEVICE FOR BLOOD UREA DETECTION", Indian patent application number 201731037223 dated 20-10-2017.
2. **Mitradip Bhattacharjee**, Sagnik Middhya, and Dipankar Bandyopadhyay, "A POINT-OF-CARE SYSTEM FOR DETECTION OF THE PHYSICAL STRESS AT DIFFERENT PARTS OF BODY", Indian patent application number 201731037222 dated 20-10-2017.
3. **Mitradip Bhattacharjee**, and Dipankar Bandyopadhyay, "A MOBILE RF RADIATION DETECTION DEVICE", Indian patent application number 201731037221 dated 20-10-2017.
4. **Mitradip Bhattacharjee**, Dipankar Bandyopadhyay, and Sunny Kumar, "A POINT-OF-CARE HAND TREMOR DETECTION DEVICE", Indian patent application number: 201731018530A dated 26-05-2017.

5. **Mitradip Bhattacharjee**, Seim Timung, Dipankar Bandyopadhyay, and Tapas Kumar Mandal, "A MICROFLUIDIC ELECTRICAL ENERGY HARVESTER", Indian patent application number: 201631036408A dated 24-10-2016.
6. **Mitradip Bhattacharjee**, Dipankar Bandyopadhyay, and Harshal B. Nemade, "A LUNG CONDITION MONITORING DEVICE.", Indian patent application number: 201631033190A dated 28-09-2016.
7. Dipankar Bandyopadhyay, Harshal B. Nemade, and **Mitradip Bhattacharjee**, "A FLEXIBLE PAPER-TOUCHPAD FOR LOW-COST ELECTRONIC APPLIANCES.", Indian patent application number: 201631017054A dated 12-08-2016.
8. **Mitradip Bhattacharjee** and Dipankar Bandyopadhyay, "METHOD TO DIAGNOSE DISEASES ASSOCIATED TO TUNNEL VISION." (Under processing)
9. **Mitradip Bhattacharjee**, Prasfutita Paul, and Dipankar Bandyopadhyay, "THERAPEUTIC TECHNIQUE TO REDUCE HEALTH PROBLEMS" (Under processing)

A1.5 Conferences

1. **Mitradip Bhattacharjee,** Harshal Nemade, and Dipankar Bandyopadhyay, "Nanoparticle based devices for diagnostic application", Research Conclave, IIT Guwahati, India, Mar 08 - 11, 2018.
2. Prashfutita Paul, **Mitradip Bhattacharjee,** and Dipankar Bandyopadhyay, "Magnetoresistance based nanosensors", Research Conclave, IIT Guwahati, India, Mar 08 - 11, 2018.
3. Sagnik Middya, **Mitradip Bhattacharjee,** and Dipankar Bandyopadhyay, "FET based bio-sensors", Research Conclave, IIT Guwahati, India, Mar 08 - 11, 2018.
4. **Mitradip Bhattacharjee**, Harshal Nemade, and Dipankar Bandyopadhyay, "Nanoparticle based sensor to diagnose lung diseases", International Conference on Advance Nanomterials and Nanotechnology (ICANN-2017), IIT Guwahati, India, Dec 18 - 21, 2017.
5. Joydip Chaudhuri, **Mitradip Bhattacharjee**, and Dipankar Bandyopadhyay, "Marangoni effect induced voltage generation from a droplet", International

Conference on Advance Nanomterials and Nanotechnology (ICANN-2017), IIT Guwahati, India, Dec 18 - 21, 2017.

6. Prasfutita Paul, **Mitradip Bhattacharjee**, and Dipankar Bandyopadhyay, "Effect of stirring and time delay on the synthesis of gold nanoparticles", International Conference on Advance Nanomterials and Nanotechnology (ICANN-2017), IIT Guwahati, India, Dec 18 - 21, 2017.
7. **Mitradip Bhattacharjee** and Dipankar Bandyopadhyay, "Enhancement of C-FET device performance by embedding silicon nanoparticles", IEEE Indian Council International Conference (INDICON-2017), IIT Roorkee, India, Dec 15 - 17, 2017.
8. Sagnik Middya, Anvesh Dixit, **Mitradip Bhattacharjee** and Dipankar Bandyopadhyay, "Polyaniline Modified Graphene Oxide for Bio-Sensing Applications", International Conference on Nano and Functional Materials (ICNFM-2017), Pilani, India, Nov 16 - 18, 2017.
9. **Mitradip Bhattacharjee** and Dipankar Bandyopadhyay, "Characteristics of Graphite Deposition on Paper by Mechanical Rubbing of Sources", IEEE Nanotechnology for Instrumentation and Measurement Workshop (NANOfIM-2017), Noida, India, Nov 16 - 17, 2017.
10. **Mitradip Bhattacharjee**, Saptak Rarotra, Sagnik Middya and Dipankar Bandyopadhyay, "The effect of annealing on band gap and optical properties of CdS/CdS-TiO2 nanoparticles", IEEE International Conference on Optoelectronics and Applied Optics (Optronix-2017), Kolkata, India, Nov 2 - 4, 2017.
11. **Mitradip Bhattacharjee**, Harshal Nemade and Dipankar Bandyopadhyay, "Nanoparticle based lung monitoring device", Reflux - 2017, IIT Guwahati, India, Mar 24 - 26, 2017.(Best Paper Award)
12. **Mitradip Bhattacharjee**, Viswanath Pasumarthi, Joydip Chaudhuri, Amit Kumar Singh, Harshal Nemade and Dipankar Bandyopadhyay, "Microfluidic vapour sensor and energy harvester", Research Conclave - 2017, IIT Guwahati, India, Mar 17 - 19, 2017. (Best Poster Award) [Selected among the top 5 research works at the institute]
13. **Mitradip Bhattacharjee**, Viswanath Pasumarthi, Joydip Chaudhuri, Amit Kumar Singh, Harshal Nemade and Dipankar Bandyopadhyay, "Organic vapour detection using nanoparticle laden droplet and the effect of viscosity and vapour-source

distance", IEEE International Conference on Emerging Electronics (ICEE-2016), IIT Bombay, India, Dec 27 - 30, 2016.

14. **Mitradip Bhattacharjee**, Viswanath Pasumarthi, Joydip Chaudhuri, Amit Kumar Singh, Harshal Nemade and Dipankar Bandyopadhyay, "Organic vapor sensing with energy harvesting using nanoparticle laden droplets", International Conference on Functional Materials (ICFM-2016), IIT Kharagpur, India, Dec 12 - 14, 2016.
15. Saptak Rarotra, **Mitradip Bhattacharjee**,and Dipankar Bandyopadhyay, "Effect of microwave assisted annealing on CdS nanoparticles.", International Conference on Functional Materials (ICFM-2016), IIT Kharagpur, India, Dec 12 - 14, 2016.
16. Siddharth Thakur, **Mitradip Bhattacharjee**, Ashok Kumar Dasmahapatra and Dipankar Bandyopadhyay, "Effect of varying semiconducting salt concentrations on the in-situ preparation of gold-cadmium sulphide nanocomposites", International Conference on Functional Materials (ICFM-2016), IIT Kharagpur, India, Dec 12 - 14, 2016.
17. **Mitradip Bhattacharjee**, Viswanath Pasumarthi, Joydip Chaudhuri, Amit Kumar Singh, Harshal Nemade and Dipankar Bandyopadhyay, "Detection of organic vapours employing droplets having nanoparticles", IEEE TechSym-2016, IIT Kharagpur, India, Sep 30-Oct 2, 2016.
18. **Mitradip Bhattacharjee**, Viswanath Pasumarthi, Joydip Chaudhuri, Amit Kumar Singh, Harshal Nemade and Dipankar Bandyopadhyay, "Droplet based organic vapor sensor", Reflux - 2016, IIT Guwahati. (Best Poster Award)
19. **Mitradip Bhattacharjee**, Harshal Nemade and Dipankar Bandyopadhyay, "Effect of Electrode Temperature on Tunneling Current in Fe/MgO/Fe Multilayer Structure", 4th International Conference on Advanced Nanomaterial and Nanotechnology (ICANN-2015), IIT Guwahati, India, December 8-11, 2015.
20. **Mitradip Bhattacharjee**, Saptak Rarotra and Dipankar Bandyopadhyay, "Change in optical absorption of CdS nanoparticles due to microwave assisted annealing", India International Science Festival (IISF-2015), IIT Delhi, India, December 4-8, 2015.
21. **Mitradip Bhattacharjee**, Harshal Nemade and Dipankar Bandyopadhyay, "Effect of Oxide Barrier Height in Spin Dependent Tunneling in MTJ of FeO-MgO Multilayer Structure",XXVII IUPAP Conference on Computational Physics (CCP-2015), IIT Guwahati, India, December 2-5, 2015.

22. **Mitradip Bhattacharjee**, Seim Timung, Nilanjan Mandal, Harshal Nemade and Dipankar Bandyopadhyay, "Self Adhesive Nature of PDMS Thin Film", Reflux -2015, IIT Guwahati, India, March 28-29, 2015.
23. **Mitradip Bhattacharjee**, Nilanjan Mandal, Satarupa Datta, Saptak Rarotra, Harshal Nemade, Tapas Kumar Mandal and Dipankar Bandyopadhyay, "Controlled Drug Release: Attachment of Drugs on Magnetic Nanoparticles", International Conference on Translational Nanomedicine (T-NANO 2014), Ahmedabad, India, December 15-17, 2014.
24. Satarupa Dutta, Nilanjan Mandal, **Mitradip Bhattacharjee**, Harshal Nemade, Arun Chattopadhyay, and Dipankar Bandyopadhyay, "Paper Based Optical Alpha Amylase Sensor", International Conference on Translational Nanomedicine (T-NANO 2014), Ahmedabad, India, December 15-17, 2014.
25. Sunny Kumar, **Mitradip Bhattacharjee**, Seim Timung, Amit Kr. Singh, Tapas Kumar Mandal, Ashok Kumar Dasmahapatra and Dipankar Bandyopadhyay, "Marangoni Effect Induced Droplet Motion For Energy Harvesting", The First International Conference on Emerging Materials: Characterization & Application (EMCA-2014), Kolkata, India, December 4-6, 2014.
26. **Mitradip Bhattacharjee**, Nilanjan Mandal, Harshal Nemade and Dipankar Bandyopadhyay, "Simulation of a Voltage Controlled Resistor Mimicking the Geometry of a MOSFET Device having Graphite Channel", In proceedings of the COMSOL conference, Bangalore, India, November 13-14, 2014.

A1.6 Awards

1. REDSTART Innovation Award – 2018

The award has been given in REDSTART Event organized by NRL in Research Conclave - 2018, in association with the Student Academic Board, Indian Institute of Technology Guwahati for the development of lung monitoring device, which is a point-of-care testing device to diagnose chronic obstruction pulmonary diseases (COPD).

2. PSG Nanochallenge Award (1st position) – 2017

The award has been given in PSG Nanochallange 2017, organized by the PSG Institute of Advanced Studies, Coimbatore in association with Department of Science and Technology, Govt. of India, Pricol Ltd., Colleges of Nanoscale Science and Engineering, State University of Newyork (SUNY) Polytechnic for the development of lung monitoring device, which is a point-of-care testing device to diagnose chronic obstruction pulmonary diseases (COPD).

3. Gandhian Young Technological Innovation (GYTI) Award - 2016.

This award has been given in the Festival of Innovation -2016, organized by Techpedia an initiative of Society for Research and Initiatives for Sustainable Technologies and Institutions (SRISTI) in Rastrapati Bhawan, New Delhi for the development of a paper based touchpad for low-cost electronic appliances.

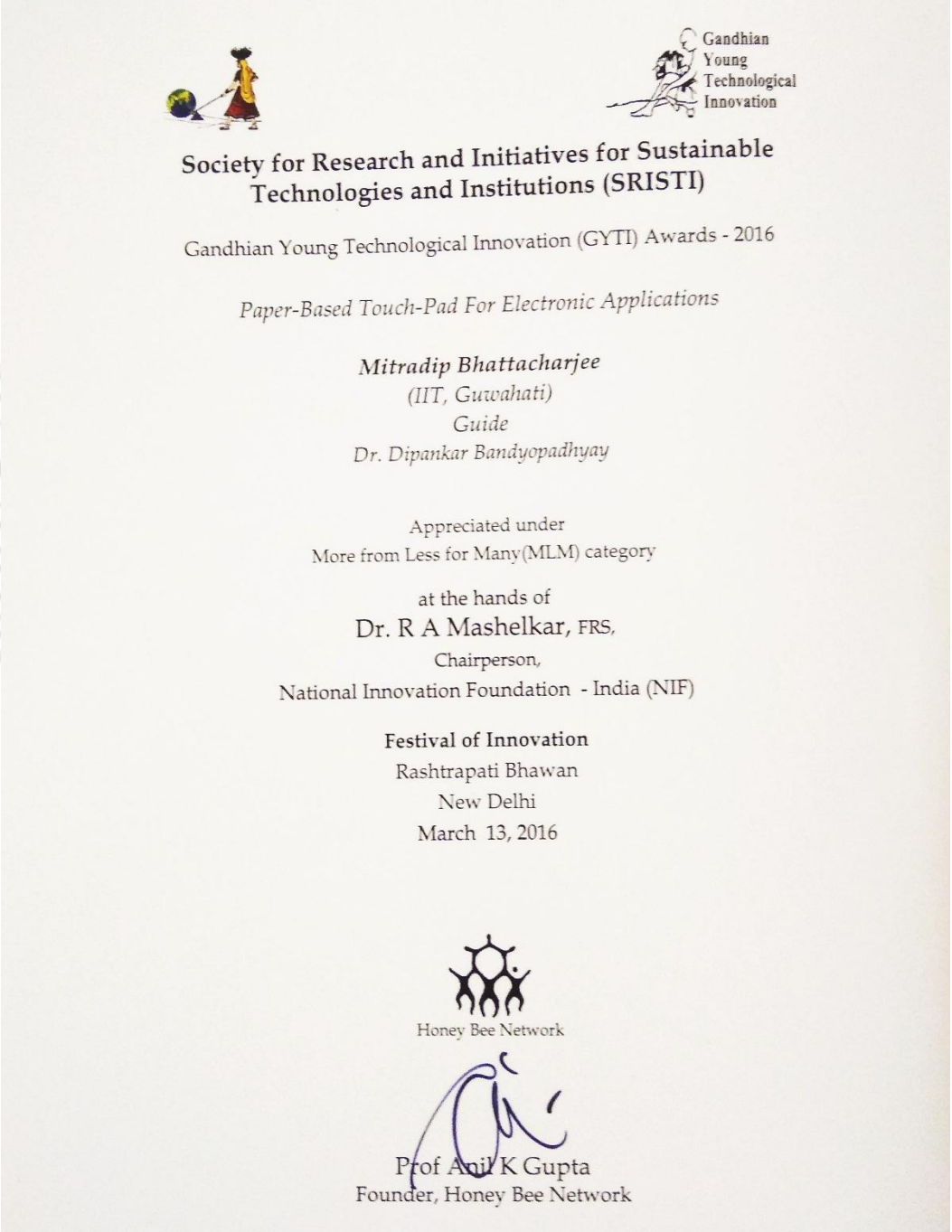

Gandhian Young Technological Innovation

Society for Research and Initiatives for Sustainable Technologies and Institutions (SRISTI)

Gandhian Young Technological Innovation (GYTI) Awards - 2016

Paper-Based Touch-Pad For Electronic Applications

Mitradip Bhattacharjee
(IIT, Guwahati)
Guide
Dr. Dipankar Bandyopadhyay

Appreciated under
More from Less for Many(MLM) category

at the hands of
Dr. R A Mashelkar, FRS,
Chairperson,
National Innovation Foundation - India (NIF)

Festival of Innovation
Rashtrapati Bhawan
New Delhi
March 13, 2016

Honey Bee Network

Prof Anil K Gupta
Founder, Honey Bee Network

Best Paper/Poster Awards

4. Best Paper Award in RESEARCH CONCLAVE – 2018.


Students' Academic Board
IIT Guwahati

Research Conclave'18
An amalgamation of Academia, Industry & Startups
March 8-11, 2018

Certificate of Appreciation

This is to certify that Mitradip Bhattacharjee of IIT Guwahati has been honored with Best Oral presentation at Research Conclave'18, organized by Students' Academic Board, Indian Institute of Technology Guwahati, India.

Chairman, Students' Academic Board
Faculty Convener, Research Conclave'18
Faculty Co-Convener, Research Conclave'18
Prince Kumar Baranwal, Student Convener, IIT Guwahati

5. Best Poster Award in REFLUX - 2017.


Department of Chemical Engineering
IIT Guwahati

Certificate

OF APPRECIAITION

This is to certify that Mr./Ms. Mitradip Bhattacharjee secured FIRST position in Paper Presentation during Reflux 2017, Annual Symposium organised by Department of Chemical Engineering, IIT Guwahati.

Dr. R.Anandalakshmi, Faculty Co-ordinator, Reflux 2017
Dr. Raghvendra Gupta, Faculty Co-ordinator, Reflux 2017
Shubham Chaturvedi, Convener, Reflux 2017

6. Best Poster Award in RESEARCH CONCLAVE - 2017.

Organized by
SAB, IITG

In association with
IIT Guwahati

Research Conclave'17

An amalgamation of Academia, Industry & Startups

16th to 19th March 2017

Certificate of Appreciation

This is to Certify that

MITRADIP BHATTACHARJEE

is the **Departmental Winner in Best Poster** Category Competition in **Research Conclave'17** organized by Students' Academic Board, Indian Institute of Technology Guwahati.

Prof. Anupam Saikia
Chairperson, SAB
IIT Guwahati

Dr. Ajaikumar B Kunnumakkara
Convener
IIT Guwahati

Dr. Prasenjit Khaniker
Co- Convener
IIT Guwahati

Mr. Arup Jyoti Borah
Student's Convener
IIT Guwahati

7. Best Paper Award in REFLUX - 2016.

Department of Chemical Engineering
Indian Institute of Technology Guwahati

REFLUX

Certificate

of

Merit

This is to certify that

Mr/Ms MITRADEEP BHATTACHARJEE

has secured 1st *in* POSTER PRESENTATION (MATERIAL SCIENCE & TECHNOLOGY)

in Reflux 2016.

Faculty Coordinator, Reflux 2016

www.reflux.in

Convener, Reflux 2016